Modeling and Control of Active Cochlear Implant

Lingxiao Xun

CENTRALE LILLE

THESE

Présentée en vue
d'obtenir le grade de

DOCTEUR

En

Spécialité : Automatique, Génie Informatique,

Traitement du Signal et des Images

Par

Lingxiao XUN

DOCTORAT DELIVRE PAR CENTRALE LILLE

Titre de la thèse :

Modélisation et Commande de L'implant Cochléaire Active

Modeling and Control of Active Cochlear Implant

Soutenue le 14 Mars 2024 devant le jury d'examen :

Président	Philippe POIGNET	Professeur, Université de Montpellier
Rapporteur	Brahim TAMADAZTE	Directeur de recherche, Sorbonne Université
Rapporteur	Guillaume LAURENT	Professeur, ENSMM
Examinateur	Philippe POIGNET	Professeur, Université de Montpellier
Examinatrice	Rosane USHIROBIRA	Chargé de recherce, INRIA Lille
Directeur du thèse	Alexandre KRUSZEWSKI	Professeur, Centrale Lille
Co-directeur du thèse	Gang ZHENG	Chargé de recherce, INRIA Lille

Thèse préparée dans le Centre de Recherche en Informatique, Signal et Automatique de Lille,
CRIStAL, CNRS UMR 9189

Ecole Doctorale MADIS-631

Contents

Abstract

According to the statistic of World Health Organization, over 5% of the world's population, i.e., 360 million people, has disabling hearing loss (328 million adults and 32 million children). Hearing aids are quite successfully used for the partially deafened people. Traditional hearing aids, while effective for partial hearing loss, often fall short for individuals with severe deafness. In such cases, cochlear implant surgery emerges as a preferable solution. Traditional manual implantation, however, grapples with the complexities of human anatomy and procedural intricacies. Among the primary challenges are the risks of damaging sensitive structures like the facial nerve and the propensity of the electrode array to bend within the cochlea, impeding complete implantation. Despite precision in manual techniques, the limited visibility and heavy reliance on the surgeon's steadiness and expertise inherently carry risks.

Robot-assisted cochlear implant surgery signifies a major breakthrough in otolaryngology, aiming to heighten the precision and effectiveness of these procedures. This innovative approach, featuring an active electrode array, addresses the limitations of traditional surgery. The distinguishing aspect of active cochlear implants is their self-adjusting electrode array, which adapts during implantation to align perfectly with the cochlea's complex spiral path. This feature not only boosts implant efficacy but also minimizes potential complications.

Present research in cochlear implant technology concentrates on refining mechanical models and improving control systems for implantation. Conventional finite element models, while standard for simulating cochlear implant mechanics, struggle with real-time simulation and responsive control due to their high-dimensional complexity. Accurately determining physical parameters is another major challenge, affecting both the precision of simulations and the effectiveness of control methods. Therefore, there is a pressing need for models that are both precise and computationally efficient, alongside advanced control systems capable of adapting to the dynamic nature of implantation.

This thesis contributes significantly in three areas. First, it introduces a novel electronic and mechanical model for the cochlear implant's electrode array, employing Cosserat rod theory. This model, in contrast to traditional finite element models, offers similar accuracy with reduced complexity, thereby enabling real-time simulation and control during implantation. Its reduced computational demands make it more viable for clinical application, and its effectiveness has been corroborated through detailed simulations and experiments. Second, the study innovates in parameter identification by integrating a visual system to measure actuator curvature, thereby deriving physical parameters through a novel nonlinear electro-mechanical coupling model. Lastly, the thesis's crowning achievement is the development of an optimal control system based on the new electro-mechanical model. This system, founded on contact mechanics models, enables advanced multi-drive coupled trajectory tracking control. Rigorous testing through experiments and simulations confirms its robustness and reliability, marking a step forward in enhancing precision and safety in cochlear implant procedures.

Acknowledgments

As I reach the end of my doctoral journey, I am deeply thankful for the many individuals whose support have been essential to my academic and personal growth. This thesis, reflecting our collective wisdom and encouragement, stands as a testament to their steadfast support.

I must first express my deepest appreciation to my supervisor, Gang Zheng and Alexandre Kruszewski, whose expertise and mentorship have been invaluable. Your insightful guidance, patience, and belief in my abilities have not only shaped my research but also my growth as a scholar and individual. Your lessons extended beyond academia, imparting wisdom that I will carry with me always.

I would like to thank Robocop project (ANR-19-CE-0026), Cosseroots project (ANR-20-CE33-0001) and the Région Hauts-de-France for the finance of my research.

Throughout my three-year PhD journey, I have been fortunate to receive support and assistance from many individuals during my experimental research. I would like to extend my gratitude to Sofiane Ghenna and Eric Cattan for their invaluable guidance and expertise during my time at IMEN. Additionally, I am grateful to Renato Torres for his exceptional mentorship and guidance in the experiments I conducted at the Institute of Audition. I also want to express my thanks to Isabelle Fournier for her gracious hospitality in the Inserm lab. Lastly, my sincere appreciation goes to Guillaume Tourrel for providing me the experimental platform of cochlea.

I sincerely appreciate Christian Duriez for his guidance and insights during my doctoral studies. I would also like to express my gratitude to Yinoussa Adagolodjo for the helps in programming and to Thor Morales-Bieze and Quentin Peyron for their support with the experimental platform. Lastly, I am grateful to all members of the Defrost team for providing a thought-provoking environment. It has been a valuable journey of learning and discovery working with such a skilled and knowledgeable group.

A special note of thanks to Shijie Li, Haihong Li, Ke Wu, Xingyu Zhou, and Paul Chaillou for the meaningful academic exchanges and invaluable assistance they have provided. Additionally, my gratitude goes to all my fellow graduate students and friends. Their companionship has been a crucial part of my PhD journey, helping to navigate challenging moments and amplifying the joy of our shared successes.

Lastly, my profound appreciation goes to my family and friends outside academia. Their constant love, encouragement, and belief in me have been the pillars of my strength and perseverance. The role they have played in my journey is beyond measure, and I am forever thankful for their presence in my life.

Nomenclature

Symbol	Unit	Definition
$\dot{}$	—	Derivative with respect to time
$'$	—	Derivative with respect to space
$\widehat{}$	—	Mapping from $\mathbb{R}^6$ to $se(3)$
$\widetilde{}$	—	Mapping from $\mathbb{R}^3$ to $so(3)$
$\otimes$	—	Kronecker tensor product
$\|\cdot\|$	—	Euclidean norm of a vector or matrix
$^\vee$	—	Mapping from a matrix to a vector
s	m	$\in [0, L] \subset \mathbb{R}$ Abscissa along the electrode array or soft lender rod
β	—	$\in [0, 2\pi] \subset \mathbb{R}$ the rotation angle in radians of the contact point around the center point
t	s	$\subset \mathbb{R}$ Time
$\boldsymbol{R}$	—	$\in SO(3)$ Orientation matrix
$\boldsymbol{d}(s, \beta)$	m	Local distance between the midline of soft slender rod and the contact point
$\boldsymbol{p}$	m	$\in \mathbb{R}^3$ Position vector
$\boldsymbol{g}(s)$	—	$= \begin{pmatrix} \boldsymbol{R} & \boldsymbol{p} \\ \boldsymbol{0}^\top & 1 \end{pmatrix} \in SE(3)$ Homogeneous transformation matrix
$\boldsymbol{g}_0(s,t)$	—	The transformation matrix from the soft slender rod's base frame to the inertial frame
$\boldsymbol{g}_c(s,t)$	—	The configuration tensor of contact frame
$\boldsymbol{g}_{bc}(s,t)$	—	the configuration tensor of contact frame with respect to body frame
$\boldsymbol{g}_d(s,t)$	—	The configuration tensor of slave contact frame.
$\boldsymbol{g}_{cd}(s,t)$	—	the configuration tensor of slave contact frame with respect to master contact frame
$\boldsymbol{\kappa}(s)$	1/m	$\in \mathbb{R}^3$ Angular strain in the body frame
$\boldsymbol{\epsilon}(s)$	—	$\in \mathbb{R}^3$ Linear strain in the body frame
$\boldsymbol{w}(s)$	1/s	$\in \mathbb{R}^3$ Angular velocity in the body frame
$\boldsymbol{v}(s)$	m/s	$\in \mathbb{R}^3$ Linear velocity in the body frame
$\widehat{\boldsymbol{\xi}}(X)$	—	$= \begin{pmatrix} \widetilde{\boldsymbol{\kappa}} & \boldsymbol{\epsilon} \\ \boldsymbol{0}^\top & 0 \end{pmatrix} \in se(3)$: Strain twist matrix
$\boldsymbol{\xi}(s)$	—	$= \left(\boldsymbol{\kappa}^\top, \boldsymbol{\epsilon}^\top\right)^\top \in \mathbb{R}^6$ Strain twist

Continued on next page

Table 1 – continued from previous page

Symbol	Unit	Definition
$\widehat{\boldsymbol{\eta}}(X)$	—	$= \begin{pmatrix} \widetilde{\boldsymbol{w}} & \boldsymbol{v} \\ \boldsymbol{0}^\top & 0 \end{pmatrix} \in se(3)$: Velocity twist matrix
$\boldsymbol{\eta}(s)$	—	$= \left(\boldsymbol{w}^\top, \boldsymbol{v}^\top\right)^\top \in \mathbb{R}^6$ Velocity twist
$\mathrm{ad}_{\boldsymbol{\xi}(s)}$	—	$= \begin{pmatrix} \widetilde{\boldsymbol{\kappa}} & \boldsymbol{0}_{3\times3} \\ \widetilde{\boldsymbol{\epsilon}} & \widetilde{\boldsymbol{\kappa}} \end{pmatrix} \in \mathbb{R}^{6\times6}$: Adjoint representation of the strain twist
$\mathrm{Ad}_{\boldsymbol{g}(\mathrm{s})}$	—	$= \begin{pmatrix} \boldsymbol{R} & \boldsymbol{0}_{3\times3} \\ \widetilde{\boldsymbol{p}}\boldsymbol{R} & \boldsymbol{R} \end{pmatrix} \in \mathbb{R}^{6\times6}$: The matrix transforming the velocity or acceleration twist from body frame to inertial frame
$\mathrm{Ad}^*_{\boldsymbol{g}(\mathrm{s})}$	—	$= \begin{pmatrix} \boldsymbol{R} & \widetilde{\boldsymbol{p}}\boldsymbol{R} \\ \boldsymbol{0}_{3\times3} & \boldsymbol{R} \end{pmatrix} \in \mathbb{R}^{6\times6}$: The matrix transforming the wrench from body frame to inertial frame
$\mathrm{ad}_{\boldsymbol{\eta}(s)}$	—	$= \begin{pmatrix} \widetilde{\boldsymbol{w}} & \boldsymbol{0}_{3\times3} \\ \widetilde{\boldsymbol{v}} & \widetilde{\boldsymbol{w}} \end{pmatrix} \in \mathbb{R}^{6\times6}$: Adjoint representation of the velocity twist
$\mathrm{d}s$	m	Infinitesimal material element
ρ	$\mathrm{kg/m^3}$	Material density
$R(s)$	m	Cross-sectional radius
$A(s)$	$\mathrm{m^2}$	Cross-sectional area
E	Pa	Young's modulus
ν	—	Poisson ratio
G	Pa	Shear modulus (For the isotropic material, $G = E/(2(1+\nu))$)
μ_e	$\mathrm{Pa \cdot s}$	Viscosity modulus
$\boldsymbol{\mathcal{I}}(s)$	$\mathrm{m^4}$	$= \begin{pmatrix} I_x & 0 & 0 \\ 0 & I_y & 0 \\ 0 & 0 & I_z \end{pmatrix} \in \mathbb{R}^{3\times3}$ ($I_y(s)$ and $I_z(s)$ about the y-axis and z-axis, the polar area moment $I_x(s)$ about the x-axis.
$\mathbf{I}_3$	—	3×3 identity matrix
$\boldsymbol{\mathcal{M}}(s)$	—	$= \begin{pmatrix} \rho\boldsymbol{\mathcal{I}}(s) & 0 \\ 0 & \rho\mathbf{I}_3 A(s) \end{pmatrix} \in \mathbb{R}^{6\times6}$: Cross-sectional mass matrix
$\boldsymbol{\Gamma}$	N	Internal force in the body frame
$\boldsymbol{\Omega}$	$\mathrm{N \cdot m}$	Internal torque in the body frame
$\boldsymbol{\Lambda}$	—	Internal wrench in the body frame
$\boldsymbol{\Lambda}_a$	—	Actuation wrench in the body frame
$\boldsymbol{\mathcal{K}}_{tb}(s)$	$\mathrm{N \cdot m^2}$	$= \begin{pmatrix} G & 0 & 0 \\ 0 & E & 0 \\ 0 & 0 & E \end{pmatrix} \boldsymbol{\mathcal{I}}(s) \in \mathbb{R}^{3\times3}$: Stiffness matrix of the cross section at s for torsion and bending
$\boldsymbol{\mathcal{K}}_{es}(s)$	$\mathrm{N \cdot m^2}$	$= \begin{pmatrix} E & 0 & 0 \\ 0 & G & 0 \\ 0 & 0 & G \end{pmatrix} A(s) \in \mathbb{R}^{3\times3}$: Stiffness matrix of the cross section at s for elongation and shear

Continued on next page

Table 1 – continued from previous page

Symbol	Unit	Definition
$\boldsymbol{\mathcal{D}}_{tb}(s)$	$\mathrm{N}\cdot\mathrm{m}^2\cdot\mathrm{s}$	$= \begin{pmatrix} \mu & 0 & 0 \\ 0 & 3\mu & 0 \\ 0 & 0 & 3\mu \end{pmatrix} \boldsymbol{\mathcal{I}}(s) \in \mathbb{R}^{3\times 3}$: Damping matrix of the cross section at s for torsion and bending
$\boldsymbol{\mathcal{D}}_{es}(s)$	$\mathrm{N}\cdot\mathrm{s}$	$= \begin{pmatrix} 3\mu & 0 & 0 \\ 0 & \mu & 0 \\ 0 & 0 & \mu \end{pmatrix} A(s) \in \mathbb{R}^{3\times 3}$: Damping matrix of the cross section at s for elongation and shear
$\boldsymbol{\mathcal{G}}$	—	$\in \mathbb{R}^6$: Gravitational acceleration twist in inertial frame
$\boldsymbol{\theta}(t)$	—	$= \left[\bar{\boldsymbol{\xi}}_0^\top \ \bar{\boldsymbol{\xi}}_1^\top \cdots \bar{\boldsymbol{\xi}}_n^\top\right]^\top \in \mathbb{R}^{6(N+1)}$: Generalized strain vector of piecewise linear approximation
$\boldsymbol{\alpha}(t)$	—	Parameter vector of $\boldsymbol{g}_0$
$\boldsymbol{q}(t)$	—	Generalized coordinates
$\boldsymbol{J}(\boldsymbol{q}, s)$	—	$\in \mathbb{R}^{6\times 6(N+1)}$ Body Jacobian matrix
n	—	Number of sections divided for strain field
m	—	Number of sections divided for contact field
$\delta_n(s,t)$	m	Normal gap of contact in contact frame
$\boldsymbol{v}_t(s,t)$	m	Relative tangent velocity of contact in contact frame
$\Lambda_n(s,t)$	N/m	Normal contact load of collision in contact frame
$\boldsymbol{\Lambda}_t(s,t)$	N/m	Tangent contact load of collision in contact frame
$\boldsymbol{\Lambda}_c(s,t)$	N/m	Contact load of collision in contact frame
$\boldsymbol{\Lambda}_a(s,t)$	N/m	Contact load of articulated constraint in contact frame
$u_n(t)$	—	Slack variable of normal contact constraint
$\boldsymbol{u}_t(t)$	—	Slack variable of tangent contact constraint
$\boldsymbol{u}(t)$	—	Slack variable of contact constraint
$\boldsymbol{\lambda}_c(t)$	—	Assembly vector of slack variable $\boldsymbol{u}$
$\boldsymbol{\lambda}_f(t)$	—	Assembly vector of contact force of articulated constraints
$\boldsymbol{\lambda}_a(t)$	—	Assembly vector of contact force of fixed constraints
$\boldsymbol{G}_c(t)$	—	Collision contact constraints
$\boldsymbol{G}_f(t)$	—	Fixed contact constraints
$\boldsymbol{G}_a(t)$	—	Articulated contact constraints

Table 1: Acronyms and glossary for the thesis.

Chapter 1

Introduction

1.1 Motivation

1.1.1 The Origin of Cochlear Implants

The origin of cochlear implants can be traced back to the early experiments with electrical stimulation of the auditory system. Alessandro Volta [1], who developed the electric battery, provided the first account of such stimulation in the early 1800s. Volta described his experience as a "jolt in the head" followed by a sound resembling crackling or bubbling after inserting metal probes connected to a battery into his ear canals. Later, in 1855, Duchenne de Boulogne stimulated the cochlea with alternating current and experienced sensations of buzzing, hissing, and ringing [2]. This line of experimentation continued, and in 1930, Wever and Bray [3] recorded electrical potentials in the cochlea that followed the waveform of the sound stimulus, suggesting the possibility of restoring lost or absent hearing through electrical replication.

A significant milestone in the development of cochlear implants was achieved by Andre Djourno and Charles Eyriès in 1957 [4]. They performed the first direct electrical stimulation of the human auditory system on a patient who had only the stump of the auditory nerve remaining after previous surgeries. Although this initial effort by Djourno and Eyriès in Paris was quickly abandoned, the publication of their results had far-reaching effects. For instance, it inspired Dr. William F. House in Los Angeles to develop an auditory prosthesis for deaf persons that could be used reliably over many years [5]. In 1961, House, in collaboration with neurosurgeon Dr. John Doyle, implanted the first patients in Los Angeles [6]. These initial implants, though promising in providing basic frequency discrimination and word identification in small closed sets, faced challenges such as insufficient biocompatibility, leading to complications and limited long-term testing. Despite these setbacks, House continued his work and, in partnership with electrical engineer Jack Urban, developed the first cochlear implant system that could be used outside of the laboratory and for many years by patients [7], as shown in Fig. 1.1. This achievement marked a landmark in cochlear implant history, with House being widely regarded as a pioneering figure in this field.

The pioneering work in the development of cochlear implants, spearheaded by figures like Alessandro Volta, Andre Djourno, Charles Eyriès, and notably Dr. William F. House, represents a seminal turning point in auditory science and medical technology. Their groundbreaking experiments and innovations laid the foundational groundwork for modern cochlear implant technology, revolutionizing the approach to auditory rehabilitation. These early efforts not only demonstrated the feasibility of electrical stimulation of the auditory system for hearing

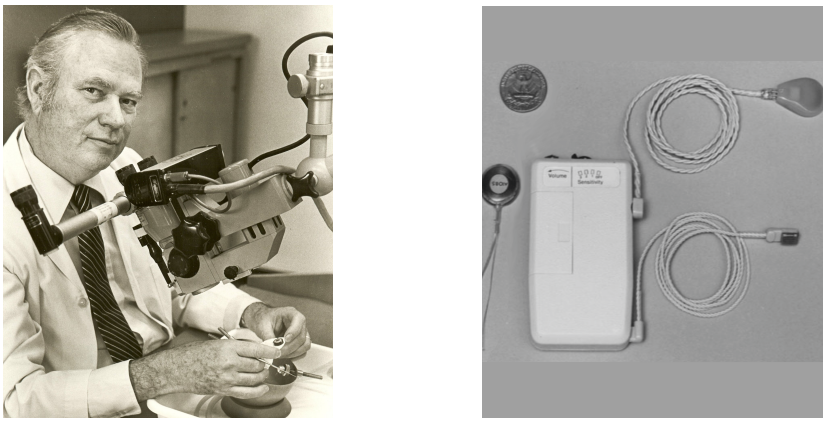

(a) (b)

Figure 1.1: (a) Dr. William Fouts House (December 1, 1923 – December 7, 2012), Inventor of cochlear implant. (b) The 3M Cochlear implant system developed by House in 1973 [8].

restoration but also paved the way for the evolution of sophisticated, biocompatible cochlear implants. Today, these implants stand as a testament to human ingenuity, profoundly impacting the lives of countless individuals with hearing impairments, offering them a transformative opportunity to experience the world of sound.

In the following section, we will first explore the mechanisms of auditory perception and the underlying causes of hearing loss. This understanding is crucial to appreciate the pivotal role cochlear implants play in restoring hearing in patients.

1.1.2 Auditory Perception and Hearing Loss

The auditory perception is a complex biological process that begins with the capture of sound waves by the external ear and extends to signal processing in the brain. This process involves the coordinated efforts of multiple structures within the ear, with each structure playing a crucial role in the formation of auditory perception [9].

As shown in Fig. 1.2.(a), firstly, sound waves are captured by the pinna (outer ear) and directed into the ear canal. The unique shape of the pinna helps collect sound waves from the surrounding air, while the ear canal slightly amplifies specific frequencies of sound to enhance speech reception. Subsequently, the sound waves reach the eardrum, causing it to vibrate. This step is crucial as it transforms sound waves into mechanical vibrations. The vibration of the eardrum is then transmitted to the three small bones of the middle ear—the hammer, anvil, and stirrup bones. These bones not only amplify the sound but also transmit it to the inner ear.

The cochlea, a spiral-shaped, fluid-filled structure in the inner ear, plays a pivotal role in sensing sound [11]. As shown in Fig. 1.2.(b), it comprises three parallel canals: the scala vestibuli (SV), scala media (SM), and scala tympani (ST), each filled with fluids crucial for sound transmission. The scala vestibuli and scala tympani contain perilymph, which transmits sound vibrations from the middle ear into the cochlea. These vibrations travel through the scala vestibuli, reach the cochlear apex, and then journey back via the scala tympani. Central to this system is the scala media, or cochlear duct, filled with endolymph and separated from the scala vestibuli by the vestibular membrane and from the scala tympani by the basilar

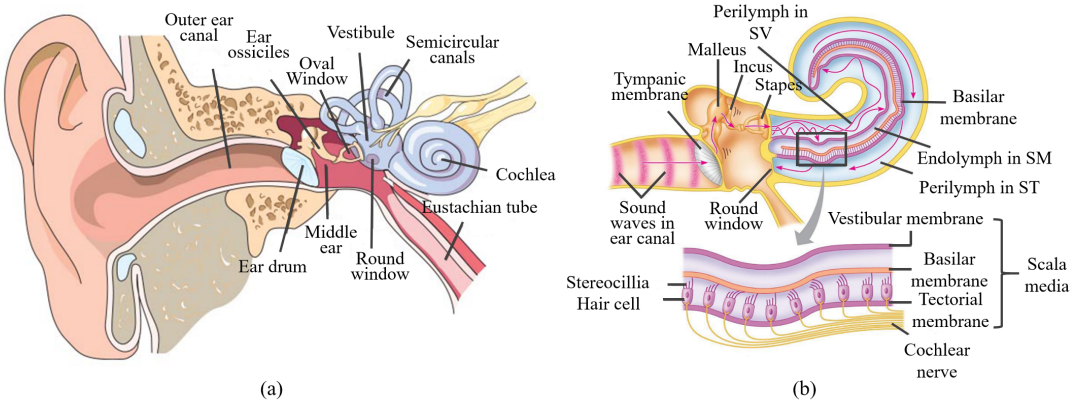

Figure 1.2: (a) The primary structures of the human ear include the outer ear, middle ear, and inner ear. (b) An anatomical diagram of the cochlea and the process of sound wave transmission within the cochlea. [10]

membrane. The basilar membrane's unique sensitivity to different sound frequencies enables the cochlea to distinguish various pitches. Resting on this membrane are the hair cells, the auditory system's sensory receptors. These cells, topped with tiny hair-like projections called stereocilia, bend in response to the basilar membrane's vibrations. This bending opens ion channels, creating electrical signals that are then transmitted to the brain. Above the hair cells lies the tectorial membrane, a gel-like structure that enhances the bending of the stereocilia, thus amplifying the electrical signal production. This sophisticated process, beginning with sound waves entering the cochlea and culminating in the conversion of mechanical energy into electrical signals, exemplifies the remarkable sensitivity and frequency discrimination of human hearing.

According to the statistic of World Health Organization, over 5% of the world's population, i.e., 360 million people, has disabling hearing loss (328 million adults and 32 million children). Hearing impairment or loss can occur at any stage of the previously introduced process [12]. Damage to the external and middle ear, such as infections or perforated eardrums, can disrupt the effective transmission of sound, resulting in conductive hearing loss. Damage to the cochlea or its hair cells, often caused by noise exposure, aging, or medication toxicity, can lead to sensorineural hearing loss [13, 14]. Once hair cells are damaged, they typically cannot repair themselves. Issues with the auditory nerve, such as the presence of tumors, can interfere with signal transmission to the brain. Lastly, damage to the brain's regions responsible for processing auditory signals, as seen in cases of stroke or brain injury, can also affect hearing [15].

1.1.3 The Working Mechanism of Cochlear Implants

Cochlear implants (CIs), ingeniously designed to simulate the natural hearing process, become essential in cases where the cochlea's hair cells are impaired, rendering them ineffective in transducing sound into neural signals. In a normal ear, sound waves are transformed into mechanical vibrations by the cochlea, with the basilar membrane playing a pivotal role and hair cells converting these vibrations into electrical signals for the brain to interpret as sound. However, when these hair cells are damaged, this process is disrupted.

A cochlear implant ingeniously bypasses this damaged mechanism by directly stimulating

Figure 1.3: (a) The external and component of cochlea implant. (b) The internal component of cochlea implant. The electrode array typically consists of multiple electrode contacts distributed along its length. Each electrode contact can independently transmit electrical signals, simulating the perception of sounds at different frequencies, akin to the natural auditory process.

the auditory nerve fibers, eliminating the need for functional hair cells [16]. As shown in Fig. 1.3, comprising an external microphone, a speech processor, a transmitter, and an internal receiver equipped with an electrode array (EA), the cochlear implant functions by capturing sound through the microphone, which is then processed into electrical signals by the speech processor. These signals are wirelessly transmitted to the internal receiver implanted under the skin.

Fig. 1.4 illustrates the detailed functioning of the cochlear implant. The EA [17], a key component of the implant, is inserted into the cochlea, where it directly stimulates the auditory nerve fibers. This array's placement is meticulously designed to mirror the cochlea's tonotopic organization, ensuring that different parts are stimulated in correspondence with the pitch of the incoming sound. The array targets the spiral ganglion neurons located in the modiolus, the cochlea's central core. These neurons are crucial for transmitting auditory information from the cochlea to the brain. By stimulating these neurons, cochlear implants effectively bypass damaged hair cells, transmitting auditory information directly to the brain and enabling sound perception.

This technological marvel, while not repairing the damaged cochlea, creates an alternative pathway for sound signal transduction directly to the auditory nerve. It represents a significant advancement in auditory prosthetics, offering individuals with severe hearing loss a new dimension of hearing and profoundly impacting their interaction with the world .

1.1.4 Types of Electrode Array

In the realm of cochlear implant (CI) surgeries, the concept of passive cochlear implants has emerged alongside the development of various electrode arrays (EAs), namely the "straight" and "precurved" types [18]. Each of these EAs comes with its set of advantages and challenges, particularly concerning intracochlear trauma and hearing outcomes.

The evolution of EAs began with single wire electrodes and has since progressed to incorporate multiple stimulation sites and advanced materials like silicone. This progression maintains the fundamental design of a flexible carrier equipped with electrode contacts. Overall, traditional EAs can be classified into the following two types:

- Straight EAs, designed to curve upon contact with the cochlea's lateral wall opposite the modiolus, typically align along this wall in both active and passive systems [19–21].

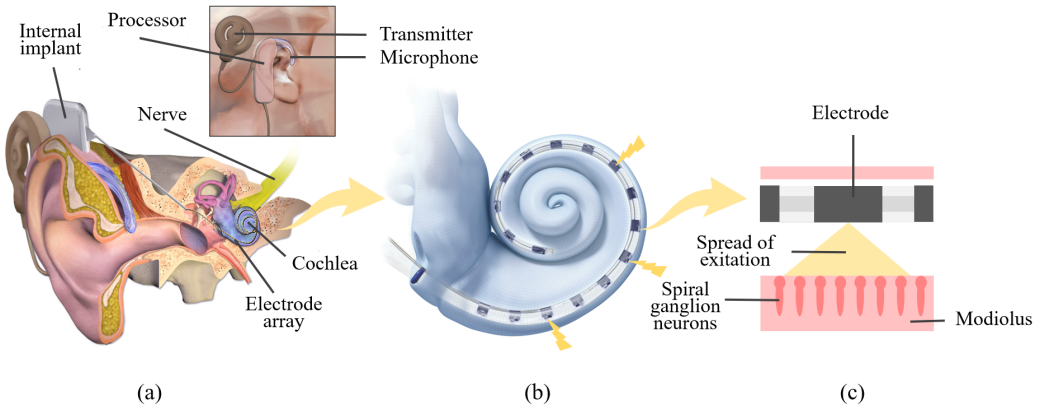

Figure 1.4: (a) The various components of the cochlear implant capture sounds and convert them into electrical signals. (b) The electrode array inside the cochlea. (c) These electrical signals are sent through a small electrode inserted into the cochlea. The electrode stimulates the spiral ganglion neurons located in the modiolus, and the information is sent to the brain through the auditory nerve for interpretation.

- The "Advanced-Off-Stylet" (AOS) technique, developed to minimize intracochlear trauma caused by the stylet's stiffness, is particularly relevant for passive CIs [22, 23]. Here, the stylet stays in place until the carrier reaches the basal turn, at which point the surgeon advances the silicone carrier while holding the stylet steady. This approach allows for a gradual curvature increase during insertion, ideally preventing contact with the lateral wall.

1.1.5 Cochlear Implant Surgery

Cochlear implant surgery, pivotal in treating severe to profound hearing loss, has seen remarkable advancements in recent years.

As shown in Fig. 1.5, initially, traditional manual cochlear implant surgery begins with a detailed assessment of the patient's anatomical structure through imaging techniques. The surgeon then performs a mastoidectomy, where part of the mastoid bone behind the ear is carefully removed. This step is crucial for gaining access to the middle and inner ear structures [24].

Following this, a posterior tympanotomy is performed. This involves creating a small opening to access the middle ear, enabling the surgeon to reach the cochlea. The delicate nature of this procedure requires precise maneuvering to avoid damaging sensitive structures like the facial nerve [25].

The core of the surgery involves the insertion of the electrode array into the cochlea. The surgeon makes a minute opening in the cochlea and carefully inserts the electrode. This process demands high precision to ensure that the implant is positioned correctly for optimal auditory results. Over the years, the traditional manual technique has seen significant advancements. Surgeons have refined their skills and techniques, leading to improved outcomes and reduced complication rates. Innovations in imaging and surgical tools have further augmented the precision of this surgery. One of the critical developments in this area has been the improvement in electrode design. Modern electrodes are designed to preserve the cochlear structure and

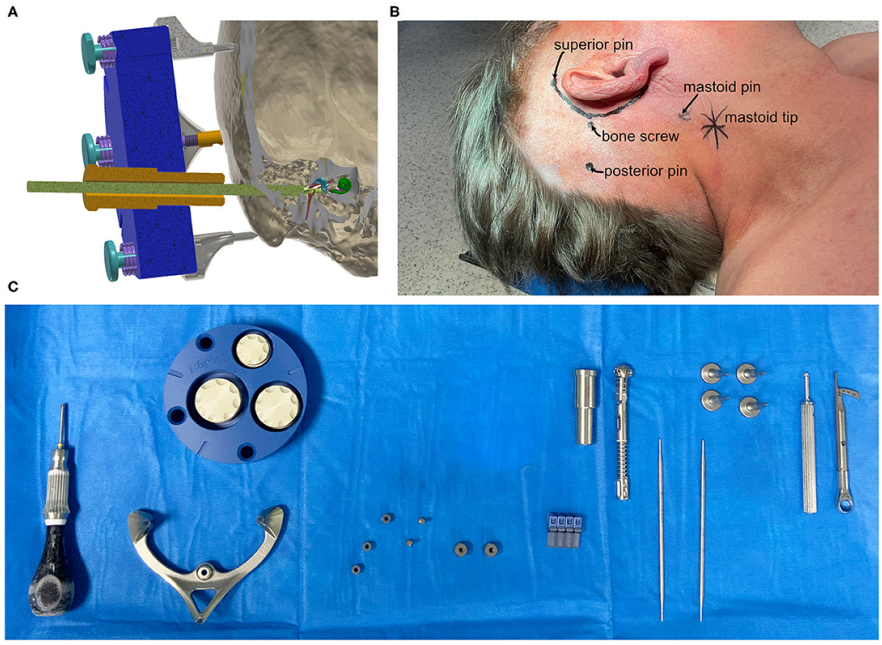

Figure 1.5: Schematic diagram of cochlear implant surgery and surgical equipment and tools.

minimize trauma, leading to better preservation of residual hearing. This advancement has been instrumental in enhancing the effectiveness of cochlear implants for a broader range of hearing impairments. Furthermore, there has been a shift towards minimally invasive approaches. These techniques aim to reduce the size of the incisions and the extent of bone removal, thereby speeding up recovery times and reducing postoperative discomfort.

Traditional manual cochlear implant surgery, while effective, faces certain limitations, primarily stemming from the intricacies of human anatomy and the complexity of the surgical procedure [26, 27]. One of the main challenges is the risk of damaging delicate inner ear structures, such as the facial nerve. Even with the utmost precision, the manual approach carries inherent risks due to the limited field of view and the surgeon's reliance on hand stability and experience [28]. Another limitation is the variability in surgical outcomes. The success of manual cochlear implant surgery heavily depends on the surgeon's skill and experience, leading to variability in patient outcomes. Additionally, the invasiveness of the procedure often results in longer recovery times and a higher risk of complications, such as infections or bleeding [29].

1.1.6 Issues of Cochlear Implantation

As shown in Fig. 1.6, sound waves of different frequencies (20 Hz-20000 Hz) stimulate different parts of the cochlear basilar membrane. High-frequency sounds peak near the base of the cochlea (close to the oval window), while low-frequency sounds peak at the top (the apex of the spiral). This spatial arrangement allows for the separation and analysis of different sound frequencies. Hence, in order to endow patients with a comprehensive auditory bandwidth, it's imperative to meticulously align the cochlear implant's electrode array. This alignment spans from the region of the cochlea attuned to higher frequencies to the area responsive to lower frequencies. Essentially, this involves the complete insertion of the electrode array into the cochlea's interior.

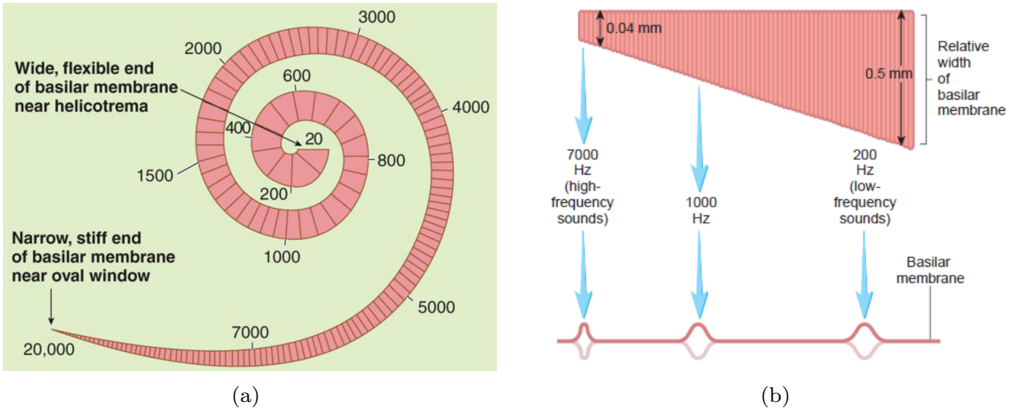

(a) (b)

Figure 1.6: Perception of sound wave frequencies at different locations inside the cochlea. [30]

However, several critical issues can arise during the insertion of the implant, each with the potential to significantly impact the surgical outcome and the patient's auditory perception.

1. Firstly, the mechanical stress and deformation of the EA during implantation pose significant risks,as shown in Fig. 1.7. Key complications include the following aspects:

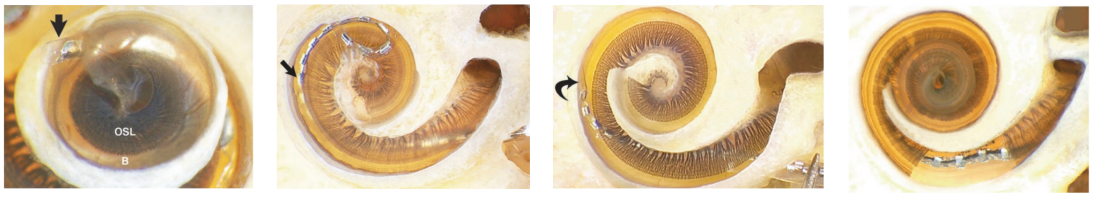

(a) (b) (c) (d)

Figure 1.7: Various instances of cochlear damage [10]: (a) Relocation of the EA from the scala tympani (ST) to the scala vestibuli (SV), (b) Folding over of the EA's tip, where the most distal section reverses upon itself, (c) Scratching or scraping of the EA's tip against the cochlear lateral wall, resulting in harm, and (d) The EA's internal buckling within the cochlea, hindering further insertion and impacting its final intracochlear position. In this particular case, the buckling event led to the fracture of the osseous spiral lamina. [10]

- Translocation [31], where the EA ruptures the basilar membrane, transitioning from the scala tympani to scala vestibuli. This displacement disrupts the usual hearing pathway, often resulting in a complete loss of residual hearing.
- Tip fold-over [32], another complication, occurs when the apical section of the EA bends back on itself, rendering the involved electrode contacts ineffective due to incorrect orientation or interference.
- Tip scraping [33], where the EA tip damages the cochlea's lateral wall, can harm structures critical for residual hearing.

- Buckling of the EA [34], either inside the cochlea, potentially damaging structures like the spiral lamina, or outside in the middle ear space, leads to a discontinuity in curvature and a shallow angular insertion depth.

The potential for cochlear damage is a paramount concern. Translocation and tip scraping directly affect the delicate inner structures of the cochlea, risking irreversible damage and loss of residual hearing. Buckling inside the cochlea can lead to trauma to critical inner ear structures. The success rate of EA implantation depends on avoiding these complications. Advanced surgical techniques, improved electrode design, robotic assistance, and enhanced imaging methods are pivotal in enhancing precision and reducing risks.

2. Depth of implantation is also a crucial factor for optimal hearing outcomes, yet deeper insertion heightens the risk of complications like translocation and buckling. Controlled insertion speeds and specially designed electrode arrays are strategies employed to mitigate these risks.

3. Accuracy in the placement of the EA is essential for effective auditory nerve stimulation. Complications like tip fold-over and buckling can severely impair the correct positioning of electrode contacts. Implementing continuous monitoring of insertion forces and utilizing real-time imaging can significantly aid in achieving accurate placement.

1.1.7 Robot-Assisted Cochlear Implantation

The development of robot-assisted cochlear implant surgery marks a significant advancement in the field of otolaryngology, aiming to enhance precision and outcomes in cochlear implant procedures [35]. This advancement is attributable to the concerted efforts of researchers and clinicians dedicated to improving surgical techniques and patient-specific outcomes. Robotic assistance systems are typically comprised of visual sensors, multi-degree-of-freedom mechanical arms, and cochlear implant clamping fixtures, as shown in Fig. 1.8.

One of the foundational aspects of robot-assisted surgery is path planning. Ferrarini et al. developed an autonomous virtual mobile robot for exploring three-dimensional medical images, planning electrode implantation paths, and estimating cochlear dimensions [39]. However, the application of this virtual robot to actual surgery was limited due to factors like robot size and operating environment constraints. Zhang and his colleagues made notable contributions by developing a new type of steerable electrode array and a cochlear implant parallel robot system, presenting an optimal path planning method for robot-assisted cochlear implant surgery [40]. The "steerable" is achieved by pulling the embedded thread within the electrode array, leading to the bending of array. However, this purely mechanical driving structure has certain drawbacks. Firstly, embedding a movable thread within such a small-sized space of the electrode array is challenging. Secondly, the degree of bending is limited, making it difficult to embed more threads to increase the flexibility of bending.

The transition to minimally invasive approaches has been a key development, with Majdani and his team pioneering a robot-guided minimally invasive approach for cochlear implant surgery [41]. Their work laid the groundwork for more advanced techniques, including virtual cochlear electrode insertion and patient-specific planning.

In the realm of automated insertion and force sensing, significant advancements have been made by researchers [37, 42, 43]. They designed tools integrating force sensing with automated insertion, comparing traditional and advanced off-stylet techniques.

Recent clinical reports and studies, such as those by Torres and Vittoria [44], have focused on optimizing robot-based techniques for cochlear implantation to reduce array insertion trauma

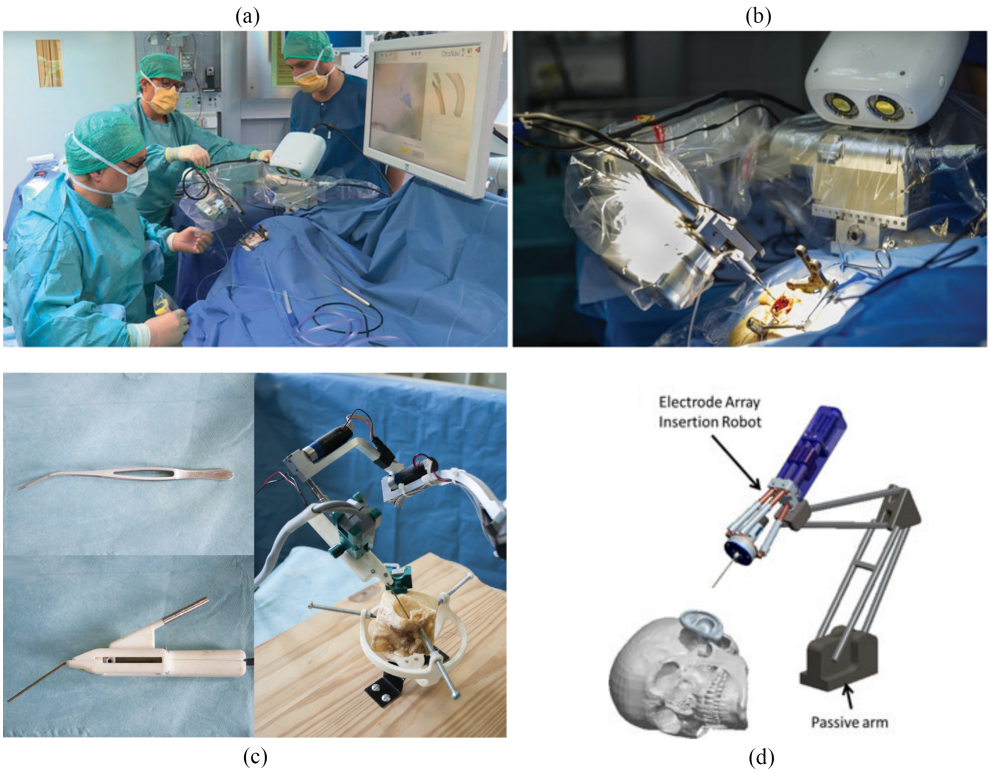

Figure 1.8: (a) Surgeons are utilizing robot-assisted devices for cochlear implant surgeries. (b) A fully automated robotic device for cochlear implant insertion. (c) The implant's clamping mechanism (right), along with the mechanical arm used for insertion. (d) A novel type of parallel mechanical arm designed specifically for cochlear implant surgeries. [36–38]

and assist in middle ear surgeries. Their work provides the first clinical reports on robot-based assistance in these surgeries.

While there has been notable progress in the realm of robot-assisted research, significant challenges and obstacles persist. The creation of a high-efficiency, controllable electrode array remains an area in need of development. This endeavor is accompanied by the necessity for advanced modeling and control mechanisms for such controllable electrode arrays. A comprehensive and systematic effort in designing, modeling, and controlling these electrode arrays is essential and must be diligently pursued.

The ROBOCOP project, a collobrative project between Inria, Inserm, LPPI, IEMN and Oticon Medical, represents a groundbreaking advancement in cochlear implantation technology. This multidisciplinary initiative is for the purpose of developing an innovative "smart" active cochlear implant (ACI) equipped with micro-actuators, enhancing precision and success rates in surgeries [45, 46]. These micro-actuators not only allow for controlled implant deformation during insertion but also function as shape sensors, facilitating real-time shape estimation and feedback control. This project signifies a major leap forward in otological surgery, promising improved outcomes and expanded treatment possibilities in cochlear implantation.

In conclusion, robotic assistance in surgical procedures offers a higher degree of stability in the implantation of electrode arrays compared to manual methods employed by doctors.

This advancement significantly enhances the overall smoothness, safety, and reliability of the implantation process. Nonetheless, a challenge persists in controlling the interaction between the electrode array and the interior of the cochlea when using external robotic systems. The forthcoming discussion on active cochlear implants presents a promising solution to this intricate issue.

1.1.8 Active Cochlea Implant

In traditional cochlear implants, a significant challenge arises during the implantation process, where controlling the interaction between the electrode array and the cochlea's inner wall proves difficult. This issue manifests in several critical implantation problems, notably the inability to precisely manage the force of contact and the prevention of buckling, a deformation phenomenon. It's in this context that active cochlear implants emerged, innovatively designed to overcome these specific limitations inherent in their traditional counterparts.

The ingenuity of active cochlear implants lies in their core feature: an electrode array capable of autonomous deformation during the implantation process. This adaptability ensures that the array aligns seamlessly with the intricate spiral trajectory of the cochlea, thus enhancing the implant's effectiveness and reducing potential complications. To achieve this remarkable functionality, the electrode array incorporates cutting-edge materials. Depending on the actuation mechanism, these include shape-memory polymers, which can return to a predetermined shape after deformation; electric polymers, known for their insulating properties and ability to change shape under an electric field. Based on the principles of deformation, autonomous cochlear implants are mainly categorized into the following types:

- Self-Shaping Cochlear Implants represent a significant innovation in the treatment of sensorineural hearing loss, offering a notable departure from traditional cochlear implants. These advanced implants utilize shape memory polymers (SMPs), a biocompatible material that can recover its original shape in response to body temperature [47]. This unique feature allows the SMP electrode array (EA) to transition from a straight shape outside the body to the curved shape of the cochlea in a controlled manner when inserted, significantly reducing trauma during the surgical process, as shown in Fig. 1.9.

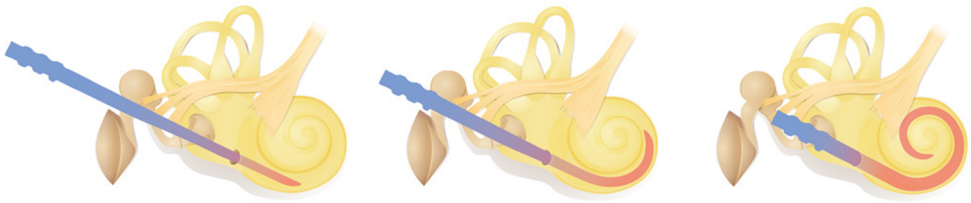

Figure 1.9: The anticipated functioning of the self-shaping cochlear implant during the insertion process. The color of the implant represents changes in temperature. [47]

The primary distinction of self-shaping CI from traditional models lies in their ability to curl actively into the cochlea, leveraging body temperature as a trigger. This capability circumvents the need for additional external mechanisms required by conventional precurved CI, which often pose a risk to hearing preservation due to their rigidity and more complex insertion requirements. Nevertheless, this active deformation approach presents inherent limitations. Precisely and sensitively manipulating the deformation of EA using

the body's internal temperature proves to be a complex task. Moreover, achieving localized deformation control of the EA through its material memory properties is a significant challenge. Consequently, the versatility of this deformation mechanism across the varied size spectrum of the cochlea is restricted.

- Another novel concept for automated cochlear implant insertion is using tubular manipulators [48], as shown in Fig. 1.10. The approach aimed to reduce trauma risks during surgery and automate the electrode insertion process. This proposed solution involved a tubular manipulator, comprising an inner wire within a helically shaped tube, integrated into the electrode array. However, integrating such a structure within the small dimensions of the electrode array is challenging. The concentric tubes will increase the radius of the electrode array, thereby enlarging its volume. Additionally, the actuating device required to rotate the concentric tubes also needs to be integrated into the cochlear implant, which further increases its structural volume and complexity.

Figure 1.10: A controllable electrode array consisting of a spiral tube (colored in red) and a wire (colored in blue) enclosed within a guiding channel designed for insertion into the scala tympani. [48]

- Confronting this challenge, the implementation of an active EA driven by micro actuators emerges as an effective solution. This variant of EA boasts two significant strengths: its compact size facilitates seamless integration, and it features a straightforward driving mechanism. The attributes of this EA form the cornerstone of the research explored in this thesis. These novel implants incorporate microfabricated EAs that are capable of actively conforming to the unique contours of the cochlea, a feature that significantly reduces surgical complexity and potential trauma. This type of implants use EAs integrated with electronic conducting polymer (ECP) [46] based micro-actuators, which enable them to actively reshape under low electrical voltage stimulation, as shown in Fig. 1.11. This dynamic capability offers a level of flexibility and adaptability previously unseen in cochlear implants.

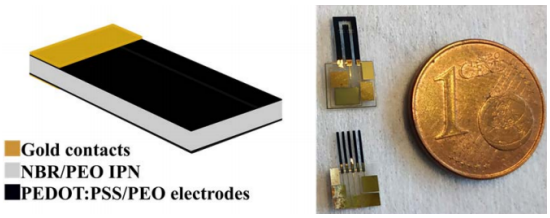

Figure 1.11: PEDOT:PSS-PEO based micro-actuators.

The smart electrode array, a key component of these implants, is designed with reduced stiffness and is functionalized with PEDOT:PSS-PEO based micro-actuators, sandwiched

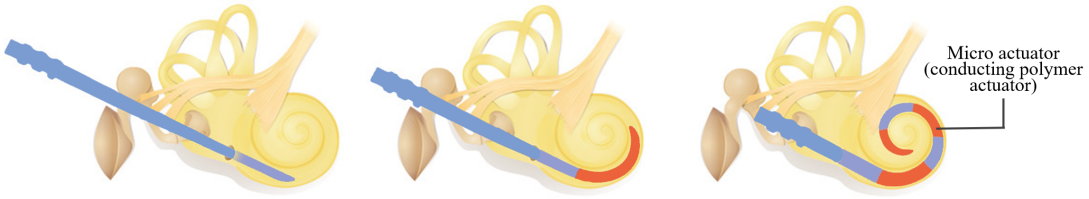

Figure 1.12: The anticipated functioning of the active cochlear implant during the insertion process. When implant is inserted in the cochlea, the actuators are activated.

between layers of nitrile butadiene rubber/poly(ethylene oxide) (NBR-PEO) [49]. This design significantly reduces the friction against the cochlear walls during insertion, minimizing the likelihood of trauma. The flexibility of these EAs is further enhanced by using materials like Polydimethylsiloxane (PDMS), which allow the array to bend and adapt during the surgical process.

Future research in this field aims to further optimize these implants, focusing on the recovery forces during insertion, determining the most effective insertion trajectories, and exploring the integration of robotic assistance for more precise and controlled implantation. These advancements will involve developing more refined self-shaping CI prototypes and specialized robotic systems, paving the way for more realistic testing scenarios. In essence, active cochlear implants represent a promising evolution in cochlear implant technology, offering more adaptable, less traumatic, and potentially more effective solutions for individuals with severe hearing loss. This technological advancement underscores a significant shift towards a more tailored and patient-centric approach in auditory prosthetics.

The advent of active cochlear implant technology heralds a multitude of challenges spanning academic and technical domains. These encompass the intricate structural design of active EA, their detailed modeling, the seamless integration of drive systems, and the nuanced control required during implantation. In this doctoral project, our emphasis will be primarily on the modeling and control dimensions of this technology. The forthcoming section will comprehensively explore and elucidate the various challenges associated with these critical facets.

1.2 Scientific Challenges

Expanding on the previous discourse, we can delineate the challenges encountered by cochlear implants in the realm of robotic surgery into two predominant domains: the need for precise physical simulation modeling of the insertion process, and the necessity for effective control mechanisms during the surgical procedure. These challenges are crucial for enhancing the efficacy of cochlear implant surgeries and driving the evolution of robotic assistance in these procedures.

1.2.1 Modeling Challenges in Cochlear Implants

The first category, which is modeling, encompasses several critical aspects:

- The mechanical modeling of the electrode array is essential in predicting how the array will behave during surgery. This involves understanding the forces at play when the electrode array, pre-formed into a spiral shape, is confined and then gradually restored

to its original state during implantation. This modeling is crucial for reducing the risk of complications such as translocation, tip fold-over, and buckling, which can severely impact the surgery's success and the patient's residual hearing.

- Modeling of micro actuators, integral to the precise control of the electrode array, is another significant challenge. These actuators are responsible for the delicate movement and positioning of the electrode array, and their accurate modeling ensures that the array can navigate the unique anatomy of each patient's cochlea without causing damage.

- Furthermore, modeling the interaction between the active electrode array and the cochlear wall is vital. This interaction needs to be well-understood to minimize trauma during implantation and ensure optimal placement of the electrode array. The mechanical stress and deformation during the implantation process, and the subsequent potential damage to the cochlea, necessitate advanced computational models and simulations for preoperative planning and assessment.

1.2.2 Control Challenges in Cochlear Implants

The second category, which is control, encompasses the establishment of control objectives, the strategic planning of robotic insertion paths, and the management of the deformation of active cochlear implants. Setting clear control objectives is critical for the success of the surgery, as it dictates the parameters within which the robotic system operates. This includes the following critical aspects:

- Establishing the depth of insertion and the exact positioning of the electrode array to maximize auditory outcomes while minimizing damage.

- Robotic path planning is pivotal in navigating the complex inner structures of the ear. Advanced algorithms and surgical simulation technologies are required to adapt to the unique cochlear anatomy of each patient, enhancing the precision and reducing the risks associated with manual insertion.

- Controlling the deformation of active cochlear implants during insertion is a complex challenge. It requires an intricate balance of mechanical force and precise manipulation to avoid complications like buckling or damage to the cochlea's delicate structures. This control is increasingly being achieved through the use of robotic systems, which offer greater precision and stability compared to manual techniques.

The complexities of mechanical modeling and the precision required in robotic control highlight the need for continued research and innovation. Addressing these challenges will not only improve the success rates of cochlear implant surgeries but will also pave the way for more advanced, automated, and patient-specific surgical techniques in the future.

1.3 State of the Art

In addressing the diverse set of challenges highlighted in the preceding section, scholars in the field have achieved notable advancements in the modeling and control of cochlear implants. In this section, we aim to present an overview of the state-of-the-art developments in this dynamic area of research.

1.3.1 Modeling of Cochlea Implant

The mechanical modeling of cochlear implants, particularly the electrode array, is a sophisticated field that intersects with the principles of continuum mechanics, often applied in the realm of soft robotics. The electrode array of a cochlear implant can be conceptualized as a continuum beam structure, similar to slender robotic elements, and thus modeled using similar theoretical frameworks. This approach has profound implications for improving cochlear implant design and surgical techniques.

The finite element method (FEM), widely used in engineering practices, finds relevance in modeling the complex geometries of cochlear implant electrode arrays. This method has been employed in various soft robotic applications, analogous to the electrode array's slender and flexible nature [50]. Given the slender geometry of cochlear implants, their degrees of freedom are subject to simplification. In this context, FEM proves to be relatively less efficient for modeling. Beam models, on the other hand, adeptly resolve this challenge, making them a more suitable choice for such applications, as shown in Fig. 1.13. Beam/rod theory, a subset of continuum mechanics, is particularly applicable to the electrode array of cochlear implants. Classical Euler-Bernoulli beam theory, for instance, provides a foundation for modeling the mechanical behavior of these slender structures. Olson et al.'s study using a quasi-static bending model based on Euler-Bernoulli formulation exemplifies this approach, offering insights relevant to cochlear implant design [51]. Beyond the Euler-Bernoulli model, the Timoshenko beam model, which accounts for shear strain, offers an enhanced perspective on the electrode array's mechanics [52, 53]. The Kirchhoff rod model extends this analysis by considering torsional strain, applicable in scenarios where the electrode array experiences complex deformations [54].

In cases of large deformations, geometrically nonlinear classical rod theory is often utilized. For instance, the pseudo-rigid body (PRB) 3R model, developed for analyzing flexible beams under tip loading, has demonstrated high computational efficiency and can be adapted for modeling the electrode array's behavior during implantation [55, 56]. Huang et al. further extended this model to three-dimensional applications, relevant for the complex geometries encountered in cochlear implant electrode arrays [57].

For large deformations, constant curvature (CC) assumptions are frequently employed, leading to the utilization of generalized elastic models like Cosserat rod theory. This theory, a generalization of Timoshenko-Reissner beams, is capable of simulating bending, torsion, shear, and tension, all of which are relevant to the electrode array's mechanics [58–60]. A comprehensive review of Cosserat-based slender elastic rod models, as presented by Till et al., offers valuable insights that can be translated to cochlear implant modeling [61]. Building upon this foundation, new methods for solving Cosserat partial differential equations (PDEs) in continuous space have been proposed in [62] based on Newton-Euler dynamics.

In the context of soft slender rod, the work in [63] introduces a Cosserat-based piecewise constant strain model where the PDEs are transformed into an approximate weak form expressed as ordinary differential equations (ODEs). Another approach, presented in [64], utilizes a Cosserat discrete solution method based on strain nonlinear parameterization and Lagrangian dynamics. However, this technique can become computationally complex when modeling involves complex deformations like buckling behavior and local strain variations due to contact. To address this challenge,this thesis will employ a piecewise local approximation of the strain field in our work. In specific engineering scenarios, the Cosserat model has been applied to simulate dynamic structures, which can be analogous to the dynamic requirements of the electrode array during surgery [65, 66]. This model's practical applications in soft robotics demonstrate its potential utility in cochlear implant technology.

The mechanical modeling of the electrode array of cochlear implants, drawing from the field

(a) FEM model of EA (b) Beam/rod model of EA

Figure 1.13: In FEM (Finite Element Method), the geometric structure of an object is determined by the position of each point on the mesh. However, in beam/rod models, the geometry of the rod is determined by slices along its centerline via rotation matrix and position.

of soft robotics and continuum mechanics, encompasses a range of sophisticated theoretical frameworks. From Euler-Bernoulli and Timoshenko beam theories to more complex models like the Kirchhoff rod and Cosserat rod theories, these approaches provide crucial insights into the mechanical behavior of the electrode array. Such modeling is essential for advancing cochlear implant technology, enhancing surgical precision, and improving patient outcomes.

1.3.2 Modeling of Interaction during Implantation

1.3.2.1 Interaction with Cochlea

The interaction between the electrode array of cochlear implants and the cochlea can be viewed through the lens of soft robotics, a field fundamentally concerned with how these flexible and deformable machines interact with and adapt to their environments [67]. The electrode array, akin to a soft robot, is composed of flexible materials, allowing for a unique set of interactions with the delicate structures of the cochlea. This resemblance positions the study of cochlear implant electrode arrays within the broader context of soft robot-environment interaction research.

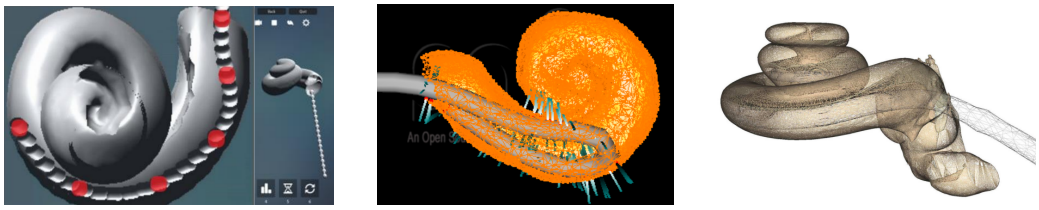

(a) (b) (c)

Figure 1.14: (a) Virtual-reality training simulator for cochlear implant surgery. (b) Cochlear implant simulation in SOFA using beam model. (c) Cochlear implant simulation using FEM method.

At present, simulations of artificial cochlear implantation utilizing contact mechanics principles have been explored by various scholars, as illustrated in the accompanying Fig. 1.14. [68] introduces a novel mechanical simulation tool for cochlear implant surgery via SOFA framework, employing patient-specific data to model the implant's 3D insertion and potentially aiding in future advancements like virtual planning and robot-assisted procedures. [56] introduces a

virtual-reality (VR) simulator designed to realistically model electrode behavior during cochlear implant surgery, aiming to enhance training for surgical trainees by allowing repeated practice of electrode insertions in a safe, controlled, and cost-effective environment

However, the interaction of soft robotics, including the electrode array of cochlear implants, faces several challenges, particularly in contact modeling [69]. The modeling complexities arise from the flexible and deformable structures, which require intricate models to predict interactions accurately. Unlike rigid robots, soft robots such as cochlear implant electrode arrays demand more complex models to account for deformations upon contact, force distributions, and frictional effects. These models are critical in applications involving grasping, manipulation, and in the case of cochlear implants, precise insertion and navigation within the cochlea.

1.3.2.2 Frictional contact

The solution to contact problems in continuum mechanics has been a subject of considerable interest in recent decades, with a wide range of contact models being employed in engineering fields. However, solving the problem of multiple frictional contacts with large deformations remains challenging [70]. Although contact research for flexible systems has made advancements [71], the development of efficient and robust frictional contact algorithms still present open challenges.

The penalty function method is widely used in computational contact mechanics due to its simplicity and directness [72]. However, stiffness and stability issues persist despite recent progress [73]. Numerical optimization-based contact solution methods often involve linear complementary programming (LCP) or nonlinear complementary programming (NCP) formulations, which offer higher accuracy at the cost of increased computational complexity and the use of frictional approximations [74, 75]. LCP can be solved using relaxation methods like projected Gauss-Seidel (PGS) or direct methods such as Dantzig's pivoting algorithm or Lemke's algorithm. In the work of Stewart and Trinkle [76], the Coulomb friction cone is linearized, and Lemke's method is used to solve the resulting polygonal pyramid LCP, handling nonlinear forces. Subsequently, [77] proposed a method based on the Gaussian Seidel iterative inverse solution to LCP, which introduced a solution framework to the field of deformable solids [78,79]. [80] introduced a contact model for asynchronously handling deformable solids by discretizing the contact barrier potential. For a comprehensive review of numerical methods for linear complementarity problems, we refer to [81].

In addition to LCP formulations, another common approach to solve contact problems is through Newton-type methods, which typically utilize the generalized projection operator and augmented Lagrangian to address contact constraints [82–84]. Recent works have applied these methods in various applications [85–87]. The complementarity problem in these works is addressed using non-smooth functions and solved from the perspective of a common Newton's method. This Newton-type optimization ensures quadratic convergence, although the number of iterations is typically higher compared to relaxation methods. For a comprehensive review of non-smooth methods applied to dynamics problems, we refer to [88].

1.3.3 Conducting Polymer Actuator

Typical conducting polymer actuators are ionic polymer–metal composites and ionic electroactive polymer (IEAP). They have specific characteristics that allow them to be now used for various applications, whether in applications requiring actuation and/or sensing mode. The main advantage of these polymers based actuator is their soft nature, good stability, sufficiently high electric conductivity [89], bio-compatibility [90], large work density, low operating

voltages (typically $\leqslant$3V) [91] that attracted a lot of attention over recent years for the realization of artificial muscles [92]. Moreover, their good electromagnetic compatibility, noise-free operation, low cost, light weight, their long life cycle [93] without degradation make these actuators a promising technology for microelectromechanical systems (MEMS). In addition, these polymers can be used as linear [94] or flexural micro-actuators [95], operating in solution [92] or in ambient air conditions [96]. Due to these advantages, they are implemented in a wide range of applications in robotics [97] or biomedical applications [91]. The work of this thesis on this topic will focuses on a typical actuator based on IEAP as the conducting polymer, which contains its nonlinear modeling, parameter estimation and control.

Precisely, the IEAP based trilayer micro-actuator was micro-fabricated according to the method described in [95]. The upper and lower layers are made of electronically conducting polymers (CP) material basically poly polystyrene sulfonate as reported in [98]. The middle layer is considered as an ion reservoir providing the system with ionic conductivity and mechanical properties [98]. This middle layer is formed with a semi-interpenetrated polymer network (IPN) composed of two polymers: poly ethylene oxide (PEO) and linear nitrile butadiene rubber (NBR) network. When a potential difference is applied to these two CP layers, one of the layers will undergo an oxidation reaction and the other one has a reduction reaction. It results in a corresponding increase or decrease in the charge density of the two layers. The change in ionic charge density will cause the two electrodes to produce opposite strains, which will cause one layer to expand and one layer to shrink. The expansion and contraction effect can be regarded as the bending of the actuator caused by the equivalent moment of force exerted on it. It should be noted that, the bending direction is occurring toward the anode [99].

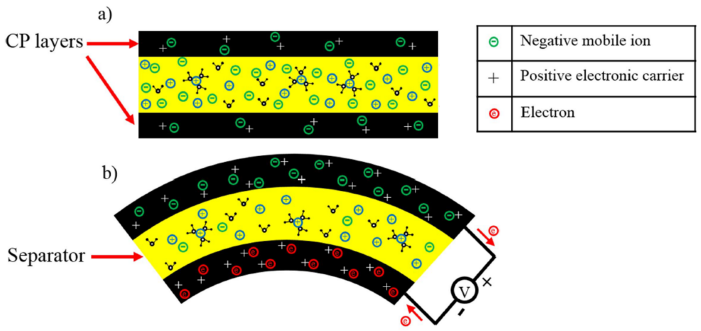

Figure 1.15: Trilayer actuator with two CP layers at the top and bottomand an ionically conductive separator in between before (a) and after (b) actuation.

Usually, an RC circuit model to describe the charge change process in the two electrode layers is used, and then the internal stress and strain are analyzed to obtain the curvature of the actuator. At present, some equivalent RC circuit models have been proposed [100, 101]. These models usually use isolated RC combinations or limited RC grid circuits to equivalent charge change processes. Although these models are efficient, their disadvantage is that they do not take into account the nonlinear changes of physical parameters in the actuator. The research of [102] shows that the resistivity and volumetric capacitance will both have greater nonlinearity during the charging process. The change interval affects the corresponding time of the actuator, so the nonlinear characteristics of the material are a consideration that can not be ignored in the modeling. [103] has proposed a finite nonlinear 2D-RC model, where this model takes into account the nonlinear characteristics of material properties following changes in charge density. In the work of Nishida [104], the infinite RC circuit was used to approximate the

real system and finite difference method was adopted to get the numerical solution. However, the methods mentioned above struggle to achieve a balance between the dimensionality and accuracy of the model.

The second part of modeling for conducting polymer actuator is calculating its deformation. It is noticed that if the charging time is enough long to reach the equilibrium charge state, the deformation will be uniform along the polymer, leading to the uniform curvature, which has been calculated by several studies [100, 105]. In fact, it usually takes a long time to reach the equilibrium charge state, thus the local deformation is necessary to study. [104] and [106] proposed the Timoshenko model to predict the deformation of conducting polymer actuator with the assumption of small deformation of 2 degrees of freedom. Meanwhile, in most cases the conducting polymer actuator does not work alone but interacts with the environment, such as external forces applying on it or multi conducting polymer actuators being connected in series.

Another difficulty related to the nonlinear model lies in the measurement of electronic model parameters. The nonlinear changing of various physical parameters of materials requires a large amount of experimental data to construct. At the same time, it is difficult to realize the control of a single variable during the experiment due to the excessive change of material parameters, which affects the accuracy of the experimental results. This process is often cumbersome and is limited by measurement accuracy, resulting in error stacking.

In terms of drive control, [107] designed PID and adaptive robust controller for controlling the displacement of conducting polymer actuator. However, the above-mentioned controller design is only based on the system model after the end point displacement is identified, which does not include the actuator curvature and bending moment information, thus this simplified model makes it difficult to further meet the control requirements of the actuator, such as actuator rotation angle control and multi-drive coupling control.

1.3.4 Control of Implantation via Robot Assistance

In the rapidly advancing field of robot-assisted cochlear implant surgery, significant strides have been made towards enhancing surgical precision and safety. Research has indicated that certain variables, such as the speed of insertion [108] and subtle manual movements during the insertion process [42], have the potential to cause added tissue trauma. In light of these considerations, an entirely navigation-controlled robotic system is a potential solution to align an insertion tool along an ideal axis and execute precise insertions, mitigating these factors [36, 109].

One pioneering study, conducted at the German Cancer Research Center in Heidelberg, Germany, explored the feasibility of robot-guided drilling for a minimally invasive cochlear implant approach [41]. This research underscored the potential of robotic assistance in cochlear implant surgery while emphasizing the need for further enhancements before its clinical application becomes viable. The primary focus was on mitigating the risks associated with traditional manual methods, especially when working near delicate structures like the facial nerve. In their work, Labadie R. F. and the collaborator proposed a manual insertion mechanism for percutaneous cochlear implantation. This innovation was part of an ongoing effort to refine cochlear implantation techniques. Their research played a pivotal role in demonstrating the feasibility of manual insertion mechanisms in conjunction with robotic assistance, opening avenues for more refined and controlled surgical procedures. Another noteworthy contribution came from Venail F and his colleagues, who explored the manual insertion of electrode arrays through a robot-assisted minimally invasive cochleostomy [110]. This study compared two different electrode array subtypes, revealing valuable insights into the practicality and comparative efficacy of robotic assistance in cochlear implant surgeries.

A novel advancement in the field was the introduction of a bone-attached parallel robot [38], renowned for its high stiffness and accuracy. This innovation offered distinct advantages over traditional serial industrial robots, particularly in reducing obtrusiveness in the operating room and eliminating the need for head fixation or optical tracking. The study highlighted the potential of parallel robots in achieving high precision in cochlear implant surgeries. In their research, Wimmer and his collaborators focused on semi-automatic cochleostomy target and trajectory planning for minimally invasive cochlear implantation. This approach marked a significant step towards fully robotic cochlear implantation. By automating parts of the surgical planning process, this research aimed to enhance the accuracy and safety of the implantation procedure. Labadie R. F. et al. contributed to the field through the clinical validation of percutaneous cochlear implant surgery [111]. Utilizing customized drill guides based on image-guided surgical technology, this study aimed to validate the practicality and effectiveness of percutaneous approaches in cochlear implant surgeries. Their research was crucial in demonstrating the clinical applicability of image-guided, robot-assisted surgical techniques.

Another notable advancement was the development of path planning software, specifically designed for robotic surgery [112]. This type of software was instrumental in automating the computation of the milling path, integrating considerations such as cutting velocity and drill angle. The work in [41] combined a robot, a surgical drill, and an Image-Guided Surgery (IGS) system in a closed-loop setup for cochlear implant surgery, where the robot-guided drill followed a preplanned trajectory to create the approach.

Lastly, in the research of Miroir et al., the friction forces were measured during cochlear implant surgery [113]. This measurement was integral to the design of a force-controlled insertion tool, aiming to enhance the precision and safety of the implantation process. The research aims to understand the influence of contact forces during surgery and how they can be optimally managed through robotic assistance.

1.4 Contributions

1.4.1 Contributions and Outline of the Thesis

The field of cochlear implant technology has witnessed remarkable advancements in recent years, especially in mechanical modeling, simulation, and control. However, as explained in the above sections, existing approaches still face significant challenges, particularly in computational complexity and accuracy in simulations. The mechanical modeling and control of CI are critical for improve the effectiveness and safety of implantation. However, traditional approaches, including finite element models, often grapple with high computational demands and limited real-time application capabilities. Moreover, the intricate nature of the cochlear environment and the interaction of implants with this environment pose significant challenges for accurate modeling and control.

Current research in cochlear implant technology primarily revolves around improving the fidelity of mechanical models and enhancing control systems for implantation. Finite element models have been the mainstay in simulating the mechanical behavior of cochlear implants. However, these models suffer from high-dimensional complexity, making real-time simulation and responsive control during implantation challenging. Furthermore, the identification of accurate physical parameters remains a significant hurdle, affecting the precision of simulations and the effectiveness of control methods. The need for robust and computationally efficient models is evident, as is the necessity for advanced control systems that can adapt to the dynamic conditions during implantation. Addressing these challenges, in this theis, our contributions are mainly summarized as follows:

1. Development of a generalized electronic and mechanical model: This research introduced a novel approach by adopting the Cosserat rod theory for the beam model of cochlear implants' electrode array. The model's reduced dimensions, as opposed to the traditional finite element models, maintain comparable accuracy. This advancement facilitates real-time simulation and control during cochlear implantation, overcoming the limitations of computational complexity and enhancing the practical application of these models in clinical settings.

2. Innovative parameter identification method: The study also pioneered a parameter identification method based on a nonlinear electro-mechanical coupling model. This method, incorporating a visual identification system to measure the curvature of the actuator, represents a substantial improvement in determining precise physical parameters. Such accuracy is vital for the reliability and effectiveness of cochlear implants.

3. Optimal controller design for implantation: Another significant contribution is the development of an optimal controller based on the proposed electro-mechanic model. This controller sets the stage for future advancements in multi-drive coupling trajectory tracking control. It has been validated through rigorous experimental and simulation methods, underscoring its robustness and reliability. This development marks a milestone in cochlear implant control systems, offering greater precision and safety in the implantation process.

In summary, this thesis is structured as follows: Chapter 1 begins with a comprehensive introduction to the background of Cochlear Implants (CI), encompassing the scientific challenges and advancements in this field. Chapter 2 introduces a Cosserat-based model for Active Cochlear Implant (ACI). This chapter delves into the mechanical modeling of the electrode array and the electro-mechanical behavior of the conducting polymer actuator, as well as their integrated coupling model. Following this, Chapter 3 explores the interaction between the CI and the cochlea, underpinned by model validation through experimental data. Chapter 4 is dedicated to the design of control strategies for CI implantation, encompassing both experimental findings and simulation results. Finally, Chapter 5 concludes the thesis, summarizing the key insights and outlining future perspectives in this field.

1.4.2 Publications and Patents

The following lists my publications during my Ph.D. study.

Journal articles:

1. Lingxiao Xun, Gang Zheng and Alexandre Kruszewski, "Cosserat-Rod Based Dynamic Modeling of Soft Slender Robot Interacting with Environment," in IEEE Transactions on Robotics, vol. 40, pp. 2811-2830, 2024, doi: 10.1109/TRO.2024.3386393.
   Paper Video

2. Lingxiao Xun, Gang Zheng, Sofiane Ghenna, Alexandre Kruszewski, Eric Cattan, Christian Duriez and Sebastien Grondel, "Modeling and Control of Conducting Polymer Actuator," in IEEE/ASME Transactions on Mechatronics, vol. 28, no. 1, pp. 495-506, Feb. 2023, doi: 10.1109/TMECH.2022.3211091.
   Paper Video

3. Haihong Li, Lingxiao Xun and Gang Zheng, "Piecewise Linear Strain Cosserat Model for Soft Slender Manipulator," in IEEE Transactions on Robotics, vol. 39, no. 3, pp. 2342-2359,

June 2023, doi: 10.1109/TRO.2023.3236942.
Paper Video

4. Haihong Li, Lingxiao Xun, Gang Zheng and Federico Renda, "Discrete Cosserat Static Model-Based Control of Soft Manipulator," in IEEE Robotics and Automation Letters, vol. 8, no. 3, pp. 1739-1746, March 2023, doi: 10.1109/LRA.2023.3243799.
Paper Video

5. Haihong Li, Lingxiao Xun and Gang Zheng, "Global Control of Soft Manipulator by Unifying Cosserat and Neural Network," in IEEE Transactions on Industrial Electronics, doi: 10.1109/TIE.2023.3331109.
Paper

6. Haihong Li, Lingxiao Xun, Gang Zheng and Frédéric Boyer, "Cosserat-Based Dynamic Control of Soft Manipulator," in IEEE Transactions on Robotics. Under review.
Video

Conferences:

1. Lingxiao Xun, Yinoussa Adagolodjo, Gang Zheng, Alexandre Kruszewski and Christian Duriez, "Real-time Simulation of Active Cochlear Implant and Its Insertion," in 2023 Conference on Implantable Auditory Prostheses
Video

2. Ahmad Itawi, Sofiane Ghenna, Guillaume Tourrel, Sébastien Grondel, Cedric Plesse, Tran Minh Giao Nguyen, Frederic Vidal, Yinoussa Adagolodjo, Lingxiao Xun, Gang Zheng, Alexandre Kruszewski, Christian Duriez and Eric Cattan, "Smart Electrode Array for Cochlear Implants," 2023 IEEE 36th International Conference on Micro Electro Mechanical Systems (MEMS), Munich, Germany, 2023, pp. 452-455, doi: 10.1109/MEMS49605.2023.10052348.
Paper

Patents:

1. Lingxiao Xun, Gang Zheng, Alexandre Kruszewski, Christian Duriez, Yinoussa Adagolodjo, Guillaume Tourrel, Raabid Hussain and Roger Calixto, "Force Minimization Algorithm for Robotized Surgery," Pending, 2023.

Chapter 2

Modeling of Active Cochlear Implant

2.1 Introduction

Building on the foundation laid in the first chapter, where we explored the evolution of cochlear implants and introduced the concept of active cochlear implants. We delved into the technical challenges inherent in these devices, particularly in the realms of modeling and control. This groundwork leads us directly into the specific focus of this chapter. As highlighted in our comprehensive review in the preceding chapter, the existing Finite Element Method (FEM) models are characterized by their high dimensionality, rendering them impractical for control applications. To facilitate effective model-based control of active cochlear implants, it becomes imperative to identify an efficient model with reduced dimensionality that can precisely depict the mechanical properties of the cochlear implant electrode array. In this chapter, we are dedicated to developing a refined model for the cochlear implant electrode array, leveraging the principles of Cosserat rod theory. This approach is strategically aimed at minimizing the complexity and dimensionality of the model.

Precisely, the primary objective of Chapter 2 is to delve deeper into our research on cochlear implant modeling. In this chapter, our research is concentrated on two key areas. Firstly, we have developed a mechanical model for the Electrode Array (EA), incorporating the Lie group to define EA's configuration. This creates a parameterized strain field that closely represents the actual system while simplifying its complexity. The model, using Cosserat rod theory, addresses nonlinearities in EA's deformations across six degrees of freedom, especially during environmental interactions. Secondly, we have created a model for the Electronic Conducting Polymer (ECP). This model helps us control the ECP's movements more accurately. We also introduce a new method for identifying uncertain parameters in these systems. This method uses a visual tool to measure the shape of actuators, making experiments simpler. Finally, we combine these models into a comprehensive system for active cochlear implants. This integrated model is crucial for controlling these implants effectively.

2.2 Modeling of Electrode Array Based on Cosserat Rod theory

2.2.1 Geometric description of EA

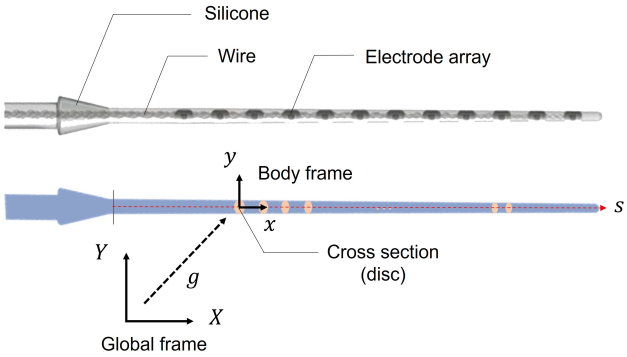

Figure 2.1: The structure of the cochlear implant electrode array and its geometric description under Cosserat rod theory.

In general, the electrode array of the cochlear implant consists of a slender electrode array, internal wires, and an outer casing, as shown in the Fig. 2.1. Due to its slender structure, it can be considered as a whole, akin to a single beam. To establish the dynamics equations for the single beam, we first need to establish its geometric representation. This involves describing the position and strain of each slice along the centerline of the cochlear implant electrode array. For this, we initially establish, we establish the overall geometric representation of this beam in space using the arc length s, as shown in Fig. 2.1. The spatial pose is defined as a mapping function relative to s, where s signifies the rod's arc length without deformation. Assuming the cross-sectional shape remains constant during implantation, obtaining the 3D position of any point along the centerline and the 3D rotational pose of the cross-section passing through that point enables the representation of the entire geometric configuration of the rod-shaped implant.

In the realm of soft robotics, Lie groups and Lie algebras serve as indispensable mathematical tools for describing the intricate deformations and kinematic characteristics of these flexible and deformable robots. Soft robots exhibit substantial changes in shape and structure based on task requirements and environmental conditions. Within this context, Lie groups and Lie algebras provide an elegant framework for representing the deformations and deformities of soft robots, enabling analysis within the overall state space. This includes a mathematical representation of deformations such as bending, twisting, and stretching. Furthermore, the application of Lie groups and Lie algebras proves beneficial in the control of soft robots, particularly in adjusting posture and shape. This mathematical framework is practically significant in soft robot path planning, optimization, and modeling within non-Euclidean state spaces. Overall, Lie groups and Lie algebras offer powerful tools for the field of soft robotics, aiding researchers in a better understanding and manipulation of the kinematic behaviors of soft robots. Consequently, in all our subsequent work, we will describe the geometric configuration of cochlear implants within the framework of Lie groups and Lie algebras.

The centerline of a cochlear implant is described by the 3D coordinates of each point, denoted as $\boldsymbol{p}(s) \in \mathbb{R}^3$, as shown in Fig. 2.1, where s represents the parameter along the centerline.

This vector is expressed in the global frame, providing a comprehensive representation of the implant's spatial configuration. Additionally, the orientation of the cross-section at each point along the centerline is characterized by the rotation matrix $\boldsymbol{R}(s) \in SO(3)$. This matrix captures the rotational aspects of the implant's geometry, ensuring a thorough representation of its orientation in three-dimensional space. Together, these descriptions in terms of position vectors and rotation matrices offer a comprehensive and precise depiction of the cochlear implant's geometric configuration.

For computational simplicity, we utilize the tensor $\boldsymbol{g}$ to denote the pose of each cross-section, as shown in Fig. 2.1. The tensor $\boldsymbol{g}$ combines the rotation matrix $\boldsymbol{R}$ and position vector $\boldsymbol{p}$, defined as follows:
For $s \in [0, L]$,

$$\boldsymbol{g}(s) = \begin{bmatrix} \boldsymbol{R}(s) & \boldsymbol{p}(s) \\ \boldsymbol{0}^\top & 1 \end{bmatrix} \in SE(3)$$

Upon completing the geometric characterization of the electrode array, the mechanical modeling of the cochlear implant's electrode array will unfold in a structured manner, as follows:

1. Kinematic model of the electrode array based on Cosserat rod theory
2. Constitutive equations of elasticity for the electrode array
3. Combining 1 and 2 to establish the dynamics equations of the electrode array based on Cosserat rod theory
4. Seeking approximate solutions to the dynamics equations: This includes spatial discretization of the Cosserat rod and establishing the weak form of the final dynamics equations.

In the subsequent sections, we will follow this outlined structure to progressively introduce the mechanics model of the electrode array based on Cosserat rod theory.

2.2.2 Kinematics

By taking the derivative of the tensor $\boldsymbol{g}$ along the arc length direction, we obtain the strain of the implant with respect to the body frame:

$$\boldsymbol{\xi} = (\boldsymbol{g}^{-1}\boldsymbol{g}')^\vee = [\boldsymbol{\kappa}^\top \ \boldsymbol{\epsilon}^\top]^\top \in \mathbb{R}^6$$

where $\boldsymbol{\kappa}$ stands for the angular strain and $\boldsymbol{\epsilon}$ represents the linear strain with respect to body frame.

Similarly, by taking the derivative of this tensor with respect to time, we can obtain the velocity of the cross-section with respect to the body frame as follows:

$$\boldsymbol{\eta} = (\boldsymbol{g}^{-1}\dot{\boldsymbol{g}})^\vee = [\boldsymbol{w}^\top \ \boldsymbol{v}^\top]^\top \in \mathbb{R}^6$$

where $\boldsymbol{w}$ stands for the angular velocity and $\boldsymbol{v}$ represents the linear velocity expressed in the body frame. After defining strain and velocity, we now seek their differential relationship, which determines the kinematic expression of the Cosserat rod. Based on the definitions of $\boldsymbol{\xi}$ and $\boldsymbol{\eta}$, we can get the following differential equations:

$$\boldsymbol{g}' = \boldsymbol{g}\widehat{\boldsymbol{\xi}} \tag{2.1}$$

$$\dot{\boldsymbol{g}} = \boldsymbol{g}\widehat{\boldsymbol{\eta}} \tag{2.2}$$

The mixed partial derivatives of $\boldsymbol{g}$ are independent of the order of differentiation. Therefore, $(\dot{\boldsymbol{g}})' = (\dot{\boldsymbol{g}'})$, we can then deduce the following equation:

$$\boldsymbol{\eta}' = \dot{\boldsymbol{\xi}} - \mathrm{ad}_{\boldsymbol{\xi}}\, \boldsymbol{\eta} \tag{2.3}$$

The above expression represents the relationship between the rate of change of strain with respect to time and velocity. The operator ad means the adjoint map, which holds the following structure:

$$\mathrm{ad}_{\boldsymbol{\xi}} = \begin{bmatrix} \hat{\boldsymbol{\kappa}} & \mathbf{0} \\ \hat{\boldsymbol{\epsilon}} & \hat{\boldsymbol{\kappa}} \end{bmatrix}$$

And as we continue to differentiate (2.3) with respect to time, we obtain the following expression:

$$\dot{\boldsymbol{\eta}}' = \ddot{\boldsymbol{\xi}} - \mathrm{ad}_{\dot{\boldsymbol{\xi}}}\, \boldsymbol{\eta} - \mathrm{ad}_{\boldsymbol{\xi}}\, \dot{\boldsymbol{\eta}} \tag{2.4}$$

which is about the acceleration.

2.2.3 Dynamics

As mentioned in [62], the Newton–Euler dynamics of the Cosserat rod can be expressed by the following equations:

$$\boldsymbol{\mathcal{I}}\dot{\boldsymbol{w}} + \boldsymbol{w} \times \boldsymbol{\mathcal{I}}\boldsymbol{w} = \boldsymbol{\Gamma}' + \boldsymbol{\epsilon} \times \boldsymbol{\Omega} + \bar{\boldsymbol{\Gamma}}_e \tag{2.5}$$

$$\boldsymbol{m}\dot{\boldsymbol{v}} + \boldsymbol{w} \times \boldsymbol{m}\boldsymbol{v} = \boldsymbol{\Omega}' + \bar{\boldsymbol{\Omega}}_e \tag{2.6}$$

where $\boldsymbol{\Gamma} \in \mathbb{R}^3$ means the inertial moment in body frame and $\boldsymbol{\Omega} \in \mathbb{R}^3$ means the inertial force in body frame. $\bar{\boldsymbol{\Gamma}}_e \in \mathbb{R}^3$ means the distributed external moment and $\bar{\boldsymbol{\Omega}}_e \in \mathbb{R}^3$ means the distributed external force in body frame. $\boldsymbol{\mathcal{I}} \in \mathbb{R}^{3\times3}$ denotes the moment of inertia matrix in body frame as $\boldsymbol{\mathcal{I}} = diag(I_x, I_y, I_z)$, where I_x, I_y, I_z are the moment of inertia about the x-axis, y-axis, and z-axis, respectively, for the beam cross-section. $\boldsymbol{m} \in \mathbb{R}^{3\times3}$ denotes the mass matrix as $\boldsymbol{m} = diag(A, A, A)\rho$, where A is the section area and ρ is mass density.

For the sake of brevity, we can write the above equations in the more compact form below:

$$\boldsymbol{\mathcal{M}}\dot{\boldsymbol{\eta}} - ad_{\boldsymbol{\eta}}^{\top}\boldsymbol{\mathcal{M}}\boldsymbol{\eta} = \boldsymbol{\Lambda}_i' - \mathrm{ad}_{\boldsymbol{\xi}}^{\top}\, \boldsymbol{\Lambda}_i + \bar{\boldsymbol{\Lambda}}_e \tag{2.7}$$

satisfying the following boundary conditions:

$$\boldsymbol{\Lambda}_i(0,t) = -\boldsymbol{\Lambda}_0(t),\ \boldsymbol{\Lambda}_i(L,t) = \boldsymbol{\Lambda}_L(t) \tag{2.8}$$

where $\boldsymbol{\mathcal{M}} \in \mathbb{R}^{6\times6}$ is the compact tensor of mass linear density along central axis as $\boldsymbol{\mathcal{M}} = diag(\boldsymbol{\mathcal{I}}, \boldsymbol{m})$. $\boldsymbol{\Lambda}_i \in \mathbb{R}^6$ is the elastic internal wrench which is defined as $\boldsymbol{\Lambda}_i = [\boldsymbol{\Gamma}^{\top}, \boldsymbol{\Omega}^{\top}]^{\top}$. $\boldsymbol{\Lambda}_e \in \mathbb{R}^6$ are the distributed external wrench along central axis defined as $\boldsymbol{\Lambda}_e = [\boldsymbol{\Gamma}_e^{\top}, \boldsymbol{\Omega}_e^{\top}]^{\top}$.

As for the external load $\boldsymbol{\Lambda}_e$, the contribution from gravity is given by $\boldsymbol{\Lambda}_e = \boldsymbol{\mathcal{M}}\mathrm{Ad}_{\boldsymbol{g}}^{-1}\boldsymbol{\mathcal{G}}$, where the inverse of adjoint representation of the Lie group is used to transform twists from the global frame to the body frame. $\boldsymbol{\mathcal{G}}$ is the gravity acceleration twist w.r.t. the global frame $\boldsymbol{\mathcal{G}} = [\mathbf{0}_{1\times5}\ \ -9.81]^{\top}$.

2.2.4 Constitutive Equation

The internal wrench of the soft slender rod is determined by strain and time rate of strain. Its constitutive equation based on Kelvin-Voigt model is as follows:

$$\boldsymbol{\Lambda}_i = \boldsymbol{\mathcal{K}}(\boldsymbol{\xi} - \boldsymbol{\xi}_0) + \boldsymbol{\mathcal{D}}\dot{\boldsymbol{\xi}} \tag{2.9}$$

with $\boldsymbol{\mathcal{K}} = diag\{GI_x, EI_y, EI_z, EA, GA, GA\} \in \mathbb{R}^{6\times6}$, the stiffness matrix of the entire electrodes plus polymer layers, where G represents the shear modulus and E represents the Young's modulus. $\boldsymbol{\mathcal{D}} = diag\{\mu_e I_x, 3\mu_e I_y, 3\mu_e I_z, 3\mu_e A, \mu_e A, \mu_e A\} \in \mathbb{R}^{6\times6}$, represents the viscosity matrices[114]. $\boldsymbol{\xi}_0 = [0\ 0\ 0\ 1\ 0\ 0]^{\top}$, represents the initial strain of the rod.

2.2.5 Discretization

In the preceding section, we successfully formulated the dynamic equations for the electrode array, framed as boundary value problems of nonlinear partial differential equations. Given the infeasibility of obtaining analytical solutions for these equations, we are compelled to employ discretization techniques to approximate their analytical solutions. Within the realm of finite element theory, the Galerkin-Ritz method stands as a prevalent approach for resolving the dynamics equations of systems characterized by partial differential equations and has been recently introduced in soft slender robot via Cosserat in [115]. This technique necessitates an initial spatial parameterization (discretization) of the equations, followed by employing a set of weak forms to approximate the original equations accurately. In this context, we intend to adopt this methodology to derive the weak form approximate solutions for the dynamic equations of the electrode array. The initial step involves the spatial parameterization of the electrode array, encompassing both its geometric and dynamic models.

As we have introduced in Section 2.2.1, the configuration of the EA's cross section can be represented by the tensor $\boldsymbol{g}$. Here, we define the continuous configuration space of the EA as follows:

$$\mathcal{U} = \{\boldsymbol{g} : s \in [0, L] \mapsto \boldsymbol{g}(s, t) \in \mathrm{SE}(3)\}$$

Then the geometric model (2.1) revealed the differential relationship between configuration space and strain field, as shown in the following equation:

$$\boldsymbol{g}' = \boldsymbol{g}\widehat{\boldsymbol{\xi}} \tag{2.10}$$

with initial condition $\boldsymbol{g}(0) = \boldsymbol{g}_0$. If the initial configuration $\boldsymbol{g}_0$ and the overall strain space $\boldsymbol{\xi}(s)$ of the soft slender rod (EA) are known for an instant, the configuration space of the soft slender rod can be constructed by solving (2.1). Consequently, the configuration space $\mathcal{U}$ of the soft slender rod can be totally defined by a set of $\{\boldsymbol{g}_0, \boldsymbol{\xi}(s)\}$, defined as follows:

$$\mathcal{U} = SE(3) \times \mathbb{S} \tag{2.11}$$

where $SE(3)$ denotes the configuration space of $\boldsymbol{g}(0)$ and $\mathbb{S}$ denotes the strain field, with $\mathbb{S} = \{\boldsymbol{\xi} : s \in [0, 1] \mapsto \boldsymbol{\xi} \in \mathbb{R}^6\}$. Therefore, the geometric parameterization of cochlear implants is divided into two parts: the parameterization of the head configuration tensor $\boldsymbol{g}_0$ and the parameterization of the strain field. In the subsequent discussion, we propose a redefinition of the EA's configuration space by parameterizing $\boldsymbol{g}_0(t)$ and $\boldsymbol{\xi}(s, t)$.

2.2.5.1 Parameterization of head configuration tensor g_0

As mentioned in Section 2.2.1, $\boldsymbol{g}_0$ is composed of a rotation matrix $\boldsymbol{R}_0$ and a position vector $\boldsymbol{p}_0$. In our approach, we use the exponential map to define the rotation matrix $\boldsymbol{R}_0$ by a vector $\boldsymbol{\phi} \in \mathbb{R}^3$:

$$\boldsymbol{R}_0(t) = \exp \tilde{\boldsymbol{\phi}}(t) \ , \ \boldsymbol{\phi}(t) \in \mathbb{R}^3 \tag{2.12}$$

Thus the configuration matrix $\boldsymbol{g}_0(t)$ is parameterized by the vector $\boldsymbol{\phi}(t)$ and $\boldsymbol{p}_0(t)$. We use vector $\boldsymbol{\alpha}(t) \in \mathbb{R}^6$ to denote their combination, i.e., $\boldsymbol{\alpha}(t) = [\boldsymbol{\phi}^\top(t) \ , \ \boldsymbol{p}_0^\top(t)]^\top$.

2.2.5.2 Parameterization of strain field

After representing the head configuration $\boldsymbol{g}_0$ of the Electrode Array (EA) via a vector, the configuration of the remaining part of the EA will then be approximated. This approximation is achieved by parametrizing the rod's configuration in terms of its strains, which are subsequently

condensed using the Ritz basis function. Precisely, the strain field can be predefined as the function of a set of parameter $\boldsymbol{\theta} \in \mathbb{R}^n$:

$$\boldsymbol{\xi}(s) = \boldsymbol{\xi}_0 + \boldsymbol{\Phi}(s)\boldsymbol{\theta} \tag{2.13}$$

where $\boldsymbol{\Phi}(s) \in \mathbb{R}^{6\times n}$ is the Ritz basis function, and $\boldsymbol{\xi}_0$ represents the initial strain of soft slender rod. By the approach above, the total deformation of rod is determined by the parameter $\boldsymbol{\theta}$.

In the Ritz method, the selection of appropriate basis functions is crucial. These basis functions are utilized to expand the solution of the problem, and the approximate solution is obtained by minimizing the residual.

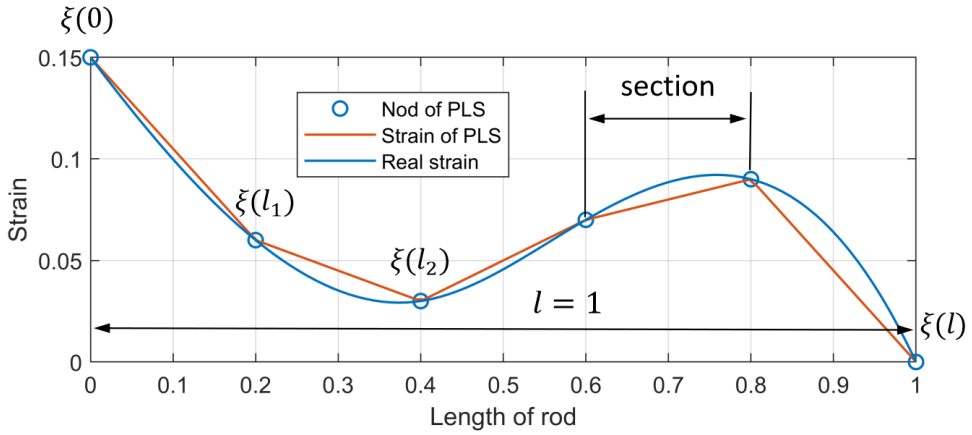

Figure 2.2: Schematic illustration of the PLS Cosserat model: soft slender rod divided into several sections.

Piecewise functions are favored as finite element basis functions due to their adaptability to represent complex and discontinuous shapes or behaviors in real-world problems. Their local adaptability allows for accurate representation of specific characteristics in different regions, making them well-suited for handling variations and abrupt changes in physical systems. This adaptability simplifies computations and facilitates convergence in finite element methods, making piecewise functions a practical choice for approximating solutions. In finite element analysis, the use of piecewise functions is driven by their ability to offer a simple and efficient representation of physical phenomena. Their capacity to capture local characteristics and handle discontinuities allows for a more accurate depiction of complex geometries or material properties. The ease of integration, simplicity in representation, and favorable convergence properties contribute to the effectiveness of piecewise functions in accurately modeling diverse and intricate systems.

Based on the above idea, we interpolate the strain field of Cosserat rod by using piecewise linear strain (PLS) interpolation methods. As shown in Fig. 2.2, in the PLS approach, the rod is discretized into sections. The points between sections are referred to as nodes, whose arc length coordinate are $\{0, l_1, l_2, \ldots, l\}$. Furthermore, we utilize the strain at these nodes to interpolate the entire strain field. In this case, the vector $\boldsymbol{\theta}$ contains the strain of all the nodes:

$$\boldsymbol{\theta} = \begin{bmatrix} \boldsymbol{\xi}^\top(0) & \boldsymbol{\xi}^\top(l_1) & \boldsymbol{\xi}^\top(l_2) & \ldots & \boldsymbol{\xi}^\top(l) \end{bmatrix}^\top$$

The interpolation posits a linear variation of strain within each section, yielding a continuous and coherent representation of the strain field. This approach not only enhances accuracy but

also streamlines computational processes, proving particularly advantageous in situations characterized by sudden or localized strain variations. The basis function of PLS can be represented by the following definition:

$$\boldsymbol{\Phi}(s) = \begin{bmatrix} \Phi_0(s)\mathbf{I}_{6\times 6} & \dots & \Phi_n(s)\mathbf{I}_{6\times 6} \end{bmatrix} \in \mathbb{R}^{6\times 6(n+1)},\ \forall\ s \in [0, l] \tag{2.14}$$

$$\Phi_i(s) = \begin{cases} \dfrac{l_i - s}{l_i - l_{i-1}} & \text{for } s \in [l_{i-1}, l_i) \\ \dfrac{s - l_i}{l_{i+1} - l_i} & \text{for } s \in [l_i, l_{i+1}] \\ 0 & \text{for } s \notin [l_{i-1}, l_{i+1}] \end{cases}$$

2.2.5.3 Generalized coordinates of cochlea implant

After parameterizing the head configuration tensor and the strain space, we obtained the generalized coordinates for the discretization of the cochlear implant space, represented by the vector as $\boldsymbol{q} = [\boldsymbol{\alpha}^\top, \boldsymbol{\theta}^\top]^\top$.

2.2.5.4 Computing of configuration space with generalized coordinates

By employing the aforementioned parameterization, the entire configuration space of soft rod is now reconstructed in the following form:

$$\mathcal{U}_d = \mathbb{R}^6 \times \mathbb{R}^{6(n+1)} \tag{2.15}$$

Subsequently, the geometric model of the EA in the PLS can be characterized via the following equations:

$$\boldsymbol{g}_0 = \begin{bmatrix} \exp \tilde{\phi} & \boldsymbol{p}_0 \\ \mathbf{0} & 1 \end{bmatrix} \tag{2.16}$$

$$\boldsymbol{\xi}(s) = \boldsymbol{\xi}_0 + \boldsymbol{\Phi}(s)\boldsymbol{\theta} \tag{2.17}$$

$$\boldsymbol{g}' = \boldsymbol{g}\widehat{\boldsymbol{\xi}} \tag{2.18}$$

If we know the generalized coordinates $\boldsymbol{q}$ which comprise $\boldsymbol{\theta}$ and $\boldsymbol{\alpha}$, we can first employ (2.16) to compute the spatial initial configuration matrix $\boldsymbol{g}_0$ and the use (2.17) to compute the strain field. Subsequently, we can determine the configuration field by solving the differential equation (2.18). However, obtaining an analytical solution for (2.18) is not feasible due to the variable nature of $\boldsymbol{\xi}$ with respect to s. Hence, we make an assumption that $\boldsymbol{\xi}$ remains constant within a very small segment Δs and use this approach to approximate the overall strain field of the PLS, as depicted in Fig. 2.3. Then, for each small segment, we can get the analytical solution from its one tip at s to another tip at $s + \Delta s$:

$$\boldsymbol{g}(s + \Delta s) = \boldsymbol{g}(s) \exp \tilde{\boldsymbol{\xi}}(s)\Delta s \tag{2.19}$$

Ultimately, we calculate (2.18) by numerically integrating (2.19) within $SE(3)$. The geometric model of the rod can then be represented by the following equation:

$$\boldsymbol{g}(s, t) = \boldsymbol{g}_0(t) \left(\prod_{i=1}^{k-1} \exp \widehat{\boldsymbol{\xi}}(s_i, t)\Delta \mathrm{s} \right) \tag{2.20}$$

where $s = k\Delta s$.

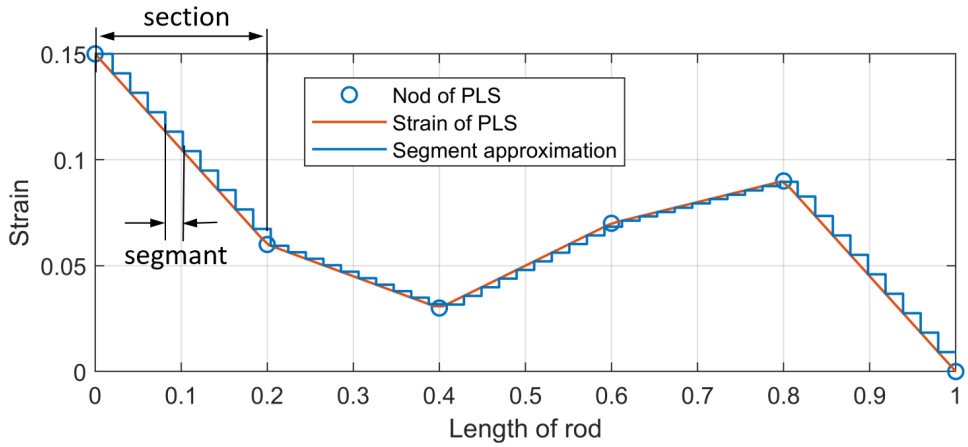

Figure 2.3: Any section subdivided into quite a few segments for numerical integration.

2.2.6 Discrete Kinematics

2.2.6.1 Jacobian matrix of soft slender rod

In the kinematics of robotics, the Jacobian matrix has consistently been a pivotal mathematical tool, primarily employed to describe the relationship between the end-effector velocity of rigid-body chain and the joint velocities. This forms the foundation for inverse kinematics problems, trajectory planning, and robot motion control. However, in the field of the modeling of soft slender rod, where the rod exhibit flexibility and deformable characteristics, the application of the Jacobian matrix requires a more profound and flexible consideration.

The distinctive nature of EA involves the description of the deformation, differing significantly from rigid-body structure. In soft slender rod, the Jacobian matrix is applied to depict the relationship between local displacement and global deformation. For EA, we will use the same way to establish this relationship, as it can be regarded as a soft slender rod. By considering the mechanical properties of EA, we can establish Jacobian matrices for deformations and displacements, thereby allowing their application in the realm of EA. Specifically, jacobian matrix is defined to map the generalized coordinates $\boldsymbol{q}(t) \in \mathbb{R}^{6(n+2)}$ to velocity field $\boldsymbol{\eta}(s,t) \in \mathbb{R}^6$ via the following form:

$$\boldsymbol{\eta}(s,t) = \boldsymbol{J}(s,t)\dot{\boldsymbol{q}}(t) \tag{2.21}$$

The Jacobian matrix is determined by the geometric configuration of EA and can be computed from the strain field. Since the strain expression involves variables of arc length s and time t, here we also represent the Jacobian matrix as a function of arc length and time.

2.2.6.2 Analytical solution of Jacobian matrix

As $\boldsymbol{q}$ contains both $\boldsymbol{\alpha}$ and $\boldsymbol{\theta}$, for ease of computation, we split the Jacobian matrix into two parts: the Jacobian matrix with respect to $\boldsymbol{\alpha}$ and the Jacobian matrix with respect to $\boldsymbol{\theta}$, as shown in the following equation:

$$\boldsymbol{\eta}(s,t) = \underbrace{\begin{bmatrix}\boldsymbol{J}_{\boldsymbol{\alpha}}(s,t) & \boldsymbol{J}_{\boldsymbol{\theta}}(s,t)\end{bmatrix}}_{\boldsymbol{J}(s,t)\in\mathbb{R}^{6\times 6(p+2)}}\dot{\boldsymbol{q}}(t) \tag{2.22}$$

where $\boldsymbol{J}_{\boldsymbol{\alpha}}(s,t) \in \mathbb{R}^{6\times 6}$ and $\boldsymbol{J}_{\boldsymbol{\theta}}(s,t) \in \mathbb{R}^{6\times 6(p+1)}$ are two Jacobian matrices respectively related with $\boldsymbol{\alpha}(t)$ and $\boldsymbol{\theta}(t)$. Here, we recall the continuous kinematic differential equations of the Cosserat rod, as follows:

$$\boldsymbol{\eta}' = \dot{\boldsymbol{\xi}} - \operatorname{ad}_{\boldsymbol{\xi}} \boldsymbol{\eta} \tag{2.23}$$

For $s \in [0, L]$, this equation describes the differential relationship between the strain field and the velocity field in this continuous space. By substituting (2.22) into (2.23), one can get:

$$\boldsymbol{J}'_{\boldsymbol{\alpha}}\dot{\boldsymbol{\alpha}} + \boldsymbol{J}'_{\boldsymbol{\theta}}\dot{\boldsymbol{\theta}} = \boldsymbol{\Phi}\dot{\boldsymbol{\theta}} - \operatorname{ad}_{\boldsymbol{\xi}}(\boldsymbol{J}_{\boldsymbol{\alpha}}\dot{\boldsymbol{\alpha}} + \boldsymbol{J}_{\boldsymbol{\theta}}\dot{\boldsymbol{\theta}}) \tag{2.24}$$

Note that the above equation holds for any $\dot{\boldsymbol{\alpha}}$ and $\dot{\boldsymbol{\theta}}$, thus the following two equations stand:

$$\boldsymbol{J}'_{\boldsymbol{\theta}} = -\operatorname{ad}_{\boldsymbol{\xi}} \boldsymbol{J}_{\boldsymbol{\theta}} + \boldsymbol{\Phi} \tag{2.25}$$

$$\boldsymbol{J}'_{\boldsymbol{\alpha}} = -\operatorname{ad}_{\boldsymbol{\xi}} \boldsymbol{J}_{\boldsymbol{\alpha}} \tag{2.26}$$

Taking derivative of the two equations above with respect to time one can get:

$$\dot{\boldsymbol{J}}'_{\boldsymbol{\theta}} = -\operatorname{ad}_{\dot{\boldsymbol{\xi}}} \boldsymbol{J}_{\boldsymbol{\theta}} - \operatorname{ad}_{\boldsymbol{\xi}} \dot{\boldsymbol{J}}_{\boldsymbol{\theta}} \tag{2.27}$$

$$\dot{\boldsymbol{J}}'_{\boldsymbol{\alpha}} = -\operatorname{ad}_{\dot{\boldsymbol{\xi}}} \boldsymbol{J}_{\boldsymbol{\alpha}} - \operatorname{ad}_{\boldsymbol{\xi}} \dot{\boldsymbol{J}}_{\boldsymbol{\alpha}} \tag{2.28}$$

Then, the Jacobian matrices and their time derivatives can be computed by numerical integration along arc space $s \in [0, 1]$ through (2.25)-(2.28) respectively starting from the initial value of $\boldsymbol{J}_{\boldsymbol{\alpha}}(0,t)$ and $\boldsymbol{J}_{\boldsymbol{\theta}}(0,t)$. It is obvious that for $s = 0$ the velocity $\boldsymbol{\eta}(0,t)$ only depends on the base parameter $\boldsymbol{\alpha}(t)$, i.e., $\boldsymbol{\eta}(0,t) = \boldsymbol{J}_{\boldsymbol{\alpha}}(0,t)\dot{\boldsymbol{\alpha}}$, thus we can directly deduce $\boldsymbol{J}_{\boldsymbol{\theta}}(0,t) = \mathbf{0}$ and $\dot{\boldsymbol{J}}_{\boldsymbol{\theta}}(0,t) = \mathbf{0}$. For the Jacobian with respect to $\boldsymbol{\alpha}(t)$ at the initial position, i.e., $\boldsymbol{J}_{\boldsymbol{\alpha}}(0,t)$, it can be derived from the derivation of exponential map.

For the exponential map of rotation matrix, the following differential relationship stands:

$$\dot{\boldsymbol{R}}_0(\boldsymbol{\phi})\boldsymbol{R}_0^{\top}(\boldsymbol{\phi}) = \widetilde{\left(\boldsymbol{J}_l(\boldsymbol{\phi})\dot{\boldsymbol{\phi}}(t)\right)} \tag{2.29}$$

where $\tilde{\cdot}$ denotes the mapping from $\mathbb{R}^3$ to $SO(3)$. $\boldsymbol{J}_l$ is the left Jacobian of group $SO(3)$, with the definition as below:

$$\boldsymbol{J}_l(\boldsymbol{\phi}) = \mathbf{I} + \frac{1-\cos\phi}{\phi^2}\tilde{\boldsymbol{\phi}} + \frac{\phi - \sin\phi}{\phi^3}\tilde{\boldsymbol{\phi}}^2$$

Using (2.29), the angular velocity of initial position with respect to body frame can be deduced:

$$\tilde{\boldsymbol{w}}(0,t) = \boldsymbol{R}_0^{\top}\dot{\boldsymbol{R}}_0 = \boldsymbol{R}_0^{\top}\widetilde{(\boldsymbol{J}_l\dot{\boldsymbol{\phi}})}\boldsymbol{R}_0$$

Notice that for any vector $\boldsymbol{x} \in \mathbb{R}^3$ and matrix $\boldsymbol{R} \in SO(3)$, one holds: $\boldsymbol{R}^{\top}\tilde{\boldsymbol{x}}\boldsymbol{R} = \widetilde{(\boldsymbol{R}^{\top}\boldsymbol{x})}$. Thus one can get

$$\boldsymbol{w}(0,t) = \boldsymbol{R}_0^{\top}(\boldsymbol{\phi})\boldsymbol{J}_l(\boldsymbol{\phi})\dot{\boldsymbol{\phi}} \tag{2.30}$$

The linear velocity of initial position with respect to body frame is

$$\boldsymbol{v}(0,t) = \boldsymbol{R}_0^{\top}(\boldsymbol{\phi})\dot{\boldsymbol{p}}_0$$

We can finally deduce the map from time derivation of vector $\boldsymbol{\alpha}$ to velocity twist of initial position with respect to body frame:

$$\boldsymbol{\eta}(0,t) = \begin{bmatrix} \boldsymbol{R}_0^{\top}(\boldsymbol{\phi})\boldsymbol{J}_l(\boldsymbol{\phi}) & \mathbf{0} \\ \mathbf{0} & \boldsymbol{R}_0^{\top}(\boldsymbol{\phi}) \end{bmatrix} \dot{\boldsymbol{\alpha}}(t) \tag{2.31}$$

where the matrix mapping $\dot{\boldsymbol{\alpha}}(t)$ to $\boldsymbol{\eta}(0,t)$ stands for the Jacobian $\boldsymbol{J}_{\boldsymbol{\alpha}}(0,t)$.

2.2.7 Weak Form of Dynamics

The unknown variables in the PDE (2.7) formed by the continuous dynamics encompass the initial pose tensor $\boldsymbol{g}_0$ at the starting end and the strain field $\boldsymbol{\xi}(s)$. In order to facilitate the solution of this partial differential equation, we aim to derive its corresponding weak form. By introducing suitable trial functions $\boldsymbol{\Phi}(s)$, the weak form of the equations can be expressed as the integration through the backbone of soft slender robot.

$$\int_0^L \boldsymbol{\Phi}(\boldsymbol{\mathcal{M}}\dot{\boldsymbol{\eta}} - ad_{\boldsymbol{\eta}}^{\top}\boldsymbol{\mathcal{M}}\boldsymbol{\eta} - \boldsymbol{\Lambda}_i' + \mathrm{ad}_{\boldsymbol{\xi}}^{\top}\,\boldsymbol{\Lambda}_i - \bar{\boldsymbol{\Lambda}}_e)\mathrm{ds} = 0 \tag{2.32}$$

Applying discretization techniques, the above integral equations of weak form are further approximated which allows transforming the weak form into ODE system about the generalized coordinates $\boldsymbol{q}$.

In our work, we choose the transpose of virtual displacement as the trial function. The transpose of virtual displacement can be got from the Jacobian matrix:

$$\boldsymbol{\Phi} = (\boldsymbol{J}\delta\boldsymbol{q})^{\top}$$

Then, taking $\boldsymbol{\phi}$ and the discrete kinematics (2.22) as well into (2.32), one can get:

$$\delta\boldsymbol{q}^{\top}\int_0^L \boldsymbol{J}^{\top}(\boldsymbol{\mathcal{M}}\boldsymbol{J}\ddot{\boldsymbol{q}} + \boldsymbol{\mathcal{M}}\dot{\boldsymbol{J}}\boldsymbol{q} - ad_{\boldsymbol{\eta}}^{\top}\boldsymbol{\mathcal{M}}\boldsymbol{J}\dot{\boldsymbol{q}} - \boldsymbol{\Lambda}_i' + \mathrm{ad}_{\boldsymbol{\xi}}^{\top}\,\boldsymbol{\Lambda}_i - \bar{\boldsymbol{\Lambda}}_e)\mathrm{ds} = 0 \tag{2.33}$$

2.2.8 ODE of Dynamics

Taking the generalized coordinates $\boldsymbol{q}$ and its time derivatives $\dot{\boldsymbol{q}}$ outside the integral, we can express the weak form mentioned above in the following shortened form:

$$\boldsymbol{M}\ddot{\boldsymbol{q}} + \boldsymbol{C}\dot{\boldsymbol{q}} + \boldsymbol{F}_i = \boldsymbol{F}_e \tag{2.34}$$

where $\boldsymbol{M}$ is the mass matrix defined as follows:

$$\boldsymbol{M}(\boldsymbol{q}) = \int_0^L \boldsymbol{J}^{\top}\boldsymbol{\mathcal{M}}\boldsymbol{J}\mathrm{ds} \in \mathbb{R}^{6(n+1)\times 6(n+1)}$$

$\boldsymbol{C}$ is the Coriolis matrix:

$$\boldsymbol{C}(\boldsymbol{q},\dot{\boldsymbol{q}}) = \int_0^L \boldsymbol{J}^{\top}(\boldsymbol{\mathcal{M}}\dot{\boldsymbol{J}} - ad_{\boldsymbol{J}\dot{\boldsymbol{q}}}^{\top}\boldsymbol{\mathcal{M}}\boldsymbol{J})\mathrm{ds} \in \mathbb{R}^{6(n+1)\times 6(n+1)}$$

$\boldsymbol{F}_e$ denotes the contribution of the external force:

$$\boldsymbol{F}_e = \int_0^L \boldsymbol{J}^{\top}\bar{\boldsymbol{\Lambda}}_e\mathrm{ds} \in \mathbb{R}^{6(n+1)}$$

$\boldsymbol{F}_i$ denotes the contribution of the internal force:

$$\boldsymbol{F}_i = \int_0^L \boldsymbol{J}^{\top}(-\boldsymbol{\Lambda}_i' + \mathrm{ad}_{\boldsymbol{\xi}}^{\top}\,\boldsymbol{\Lambda}_i)\mathrm{ds} \in \mathbb{R}^{6(n+1)} \tag{2.35}$$

then (2.35) can be simplified by integration by parts:

$$\boldsymbol{F}_i = -(\boldsymbol{J}^{\top}\boldsymbol{\Lambda}_i)|_0^L + \int_0^L \boldsymbol{J}^{\top\prime}\boldsymbol{\Lambda}_i + \boldsymbol{J}^{\top}\,\mathrm{ad}_{\boldsymbol{\xi}}^{\top}\,\boldsymbol{\Lambda}_i\mathrm{ds} \tag{2.36}$$

To further simplify (2.36), we first define the augmented basis function as $\bar{\boldsymbol{\Phi}} = [\mathbf{0}_{6\times6}, \boldsymbol{\Phi}]$. Subsequently, we modify (2.13) to:

$$\boldsymbol{\xi}(s) = \boldsymbol{\xi}_0 + \bar{\boldsymbol{\Phi}}(s)\boldsymbol{q} \tag{2.37}$$

Similarly, we update (2.25) as follows:

$$\boldsymbol{J}' = -\operatorname{ad}_{\boldsymbol{\xi}} \boldsymbol{J} + \bar{\boldsymbol{\Phi}} \tag{2.38}$$

Consequently, (2.36) can be simplified by incorporating (2.38):

$$\boldsymbol{F}_i = -(\boldsymbol{J}^\top \boldsymbol{\Lambda}_i)|_0^L + \int_0^L \bar{\boldsymbol{\Phi}}^\top \boldsymbol{\Lambda}_i \mathrm{ds} \tag{2.39}$$

Considering the constitutive relationship between stress and strain, i.e.,

$$\boldsymbol{\Lambda}_i = \boldsymbol{\mathcal{K}}(\boldsymbol{\xi} - \boldsymbol{\xi}_0) + \boldsymbol{\mathcal{D}}\dot{\boldsymbol{\xi}} = \boldsymbol{\mathcal{K}}\bar{\boldsymbol{\Phi}}\boldsymbol{q} + \boldsymbol{\mathcal{D}}\bar{\boldsymbol{\Phi}}\dot{\boldsymbol{q}}$$

we can further simplify the internal force vector (2.39):

$$\boldsymbol{F}_i = -\boldsymbol{J}^\top \boldsymbol{\Lambda}_i|_0^L + \int_0^L \bar{\boldsymbol{\Phi}}^\top \mathcal{K}\bar{\boldsymbol{\Phi}}\mathrm{ds}\boldsymbol{q} + \int_0^L \bar{\boldsymbol{\Phi}}^\top \mathcal{D}\bar{\boldsymbol{\Phi}}\mathrm{ds}\dot{\boldsymbol{q}} = -\boldsymbol{J}^\top \boldsymbol{\Lambda}_i|_0^L + \boldsymbol{K}\boldsymbol{q} + \boldsymbol{D}\dot{\boldsymbol{q}} \tag{2.40}$$

where matrix $\boldsymbol{K}$ is the stiffness matrix, defined as:

$$\boldsymbol{K} = \int_0^L \bar{\boldsymbol{\Phi}}^\top \mathcal{K}\bar{\boldsymbol{\Phi}}\mathrm{ds}$$

Matrix $\boldsymbol{D}$ is the damping matrix, defined as

$$\boldsymbol{D} = \int_0^L \bar{\boldsymbol{\Phi}}^\top \mathcal{D}\bar{\boldsymbol{\Phi}}\mathrm{ds}$$

The term $-(\boldsymbol{J}^\top \boldsymbol{\Lambda}_i)|_0^L$ in (2.40) represents the contribution of the internal force exerted by the two tips of the rod. By incorporating the boundary conditions specified in Equation (2.8) into this term, we obtain the following result:

$$-(\boldsymbol{J}^\top \boldsymbol{\Lambda}_i)|_0^L = \boldsymbol{J}_0^\top \boldsymbol{\Lambda}_0 + \boldsymbol{J}_1^\top \boldsymbol{\Lambda}_L$$

where $\boldsymbol{J}_0$ and $\boldsymbol{J}_1$ denote the kinematic Jacobian of two tips respectively, $\boldsymbol{\Lambda}_0$ and $\boldsymbol{\Lambda}_1$ denote the external force applied on the two tips respectively. Consequently, we are able to transfer the term $-(\boldsymbol{J}^\top \boldsymbol{\Lambda}_i)|_0^L$ from the contribution of internal force to the contribution of external force. In light of this adjustment, the expressions for $\boldsymbol{F}_i$ and $\boldsymbol{F}_e$ are revised:

$$\boldsymbol{F}_i = \boldsymbol{K}\boldsymbol{q} + \boldsymbol{D}\dot{\boldsymbol{q}},\ \boldsymbol{F}_e = \int_0^L \boldsymbol{J}^\top \bar{\boldsymbol{\Lambda}}_e \mathrm{ds} + \boldsymbol{J}_0^\top \boldsymbol{\Lambda}_0 + \boldsymbol{J}_1^\top \boldsymbol{\Lambda}_L$$

Following the aforementioned simplification, we arrive at the final form of the dynamic equation for the EA, which is articulated as follows:

$$\boldsymbol{M}\ddot{\boldsymbol{q}} + (\boldsymbol{C} + \boldsymbol{D})\dot{\boldsymbol{q}} + \boldsymbol{K}\boldsymbol{q} = \boldsymbol{F}_e \tag{2.41}$$

2.3 Modeling of Conducting Polymer Actuator

In the preceding sections, we explored the modeling process of the electrode array. For active electrode arrays, which incorporate an internal drive mechanism, this thesis utilizes Electronic Conducting Polymers (ECP) as micro actuators. As such, developing both the electrical and mechanical models of this actuator is crucial. This foundational work paves the way for constructing the comprehensive model of the active Electrode Array (EA), encompassing the coupled dynamics of the EA and its actuator. In the sections that follow, we will delve into the detailed electrical and mechanical modeling of the ECP. The approach mirrors the modeling framework established for the EA and will proceed in the following order:

1. Formulation of the electrical dynamic equations (partial differential equations).
2. Spatial discretization of these equations and the pursuit of their weak form approximate solutions.
3. Creation of mechanical equations grounded in Cosserat rod theory, akin to the mechanical model of the EA.
4. Finalization of the electromechanical coupling model of the ECP.

Based on this structure, in the following sections, we will separately introduce the electrical and mechanical models of the ECP.

2.3.1 Nonlinear Model

As mentioned above, the modeling task of conducting polymer can be mainly divided into two parts: the electronic model and the mechanic model. Noting that the working state of IEAP actuator depends on the actuation frequency [116] , it can be classified into two cases:

1. When the actuation frequency is below the mechanical resonance frequency of the actuator, the deformation is quasi-static.
2. When the actuation frequency is greater than the mechanical resonance frequency, the deformation varies mainly due to inertial mass effects. Thus the dynamics in mechanic model is necessary.

Based on the above two different cases, the following investigates different types of models: a nonlinear electronic dynamic model in Section 2.3.2, a mechanic quasi-static model for case 1 and a mechanic dynamic model for case 2 in Section 2.3.4. The final coupling model is then deduced in Section 2.3.5.

2.3.2 Electronic Model

In this part we will first build the continuous electronic model which describes the dynamic evolution of charge along actuator. Then the discrete model is built by discretization of the continuous model.

2.3.2.1 Strong form of electronic dynamics

Denote the total length of polymer as L where two electrode layers outside wrap the middle ion reservoir membrane. When the polymer is charged, the research in [116] shows that the process of charge can be regarded as an infinity RC circuit grid (see Fig. 2.4(a)). Let us

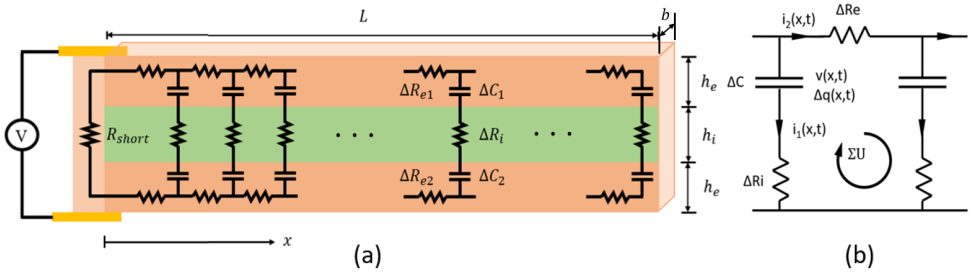

Figure 2.4: 2D-RC infinite grid for electronic model.

consider an infinitesimal element dx, and denote ΔR_{e1} and ΔR_{e2} as the electric resistance of outer layers and ΔR_i as the ionic resistance of middle layer, ΔC_1 and ΔC_2 as the corresponding capacitances of outer layers, which satisfy the following equations according to its definition:

$$\Delta R_{e1} = \frac{\mathrm{dx}}{\omega_{e1} b h_e} \ , \ \Delta R_{e2} = \frac{\mathrm{dx}}{\omega_{e2} b h_e} \ , \ \Delta R_i = \frac{h_i}{\omega_i b dx}$$

$$\Delta C_1 = C_{v1} b h_e \mathrm{dx} \ , \ \Delta C_2 = C_{v2} b h_e \mathrm{dx},$$

where b represents the width of polymer, h_e is the thickness of the CP layer, C_{v1} and C_{v2} are the volumetric capacitance of the top CP layer and the bottom CP layer , ω_{e1} and ω_{e2} are the volumetric conductivity of the top CP layer and the under CP layer, ω_i is the volumetric conductivity of the separator layer. For each RC grid element depicted in Fig. 2.4(a), its scheme can be simplified as Fig. 2.4(b), where

$$\begin{cases} \Delta R_i = \frac{h_i}{\omega_i b \mathrm{dx}} = \frac{r_i}{\mathrm{dx}} \\ \Delta R_e = \Delta R_{e1} + \Delta R_{e2} = (\frac{\mathrm{dx}}{\omega_{e1} b h_e} + \frac{\mathrm{dx}}{\omega_{e2} b h_e})\mathrm{dx} = r_e \mathrm{dx} \\ \Delta C = \Delta C_1 + \Delta C_2 = (C_{v1} b h_e + C_{v2} b h_e)\mathrm{dx} = c_e \mathrm{dx} \end{cases} \tag{2.42}$$

Without loss of generality, it is assumed that the electric resistances and ionic resistance are not constant. In fact, this electronic nonlinear characteristic has been observed in [103], which implies that the values of those resistances depend on the local charge.

As shown in Fig. 2.4(b), for the RC grid element located at x with dx length, denote v as the voltage of capacity ΔC, Δq as the charge of ΔC, i_1 and i_2 as the currents of the two branches, λ as the linear charge density at x, then v, i_1 and i_2 can be represented by $\lambda(x,t)$ via the following equations:

$$v(x,t) = \frac{\lambda}{c_e}, \ i_1(x,t) = \frac{\partial \lambda}{\partial t}\mathrm{ds}, \ i_2(x,t) = \int_x^l \frac{\partial \lambda}{\partial t}\mathrm{ds}. \tag{2.43}$$

For each grid as Fig. 2.4(b), according to Kirchhoff laws (i.e., $\sum U = 0$), we have

$$i_2(x,t)\Delta Re + \tfrac{\lambda(x+\mathrm{dx},t)}{c_e} + i_1(x+\mathrm{dx},t)\Delta R_i - i_1(x,t)\Delta R_i - \tfrac{\lambda(x,t)}{c_e} = 0,$$

With (2.42) and (2.43), we can then get the strong form of electronic dynamics from the above equation:

$$r_e(\lambda)\int_x^L \frac{\partial \lambda}{\partial t}\mathrm{ds} + \frac{1}{c_e}\frac{\partial \lambda}{\partial x} + r_i(\lambda)\frac{\partial^2 \lambda}{\partial x \partial t} = 0, \tag{2.44}$$

which is a partial differential equation (PDE) describing the charge density along the polymer, satisfying the following boundary conditions:

$$\lambda(x,0)=0,\ \frac{\lambda(0,t)}{c_e}+r_i(\lambda(0,t))\frac{\partial\lambda(0,t)}{\partial t}-V_{in}=0, \tag{2.45}$$

where V_{in} is the tension input applied on the two CP layers.

Remark 1. Due to the balance of charge in the charging process, the charge along actuator will tend to become stable when time tends to infinity, which means $\frac{\partial\lambda}{\partial t}=0$, thus $\frac{\partial\lambda}{\partial x}=0$ according to (2.44). Consequently, the distribution of charge along actuator at the equilibrium point will become geometrically uniform.

Up to now, we have built the continuous equation of charge density as PDE (2.44), and with (2.45) they compose a BVP (Boundary Value Problem). However, analytically solving such a highly nonlinear BVP is quite complicated or even impossible. In the following, we derive its weak form by applying Galerkin method to approximate the solution via spatially parameterizing the charge field.

2.3.2.2 Weak form of electronic dynamics

In order to simplify the writing of (2.44) and (2.45), we use prime in place of $\frac{\partial}{\partial x}$ and dot in place of $\frac{\partial}{\partial t}$. Thus (2.44) and (2.45) can be written as follows:

$$r_e(\lambda)\int_x^L\dot{\lambda}\mathrm{ds}+{c_e}^{-1}(\lambda)\lambda'+r_i(\lambda)\dot{\lambda}'=0, \tag{2.46}$$

with the boundary condition:

$${c_e}^{-1}(\lambda(0,t))\lambda(0,t)+r_i(\lambda(0,t))\dot{\lambda}(0,t)-V_{in}(t)=0. \tag{2.47}$$

Now we can define the "virtual charge displacement" $\delta\lambda$ of each micro RC grid, then the energy balance equation of conducting polymer might be deduced, which corresponds to the weak form of PDE (2.46) as follows:
$\forall x\in[0,\ L]\mapsto\delta\lambda(x)\in\mathbb{R}$,

$$\int_0^L\delta\lambda^T(x)\left\{r_e\int_x^L\dot{\lambda}dr+{c_e}^{-1}\lambda'+r_i\dot{\lambda}'\right\}\mathrm{dx}=0. \tag{2.48}$$

To obtain the complete weak form, we need to discretize the parameterization of the charge field. This process will be explained in the subsequent subsection.

2.3.2.3 Parameterization charge field

Note that the solution of (2.48) is defined in an infinite set. To discretize the system and find the numerical solution, we consider that the field of charge can be approximated by a set with limited degrees of freedom. To generically handle this kind of approximation, the field of charge λ is defined by the product of basis function and coefficients. i.e.,

$$\lambda(x,t):=\boldsymbol{\psi}(x)\boldsymbol{\lambda}(t),\ x\in[0,\ L], \tag{2.49}$$

where $\boldsymbol{\psi}(x)=[\psi_0,\ \psi_1,\ldots,\ \psi_m]\in\mathbb{R}^{1\times m}$ is the basis function and $\boldsymbol{\lambda}=[\lambda_0,\ \lambda_1,\ldots,\ \lambda_m]^T\in\mathbb{R}^{m\times 1}$ is the coefficients. In order to globally parameterize the charge field without losing physical meaning, the basis function $\boldsymbol{\psi}(x)$ is chosen by these two assumptions below:

Assumption 1: The conducting polymer can be divided into several sections and for each section the charge density is distributed linearly.
Assumption 2: All the physical parameters are homogeneous in each section.

Based on the piece-wise linear assumption 1, basis function $\boldsymbol{\psi}(x)$ holds the following structure:

$$\boldsymbol{\psi} = \begin{cases} \left[\frac{l-s}{l}, \frac{x}{l}, 0, \ldots, 0\right], & 0 \leqslant x < l \\ \vdots & \vdots \\ \left[0, \ldots, 0, \frac{kl-x}{l}, \frac{x-(k-1)l}{l}, 0, \ldots, 0\right], & (k-1)l \leqslant x < kl \\ \vdots & \vdots \\ \left[0, \ldots, 0, \frac{nl-x}{l}, \frac{x-(n-1)l}{l}\right], & (n-1)l \leqslant x < nl \end{cases}$$

As a result, (2.49) leads to two relations:

$$\delta\lambda(x) = \boldsymbol{\psi}\delta\boldsymbol{\lambda},\ \lambda(x)' = \boldsymbol{\psi}'\boldsymbol{\lambda}. \tag{2.50}$$

2.3.2.4 Discrete electronic model

Note that the weak form (2.48) is equivalent to (2.44). This weak form holds the advantage of realizing the approximation from the continuous dynamics of electronic model to discrete dynamics. Concretely, by substituting (2.49)-(2.50) into (2.48), one can get:

$$\delta\boldsymbol{\lambda}^T \int_0^L \boldsymbol{\psi}^T \left\{ r_e \int_x^L \boldsymbol{\psi}\dot{\boldsymbol{\lambda}} dr + {c_e}^{-1}\boldsymbol{\psi}'\boldsymbol{\lambda} + r_i\boldsymbol{\psi}'\dot{\boldsymbol{\lambda}} \right\} \mathrm{dx} = 0.$$

The equation above should hold for any $\delta\boldsymbol{\lambda}$, thus after removing $\delta\boldsymbol{\lambda}^T$ and adding the boundary condition (2.47), we obtain the following succinct ODE representation of the electronic model:

$$(\boldsymbol{R_e}\begin{bmatrix}\mathbf{0}\\ \mathbf{P}\end{bmatrix} + \boldsymbol{R_i}\begin{bmatrix}\mathbf{W}\\ \mathbf{Q}\end{bmatrix})\dot{\boldsymbol{\lambda}} + \boldsymbol{C_e}^{-1}\begin{bmatrix}\mathbf{W}\\ \mathbf{Q}\end{bmatrix}\boldsymbol{\lambda} = \begin{bmatrix}V_{in}\\ \mathbf{0}\end{bmatrix}, \tag{2.51}$$

with

$$\mathbf{W} = \begin{bmatrix}1 & 0 & \ldots & 0\end{bmatrix} \in \mathbb{R}^{m+1},$$

$$\boldsymbol{P} = \int_0^L \boldsymbol{\psi}^T(x) \int_x^L \boldsymbol{\psi}(s)\mathrm{dsdx},\ \boldsymbol{Q} = \int_0^L \boldsymbol{\psi}^T(x)\boldsymbol{\psi}'(x)\mathrm{dx},$$

$$\boldsymbol{R_e} = diag\{r_e(\lambda_0), r_e(\frac{\lambda_0+\lambda_1}{2}), \ldots, r_e(\frac{\lambda_{m-1}+\lambda_m}{2})\},$$

$$\boldsymbol{R_i} = diag\{r_i(\lambda_0), r_i(\frac{\lambda_0+\lambda_1}{2}), \ldots, r_i(\frac{\lambda_{m-1}+\lambda_m}{2})\},$$

$$\boldsymbol{C_e} = diag\{c_e(\lambda_0), c_e(\frac{\lambda_0+\lambda_1}{2}), \ldots, c_e(\frac{\lambda_{m-1}+\lambda_m}{2})\}.$$

After having established the discrete dynamic equation (2.51) of electronic model to describe the evolution of charge density along actuator, the next step is to show how the charge density of each section can create the deformation of polymer.

2.3.3 From Electric Charge to Actuation Moment

Consider now one element of 3-layer polymer depicted in Fig. 2.5 with E_e and E_i being the Young's modulus of the CP layer and the separator layer respectively. Denote α as the strain-to-charge ratio of the CP layers, and λ as the linear charge density of CP layers. Obviously, the values of charge density for these two CP layers should be opposite due to the balance of charge. Thus we define the linear charge density of the upper CP layer as λ, so that of the bottom CP layer should be $-\lambda$. As shown in Fig. 2.5, for a micro element of the actuator, the stress on its cross section S is comprised with two parts (see Fig. 2.5): the elastic stress σ_e and the redox stress σ_r. Since the redox strain is proportional with charge density [102], the equivalent redox stress can be calculated as follows:

$$\sigma_r(y) = \begin{cases} -E_e \frac{\alpha\lambda}{bh_e}, & \frac{h_i}{2} < y \leqslant \frac{h_i}{2} + h_e \\ 0, & -\frac{h_i}{2} \leqslant y \leqslant \frac{h_i}{2} \\ E_e \frac{\alpha\lambda}{bh_e}, & -\frac{h_i}{2} - h_e \leqslant y < -\frac{h_i}{2} \end{cases}$$

Consequently, for any cross section we can compute its actuated force defined in the local frame

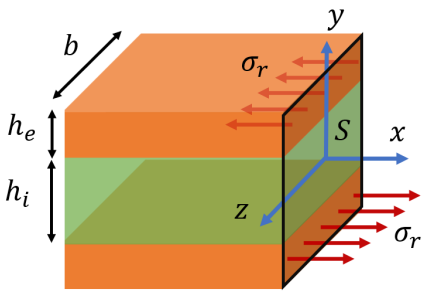

Figure 2.5: The equivalent redox stress distribution on the cross section S of polymer based actuator.

of cross section. It can be deduced directly that the total contribution of the electric stress is a moment while the forces of the two CP layers counteract with each other:

$$\boldsymbol{\mathcal{F}_a} = \iint_S \boldsymbol{\sigma_r} \mathrm{dS} = \boldsymbol{u_1} \iint_S \sigma_r \mathrm{dS} = \int \boldsymbol{u_1} \int_{-\frac{h_i}{2}-h_e}^{\frac{h_i}{2}+h_e} \sigma_r \mathrm{dydz},$$

where vector $\boldsymbol{u_1}$ is the identical direction vector of σ_r (i.e., $\boldsymbol{u_1} = \begin{bmatrix} 1 & 0 & 0 \end{bmatrix}^T$). The integral part $\int_{-\frac{h_i}{2}-h_e}^{\frac{h_i}{2}+h_e} \sigma_r \mathrm{dy} = 0$, which yields $\boldsymbol{\mathcal{F}_a} = \begin{bmatrix} 0 & 0 & 0 \end{bmatrix}^T$,

$$\begin{aligned} \boldsymbol{\mathcal{M}_a} &= \iint_S \boldsymbol{y} \times \boldsymbol{\sigma_r} \mathrm{dS} = \iint_S \boldsymbol{u_2} \times \boldsymbol{u_1} \sigma_r y \mathrm{dS} \\ &= \int_0^b \boldsymbol{u} \int_{-\frac{h_i}{2}-h_e}^{\frac{h_i}{2}+h_e} \sigma_r y \mathrm{dydz} = \boldsymbol{u} \int_0^b \frac{E_e \alpha (h_e + h_i)\lambda}{b} \mathrm{dz} \\ &= \boldsymbol{u} E_e \alpha (h_e + h_i)\lambda = \boldsymbol{u}\beta\lambda = \begin{bmatrix} 0 & 0 & \beta\lambda \end{bmatrix}^T, \end{aligned} \tag{2.52}$$

where $\boldsymbol{u_2}$ is the identical direction vector of $\boldsymbol{y}$ (i.e., $\boldsymbol{u_2} = \begin{bmatrix} 0 & 1 & 0 \end{bmatrix}^T$), $\boldsymbol{u} = \boldsymbol{u_2} \times \boldsymbol{u_1} = \begin{bmatrix} 0 & 0 & -1 \end{bmatrix}^T$, $\gamma = E_e \alpha (h_e + h_i)\lambda$. For ease of expression, we use an actuation wrench $\boldsymbol{\Lambda}_a \in \mathbb{R}^6$

to represent $\boldsymbol{\mathcal{F}_a}$ and $\boldsymbol{\mathcal{M}_a}$:

$$\boldsymbol{\Lambda}_a = \begin{bmatrix} \boldsymbol{\mathcal{M}_a}^T & \boldsymbol{\mathcal{F}_a}^T \end{bmatrix}^T = \begin{bmatrix} 0 & 0 & \gamma\lambda & 0 & 0 & 0 \end{bmatrix} = \boldsymbol{\mathcal{P}}\gamma\lambda \tag{2.53}$$

where $\boldsymbol{\mathcal{P}} = \begin{bmatrix} 0 & 0 & 1 & 0 & 0 & 0 \end{bmatrix}^T$.

Once we deduced the actuation moment of polymer actuator, the dynamic state of polymer actuator can be then analyzed, which will be detailed in the following sections.

2.3.4 Mechanic Model

In the aspect of mechanic analysis, it is natural that the polymer actuator can be regarded as a slender beam because of its high length -width ratio . The accumulation of local charge within the polymer induces internal stress, leading to the deformation of the actuator. In this subsection, we will first establish a relationship between the internal force and the local charge. Subsequently, we will delve into the dynamics of the polymer actuator in the ensuing subsections. Here, the actuator will be conceptualized as a Cosserat beam, influenced by both actuation and external forces. This approach is consistent with the model previously introduced in subsection 2.2, ensuring continuity and coherence in our analysis.

2.3.4.1 Strong form of dynamics

To analyze the mechanic behavior of beam such as polymer actuator, the Cosserat based strong form of dynamic model can be represented as the following PDE:

$$\boldsymbol{\mathcal{M}}\dot{\boldsymbol{\eta}} - ad^T_{\boldsymbol{\eta}}\boldsymbol{\mathcal{M}}\boldsymbol{\eta} = \boldsymbol{\Lambda}_i' - \mathrm{ad}^T_{\boldsymbol{\xi}}\,\boldsymbol{\Lambda}_i - \boldsymbol{\Lambda}_a' + \mathrm{ad}^T_{\boldsymbol{\xi}}\,\boldsymbol{\Lambda}_a + \overline{\boldsymbol{\Lambda}}_e, \tag{2.54}$$

satisfying the following boundary conditions:

$$\boldsymbol{\Lambda}_i(L) - \boldsymbol{\Lambda}_a(L) = \boldsymbol{\Lambda}_e(L), \tag{2.55}$$

2.3.4.2 Weak form of dynamics

Mirroring the approach for establish the weak form of EA, we apply the Lagrange–d'Alembert principle to define the virtual displacement of each disc along the polymer actuator, denoted as $\delta\boldsymbol{r}(x)$. Utilizing this definition, we can express the virtual work done by the polymer actuator, which subsequently yields the weak form of equation (2.54) as outlined below:
$\forall x \in [0,\ L] \mapsto \delta\boldsymbol{r}(x) \in \mathbb{R}^6$,

$$\int_0^L \delta\boldsymbol{r}^T(x)(\boldsymbol{\mathcal{M}}\dot{\boldsymbol{\eta}} - ad^T_{\boldsymbol{\eta}}\boldsymbol{\mathcal{M}}\boldsymbol{\eta} - \boldsymbol{\Lambda}_i' + \mathrm{ad}^T_{\boldsymbol{\xi}}\,\boldsymbol{\Lambda}_i + \boldsymbol{\Lambda}_a' - \mathrm{ad}^T_{\boldsymbol{\xi}}\,\boldsymbol{\Lambda}_a - \overline{\boldsymbol{\Lambda}}_e)dx = 0 \tag{2.56}$$

2.3.4.3 Parameterization strain field

The strain field of CPA is interpolated as follows:

$$\boldsymbol{\xi}(x) := \boldsymbol{\xi}_0 + \boldsymbol{\Phi}(x)\boldsymbol{q},\ x \in [0,\ L], \tag{2.57}$$

where $\boldsymbol{\Psi}(x) = [\Psi_0,\ \Psi_1, \ldots,\ \Psi_n] \in \mathbb{R}^{6\times n}$ is the basis function of piecewise linear interpolation, which we firstly introduced earlier as (2.14). $\boldsymbol{q} = [\boldsymbol{\xi}_0,\ \boldsymbol{\xi}_1, \ldots,\ \boldsymbol{\xi}_n]^T \in \mathbb{R}^{n\times 1}$ is the coefficients. $\boldsymbol{\xi}_0$ stands the initial value of $\boldsymbol{\xi}$.

2.3.4.4 Discrete mechanic model

The mechanical modeling of the CPA shares the same methodology as our previous mechanical modeling of the EA. As a result, the matrix structure in the dynamical equations is identical for both. However, unlike the EA's mechanical model, the CPA incorporates a driving force, adding an additional actuation term to its dynamical equations. In this context, We will derive this term here.

Based on the weak form as presented in equation (2.56), the general actuation force $\boldsymbol{F_a}$ of dynamics can be represented as follows:

$$\begin{aligned}\boldsymbol{F_a} &= \int_0^L (\boldsymbol{J}^\top \boldsymbol{\Lambda}_a)' - (-\operatorname{ad}_{\boldsymbol{\xi}} \boldsymbol{J} + \boldsymbol{\Psi})^\top \boldsymbol{\Lambda}_a - \boldsymbol{J}^\top \operatorname{ad}_{\boldsymbol{\xi}}^\top \boldsymbol{\Lambda}_a \mathrm{dx} \\ &= \int_0^L (\boldsymbol{J}^\top \boldsymbol{\Lambda}_a)' - \boldsymbol{\Psi}^\top \boldsymbol{\Lambda}_a \mathrm{dx} = \boldsymbol{J}^\top \boldsymbol{\Lambda}_a|_0^L - \int_0^L \boldsymbol{\Psi}^\top \boldsymbol{\Lambda}_a \mathrm{dx}.\end{aligned}$$

The piecewise linear charge assumption and (2.53) leads to $\boldsymbol{\Lambda}_a = \boldsymbol{\mathcal{P}}\gamma\lambda = \boldsymbol{\mathcal{P}}\gamma\boldsymbol{\psi}\boldsymbol{\lambda}$. As a result, $\boldsymbol{F_a}$ can be simplified as follows:

$$\boldsymbol{F_a} = -\boldsymbol{J}^\top(L)\boldsymbol{\mathcal{P}}\gamma\boldsymbol{\psi}(L)\boldsymbol{\lambda} + \int_0^L \boldsymbol{\Phi}^T\boldsymbol{\mathcal{P}}\boldsymbol{\psi}\mathrm{dx}\gamma\boldsymbol{\lambda} = \boldsymbol{H}\boldsymbol{z} \tag{2.58}$$

Here, we transfer the input variable $\boldsymbol{\lambda}$ to $\boldsymbol{z}$ with $\boldsymbol{z} = \gamma\boldsymbol{\lambda}$. The actuation matrix $\boldsymbol{H}$ is defined as follows:

$$\boldsymbol{H} = \int_0^L \boldsymbol{\Phi}^T\boldsymbol{\mathcal{P}}\boldsymbol{\psi}\mathrm{dx} - \boldsymbol{J}^\top(L)\boldsymbol{\mathcal{P}}\boldsymbol{\psi}(L)$$

After deducing $\boldsymbol{F_a}$, the final mechanic model can be rewritten as follows:

$$\boldsymbol{M}\ddot{\boldsymbol{q}} + (\boldsymbol{C} + \boldsymbol{D})\dot{\boldsymbol{q}} + \boldsymbol{K}\boldsymbol{q} = \boldsymbol{F}_e + \boldsymbol{H}\boldsymbol{z} \tag{2.59}$$

2.3.5 Whole coupling model of single CPA

After having deduced the electric model and the mechanical model of polymer, we can then gather these two models together to describe the whole dynamics of input tension and the corresponding deformation by the combination of the deduced electric system:

$$(\boldsymbol{Q_1}\boldsymbol{\Sigma_1} + \boldsymbol{Q_2}\boldsymbol{\Sigma_2})\dot{\boldsymbol{z}} + \boldsymbol{Q_3}\boldsymbol{\Sigma_2}\boldsymbol{z} = \boldsymbol{U}V_{in}, \tag{2.60}$$

with

$$\boldsymbol{Q_1} = \frac{1}{\gamma}\boldsymbol{R_e},\ \boldsymbol{Q_2} = \frac{1}{\gamma}\boldsymbol{R_i},\ \boldsymbol{Q_3} = \frac{1}{\gamma}{\boldsymbol{C_e}}^{-1},$$

$$\boldsymbol{\Sigma_1} = \begin{bmatrix}\mathbf{0}\\ \mathbf{P}\end{bmatrix},\ \boldsymbol{\Sigma_2} = \begin{bmatrix}\mathbf{W}\\ \mathbf{Q}\end{bmatrix},\ \boldsymbol{U} = \begin{bmatrix}1\\ \mathbf{0}\end{bmatrix},$$

and the obtained mechanic system:

$$\boldsymbol{M}\ddot{\boldsymbol{q}} + \boldsymbol{C}\dot{\boldsymbol{q}} + \boldsymbol{K}\boldsymbol{q} = \boldsymbol{H}\boldsymbol{z} + \boldsymbol{P}. \tag{2.61}$$

If the actuator works in quasi-static state, one can obtain its static model by just removing the first two terms $\boldsymbol{M}\ddot{\boldsymbol{q}}$ and $\boldsymbol{C}\dot{\boldsymbol{q}}$ of (2.61).

2.3.6 Parameters Identification

In the case of polymer actuator, the parameters of electric system are normally hard to measure directly, thus an identification work is necessary via which we can estimate the parameters from the data that are easily to measure. The electric model (2.60) deduced in the above section is nonlinear and contains unknown matrix $\boldsymbol{Q_1}$, $\boldsymbol{Q_2}$, $\boldsymbol{Q_3}$ which are nonlinear function of $\boldsymbol{z}$. Therefore, a parameter identification procedure is presented in this section to reveal the nonlinearlity of those parameters.

From the definition of $\boldsymbol{R_e}$, $\boldsymbol{R_i}$ and $\boldsymbol{C_e}$, we define:

$$\boldsymbol{Q_1} = diag\{q_1(z_0), q_1(\frac{z_0+z_1}{2}), q_1(\frac{z_1+z_2}{2}), \ldots, q_1(\frac{z_{m-1}+z_m}{2})\},$$

$$\boldsymbol{Q_2} = diag\{q_2(z_0), q_2(\frac{z_0+z_1}{2}), q_2(\frac{z_1+z_2}{2}), \ldots, q_2(\frac{z_{m-1}+z_m}{2})\},$$

$$\boldsymbol{Q_3} = diag\{q_3(z_0), q_3(\frac{z_0+z_1}{2}), q_3(\frac{z_1+z_2}{2}), \ldots, q_3(\frac{z_{m-1}+z_m}{2})\}.$$

It is assumed that these nonlinearlities of function q can be approximated by polynomials with certain order k, i.e.,

$$q_1(s) = \sum_{i=0}^{k} a_i s^i \ , \ q_2(s) = \sum_{i=0}^{k} b_i s^i \ , \ q_3(s) = \sum_{i=0}^{k} c_i s^i. \tag{2.62}$$

By noting $\boldsymbol{a} = \begin{bmatrix} a_0, \ldots, a_k \end{bmatrix}, \boldsymbol{b} = \begin{bmatrix} b_0, \ldots, b_k \end{bmatrix}, \boldsymbol{c} = \begin{bmatrix} c_0, \ldots, c_k \end{bmatrix}$ and

$$\boldsymbol{\Pi} = \begin{bmatrix} \boldsymbol{I} & diag(\boldsymbol{z}) & diag^2(\boldsymbol{z}) & \ldots & diag^k(\boldsymbol{z}) \end{bmatrix}$$

, the matrix $\boldsymbol{Q_1}$, $\boldsymbol{Q_2}$ and $\boldsymbol{Q_3}$ can be represented as: $\boldsymbol{Q_1} = \boldsymbol{\Pi a}^\top, \boldsymbol{Q_2} = \boldsymbol{\Pi b}^\top, \boldsymbol{Q_3} = \boldsymbol{\Pi c}^\top$. Set $\boldsymbol{\theta}_s = \begin{bmatrix} \boldsymbol{a} & \boldsymbol{b} & \boldsymbol{c} \end{bmatrix}^\top$ and concatenate the following values at different time from t_1 to t_{n_p} with $n_p > m$ where m is the dimension of $\boldsymbol{z}$:

$$\boldsymbol{\Xi} = \begin{bmatrix} \boldsymbol{\Sigma_1 \Pi}(t_1)\dot{\boldsymbol{z}}(t_1) & \boldsymbol{\Sigma_2 \Pi}(t_1)\dot{\boldsymbol{z}}(t_1) & \boldsymbol{\Sigma_2 \Pi}(t_1)\boldsymbol{z}(t_1) \\ \vdots & \vdots & \vdots \\ \boldsymbol{\Sigma_1 \Pi}(t_{n_p})\dot{\boldsymbol{z}}(t_{n_p}) & \boldsymbol{\Sigma_2 \Pi}(t_{n_p})\dot{\boldsymbol{z}}(t_{n_p}) & \boldsymbol{\Sigma_2 \Pi}(t_{n_p})\boldsymbol{z}(t_{n_p}) \end{bmatrix}$$

System (2.60) can be written into the following algebraic form: $\boldsymbol{\Xi \theta}_s = \boldsymbol{\Psi}$, where

$$\boldsymbol{\Psi} = \begin{bmatrix} \boldsymbol{U}^T V_{in}(t_1), & \cdots, & \boldsymbol{U}^T V_{in}(t_{n_p}) \end{bmatrix}^\top$$

. It is clear that, if all the $\boldsymbol{z}$ can be measurable and $\boldsymbol{\Xi}$ is full row rank, then $\boldsymbol{\theta}_s$ can be identified by using classical least square method.

2.3.7 Nonlinear Model Validation

2.3.7.1 Experimental setup

As shown in Fig. 2.6, our platform contains the polymer actuator which is connected to Arduino card and a camera (Microscope USB Dino-Lite) which enables us to catch the deformation of actuator with 20 fps. Specific image processing program has been developed by us to track the shape of polymer actuator in real time and compute the corresponding curvatures and its time

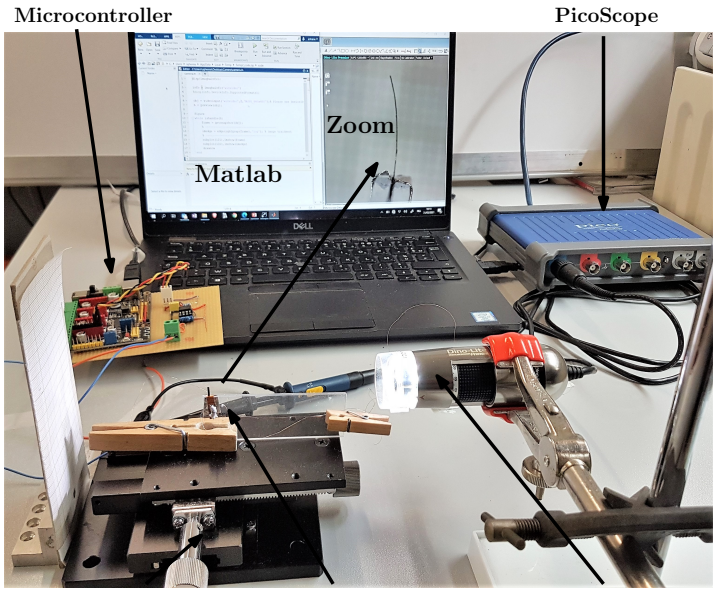

Figure 2.6: Experiment device. The actuator is fixed on the workbench and charged by microcontroller (MakeBlock MegaPi). A Dino-Lite micro camera on the right side is installed for observing the deformation of actuator.

Table 2.1: Measured parameters

Length L	Width b	Thickness h
5.87 mm	1.37 mm	0.035 mm
Strain to stress ratio α	Mean Young's modulus E	Mass density ρ
$7.31\times10^{-10}\mathrm{m}^3/\mathrm{C}$	2.53 GPa	2.42×10^3 kg/m^3

derivatives for each divided segment, which will be detailed in the next subsection. Tab.2.1 shows the measured parameters of the tested actuator.

In order to identify the unknown parameters (q_1, q_2, q_3), we use a ramp signal $V_{in} = at$ with $a = 0.01\ V/s$ as the excitation input signal to deform the polymer. In the work of Section 2.3.6, the variable $\boldsymbol{z}$ is calculated from the curvature of actuator, which can be measured directly by our designed visual system. Since the actuation speed is very low, the actuator can be regarded as quasi-static state. Since there is no external force applied on the actuator, the internal force equals to the actuation one, i.e., for $s \in [0,\ L]$, $\boldsymbol{\Lambda}_i(s) = \boldsymbol{\Lambda}_a(s)$, which means:

$$\kappa(s,t) = \frac{\gamma\lambda(s,t)}{EI_z} = \frac{z(s,t)}{EI_z}, \tag{2.63}$$

where κ is the curvature along axis z of polymer actuator. Thus z can be calculated by observing κ:

$$z(s,t) = EI_z\kappa(s,t). \tag{2.64}$$

Based on the image captured by the rapid camera, the shape of actuator can be extracted, from

which we can compute the curvature along actuator and its derivative of time. An algorithm

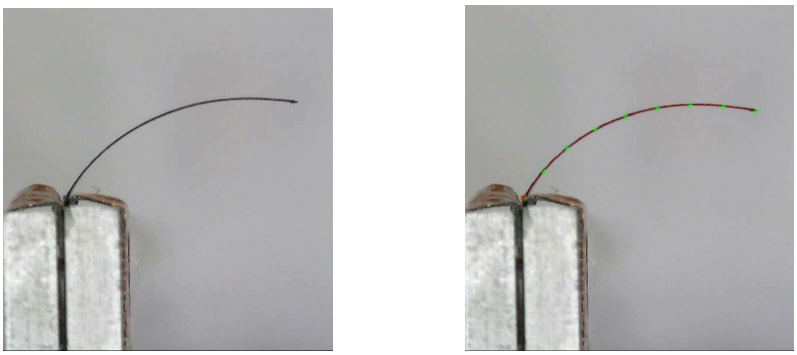

(a) (b)

Figure 2.7: The image recognition algorithm is capable of autonomously identifying and extracting the central line of the conducting polymer actuator. It then proceeds to segment this line into equal-length sections, as illustrated in (b). The points of division are marked in green for clear visualization.

of image binarization, inter-frame difference [117] and skeleton extraction [118] is applied via Matlab for obtaining the center skeleton of actuator, as shown in Fig. 2.7. Then the curvature could be calculated by the following equation:

$$\kappa = \frac{y''}{(1+y'^2)^{3/2}},\ \dot{\kappa} = \frac{\partial \kappa}{\partial t}. \tag{2.65}$$

However, it is inconvenient to compute the curvature and its derivative directly by the point data set of skeleton, due to the repeated calculation and discontinuity of data. To overcome this problem a polynomial curve fitting method is used here to get the curve function of actuator in real time which is of the following form:

$$y = \sum_{i=0}^{w} p_i x^i. \tag{2.66}$$

The analytical expression of the curvature and its derivative can be obtained directly by taking (2.66) into (2.65):

$$\kappa = \frac{\sum_{i=0}^{w} i(i-1)p_i x^{i-2}}{(1+(\sum_{i=0}^{w} i p_i x^{i-1})^2)^{3/2}},\ \dot{\kappa} = \frac{\partial \kappa}{\partial t}. \tag{2.67}$$

Based on the methods above, we got the curvature and its derivative of all sections as shown in Fig. 2.8. From the figure we can observe that the overall derivative of curvature of the actuator shows a trend of increasing first and then becoming steady. This is because the charge inside actuator gradually reaches saturation from the near power end (section 1) to the far power end (section 10).

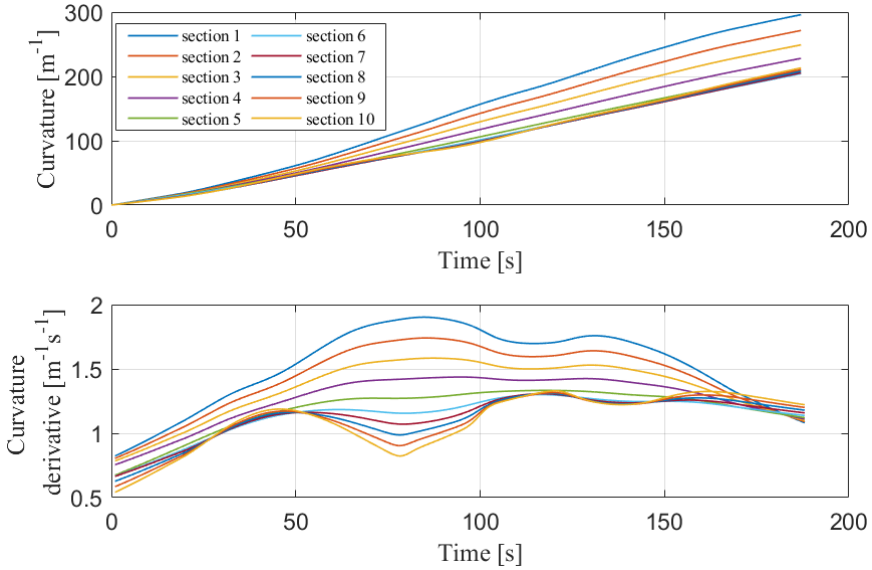

Figure 2.8: Curvature and its derivative measured under input $u = 0.01t$.

From the physical analysis about the micro structure of conducting polymer actuator [103], the resistance of the inter-layer is little varied by the charge density. Thus it is reasonable to suppose that q_2 in our model is constant, which mostly corresponds to the ionic mass transport. On the contrary, there exists a variation of conductivity and volumetric capacitance of the electrode which can not be ignored during the procedure of charge [103]. Indeed the electrical conductivity of the conducting polymer is a nonlinear function of redox level and the volumetric capacitance changes with the oxidation state. Hence, in the identification process, we finally adopt the following 5-order polynomial to represent the nonlinearity of q_1, and q_3:

$$q_1(s) = \sum_{i=0}^{5} a_i s^i \ , \ q_2(s) = b_0 \ , \ q_3(s) = \sum_{i=0}^{5} c_i s^i.$$

The identified values are given in Tab. 2.2.

Table 2.2: Identified result of q_1, q_2, q_3

i	0	1	2	3	4	5
a_i	526	249	-6.814	0.111	$-6.9e^{-4}$	$1.4e^{-6}$
b	0.0275	-	-	-	-	-
c_i	0.0110	$-5.9e^{-5}$	$-2.4e^{-7}$	$6.1e^{-9}$	$2.8e^{-11}$	$4.2e^{-14}$

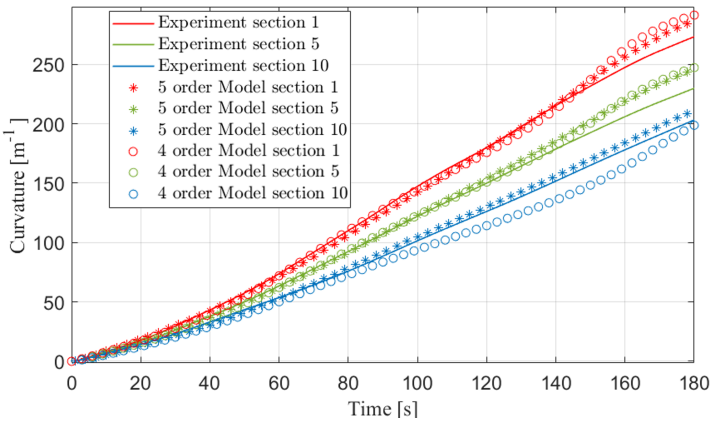

Figure 2.9: The evolution of the curvature for each segment of the actuator.

In order to show the deduced model is reliable, we simulate our model with the identified nonlinearity of q_1, q_2 and q_3, and compare the deformation result with experimental measurements. Fig. 2.9 shows the evolution of the curvature for the 1st section, the 5th section and the 10th section, indicating the fitting level between the experiment and the deduced model with the parameter fitting function of 4 order and 5 order. The error percentage of average curvature of the latter is less than 5% which is acceptable in our study.

Fig. 2.10 shows the coincidence level of the deformation of actuator with time between the experiment and the simulation via quasi-static model and dynamic model, under a ramp input voltage $u = 0.0075t$ and a step input voltage of amplitude 1.5V respectively.

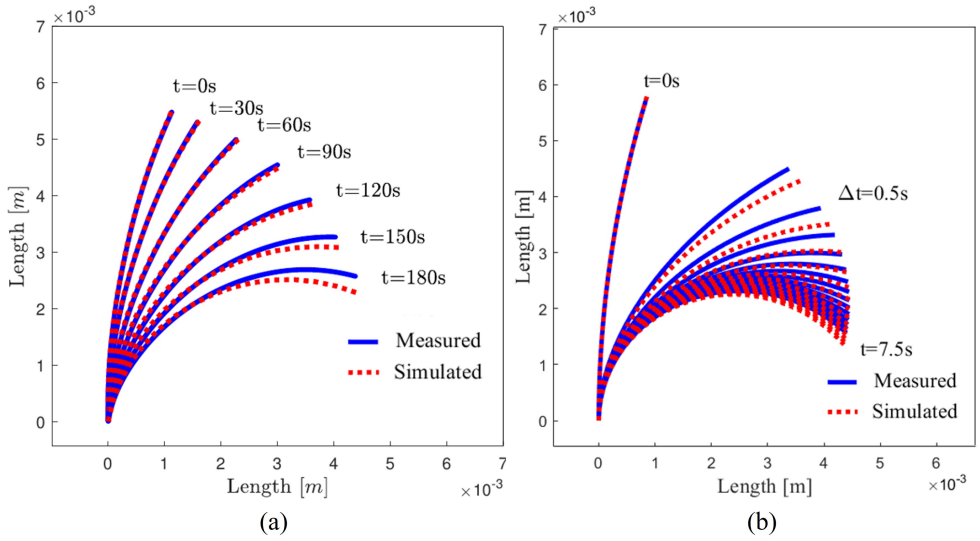

Figure 2.10: (a). Deformation of the polymer actuator under the ramp input comparing with mechanical static model; (b). Deformation of the polymer actuator under the step input comparing with mechanical dynamic model.

An experiment with external load is also carried out. As shown in Fig. 2.11, a payload

mass of 63mg is fixed on the tip of actuator. In this case, the mechanical dynamics of system is as follows:

$$\boldsymbol{M}\ddot{\boldsymbol{q}} + (\boldsymbol{C} + \boldsymbol{D})\dot{\boldsymbol{q}} + \boldsymbol{K}\boldsymbol{q} = \boldsymbol{J}^{\top}(L)\boldsymbol{\Lambda}_e(L) + \boldsymbol{H}\boldsymbol{z} \tag{2.68}$$

$$\mathcal{M}_p\dot{\boldsymbol{\eta}}_L - ad^{\top}_{\boldsymbol{\eta}_L}\mathcal{M}_p\boldsymbol{\eta}_{\boldsymbol{L}} = -\boldsymbol{\Lambda}_e(L) - \mathrm{Ad}^{-1}_{\boldsymbol{g}_{\mathrm{L}}}\mathcal{M}_{\mathrm{p}}\mathcal{G} \tag{2.69}$$

where (2.69) is the mechanical dynamics of the payload. $\mathcal{M}_p$ is the inertial matrix of payload and $\mathrm{Ad}_{\boldsymbol{g}_{\mathrm{L}}}$ is the transformation matrix. The comparison between simulation and experiment is shown in Fig. 2.11 under the step input voltage of amplitude 1.5V and 0.1Hz.

For the deduced model (2.60) and (2.61), the corresponding control has been developed and validated in [119]. In this section, we successfully developed a model for individual CPAs. Moving forward, the subsequent section will delve into the architecture of an active EA encompassing multiple CPAs. Additionally, we will elaborate on the associated coupled model tailored for this configuration.

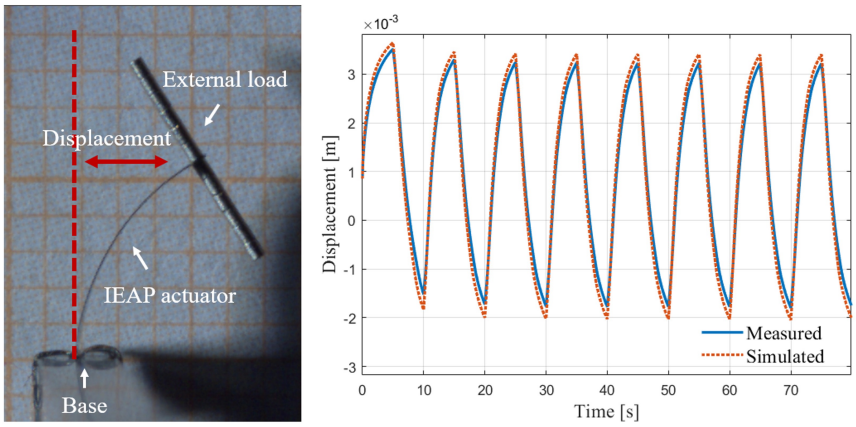

Figure 2.11: Displacement of tip of the polymer actuator with external load under the step input voltage of amplitude 1.5V and 0.1Hz comparing with mechanic dynamic model.

2.4 Coupling Model of Implant and Multi-Actuator

The new type of active cochlear implant consists of three components: an electrode array, a actuator array, and a flexible casing. Among these, the electrode array and the driver array are positioned in parallel, enclosed by the silicone carrier, creating an overall sandwich-like structure, as depicted in Fig. 2.12.

2.4.1 Electric model of actuator array

Similar to the conducting polymer actuator, the implant coupling model also includes electrical and mechanical components. The electrical model consists of a series of conducting polymer actuator models. In this subsection, we will introduce the series electrical model of the conducting polymer actuator. If N conducting polymer actuators are connected in series, the series

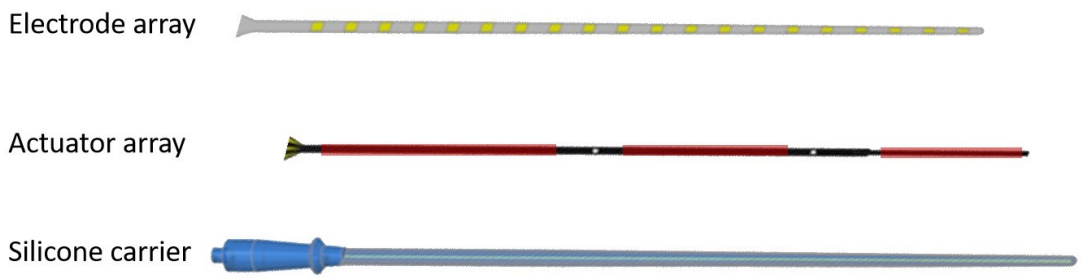

Figure 2.12: The sandwich structure of the active artificial cochlear implant consists of an electrode array comprising rigid electrodes and flexible wires, a driver array consisting of conducting polymer actuators and flexible wires, all enclosed within a flexible silicone casing.

model is as follows:

$$\underbrace{\begin{bmatrix} \boldsymbol{A}_1 & & \\ & \boldsymbol{A}_2 & \\ & & \ddots \\ & & \boldsymbol{A}_N \end{bmatrix}}_{\boldsymbol{A}} \underbrace{\begin{bmatrix} \dot{\boldsymbol{z}}_1 \\ \dot{\boldsymbol{z}}_2 \\ \vdots \\ \dot{\boldsymbol{z}}_N \end{bmatrix}}_{\dot{\boldsymbol{z}}} + \underbrace{\begin{bmatrix} \boldsymbol{B}_1 & & \\ & \boldsymbol{B}_2 & \\ & & \ddots \\ & & \boldsymbol{B}_N \end{bmatrix}}_{\boldsymbol{B}} \underbrace{\begin{bmatrix} \boldsymbol{z}_1 \\ \boldsymbol{z}_2 \\ \vdots \\ \boldsymbol{z}_N \end{bmatrix}}_{\boldsymbol{z}} = \underbrace{\begin{bmatrix} \boldsymbol{U}_1 & & \\ & \boldsymbol{U}_2 & \\ & & \ddots \\ & & \boldsymbol{U}_N \end{bmatrix}}_{\boldsymbol{U}} \underbrace{\begin{bmatrix} V_{in1} \\ V_{in2} \\ \vdots \\ V_{inN} \end{bmatrix}}_{\boldsymbol{V}_{in}} \tag{2.70}$$

where $\boldsymbol{z}_i$ denotes the electric charge state of the ith conducting polymer actuator. V_{in1} is the input voltage of the ith conducting polymer actuator. The matrix $\boldsymbol{A}_i$ and $\boldsymbol{B}_i$ are defined as follows:

$$\boldsymbol{A}_i = (\boldsymbol{Q_1}\boldsymbol{\Sigma_1} + \boldsymbol{Q_2}\boldsymbol{\Sigma_2})_i,\ \boldsymbol{B}_i = (\boldsymbol{Q_3}\boldsymbol{\Sigma_2})_i$$

2.4.2 Mechanical model

Upon establishing the electrical model of the implant, we now turn our focus in this subsection to the development of the implant's mechanical model. Initially, given that conducting polymer actuators are distributed throughout the implant, we introduce an actuation field function. This function is designed to pinpoint the locations of the conducting polymer actuators within the implant, effectively indicating the specific areas where the actuation force originates.

As shown in Fig.2.13, assuming there are N conducting polymer actuators within the implant, each located along the implant's axial direction at $[l_{1-}, l_{1+}], [l_{2-}, l_{2+}], ..., [l_{N-}, l_{N+}]$, the actuation field function is defined as: $\boldsymbol{\psi} = [\boldsymbol{\psi}_1, \ldots, \boldsymbol{\psi}_N]$,

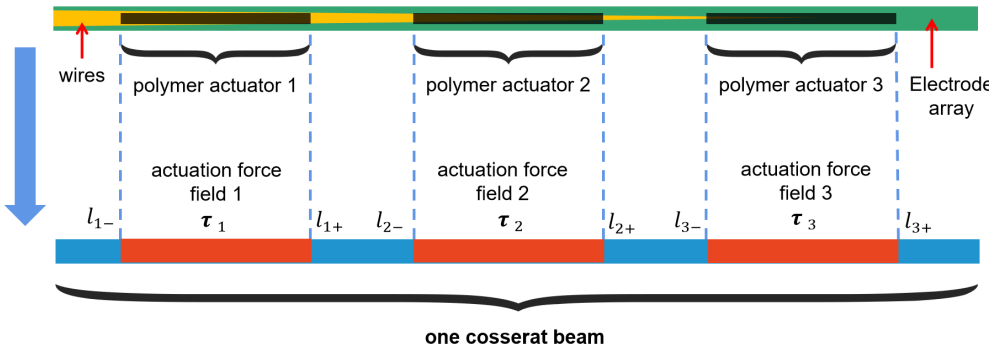

Figure 2.13: Schematic of active implant coupling model. Conducting polymer actuator, electrode array, and wires, along with the casing, are conceptualized as integral beams. The coupling model for this monolithic beam simulates the structure of the entire active implant by defining stiffness distribution and drive force field parameters for the monolithic beam.

where for $x \in \{[l_{i-}, l_{i+}]|i = 1, \ldots, N\}$, if $j = i$,

$$\boldsymbol{\psi}_j = \begin{cases} \left[\frac{l-x}{l}, \frac{x}{l}, 0, \ldots, 0\right], & l_{i-} \leqslant x < l_{i-} + l \\ \vdots & \vdots \\ \left[0, \ldots, 0, \frac{kl-x}{l}, \frac{x-(k-1)l}{l}, 0, \ldots, 0\right], & l_{i-} + (k-1)l \leqslant x < l_{i-} + kl \\ \vdots & \vdots \\ \left[0, \ldots, 0, \frac{nl-x}{l}, \frac{x-(n-1)l}{l}\right], & l_{i-} + (n-1)l \leqslant x < l_{i-} + nl \end{cases}$$

$$\text{if } j \neq i, \ \boldsymbol{\psi}_j = \mathbf{0}_{1\times n}$$

for $x \notin \{[l_{i-}, l_{i+}]|i = 1, \ldots, N\}$, $\boldsymbol{\psi}_j = \mathbf{0}_{1\times n}$.
Taking the actuation field function into (2.58) one can get the actuation matrix:

$$\boldsymbol{H} = \int_0^L \bar{\boldsymbol{\Phi}}^T \boldsymbol{\mathcal{P}} \boldsymbol{\psi} ds \in \mathbb{R}^{n\times m}$$

where $\bar{\boldsymbol{\Phi}}$ is the Ritz base function of EA, $\boldsymbol{\mathcal{P}}$ is the matrix defined in (2.53). The entire electric-mechanic coupling equation for the active implant is as follows:

$$\boldsymbol{A}\dot{\boldsymbol{z}} + \boldsymbol{B}\boldsymbol{z} = \boldsymbol{U}\boldsymbol{V}_{in} \tag{2.71}$$

$$\boldsymbol{M}\ddot{\boldsymbol{q}} + (\boldsymbol{C} + \boldsymbol{D})\dot{\boldsymbol{q}} + \boldsymbol{K}\boldsymbol{q} = \boldsymbol{F}_e + \boldsymbol{H}\boldsymbol{z} \tag{2.72}$$

Up to this point, we have derived the electrical and mechanical equations for the active electrode array, which constitute a set of ordinary differential equations. Finding an analytical solution to these equations is extremely complex and often impossible. In the simulation of complex system dynamics, numerical methods are typically employed to compute the numerical solutions of ordinary differential equations. In the following section, we will introduce the numerical solution methods for the ordinary differential equations of the dynamics of the active electrode array.

2.5 Numerical Implementation

As previously discussed, deriving analytical solutions for nonlinear ordinary differential equations is often a complex task, leading to the necessity of employing numerical methods to ascertain numerical solutions. Within the realm of finite element dynamics simulation, Euler methods are extensively utilized, encompassing both the explicit and implicit variants. The subsequent sections will provide a basic overview of each of these methods in turn.

2.5.1 Explicit Euler methods

The explicit Euler method is a common and fundamental numerical technique for solving nonlinear ordinary differential equations (ODEs). Its basic principle involves discretizing the continuous time axis into small steps and iteratively approximating the solution to the differential equation. The method is called "explicit" because all the necessary information for updating the solution is directly visible.

In the explicit Euler method, the first step is to calculate the derivative of the differential equation at the current time point. This derivative value represents the rate of change of the system in the current state. Subsequently, by multiplying the derivative value by the time step, we obtain the change in the solution within this small step. Adding this change to the current solution gives us the solution at the next time step. This process iterates continuously, progressively approaching the solution to the differential equation.

One of the advantages of the explicit Euler method is its intuitive and easily understandable nature. Its calculations are relatively simple, making it suitable for initial numerical simulations or educational purposes. However, like many numerical methods, the explicit Euler method has limitations. Due to its first-order nature, it may lack stability, especially when dealing with systems exhibiting stiffness or requiring higher numerical accuracy.

2.5.2 Implicit Euler methods

The Implicit Euler method, a variant of the backward differentiation formula, is frequently employed in computations to solve the differential equations governing system dynamics. This method stands in contrast to the explicit Euler method. In the explicit version, solutions are directly calculated using the derivative values at the current time point, multiplied by the time step. However, the implicit Euler method adopts a different approach. It iteratively solves an algebraic equation that includes the solution for the subsequent time step. This method offers increased flexibility and has shown superior performance, especially when dealing with stiff systems. The process of calculation proceeds as follows:

1. Formulation of the differential equation: Begin by formulating the differential equation governing the system dynamics. In our case, the system dynamic differential equations is given by (2.72):

$$\boldsymbol{M}\ddot{\boldsymbol{q}} + \bar{\boldsymbol{C}}\dot{\boldsymbol{q}} + \boldsymbol{K}\boldsymbol{q} = \boldsymbol{F}_e \tag{2.73}$$

where $\bar{\boldsymbol{C}}$ denotes $\boldsymbol{C} + \boldsymbol{D}$.

2. Discretization in time: The Implicit Euler method requires time discretization. Divide the time interval of interest into small steps, Δt.

3. Implicit Euler scheme: The method uses the following scheme for integration:

$$\boldsymbol{q}_{k+1} = \boldsymbol{q}_k + \Delta t \dot{\boldsymbol{q}}_{k+1}$$

$$\dot{\boldsymbol{q}}_{k+1} = \dot{\boldsymbol{q}}_k + \Delta t \ddot{\boldsymbol{q}}_{k+1}$$

Here, $\boldsymbol{q}_{k+1}$ and $\dot{\boldsymbol{q}}_{k+1}$ are the displacement and velocity at time $t_{k+1} = t_k + +\Delta t$, respectively.
4. Rearranging the equation: Substitute the expressions for $\boldsymbol{q}_{k+1}$ and $\dot{\boldsymbol{q}}_{k+1}$ into the dynamic equation and express $\ddot{\boldsymbol{q}}_{k+1}$ in terms of known quantities at time t_k.
5. Assembly of system equations: Formulate the system of equations at each time step. This results in a set of algebraic equations. One can reformulate (2.73) to the following equations at each time step to the following algebraic equations:

$$(\boldsymbol{M} + \Delta t\bar{\boldsymbol{C}})\dot{\boldsymbol{q}}_{k+1} - \Delta t\boldsymbol{M}\dot{\boldsymbol{q}}_k + \Delta t\boldsymbol{K}\boldsymbol{q}_{k+1} - \Delta t\boldsymbol{F}_e = \boldsymbol{0} \tag{2.74}$$

$$\boldsymbol{q}_{k+1} - \boldsymbol{q}_k - \Delta t\dot{\boldsymbol{q}}_{k+1} = \boldsymbol{0} \tag{2.75}$$

6. Solving the equations: In the equation under discussion, the matrices $\boldsymbol{M}$ and $\bar{\boldsymbol{C}}$, as well as the external force term $\boldsymbol{F}_e$, functionally depend on $\boldsymbol{q}_{k+1}$ and $\dot{\boldsymbol{q}}_{k+1}$, thus constituting a nonlinear system of equations. A common strategy for resolving this involves linearization to simplify the problem. This process typically entails performing a Taylor series expansion of the equations in the vicinity of the solution at the current time step, specifically by determining the partial derivatives of $\boldsymbol{M}$, $\bar{\boldsymbol{C}}$ and $\boldsymbol{F}_e$ with respect to $\boldsymbol{q}_{k+1}$ and $\dot{\boldsymbol{q}}_{k+1}$. However, computing these partial derivatives can often be intricate and time-intensive. In practical scenarios, we approximate these matrices as constants within each time step, effectively using the matrices at time t_k to approximate those at the current time t_{k+1}. When we arrive at a linearized equation set, selecting an appropriate numerical solver becomes crucial. Direct solvers, like Gaussian elimination, are suited for medium and small-scale systems, while iterative solvers, such as the conjugate gradient method, are ideal for large, sparse systems. An alternative method for tackling these equations is the Newton-Raphson technique or its variants, which involve iterative resolution of the nonlinear equation set. Fundamentally, this first approach is essentially the initial phase in the nonlinear iterative solving process.
7. Updating the solution: Once the unknowns at t_{k+1} are computed, update the state of the system (configuration, strain, velocity).
8. Iteration: Repeat steps 2 to 7 for each time step until the end of the time interval is reached.

The steps outlined above summarize the process of using the implicit Euler method to solve the dynamics equations of a cochlear implant. One notable advantage of the implicit Euler method is its improved numerical stability. Since the implicit method involves solving an algebraic equation at each time step, which includes information about the future solution, it exhibits enhanced stability, especially when addressing stiff systems. Explicit methods may require very small time steps to ensure numerical stability, whereas implicit methods often maintain stability even with larger time steps, reducing computational complexity.

Another significant advantage is the suitability of the implicit Euler method for addressing problems with more complex physical structures. In certain scenarios, explicit methods may incur higher computational costs due to the necessity of smaller time steps. Implicit methods, on the other hand, tend to offer advantages, especially when dealing with systems exhibiting multiscale behavior or strong nonlinearity.

2.6 Simulation

In the preceding section, we discussed various numerical solution methods for dynamic systems. This section will concentrate on the simulation of active electrode arrays, specifically utilizing the implicit Euler numerical solution method. It includes a thorough validation of the proposed

Cosserat model and presents simulation results depicting the deformation of active electrode sequences under various loads and inputs.

2.6.1 Model validation

FEM can be regarded as a reliable tool (and reference) to verify the modeling result by selecting finer mesh, since it discretizes the space in a very generic manner without introducing restrictive assumptions. Hence, we used the FEM approach as an alternative of the real soft slender rod. In short, the main idea of FEM is to discretize the geometric shape of the rod by employing finite number of finer elements. The geometric model of the rod is established in the SolidWorks, we then use the FEM in Comsol which is a general FEM software to obtain the equilibrium position of the cantilever rod.

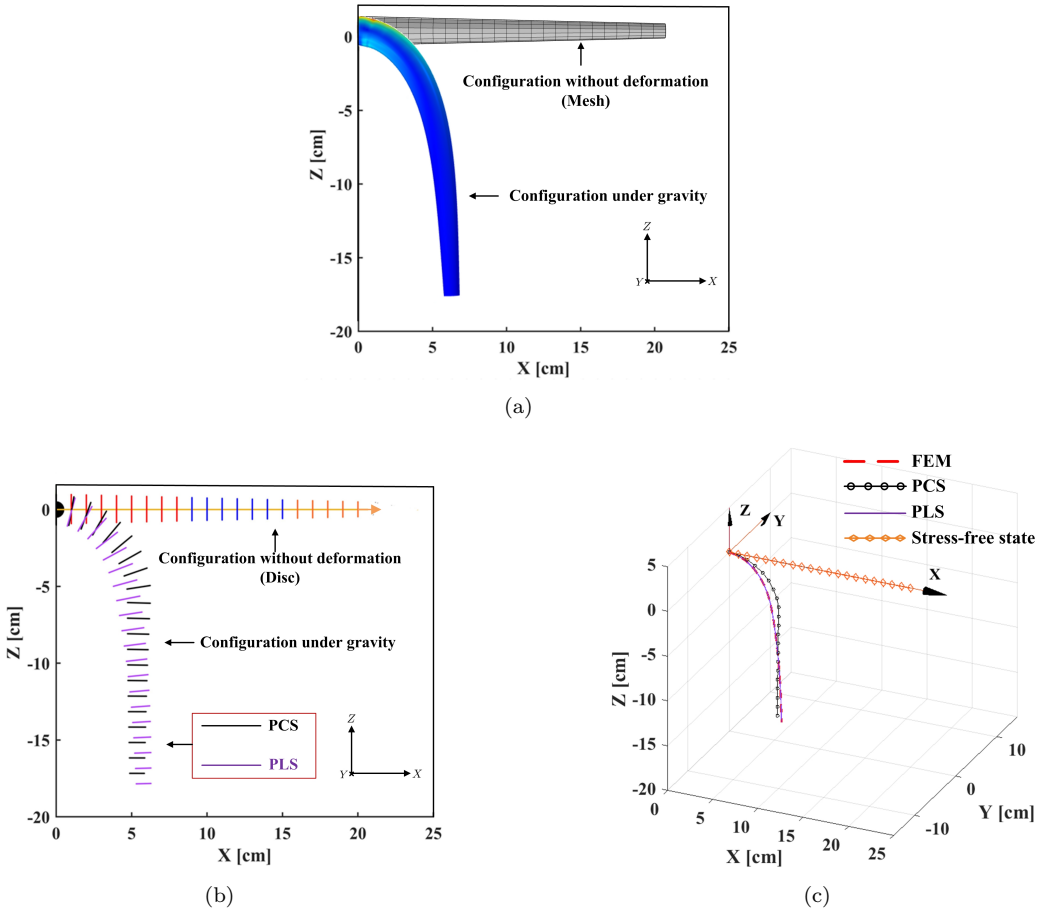

Figure 2.14: Simulation comparison of three different modeling methods for the cantilever rod before and after deformation. (a) FEM. (b) PCS and PLS Cosserat models in MATLAB. (c) Configuration of the soft manipulator under gravity in three-dimensional space.

Specifically, in terms of spatial discretization of the studied cantilever rod, quadrilateral mesh elements are used, and the rod is spatially discretized into 650 elements along the X-axis

regarding the trade-off between the accuracy and computation expense. The mesh average element quality, equals to 0.8033, indicates the high discretization accuracy of the model. The simulation result by our proposed PLS method is compared with piecewise constant strain method (PCS)[120] and FEM.

The rod modeled by PLS is divided into three sections, and the length of each section is separately 9×10^{-2} m, 7×10^{-2} m and 4×10^{-2} m from base to tip. For a more specific comparison and evaluation, the material and geometric parameters for the discrete Cosserat models with the same sections in MATLAB are in accordance with those of the FEM. From the simulation results, the equilibrium position of the end-effector of the cantilever rod via FEM under gravity is $\boldsymbol{u}_e = [5.8479, 0, -17.8395]^\top$, as shown in Fig. 2.14(a). It took around 14 seconds to complete one simulation because the FEM for large deformations always requires heavy computation. Likewise, we can derive the positions of the end-effector of the discrete Cosserat static models by using the Newton method. From the perspective of computation time of discrete Cosserat static models, we observe that the systems can converge in less than 2 seconds (i.e., 1.3 s for PCS, and 1.2 s for PLS) mainly due to the use of the basic idea of model-order reduction. To intuitively demonstrate the whole shape accuracy of the soft rod modeled by different modeling methods, the spatial configurations of the models under gravity have been depicted in Fig. 2.14(c) which highlights the high deformation similarity of the PLS and FEM. Comprehensively considering the comparison results among them illustrated in Table 2.3 and Fig. 2.14, we come to a conclusion that, compared to the PCS, the model via the PLS Cosserat modeling approach fits much better the results obtained by the FEM, with the relative error of the end-effector position less than 5%. In other words, the PLS Cosserat static model is essentially comparable to the FEM in terms of accuracy, which can be further verified by the purple PLS configuration tendency plotted in Fig. 2.14(b)-(c), almost the same as the FEM in Fig. 2.14(a). Logically, this can be explained by the fact that the piecewise linear interpolation technique applied to all cross sections of the proposed PLS Cosserat model allows to precisely approximate the deformation behavior of the soft slender rod in the real scenario. In this

Table 2.3: Comparison results of PCS and PLS Cosserat static models w.r.t. FEM under gravity in terms of end-effector position and its relative error

Modeling method	Position of end-effector (Unit:cm)			Relative error of end-effector position w.r.t. FEM (Unit: %)		
	u_x	u_y	u_z	e_x	e_y	e_z
FEM	5.8479	0.0000	-17.8395	×	×	×
PCS [120]	5.3450	0.0000	-17.1693	-8.60	0.00	-16.88
PLS	5.7787	0.0000	-17.8394	-1.18	0.00	-0.01

section, we conducted a thorough comparison between the PLS model and the FEM model for general soft slender rods. This comparison has effectively validated the precision of the PLS approach in slender rod modeling. Moving forward, the next chapter will pivot towards active electrode arrays. We will examine their deformational responses under a range of external forces and diverse actuation voltages, further expanding our understanding of their behavior in varied conditions.

2.6.2 Passive Electrode Array

2.6.2.1 Geometric dimensions

The geometric dimensions of the EA of cochlea implant are as follows: the radius at the wider end is 0.5mm and the radius at the narrower end is 0.3mm. The electrode array is composed of 12 electrodes. The total length is 30mm, the length of electrode is 1mm and the electrode spacing is 1mm, as shown in Fig. 2.15(a). The Young's modulus of the soft part of the EA is set as 25 MPa.

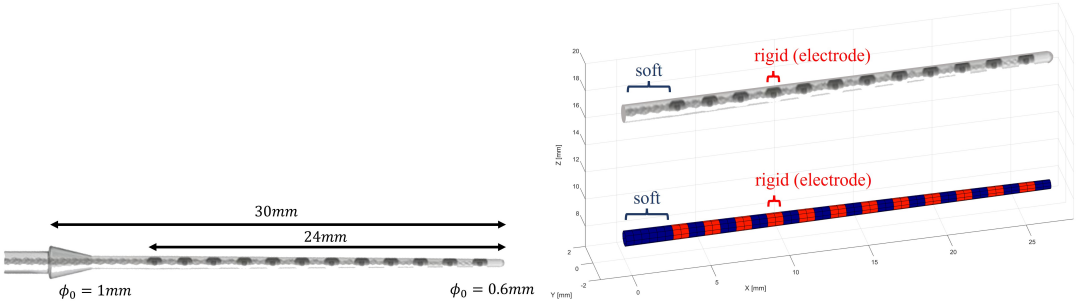

(a) (b)

Figure 2.15: (a) The dimension of EA. (b)The 3D geometry setting of electrode array.

2.6.2.2 Soft-rigid coupling

As shown in Fig. 2.15(b), the EA includes internal electrodes and an external shell. The electrodes can be considered rigid bodies, while the non-electrode parts can be considered flexible bodies. Therefore, the corresponding cosserat beam for the implant is a rigid-flexible coupled beam. We achieve rigid-flexible coupling by setting the stiffness distribution function. The red region represents areas with higher stiffness, corresponding to the rigid electrode, and the blue region represents areas with lower stiffness, corresponding to the flexible body.

2.6.2.3 Simulation with tip load

Simulation 1: We applied a torque load along the y-axis at the end of the implant. The magnitude of the torque ranged from 0mN to 120mN. The static simulation results are shown in Fig. 2.16(a).
Simulation 2: We applied a force load along the z-axis at the end of the implant. The force magnitude ranged from 0mN to 30mN. The static simulation results are presented in Fig. 2.16(b).

Through simulation, we can observe that when different forces and torques are applied to the end point of the EA, it undergoes deformation. As the magnitude of the force or torque gradually increases, the bending degree of the EA also increases. Additionally, it can be seen from the figures that the bending always occurs in the flexible part of the EA, while the section containing the rigid electrodes remains undeformed.

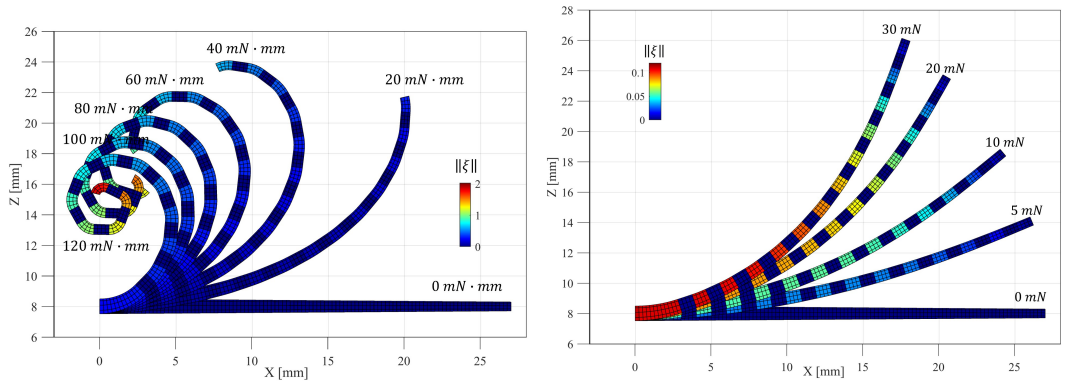

(a) (b)

Figure 2.16: (a) The deformation of the implant when a torque load is applied to its tip. (b) The deformation of the implant when a force load is applied to its tip.

2.6.3 Active implant

The simulation parameters for the active implant are as follows: the total length is 26mm, with diameters of 0.6mm at one end and 0.4mm at the other. The Young's modulus is 30 MPa. The three conducting polymer actuators each have a length of 7mm, and their other physical parameters are determined from the identification process mentioned in the previous section. These three conducting polymer actuators are positioned at distances of 3mm, 11mm, and 19mm from the left end of the implant. At the same time, the stiffness of the wires used to power the actuators is considered. We achieve the variation of wire stiffness along the axis of the implant by setting the stiffness function.

The evolution of input voltage over time is depicted in Fig. 2.17, following a linear change with time. The sequential activation order of the three actuators from right to left is achieved through a temporal offset in the voltages. Thus, simulating the process of the implant entering the cochlea in a spiral manner.

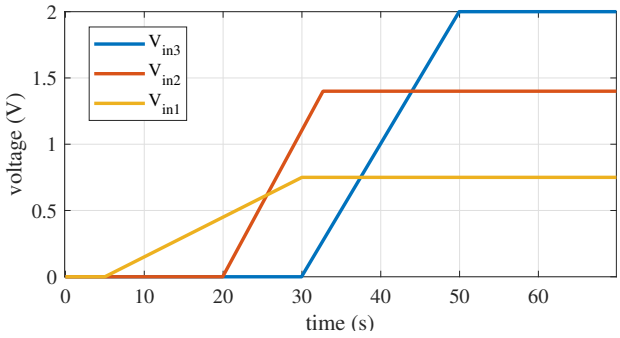

Figure 2.17: The input voltage of three actuators in active cochlear implant.

Fig. 2.18 illustrates the simulated deformation results of the active implant under this evolving voltage. The simulation results reveal that when the CPAs within the EA are powered

sequentially, they are activated in order. Consequently, the front part of the EA bends first, followed by the middle section, and finally the tail end. This mimics the curvature change of the EA when it is implanted into the cochlea, with the curvature varying from the front end to the tail end along the cochlear's spiral trajectory.

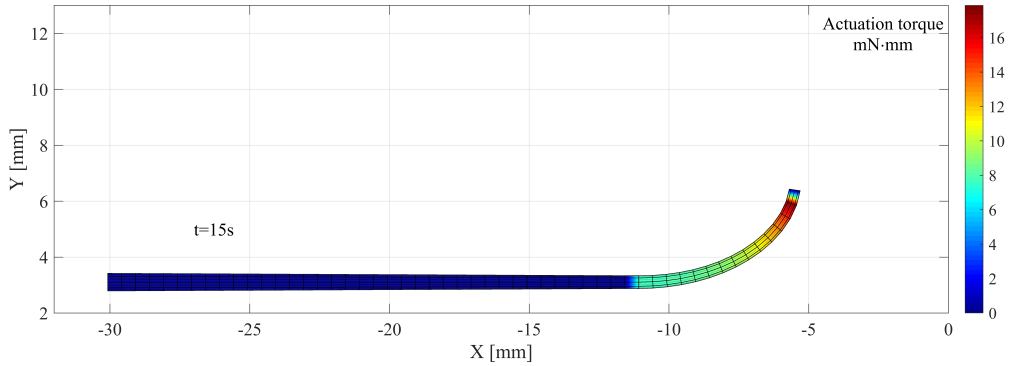

(a) The first conducting polymer actuator has been activated

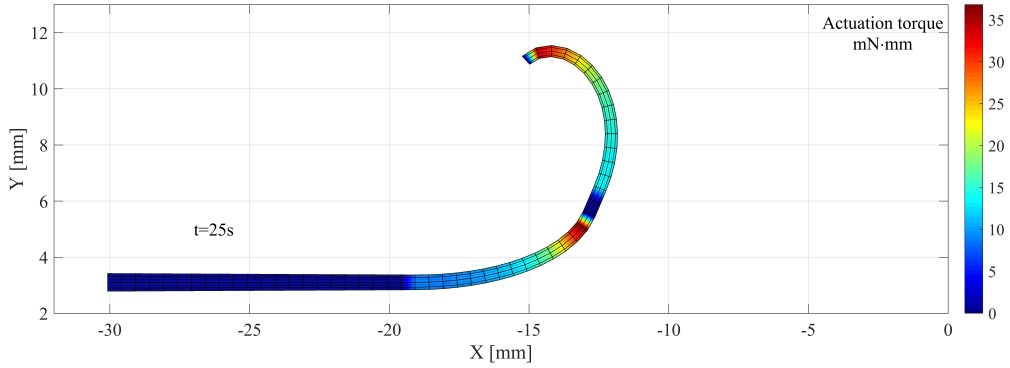

(b) The second conducting polymer actuator has been activated

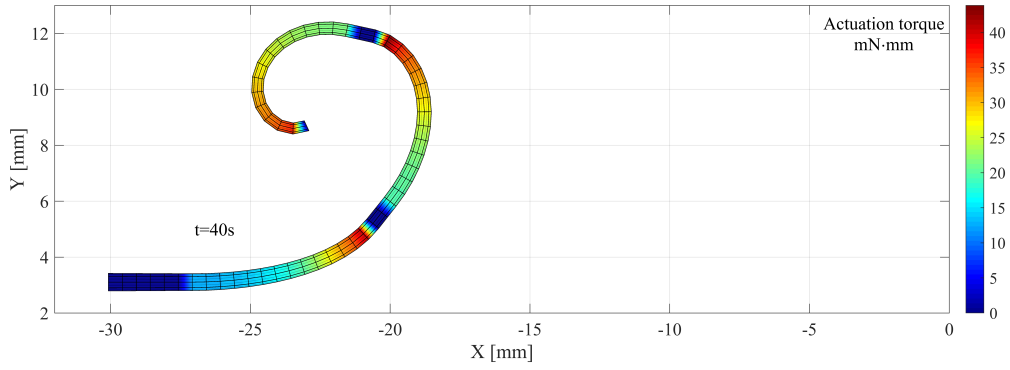

(c) The third conducting polymer actuator has been activated

Figure 2.18: When subjected to the applied voltage, the three CPAs were sequentially activated, resulting in the bending of the active electrode array.

2.7 Conclusion

In this chapter, we represents an earnest effort in advancing the field of Active Cochlear Implants, particularly in modeling of ACI systems. Our research has focused on overcoming existing limitations in CI studies, leading to substantial advancements in both the functionality and effectiveness of these implants.

Our first major accomplishment is the development of a generalized mechanical model for the Electrode Array. By integrating the Lie group and leveraging the Cosserat rod theory, we have created a parameterized strain field that accurately represents the real system with reduced dimensionality. This model excels in handling the nonlinearities associated with large deformations of EA and is notable for its balance between accuracy, robustness, and computational efficiency. It sets a new standard for real-time simulation and control applications in the field.

The second notable achievement is the formulation of a generalized electronic-mechanic model for the Electronic Conducting Polymer. Similar to the EA model, this model reduces complexity through parameterization and precisely manages nonlinear deformations using the Cosserat rod theory. It stands out for its ability to balance dimensionality, accuracy, and computational feasibility, laying a solid foundation for future simulations and control projects in CI technology.

Addressing the challenges of unknown or imprecise physical parameters, we introduced an innovative parameter identification method based on a nonlinear electro-mechanical coupling model. The development of a bespoke visual identification system has simplified the experimental process, enhancing the practicality of our approach.

The culmination of our work is the introduction of a comprehensive coupling model that integrates both EA and ECP for active cochlear implants. This groundbreaking model serves as a fundamental framework for model-based control of active cochlear implants, representing a significant leap in our understanding and manipulation of these complex systems.

Overall, the methodologies and findings presented in this chapter paves the way for more advanced, efficient, and effective model of CIs, laid the foundation for a theoretical model for subsequent research work.

Up to now, we've developed a dynamic model for EA to predict its deformation under external forces. Given our goal to simulate the entire cochlear implantation process of the EA, it's crucial to go beyond this isolated dynamic model. We need to explore the interaction between the EA and the cochlea during implantation. The next chapter will focus on building a contact model between the EA and the cochlea, leveraging the foundations laid by the EA's dynamic model we have established.

Chapter 3

Modeling of the Interaction between Implant and Cochlea

3.1 Introduction

In Chapter 2, we delved into the complex modeling of active electrode arrays for cochlear implants. This encompassed the mechanical model of the electrode array, the electromechanical coupling model of the ECP actuator, and the integrative model of the active electrode array. A critical aspect during the implantation process of the electrode array is its continual contact with the cochlea's inner wall. As previously discussed in Chapter One, this contact can lead to various complications during implantation, such as folding over, scratching, and buckling. These issues arise from the interaction between the electrode array and the cochlea's inner wall, underscoring the importance of developing a comprehensive contact model. This model is essential for predicting and analyzing potential implantation issues.

In this chapter, we build upon the mechanical model of the electrode array introduced in Chapter Two. We extend the Cosserat model to encompass contact phenomena, establishing a detailed contact model between the electrode array and the cochlear wall. This development includes identifying instances of contact, analyzing contact and frictional forces, all intricately integrated with the Cosserat beam model. These elements will be thoroughly examined and analyzed in Chapter Three, providing a deeper understanding of the electrode array's behavior during implantation.

Building upon the Cosserat model for cochlear implants, this chapter delves into the incorporation of frictional contact constraints and the facilitation of rapid simulations by converting these constraints into equality conditions. We introduce an innovative formulation for resolving dynamics in systems with frictional contact constraints. This approach diverges from the conventional nonsmooth LCP or NCP methods by employing smooth NCP functions for reconstructing contact constraints, an extension we apply to the domain of cochlear implant. This formulation, amenable to solution via standard direct Newtonian methods, adeptly navigates the complexities of nonlinear friction models.

This chapter seeks to address several pivotal questions:

1. How can we construct a contact problem with a reduced number of degrees of freedom, including the geometric model of the cochlea and the establishment of contact pairs?

2. How can contact dynamics be expressed using a mathematical model, including dynamical equations and contact constraints?

3. How can contact constraints in dynamics be managed efficiently and effectively?

Through answering these questions, we endeavor to shed new light on modeling and simulation techniques in the realm of contact mechanics for cochlear implant, with a special focus on applications like cochlear implants that have far-reaching implications in the medical field.

3.2 Geometric Description of Cochlea

In order to develop a contact model between the electrode array and the cochlea, our initial step involves determining if contact has occurred between them. Following this, we set up contact constraints and formulate the forces involved in the contact. This process necessitates first acquiring the three-dimensional geometric models of both the electrode array and the cochlea, crucial for assessing contact instances.

In many Finite Element Method (FEM) models, the geometric depiction of 3D objects is often defined by a mesh model, where the object's surface is segmented into numerous small polygons. For precise geometric representation, this could entail utilizing thousands of polygons. However, employing these polygons for contact detection significantly elevates the system's dimensionality, consequently impeding the computational efficiency of the model.

In Chapter Two, we crafted the geometric model of the electrode array. It is defined comprehensively along its central backbone. The overall deformation of the array is depicted through the positions of each cross-sectional slice along this central line. This method of geometric division, in contrast to traditional polygonal meshes, capitalizes on the inherent geometric properties of slender rod-like structures, markedly reducing the geometric dimensions and curbing the need for superfluous computations.

Regarding the three-dimensional geometric modeling of the cochlea, which shares a similar tubular structure, we can employ a methodology akin to that used for the electrode array. We envision the cochlea as a series of closed loops encircling its central line. These loops, as they sweep along this central line, create a surface that effectively and efficiently represents the cochlea's three-dimensional form.

3.2.1 Center-line of cochlea

The trajectory of the cochlea is defined as the centerline of the cochlea, which is a three-dimensional line segment in the Cartesian coordinate system. To define the centerline, we used a parameterized equation, employing a B-spline definition of the curve equation to achieve a smoother fit.

The B-spline of order $k+1$ is essentially a segmented polynomial function, where the degree of each segment is k, and the variable of interest is s. This concept was discussed by Prautzsch in their work on Bezier and B-spline techniques [121]. The foundational elements of a B-spline are its basis functions, denoted as $B_{i,k}(s)$, and a set of control points $\boldsymbol{r}_i$, $i = 0, \ldots, p$. The transition points between these polynomial segments are called knots. These knots, represented as $\{s_0, s_1, s_2, \ldots, s_{k+p}\}$, are arranged in a nondecreasing sequence. The comprehensive expression of a b-spline, $\mathcal{C}$, as defined through these parameters, is formulated based on these basis functions and control points:

$$\mathcal{C}(s) = \Sigma_{i=0}^{i=p} B_{i,k}(s)\boldsymbol{r}_i$$

where basis function $B_{i,k}(s)$ is calculated from $B_{i,0}(s)$ to $B_{i,k}(s)$ by the recursive formula below: for $d = 0$ and $0 \leq i \leq k + p$,

$$B_{i,0}(s) = \begin{cases} 1 & \text{if } s_i < s < s_{i+1} \\ 0 & \text{else} \end{cases}$$

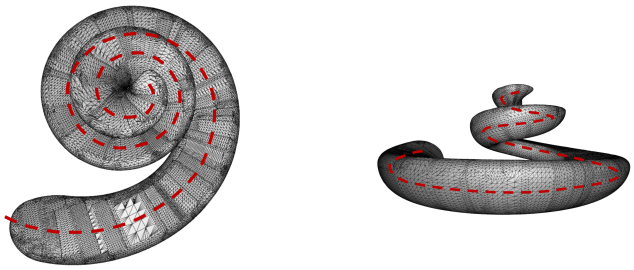

(a) (b)

Figure 3.1: A three-dimensional scan mesh depicting the cochlea and its B-spline based centerline.

for $d > 0$ and $0 \leq i \leq k + p - d$,

$$B_{i,d}(s) = \frac{s - s_i}{s_{i+d-1} - s_i} B_{i,d-1}(s) + \frac{s_{i+d} - s}{s_{i+d} - s_{i+1}} B_{i+1,d-1}(s)$$

In this subsection, we employed B-spline curves to delineate the spiral central line of the cochlea. As we have earlier discussed, the geometric portrayal of the cochlea is defined as a surface created by sweeping a series of closed loops along this spiral central line. To put it more clearly, the comprehensive geometric characterization of the cochlea ought to be represented as a tubular structure. This representation should encompass not only the central positions of any given cross-sectional area along the tubular structure but also account for the rotational aspect of these cross-sections. At present, our model is limited to merely defining positional information. Consequently, there is a need to develop a more advanced tubular structure model that incorporates considerations of the cross-sectional rotations, thereby fitting the cochlea's central line more accurately. We will elaborate on the methodology for achieving this in the subsequent sections.

3.2.2 Euler-Bernoulli tubular fitting

We conceptualize the overall geometrical structure of the cochlea using the Euler-Bernoulli beam, whose configuration can be represented by the configuration matrix $\boldsymbol{g}_e$ of each disc along to beam, as shown in Fig. 3.2(b):

$$\boldsymbol{g}_e(s_e) = \begin{bmatrix} \boldsymbol{R}_e(s_e) & \boldsymbol{p}_e(s_e) \\ \boldsymbol{0}^\top & 1 \end{bmatrix} \in SE(3), \ \forall s_e \in [0, L_e]$$

where s_e is the arc length coordinate of Euler-Bernoulli beam, L_e is the total length of this beam.

Within this three-dimensional framework, the cochlea is subjected exclusively to bending angular strains, while both torsional and linear strains are essentially non-existent. In other words, the Euler-Bernoulli beam can be regarded as a Cosserat beam that only exhibits bending. In this case, the strain with respect to its body frame can be expressed by the following formula:

$$\boldsymbol{\xi}_e(s_e) = \begin{bmatrix} 0 & \kappa_y(s_e) & \kappa_z(s_e) & 1 & 0 & 0 \end{bmatrix}^\top, \ \forall s_e \in [0, L_e] \tag{3.1}$$

where κ_y and κ_z are two angular strains of bending, s_e is the arc length coordinate of Euler-Bernoulli tubular, L_e is the total length of this tubular.

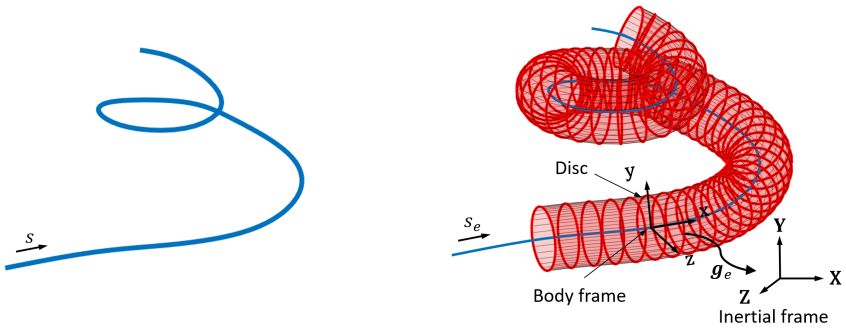

(a) B-spline (b) Euler-Bernoulli tubular

Figure 3.2: (a) The cochlear central line represented by B-spline, with the parameter coordinate s. (b) The Euler-Bernoulli tubular cochlea corresponding to the B-spline, with the parameter coordinate s_e. The red circles represent discs, and at each disc, there is an attached body frame, determined by the matrix $\boldsymbol{g}_e$, which indicates the position and orientation of the disc.

Next, we use our PLS technique to interpolate (3.1) in the interval $[0, L_e]$. Dividing this tubular into M sections by the nodes $\{0, \frac{L_e}{M}, 2\frac{L_e}{M}, 3\frac{L_e}{M}, \dots, L_e\}$, the bending strain of all nodes of all sections can written as a compact vector as follows:

$$\mathbb{R}^{2(M+1)} \ni \boldsymbol{\theta}_e = \begin{bmatrix} \kappa_y(0) & \kappa_z(0) & \kappa_y(\frac{L_e}{M}) & \kappa_z(\frac{L_e}{M}) & \dots & \kappa_y(L_e) & \kappa_z(L_e) \end{bmatrix}^\top \tag{3.2}$$

Recalling the parameterization formula (2.13), (3.1) can be interpolated via the following formula:

$$\boldsymbol{\xi}_e(s_e) = \boldsymbol{\xi}_0 + \boldsymbol{B}_e \boldsymbol{\Phi}_e(s_e) \boldsymbol{\theta}_e \tag{3.3}$$

where $\boldsymbol{\xi}_0 = [0\ 0\ 0\ 1\ 0\ 0]^\top$ is the initial strain, $\boldsymbol{\Phi}_e$ is the Ritz basis function, $\boldsymbol{B}_e$ is the strain augmentation matrix, whose role is to expand the 2-dimensional strain to 6 dimensions. Their definitions are given by the following formulas:

- Ritz basis function

$$\boldsymbol{\Phi}(s_e) = \begin{bmatrix} \Phi_0(s_e)\mathbf{I}_{2\times 2} & \dots & \Phi_M(s_e)\mathbf{I}_{2\times 2} \end{bmatrix} \in \mathbb{R}^{2\times 2(M+1)},\ \forall\ s_e \in [0, L_e] \tag{3.4}$$

with

$$\Phi_i(s_e) = \begin{cases} \dfrac{iL_e - Ms_e}{iL_e - (i-1)L_e} & \text{for } s_e \in [(i-1)\dfrac{L_e}{M}, i\dfrac{L_e}{M}) \\ \dfrac{Ms_e - iL_e}{(i+1)L_e - iL_e} & \text{for } s_e \in [i\dfrac{L_e}{M}, (i+1)\dfrac{L_e}{M}] \\ 0 & \text{for } s_e \notin [(i-1)\dfrac{L_e}{M}, (i+1)\dfrac{L_e}{M}] \end{cases}$$

- Strain augmentation matrix

$$\boldsymbol{B}_e = \begin{bmatrix} 0 & 1 & 0 & 0 & 0 & 0 \\ 0 & 0 & 1 & 0 & 0 & 0 \end{bmatrix}^\top$$

As mentioned in Chapter 2, the configuration of a beam is inferable from its strain field. This implies that there is an equivalence between the strain field and the configuration of a tubular cochlea. Specifically, for a tubular cochlea, it's possible to determine the central position of each individual disc by extracting data from the configuration matrix:

$$\mathbb{R}^3 \ni \boldsymbol{p}_e(s_e) = \boldsymbol{P}\boldsymbol{g}_e\boldsymbol{A},\ \forall s_e \in [0, L_e] \tag{3.5}$$

where $\boldsymbol{p}_e(s_e)$ is the central position of disc of the tubular cochlea at s_e, $\boldsymbol{P}$ and $\boldsymbol{A}$ are two matrix for picking up $\boldsymbol{p}_e$ from $\boldsymbol{g}_e$, with:

$$\boldsymbol{P} = \begin{bmatrix} 1 & 0 & 0 & 0 \\ 0 & 1 & 0 & 0 \\ 0 & 0 & 1 & 0 \end{bmatrix},\ \boldsymbol{A} = \begin{bmatrix} 0 & 0 & 0 & 1 \end{bmatrix}^\top$$

Our current objective, therefore, is to identify a series of interpolation points within the strain field, i.e., $\boldsymbol{\theta}_e$, such that the central positions of the interpolation points on the tubular cochlea accurately match the B-spline curve we defined in Subsection 3.2.1, as shown in Fig. 3.2. To accomplish this, we are required to formulate and solve $3(M+1)$ nonlinear equations as follows:

$$\boldsymbol{p}_e(0) = \mathcal{C}(s_0),\ \boldsymbol{p}_e(\frac{L_e}{M}) = \mathcal{C}(s_1),\ \boldsymbol{p}_e(2\frac{L_e}{M}) = \mathcal{C}(s_2),\ \ldots,\ \boldsymbol{p}_e(L_e) = \mathcal{C}(s_M) \tag{3.6}$$

In the aforementioned set of nonlinear equations, the unknowns are the strain interpolation vector $\boldsymbol{\theta}_e \in \mathbb{R}^{2(M+1)}$ and the parameter coordinates $\{s_0, s_1, \ldots, s_M\}$ corresponding to the B-spline curve, thus we have also $3(M+1)$ unknown variables. Given that we are aware of the functional form of the aforementioned set of equations, they can be solved using a nonlinear solver. This will ultimately yield the strain interpolation variable $\boldsymbol{\theta}_e$, which describes the configuration of tubular cochlea.

In this subsection, we have utilized the Euler-Bernoulli beam to model the configuration of the cochlea. As previously discussed, we conceptualize the geometry of the cochlea as a surface formed by sweeping a sequence of closed loops along its spiraling central line. We already possess the function describing this spiral central line and the rotational information for each disc along it. What remains to be determined is the cross-section, i.e., the closed loop, for each disc.

In the following discussion, we will detail the process for defining these closed loops. These loops are critical as they constitute the cross-sectional profiles of the cochlea, arranged perpendicularly to its central line.

3.2.3 Cross section of cochlea

Having modeled the cochlear central line with the Euler-Bernoulli beam approach, we've acquired the position and orientation for each disc, essentially every body frame along this line. However, our model is still incomplete as it doesn't yet define the cochlear surface. To address this, our next step involves defining the cross-sectional contours of the cochlea in relation to each body frame.

To describe the coordinates for every point on the surface of cochlea, we introduce the second coordinate $\beta \in \mathbb{R}$. This new coordinate defines the position of a point on the disc relative to its center. As illustrated in Fig. 3.3, β represents the rotation angle in radians of the contact point around the center point in the direction of x-axis. By using the coordinate $\boldsymbol{X} = [s_e, \beta]^\top$, we can precisely locate any point on the surface of the cochlea, which allows us to analyze the

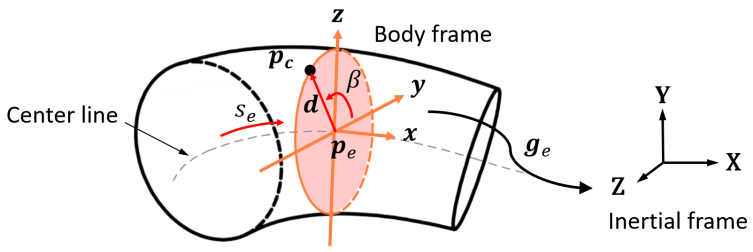

Figure 3.3: Defining the cross-sectional contours of cochlea in the body frame of Euler-Bernoulli tubular.

contact situation during the interactions between EA and cochlea. For any point on the surface of cochlea, its position can be given by:

$$\boldsymbol{p}_c(s_e, \beta) = \boldsymbol{p}_e(s_e) + \boldsymbol{R}_e(s)\boldsymbol{d}(s_e, \beta) \tag{3.7}$$

where $\boldsymbol{d}(s_e, \beta)$ is the local distance vector from the center-line of cochlea to the point on the surface, which is defined in the body frame, describing the cross-sectional contours of cochlea. Since we assume that the form of cross-section of cochlea never changes during the implantation, this vector only depends on robot's original geometries of the cochlea.

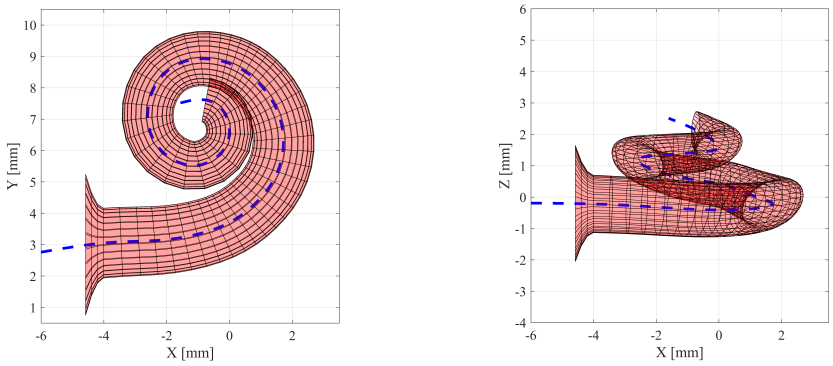

(a) (b)

Figure 3.4: The 3D geometric model of the cochlea, showcasing its B-spline based center-line and the elliptical cross section.

Thus far, we have successfully established the geometric model for the surface of the cochlea. The next step involves identifying contact points on this surface. In contact calculations between two objects, the formation of contact is characterized by the emergence of pairs. This entails pinpointing a set of potential contact points, each located on the surfaces of the interacting objects. These points are collectively referred to as a contact pair. The procedure for finding these potential contact pairs is known as collision detection. In the ensuing section, we will delve into the methodology for performing collision detection.

3.3 Collision Detection

3.3.1 Continuous Search of Contact Pair

To calculate the contact distance between the EA and the cochlea, we first need to obtain the contact model of the implant and cochlea. Next, we define the contact object, which in our work, consists of a contact pair composed of two contact points, located on the 3D geometric models of the implant and cochlea respectively. A contact pair consists of two contact points, including the master contact point and the slave contact point. The master contact point is located on the centerline of the implant and is a predefined hypothetical point that is fixed and does not change with the contact position. The slave contact point is located on the centerline of the cochlea and changes as the master contact point moves.

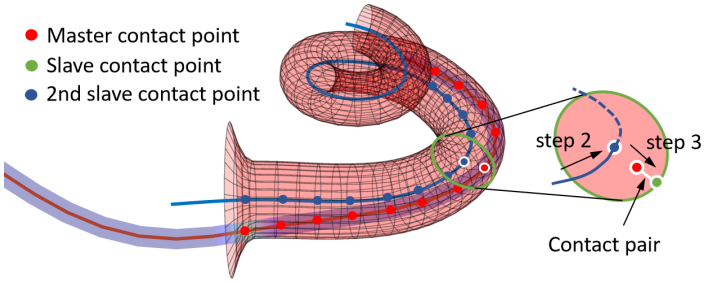

Figure 3.5: The figure displays collision detection and contact pairs.

When the master contact point moves, the corresponding slave contact point is defined as the contact point closest to the master contact point, i.e., the slave contact point is obtained by minimizing the contact distance. The searching process is as follows:

- **Step 1. Chose the master object and slave object**

  As shown in Fig. 3.5, we first determine the master object as electrode array and fix the contact nods on the electrode array. The cochlea is chosen as slave object.

- **Step 2. Search of contact cross-section in direction of length**

  As shown in Fig. 3.5, once the master contact point is fixed, we will first search the cross-section of cochlea which pass through the master point. This equals to find a point $\boldsymbol{p}_e(s_e)$, namely the secondary slave point, on the center-line of cochlea which is closest to the master contact point and the coordinate s_e of the point $\boldsymbol{p}_e(s_e)$ determines the targeted cross-section, as shown in Fig. 3.6(a). Denoting $\boldsymbol{p}_m$ as the master point and $\boldsymbol{d}_s = \boldsymbol{p}_e(s_e) - \boldsymbol{p}_m$, the search of cross-section could be realized by solving the minimization as follows:

  $$s_e = \text{argmin} \quad \mathscr{Y}_1 = \frac{1}{2}\boldsymbol{d}_s^\top \boldsymbol{d}_s \tag{3.8}$$

  (3.8) could be solved by the following Newton iteration:

  $$s_{e,j+1} = s_{e,j} - \boldsymbol{H}_{s_e}^{-1}\boldsymbol{J}_s^\top \boldsymbol{d}_s \tag{3.9}$$

  where $\boldsymbol{J}_s$ is the Jacobian of $\boldsymbol{d}_s$, i.e., $\boldsymbol{J}_s = \frac{\partial \boldsymbol{p}_e}{\partial s_e}$. $\boldsymbol{H}_s$ is the Hessian matrix, which can be approximated by Jacobian of $\boldsymbol{d}_s$ as $\boldsymbol{H}_s = \boldsymbol{J}_s^\top \boldsymbol{J}_s$.

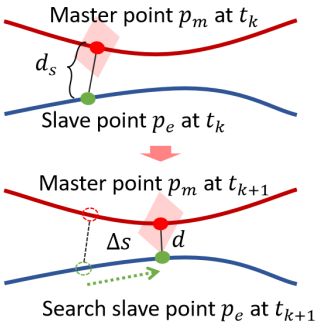

(a) Searching the cross-section

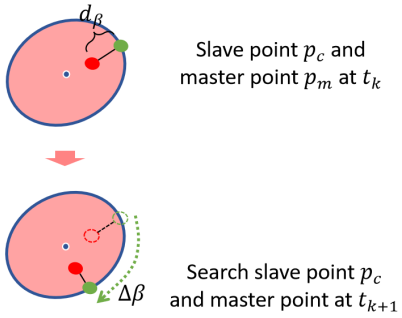

(b) Searching the contact point in the cross-section

Figure 3.6: By employing a continuous search algorithm via Newton method to identify the slave point closest to the master point at each moment.

- **Step 3. Search of contact point on cross-section**

  Once the cross-section is found, i.e., one coordinate s of $\boldsymbol{p}_c(s,\beta)$ is fixed, the slave contact point $\boldsymbol{p}_c$ on the cross section at s can be searched by the same idea of step 2, as shown in Fig. 3.5(b). Denoting $\boldsymbol{d}_\beta = \boldsymbol{p}_c(s,\beta) - \boldsymbol{p}_m$, it could be searched by solving the minimization as follows:

$$\beta = \text{argmin} \quad \mathscr{Y}_2 = \frac{1}{2}\boldsymbol{d}_\beta{}^\top \boldsymbol{d}_\beta \tag{3.10}$$

  (3.10) could be solved by the following Newton iteration:

$$\beta_{j+1} = \beta_j - \boldsymbol{H}_\beta^{-1}\boldsymbol{J}_\beta^\top \boldsymbol{d}_\beta \tag{3.11}$$

  where $\boldsymbol{J}_\beta$ is the Jacobian of $\boldsymbol{d}_\beta$ with respect to β, i.e., $\boldsymbol{J}_\beta = \frac{\partial \boldsymbol{p}}{\partial \beta}$. $\boldsymbol{H}_\beta$ is the Hessian matrix, which can be approximated by Jacobian of $\boldsymbol{d}_\beta$ as $\boldsymbol{H}_\beta = \boldsymbol{J}_\beta^\top \boldsymbol{J}_\beta$.

Through the outlined procedure, we can ultimately establish a set of coordinates (s,β) which allows us to locate the slave contact point corresponding to the master contact point. When the master contact point comes into contact with this slave contact point, contact forces are generated at the contact point. Therefore, it is essential to determine the direction of these contact forces, which includes both the normal contact force and the tangential contact force. We have predefined that these contact forces will be generated at the slave contact point and applied to the master contact point. In the subsequent subsections, we will establish a contact frame for the slave contact point which helps us better represent the contact force.

3.3.2 Contact frame of contact pair

Once we find the slave contact point on the surface of cochlea, the contact frame at this point can be represented by a contact plane which is tangent to the surface of cochlea, as shown in Fig. 3.7. This plane, noted as Γ, can be defined by a pair of covariant tangent vectors $\{\boldsymbol{\tau}_1, \boldsymbol{\tau}_2\}$, with:

$$\boldsymbol{\tau}_1 = \frac{\partial \boldsymbol{p}_c}{\partial s_e} = \frac{\partial \boldsymbol{p}}{\partial s_e} + \frac{\partial \boldsymbol{R}}{\partial s_e}\boldsymbol{d} + \boldsymbol{R}\frac{\partial \boldsymbol{d}}{\partial s} = \boldsymbol{R}(\boldsymbol{\epsilon} + \tilde{\boldsymbol{\kappa}}\boldsymbol{d} + \frac{\partial \boldsymbol{d}}{\partial s_e})$$

$$\boldsymbol{\tau}_2 = \frac{\partial \boldsymbol{p}_c}{\partial \beta} = \frac{\partial \boldsymbol{d}}{\partial \beta}$$

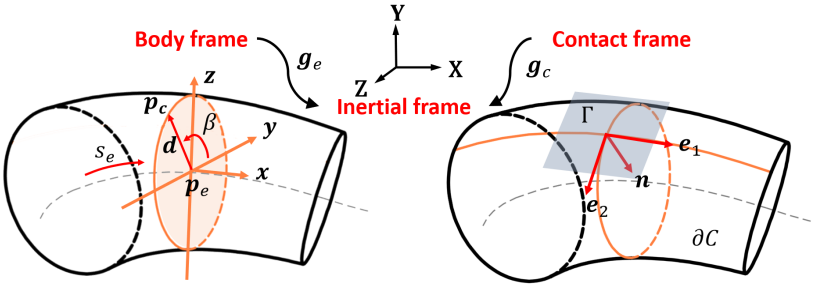

Figure 3.7: Coordinates of surface of cochlea and contact frame.

The unit normal vector of this tangent surface is then given by:

$$\boldsymbol{n} = \frac{\boldsymbol{\tau}_1 \times \boldsymbol{\tau}_2}{\|\boldsymbol{\tau}_1 \times \boldsymbol{\tau}_2\|} \tag{3.12}$$

Note that the basis $\{\boldsymbol{\tau}_1, \boldsymbol{\tau}_2, \boldsymbol{n}\}$ is not necessarily orthogonal in the deformed configuration, i.e., $\boldsymbol{\tau}_1^\top \boldsymbol{\tau}_2 \neq 0$, thus a new orthogonal basis can be defined from $\{\boldsymbol{\tau}_1, \boldsymbol{\tau}_2, \boldsymbol{n}\}$ by replacing $\boldsymbol{\tau}_1$ and $\boldsymbol{\tau}_2$ with:

$$\boldsymbol{e}_1 = \frac{\boldsymbol{\tau}_1}{\|\boldsymbol{\tau}_1\|} \ , \ \boldsymbol{e}_2 = \frac{\boldsymbol{n} \times \boldsymbol{\tau}_1}{\boldsymbol{n} \times \|\boldsymbol{\tau}_1\|}$$

We can finally use the orthogonal basis $\{\boldsymbol{e}_1, \boldsymbol{e}_2, \boldsymbol{n}\}$ to define the contact frame. Note that these three unit vectors are all defined in the global frame, thus can be regarded as a rotation matrix noted as $\boldsymbol{R}_c$ which transfers the contact frame to global frame:

$$\boldsymbol{R}_c = \begin{bmatrix} \boldsymbol{n} & \boldsymbol{e}_1 & \boldsymbol{e}_2 \end{bmatrix}$$

Based on this matrix, we can then define a configuration tensor $\boldsymbol{g}_c \in SE(3)$ which represents the position and orientation of the contact frame with respect to the global frame:

$$\boldsymbol{g}_c = \begin{bmatrix} \boldsymbol{R}_c & \boldsymbol{p}_c \\ \boldsymbol{0}^\top & 1 \end{bmatrix}$$

3.3.3 Contact force

When objects come into contact with each other, contact forces are generated in the contact region (contact point), and these contact forces contribute to the dynamics of the objects. Therefore, we need to incorporate the contact forces into the dynamic equation, as shown below:

$$\boldsymbol{\mathcal{M}}\dot{\boldsymbol{\eta}} - ad_{\boldsymbol{\eta}}^\top \boldsymbol{\mathcal{M}}\boldsymbol{\eta} = \boldsymbol{\Lambda}_i' - \mathrm{ad}_{\boldsymbol{\xi}}^\top \boldsymbol{\Lambda}_i + \boldsymbol{\Lambda}_e + \boldsymbol{\Lambda}_c^* \tag{3.13}$$

where $\boldsymbol{\Lambda}_c^* \in \mathbb{R}^6$ denotes the contact wrench. Referring to Fig. 3.8, the contact frame clearly defines the orientations of contact forces. Specifically, the $\boldsymbol{n}$ axis represents the direction of the normal contact force, while the $\boldsymbol{e}_1$ and $\boldsymbol{e}_2$ axes correspond to the directions of tangential contact forces (likewise for contact moments). Denote $\boldsymbol{\Lambda}_c$ represents the wrench generated by contact expressed in contact frame. Nevertheless, it becomes necessary to transfer it into the body-fixed coordinate system, as the dynamic equations for the electrode array are formulated in the body frame. Then, we denote $\boldsymbol{\Lambda}_c^*$ as the equivalent wrench with respect to the body frame, which is

generated by translating the distributed contact force onto the center of cross-section. There exists the following relationship between $\mathbf{\Lambda}_c$ and $\mathbf{\Lambda}_c^*$:

$$\mathbf{\Lambda}_c^* = \mathrm{Ad}^*_{\boldsymbol{g}_{bc}} \mathbf{\Lambda}_c \tag{3.14}$$

where the coadjoint representation of the Lie group Ad^* allows changing the wrench from the contact frame to the body frame, with $\boldsymbol{g}_{bc} = \boldsymbol{g}^{-1}\boldsymbol{g}_c$, being the configuration tensor of the contact frame with respect to the body frame.

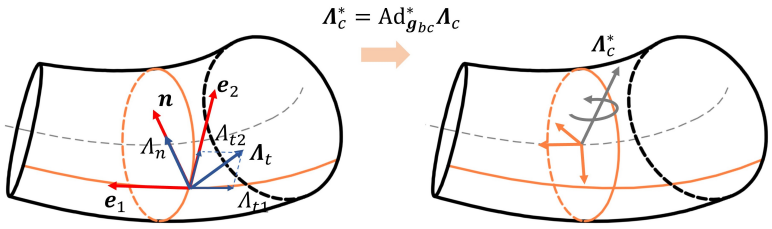

Figure 3.8: Transformation of contact load from contact frame to body frame.

After having discussed the contact frame and contact forces, we also need to consider the corresponding contact constraints. In the following section, we will introduce various types of contact constraints.

3.4 Contact Constraints

In the above sections, we have established the geometric model of the cochlea, defined the contact frame, and introduced the contact force. We are now able to conceptualize the interaction between the electrode array of a cochlear implant and the cochlea as a contact problem. Within the context of contact dynamics, two key elements come into play. The first element is the contact force, as discussed in the preceding sections. The second element is the contact constraint, which necessitates the absence of penetration during contact and adherence to the principles of friction. To enhance our understanding and investigate a broader spectrum of contact models, the upcoming sections will be dedicated to introducing and elaborating on the contact model for a general soft slender rod. In the culmination of this study, the final simulation section will circle back to the specific scenario of the interaction between the cochlear implant electrode array and the cochlea, applying our broader findings to this particular case.

As depicted in the Fig. 3.9, contact will be formulated as constrains in the deduced implant dynamics. From a consideration of the geometric mechanism of contact, three potential contact constraints may arise, include fixed constraints, articulated constraints, and collision constraints. Among these, fixed constraints and articulated constraints can be represented using equalities and fall into the category of bilateral constraints. On the other hand, collision constraints are typically expressed using inequalities and fall into the category of unilateral constraints[122]. All contact constraints give rise to contact forces at the contact points. The following will firstly introduce the bilateral contact constraint and secondly the unilateral contact constraint.

3.4.1 Bilateral contact constrain

Bilateral constraints are mathematical representations of kinematic pairs, such as spherical, or revolving joints. These constraints can be expressed as algebraic equations that impose

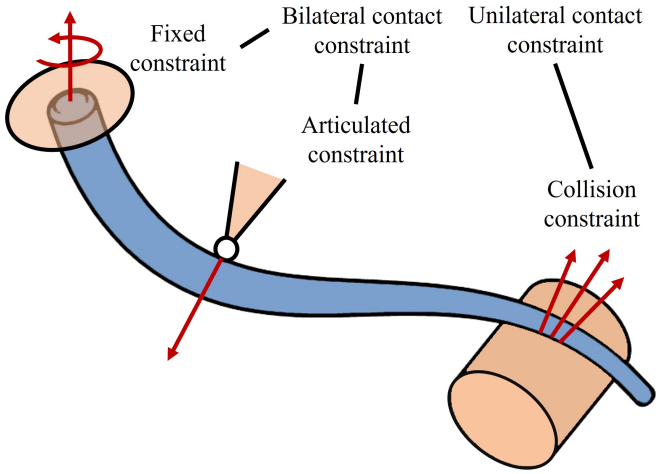

Figure 3.9: Different contact constraints of soft slender rod.

restrictions on the relative positions of the two bodies.

3.4.1.1 Fixed constraint

In engineering applications or some simulation scenarios, some parts of the soft slender rod will be totally fixed by the external environment. For example, the head section of the soft slender rod is fixed on a mobile base or some of its parts are hinged to external objects like truss system[123]. These persistent constraints can be regarded as bilateral constraints. Specifically, the satisfaction of bilateral constraints can be realized by adding Lagrangian multipliers in the system. For any points $s \in [0,1]$ along the centerline of the soft slender rod, if we want to fix some sections of soft slender rod to the desired configuration, that is, given a constrained configuration matrix $\boldsymbol{g}_f(s)$, then the bilateral constraint can be expressed as:

$$\mathbb{R}^6 \ni \boldsymbol{G}_f(s) = \left(\log(\boldsymbol{g}_f^{-1}\boldsymbol{g})\right)^{\vee} = \mathbf{0}$$

which is equivalent to the following bilateral constriant $\boldsymbol{g}_f(s) - \boldsymbol{g}(s) = \mathbf{0}$, stated in the matrix form.

3.4.1.2 Articulated constraint

Articulatd constraints in soft slender rods impose limitations on the translation of contact points while permitting rotational freedom at the cross-sections of these points. Consequently, only the three translational degrees of freedom are constrained by articulated constraints. For $s \in [0,1]$, denoting the desired position of the joint as $\boldsymbol{p}_a(s)$ with respect to the global frame, the articulated constraint is given by the following equation:

$$\mathbb{R}^3 \ni \boldsymbol{G}_a(s) = \boldsymbol{p}_a - \mathbf{U}\boldsymbol{g}_c(s,\beta)\mathbf{A} = \mathbf{0}$$

where $\mathbf{U} = [\mathbf{I}_{3\times 3}\ \mathbf{0}_{1\times 3}]$ and $\mathbf{A} = [0\ 0\ 0\ 1]^{\top}$. Note that for the articulated constraint, the joint can only generate the force but not the moment, which means that $\boldsymbol{\Lambda}_c$ is not fully filled. Denoting the generated force as $\boldsymbol{\Lambda}_a \in \mathbb{R}^3$, (3.14) should be rewritten as:

$$\boldsymbol{\Lambda}_c^* = \mathrm{Ad}^*_{\boldsymbol{g}_{bc}}\mathbf{B}^{\top}\boldsymbol{\Lambda}_a$$

where $\mathbf{B} = [\mathbf{0}_{3\times3}\ , \mathbf{I}_{3\times3}]$.

3.4.2 Unilateral contact constrain

In the field of contact mechanics, the unilateral constraint refers to a mechanical constraint that prohibits any form of penetration or interpenetration between two bodies, whether they are rigid or flexible. This constraint ensures that the tangential contact forces between the bodies adhere to the contact law, which governs the interaction between contacting surfaces.

For collision constraint, the generated force is composed by the normal contact force and tangent friction force, i.e., $\mathbf{\Lambda}_c = [\mathbf{0}_{1\times3}, \Lambda_n, \Lambda_{t1}, \Lambda_{t2}]^\top$, where Λ_n, Λ_{t1} and Λ_{t2} denote respectively the normal contact force in the direction of $\boldsymbol{n}$, the friction force in the direction of $\boldsymbol{e}_1$ and $\boldsymbol{e}_2$. Thus (3.14) should be rewritten as:

$$\mathbf{\Lambda}_c^* = \mathrm{Ad}^*_{\boldsymbol{g}_{bc}}(\mathbf{B}_n^\top \Lambda_n + \mathbf{B}_t^\top \mathbf{\Lambda}_t) \tag{3.15}$$

where $\mathbf{B}_n = [\mathbf{0}_{1\times3}, 1, \mathbf{0}_{1\times2}]$, $\mathbf{B}_t = [\mathbf{0}_{2\times4}, \mathbf{I}_{2\times2}]$ and $\mathbf{\Lambda}_t = [\Lambda_{t1}, \Lambda_{t2}]^\top$.

In accordance with the problem statement, the collision constraints encompass a set of inequalities that involve contact gaps and contact sliding velocities. Hence, our initial objective is to elucidate how to define contact gaps and contact sliding velocities within the framework of Cosserat rod theory.

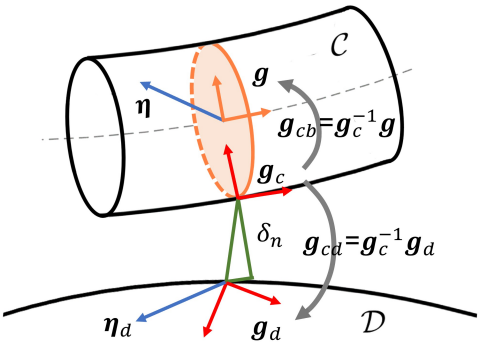

Figure 3.10: Geometries of the contact pair.

As shown in Fig. 3.10, we designate the contact frame of the soft slender rod as $\boldsymbol{g}_c$, serving as the master contact frame. We also denote a known slave contact frame $\boldsymbol{g}_d$, located on the surface $\partial\mathcal{D}$ of another body $\mathcal{D}$. These two frames constitute a contact pair. In order to represent the relative position and orientation of slave contact frame on $\partial\mathcal{D}$ with respect to contact frame $\boldsymbol{g}_c$ on $\partial\mathcal{C}$, we employ a tensor denoted as $\boldsymbol{g}_{cd} = \boldsymbol{g}_c^{-1}\boldsymbol{g}_d$.

The normal gap is the relative position vector projected on the opposite direction of normal vector $\boldsymbol{n}$ and can be obtained from the relative configuration tensor of contact via the following relation:.

$$\delta_n = -\mathbf{P}\boldsymbol{g}_{cd}\mathbf{A} \tag{3.16}$$

with $\mathbf{P} = [1\ 0\ 0\ 0]$ and $\mathbf{A} = [0\ 0\ 0\ 1]^\top$.

The normal force and normal gap should always be non-negative, i.e., $\delta_n \geq 0$, $\Lambda_n \geq 0$. This principle imposes a constraint on the occurrence of mutual penetration among objects in contact, thereby prohibiting their ability to traverse another one. The magnitude of the normal contact force is invariably non-negative, and contact forces are solely generated upon contact establishment.

The friction force is constrained within a convex set $\mathcal{C}_f$ corresponding to the friction cone, such that $\mathbf{\Lambda}_t \in \mathcal{C}_f$. In our work we use the Coulomb's law to model the friction, as illustrated in Fig. 3.11. The section of the Coulomb's friction cone, i.e., the disk $\mathcal{D}(\mu\Lambda_n)$ is defined by

$$\mathcal{D}(\mu\Lambda_n) = \{\Lambda_t | \mu\Lambda_n - \Lambda_t \geq 0\} \tag{3.17}$$

with μ being the coefficient of friction.

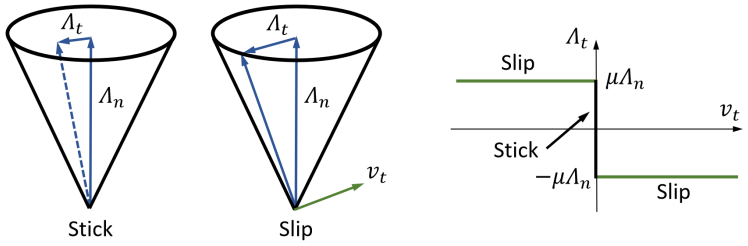

Figure 3.11: Coulomb's law of friction states that the reactionary force remains completely within the cone during adhesion between objects, and it aligns with the perimeter of the cone at the onset of slipping.

Denoting the velocity of backbone of soft slender rod with respect to the body frame as $\boldsymbol{\eta}$ and supposing the velocity of the slave contact point on object $\mathcal{D}$ with respect to the slave contact frame $\boldsymbol{g}_d$ is $\boldsymbol{\eta}_d$. The slip velocity is defined as the projection of the relative contact velocity onto the tangential plane at the contact point. Thus, the relative velocity twist of contact point with respect to contact frame $\boldsymbol{g}_c$ of $\partial\mathcal{C}$ can be then given by:

$$\boldsymbol{\eta}_c = \mathrm{Ad}_{\boldsymbol{g}_{cb}}\boldsymbol{\eta} - \mathrm{Ad}_{\boldsymbol{g}_{cd}}\boldsymbol{\eta}_d \tag{3.18}$$

where $\boldsymbol{g}_{cb} = \boldsymbol{g}_c^{-1}\boldsymbol{g}$ and the adjoint representation of the Lie group $\mathrm{Ad}_{\boldsymbol{g}_i^{-1}\boldsymbol{g}_j}$ allows changing the velocity twist from frame j to frame i. Consequently the slip tangent velocity $\boldsymbol{v}_t \in \mathbb{R}^2$ on $\partial\mathcal{C}$ with respect to contact frame equals to:

$$\boldsymbol{v}_t = \mathbf{B}_t\boldsymbol{\eta}_c \tag{3.19}$$

where $\mathbf{B}_t$ was defined in (3.15).

As shown in Fig.3.11, the Coulomb's friction cone contains two different states (stick $v_t = 0$ or slide $v_t \neq 0$) of a contact point which is given by:

$$\begin{cases} \text{Stick} : \mu\Lambda_n - \|\mathbf{\Lambda}_t\| > 0 \ , \ \boldsymbol{v}_t = \mathbf{0} & \text{(3.20a)} \\ \text{Silde} : \mathbf{\Lambda}_t = -\mu\Lambda_n\mathbf{T} \ , \ \boldsymbol{v}_t \neq \mathbf{0} & \text{(3.20b)} \end{cases}$$

Here $\mathbf{T}$ is an identity vector which indicates the tangential sliding direction with $\mathbf{T} = \frac{\boldsymbol{v}_t}{\|\boldsymbol{v}_t\|}$.

There are two main approaches to model the above unilateral constraints. The first is based on the regularization of contact constraint such as penalty methods [124], while the second is based on non-smooth contact dynamics [124], modeling the contact constraint as the exact inequalities.

Within penalty methods, the constraint is characterized as soft, allowing for the possibility of penetration between two contacting bodies. In the event of geometric penetration between these bodies, a penalty potential energy term is incorporated into the studied system, wherein

its magnitude is directly proportional to the degree of penetration. The penalty potential will generate the resisted forces in normal and tangential directions. Penalty formulations in constraint-based simulations offer the advantage of being unconstrained and relatively straightforward to simulate and differentiate. They are particularly useful when it comes to stability, as implicit integration methods allow for stable simulations across a wide range of stiffness values. However, one limitation of penalty methods is that they allow for small constraint violations. While minor violations of normal constraints may not be visually apparent, softening the static friction constraint can lead to undesirable artifacts in certain scenarios. For example, when simulating a heavy object resting on an inclined surface under static friction, if the simulation runs for a long duration, the introduction of tangential slipping due to softened stick constraints can eventually become visually noticeable. Therefore, in our work, we did not utilize this method, but instead, we consistently treated contact as a hard constraint throughout, which will be introduced in the next subsection.

3.4.3 NCP formulation of contact constraints

As discussed in the previous subsection, the precise approach involves formulating the contact as a hard constraint. In the case of unilateral constraints, this formulation is commonly expressed as nonlinear complementary problem (NCP), which will be detailed in the following subsections. In such formulation, the unilateral constraints are decomposed into normal contact constraint (for modeling the contact force between the contact surfaces) and tangential contact constraint (for modeling the friction between the contact surfaces).

3.4.3.1 Normal contact constraint

In our work, the NCP of normal contact is modeled by the Signorini's condition [124]:

$$0 \leq \delta_n \perp \Lambda_n \geq 0 \tag{3.21}$$

where the symbol "$\perp$" denotes that the product of δ_n and Λ_n equals to zero, where δ_n represents the normal distance between the contact pairs in contact frame and Λ_n represents the contact force in the normal direction in contact frame, both should be either positive or zero.

3.4.3.2 Tangential contact constraint

Concerning the tangential contact constraint which is used to determine the friction, between the contact surfaces, let us first denote $\boldsymbol{\Lambda}_t \in \mathbb{R}^2$ as the friction force of any contact point in contact frame on the surface $\partial\mathcal{C}$. $\boldsymbol{v}_t \in \mathbb{R}^2$ stands for the slip velocity. Then according to the maximal dissipation principle [125], the instantaneous power of friction force at this contact point given by $\boldsymbol{\Lambda}_t^\top \boldsymbol{v}_t$ should always takes the minimum within the limit of friction cone, i.e., $\boldsymbol{\Lambda}_t$ should satisfy the following minimization problem:

$$\begin{aligned} \boldsymbol{\Lambda}_t = \text{argmin} \quad & \boldsymbol{\Lambda}_t^\top \boldsymbol{v}_t \\ \text{subject to} \quad & \mu\Lambda_n - \|\boldsymbol{\Lambda_t}\| \geq 0 \end{aligned}$$

where μ is the coefficient of friction. The first order Karush-Kuhn-Tucker conditions of above minimization problem can be then given by:

$$\boldsymbol{v}_t + \lambda_{sl} \nabla \|\boldsymbol{\Lambda}_t\| = \boldsymbol{0} \tag{3.22}$$

$$0 \leq \lambda_{sl} \perp \mu\Lambda_n - \|\boldsymbol{\Lambda}_t\| \geq 0 \tag{3.23}$$

with λ_{sl} the Lagrange multiplier. In fact, the above two equations can be further simplified. First, one can derive $\nabla\|\boldsymbol{\Lambda}_t\| = \boldsymbol{\Lambda}_t/\|\boldsymbol{\Lambda}_t\|$. Subsequently, taking this equation into (3.22) we can get $\boldsymbol{v}_t = -\lambda_{sl}\boldsymbol{\Lambda}_t/\|\boldsymbol{\Lambda}_t\|$. Then taking the norm of both two sides derives $\lambda_{sl} = \|\boldsymbol{v}_t\|$. Finally, (3.22) and (3.23) are transferred to the following complementary conditions where the Lagrange multiplier is eliminated:

$$\|\boldsymbol{\Lambda}_t\|\boldsymbol{v}_t + \|\boldsymbol{v}_t\|\boldsymbol{\Lambda}_t = \mathbf{0} \tag{3.24}$$

$$0 \leq \|\boldsymbol{v}_t\| \perp \mu\Lambda_n - \|\boldsymbol{\Lambda}_t\| \geq 0 \tag{3.25}$$

However, it is clear that the coupling between normal and frictional complementarity is non-convex and non-smooth. In the next section, we propose a smoothing method to solve this issue. Mathematically, the nonlinear complementary constraint (3.21) can be linearized to form a linear complementary problem (LCP). However, the tangential constraints (3.24) and (3.25) cannot be directly formulated as an LCP due to the nonlinearity of the friction cone. A common approach is to approximate the Coulomb's friction cone with a pyramid. This allows for the utilization of LCP solvers such as Lemke's algorithm [76] and Gauss-Seidel method [78]. Despite some advancements made in these methods specifically for simulating contact dynamics, the computational efficiency remains a challenge. In order to ensure both accuracy and efficiency, the following proposes propose a novel approach to reformulate the contact constraint as a smooth equality constraint. This new formulation aims to strike a balance between computational accuracy and efficiency.

3.4.4 NCP-function and slack variable

The idea of the proposed approach is to convert the NCP into a nonlinear function (NCP-function) in order to formulate the NCP as the equality constraint. Since the work by Mangasarian [126] it has been well known that by means of a suitable function $\phi : \mathbb{R}^2 \to \mathbb{R}$, the complementary condition $a \geq 0, b \geq 0, ab = 0$ can be transferred to an equivalent nonlinear equation: $\phi(a, b) = 0$. This technique has drawn interest for solving complementary programming in the field of mathematics in these years [127]. Our work is mainly based on this idea, using a slack variable to define both a and b.

Denoting $u \in \mathbb{R}$ as the slack variable and $D(u)$ as the Heaviside function with $D(u) = (\mathrm{sgn}(u) + 1)/2$. The complementary condition of a, b is equivalent to the following definition:

$$a = D(u)u \ , \ b = D^*(u)u \tag{3.26}$$

with $D^*(u) = -D(-u)$. It is evident that with the aforementioned definitions, the complementary condition holds for any $u \in \mathbb{R}$. Consequently, the nonlinear complementary constraint can be transformed into a manifold defined by (3.26) with respect to the slack variable u. With this new transformation, we should revise the normal contact and tangential contact constraint and transform them as well under this new framework, which will be discussed hereafter.

3.4.4.1 NCP-function of Normal Contact

Concerning the topic of normal contact, we can utilize a variable $u_n \in \mathbb{R}$ to represent both the normal contact force Λ_n and the normal gap δ_n at each contact point as the following definitions:

$$\Lambda_n = D(u_n)u_n \ , \ \delta_n = D^*(u_n)u_n \tag{3.27}$$

3.4.4.2 NCP-function of Tangential contact

Concerning the equality constraint (3.24) which means that $\boldsymbol{v}_t$ and $\boldsymbol{\Lambda}_t$ are always parallel and opposite, hence it is possible to define them by the parametric equation. At this aim, we first represent them in the polar coordinates, i.e., (3.24) equals to the following representation:

$$\boldsymbol{v}_t = \rho_1 \begin{bmatrix} \sin\theta \\ \cos\theta \end{bmatrix} \ , \ \boldsymbol{\Lambda}_t = -\rho_2 \begin{bmatrix} \sin\theta \\ \cos\theta \end{bmatrix} \tag{3.28}$$

where $\rho_1 \geq 0$ and $\rho_2 \geq 0$. Therefore, we can rewrite the complemantarity (3.25) as:

$$0 \leq \rho_1 \perp \mu\Lambda_n - \rho_2 \geq 0$$

which is equivalent to:

$$\rho_1 = f(u_t - \mu\Lambda_n) \ , \ \rho_2 = \mu\Lambda_n - f(\mu\Lambda_n - u_t) \ , \ \forall u_t > 0 \tag{3.29}$$

where function $f(x)$ denotes $D(x)x$. Then by taking the above representation into (3.28) one can get:

$$\boldsymbol{v}_t = f(1 - \frac{\mu\Lambda_n}{u_t}) \begin{bmatrix} u_t \sin\theta \\ u_t \cos\theta \end{bmatrix} \ , \ \forall u_t > 0 \tag{3.30}$$

$$\boldsymbol{\Lambda}_t = \left(-\frac{\mu\Lambda_n}{u_t} + f(\frac{\mu\Lambda_n}{u_t} - 1) \right) \begin{bmatrix} u_t \sin\theta \\ u_t \cos\theta \end{bmatrix} \ , \ \forall u_t > 0 \tag{3.31}$$

Note that the vector part $\begin{bmatrix} u_t \sin\theta & u_t \cos\theta \end{bmatrix}^\top$ represents an arbitrary vector defined in the polar coordinates, thus it can be rewritten in the Cartesian coordinates as $\boldsymbol{u}_t \in \mathbb{R}^2$ with $u_t = \|\boldsymbol{u}_t\|$. By doing so, we can describe (3.30) and (3.31) again in the Cartesian coordinates:

$$\boldsymbol{\Lambda}_t = W(\boldsymbol{u}_t)\boldsymbol{u}_t \ , \ \boldsymbol{v}_t = W^*(\boldsymbol{u}_t)\boldsymbol{u}_t \tag{3.32}$$

where

$$W(\boldsymbol{u}_t) = -\frac{\mu\Lambda_n}{u_t} + f(\frac{\mu\Lambda_n}{u_t} - 1) \ , \ W^*(\boldsymbol{u}_t) = f(1 - \frac{\mu\Lambda_n}{u_t})$$

Remark 2. *Note that (3.32) has no definition when $\boldsymbol{u}_t = \mathbf{0}_{2\times 1}$, thus we define $W(0,0) = W^*(0,0) = \mathbf{0}_{2\times 1}$ and $\nabla W(0,0) = \frac{\mu\Lambda_n}{l}\mathbf{I}_{2\times 2}$, $\nabla W^*(0,0) = \mathbf{0}_{2\times 2}$ to avoid the singularity.*

Following the above analysis, we can then define the slack vector $\boldsymbol{u} = [u_n \ \boldsymbol{u}_t^\top]^\top$ to cover both normal constraint and friction constraint. Based on the previous expression (3.15) of tangential contact forces, we can finally establish the relationship between the relaxation vector and contact forces using the following equation:

$$\boldsymbol{\Lambda}_c = (\mathbf{B}_n^\top D\mathbf{C}_n + \mathbf{B}_t^\top W\mathbf{C}_t)\boldsymbol{u} \tag{3.33}$$

where $\mathbf{C}_n = [1 \ \mathbf{0}_{1\times 2}]$ and $\mathbf{C}_t = [\mathbf{0}_{2\times 1} \ \mathbf{I}_{2\times 2}]$. $\mathbf{B}_n$ and $\mathbf{B}_t$ have been defined in (3.15). Similarly, the constraints of normal gap and the slip tangent velocity, written as:

$$\delta_n = D^*\mathbf{C}_n\boldsymbol{u} \ , \ \boldsymbol{v}_t = W^*\mathbf{C}_t\boldsymbol{u} \tag{3.34}$$

By employing the NCP-function, we have successfully reformulated both the normal and tangential contact constraints into a set of equality constraints. This reformulation allows us to apply established methods tailored for equality constraints to manage the contact constraints effectively. Nevertheless, a challenge arises due to the non-smooth nature of the Heaviside function we are utilizing, which leads to non-differentiable points during the process of addressing contact constraints. In the following sections, we will present the smoothed versions of the Heaviside function, which will be incorporated into the contact constraint framework.

3.4.5 Smooth reformulation of NCP-function

As mentioned above, the aforementioned formulation includes the Heaviside function, which is known to be discontinuous. Additionally, the function $f(x)$ in (3.29) possesses C^0 continuity, meaning that it is only continuous but not necessarily to be smooth. As a consequence, during the numerical solution process of dynamics, the presence of these functions leads to sudden changes, requiring additional iterations to achieve a solution. To address this concern, we propose a smooth approximation in our work, whereby the Heaviside function in (3.26) is replaced by some well-known smooth functions[128], which will be discussed hereafter.

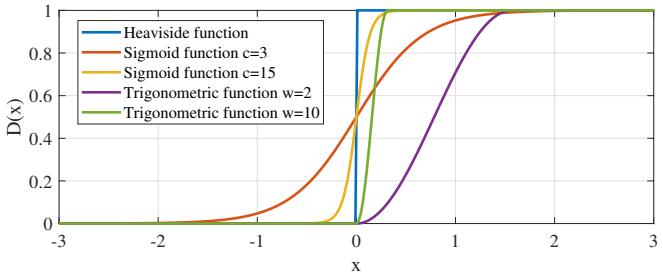

Figure 3.12: Proposed function for the reformulation of complementary constraint.

3.4.5.1 Sigmoid function

The first smooth function we proposed is based on the sigmoid function defined as follows:

$$D(x) = \frac{1}{1+e^{-cx}} \ , \ c > 0 \tag{3.35}$$

The parameter c plays a crucial role in determining the level of smoothing in (3.35). As c approaches infinity, (3.35) progressively converges to the Heaviside function, as depicted in Fig. 3.12. It is important to note that this approximation of complementarity is not perfectly accurate in the vicinity of the critical state. In situations where c is chosen to be extremely small, significant errors may occur when x approaches zero, potentially leading to penetrations of contact. In addition, the friction behavior no longer adheres strictly to Coulomb's friction law. In practical simulation computations, it is essential to meticulously select the parameter c to strike a balance between accuracy and the numerical robustness of the calculations.

3.4.5.2 Trigonometric function

As depicted in Fig. 3.12, the second smooth function we proposed is based on trigonometric function as follows:

$$D(x) = \begin{cases} 0 \ , \ x < 0 \\ \dfrac{1-\cos(wx)}{2} \ , 0 \leq \ x < \dfrac{\pi}{w} \\ 1 \ , \ x \geq \dfrac{\pi}{w} \end{cases} \tag{3.36}$$

where w is a positive parameter.

In contrast to the sigmoid function, the function described by (3.36) rigorously fulfills the complementarity condition. This is attributed to their positive definiteness in the positive half-axis of x, while being identically zero in the negative half-axis of x. In this case, the parameter

w solely affects the robustness of numerical optimization but does not impact the dynamics of the soft rod.

By utilizing the aforementioned function as a substitute for the impact function, we obtain the smoothed contact constraints, as depicted in Fig. 3.13. At the critical state between sticking and sliding, a sudden change in gradient can be observed in the left image of Fig. 3.13 which is non smooth, whereas the gradient in the right image of Fig. 3.13 exhibits a continuous transition using trigonometric function.

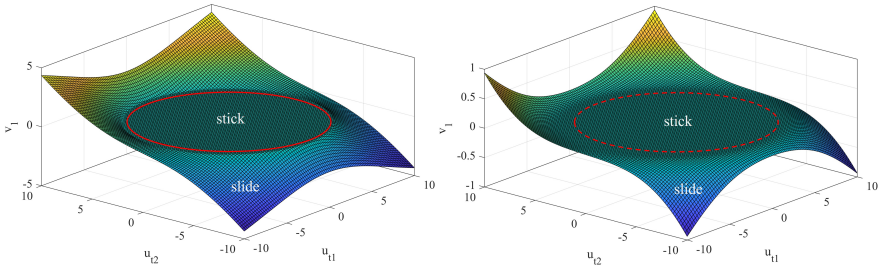

Figure 3.13: The manifold of tangent velocity with respect of slack variable. The figure illustrates a comparison between the non-smooth case utilizing the Heaviside function (on the left) and the smooth case employing a trigonometric function (on the right).

Having tackled the various types of contact constraints, we have now converted them into smoothed equality constraints. With the contact force and constraints in hand, our next step is to delve into the dynamics of soft slender rods, specifically the electrode array, under these contact constraints. A comprehensive introduction to this topic will be provided in the following section.

3.5 Contact dynamics

To incorporate the interactive forces, stemming from both bilateral and unilateral constraints, into the dynamics of the cochlear implant, we need to first revisit the Cosserat rod dynamics (3.13) delineated in Section 3.3.1. Subsequently, we will implement the linear discretization scheme introduced in Section 3.5.2. This will lead us to derive the weak form of the dynamics introduced in Section 3.5.3, which is suitable for real-time simulation and control design.

3.5.1 Strong form of dynamics

3.5.1.1 PDE

To account for the contact force during environmental interactions, the corresponding dynamic model in the body frame can be rewritten as a set of partial differential equations (PDEs).

$$\boldsymbol{\mathcal{M}}\dot{\boldsymbol{\eta}} - ad_{\boldsymbol{\eta}}^{\top}\boldsymbol{\mathcal{M}}\boldsymbol{\eta} = \boldsymbol{\Lambda}_i' - \mathrm{ad}_{\boldsymbol{\xi}}^{\top}\,\boldsymbol{\Lambda}_i + \boldsymbol{\Lambda}_e + \mathrm{Ad}^{*}_{\boldsymbol{g}_{bc}}\boldsymbol{\Lambda}_c + \boldsymbol{\Lambda}_f + \mathrm{Ad}^{*}_{\boldsymbol{g}_{bc}}\mathbf{B}^{\top}\boldsymbol{\Lambda}_a \tag{3.37}$$

satisfying the following boundary conditions:

$$\begin{aligned}\boldsymbol{\Lambda}_i(0,t) &= -\boldsymbol{\Lambda}_0(t)\ ,\ \text{or}\ \boldsymbol{g}(0,t) = \boldsymbol{g}_0(t)\\ \boldsymbol{\Lambda}_i(L,t) &= \boldsymbol{\Lambda}_L(t)\ ,\ \text{or}\ \boldsymbol{g}(L,t) = \boldsymbol{g}_L(t)\end{aligned} \tag{3.38}$$

where $\boldsymbol{\mathcal{M}} \in \mathbb{R}^{6\times6}$ is the tensor of mass linear density along central axis, $\boldsymbol{\Lambda}_i \in \mathbb{R}^6$ is the elastic internal wrench, $\boldsymbol{\Lambda}_c \in \mathbb{R}^6$ is the contact force produced by collision, $\boldsymbol{\Lambda}_f \in \mathbb{R}^6$ is the contact force produced by fixed constraints and $\boldsymbol{\Lambda}_a \in \mathbb{R}^3$ is the contact force produced by articulated constraints. $\boldsymbol{\Lambda}_e \in \mathbb{R}^6$ are the distributed external wrench applied on the soft slender rod. One contribution of $\boldsymbol{\Lambda}_e$ comes from the gravity which can be given by $\boldsymbol{\Lambda}_e = \boldsymbol{\mathcal{M}}\mathrm{Ad}_{\boldsymbol{g}}^{-1}\boldsymbol{\mathcal{G}}$, where the inverse of adjoint representation of the Lie group is used to transform twists from the global frame to the body frame. $\boldsymbol{\mathcal{G}}$ is the gravity acceleration twist w.r.t. the global frame $\boldsymbol{\mathcal{G}} = [\mathbf{0}_{1\times5} \ -9.81]^\top$.

3.5.1.2 Constraints

Except the boundary condition (3.38) which should be satisfied by the revised strong form (3.37), we need also to take into account the bilateral and unilateral constraints when investigating the interaction between the cochlear implant ant the cochlea. In this case, if all contact constraints introduced in Section 3.4.1 and 3.4.2 are considered, the dynamics must also satisfy the following constraint conditions:

$$\boldsymbol{G}_f = \mathbf{0} \tag{3.39}$$

$$\boldsymbol{G}_a = \mathbf{0} \tag{3.40}$$

$$\boldsymbol{\Lambda}_c - (\mathbf{B}_n^\top D\mathbf{C}_n + \mathbf{B}_t^\top W\mathbf{C}_t)\boldsymbol{u} = \mathbf{0} \tag{3.41}$$

$$\mathbf{P}\boldsymbol{g}_{cd}\mathbf{A} + D^*\mathbf{C}_n\boldsymbol{u} = 0 \tag{3.42}$$

$$\mathrm{Ad}_{\boldsymbol{g}_{cb}}\boldsymbol{\eta} - \mathrm{Ad}_{\boldsymbol{g}_{cd}}\boldsymbol{\eta}_d - W^*\mathbf{C}_t\boldsymbol{u} = \mathbf{0} \tag{3.43}$$

where (3.39) and (3.40) contains all bilateral constraints and (3.41)-(3.43) denote the reformulation of the unilateral constraint based on the slack variable. (3.41) represents the constraint of contact force. (3.42) and (3.43) describe the constraint on normal contact gap and the constraint on tangential sliding respectively. The unknown variables in the partial differential-algebraic system formed by the dynamics and constraints discussed above encompass the initial pose tensor $\boldsymbol{g}_0(t)$ at the starting end, the strain field $\boldsymbol{\xi}(s,t)$, the contact force $\boldsymbol{\Lambda}_f(s,t)$, $\boldsymbol{\Lambda}_a(s,t)$ and the contact field represented by slack variables $\boldsymbol{u}(s,t)$. In order to facilitate the solution of this partial differential-algebraic system, we aim to derive its corresponding weak form. By introducing suitable test functions $\boldsymbol{\Phi}_{\boldsymbol{\xi}}(s)$ and $\boldsymbol{\Phi}_u(s)$, the weak form of (3.37) can be expressed as the integration through the backbone of EA:

$$\int_0^L \boldsymbol{\Phi}_{\boldsymbol{\xi}}^\top(\boldsymbol{\mathcal{M}}\dot{\boldsymbol{\eta}} - ad_{\boldsymbol{\eta}}^\top\boldsymbol{\mathcal{M}}\boldsymbol{\eta} - \boldsymbol{\Lambda}_i' + \mathrm{ad}_{\boldsymbol{\xi}}^\top\boldsymbol{\Lambda}_i - \boldsymbol{\Lambda}_e - \mathrm{Ad}_{\boldsymbol{g}_{bc}}^*\boldsymbol{\Lambda}_c - \boldsymbol{\Lambda}_f - \mathrm{Ad}_{\boldsymbol{g}_{bc}}^*\mathbf{B}^\top\boldsymbol{\Lambda}_a)\mathrm{ds} = 0 \tag{3.44}$$

and the weak form of constraints (3.42) and (3.43) are given by:

$$\int_0^L \boldsymbol{\Phi}_{\boldsymbol{u}}^\top \begin{bmatrix} \mathbf{P}\boldsymbol{g}_{cd}\mathbf{A} - D^*\mathbf{C}_n\boldsymbol{u} \\ \mathrm{Ad}_{\boldsymbol{g}_{cb}}\boldsymbol{\eta} - \mathrm{Ad}_{\boldsymbol{g}_{cd}}\boldsymbol{\eta}_d - W^*\mathbf{C}_t\boldsymbol{u} \end{bmatrix} \mathrm{ds} = 0 \tag{3.45}$$

As for the bilateral constrain (3.39) and (3.40), their weak forms retain the same representation as the strong form since they are normally discretely located on the soft slender rod.

We have derived the weak form, wherein the virtual displacement must be expressed through generalized variables. The spatial discretization of the strain field, denoted as $\boldsymbol{\Phi}_{\boldsymbol{\xi}}$, has been adequately addressed in Section 2.2.7. However, a pertinent question arises: How should we handle $\boldsymbol{\Phi}_{\boldsymbol{u}}$, given its association with contact constraints? The treatment of this issue will be thoroughly analyzed in the subsequent discussion.

3.5.2 Spatial interpolation of contact field

It is clear that the distribution of contact forces depends on the arc length parameter s, thus similar to the interpolation of the strain field, we employ the concept of piecewise linear interpolation to approximate the distribution of contact forces through interpolating the corresponding slack variable along the length of the center line. As shown in Fig. 3.14, by dividing the soft slender rod into m sections along the s direction, denoted as $[0, s_1]$, $[s_1, s_2]$, $\ldots$, $[s_{m-1}, 1]$, the entire contact field $\mathbf{\Lambda}_c(s)$ can be expressed as a linear combination of interpolation basis functions $\mathbf{\Psi}(s)$ and a discrete set of slack variable $\boldsymbol{\lambda}_c$:

$$\mathbf{\Lambda}_c(s) = (\mathbf{B}_n^\top D\mathbf{C}_n + \mathbf{B}_t^\top W\mathbf{C}_t)\mathbf{\Psi}(s)\boldsymbol{\lambda}_c \tag{3.46}$$

where $\boldsymbol{\lambda}_c = [u_0\ u_1\ \ldots\ u_m]^\top \in \mathbb{R}^{m+1}$ contains the slack variables of each node along centerline. The interpolation basis functions $\mathbf{\Psi}(s)$ capture the linear variation of contact forces within each section of the soft slender rod (EA), which are defined as follows:

$$\mathbf{\Psi}(s) = \begin{bmatrix} \Psi_0\mathbf{I}_{3\times3} & \Psi_1\mathbf{I}_{3\times3} & \ldots & \Psi_m\mathbf{I}_{3\times3} \end{bmatrix} \in \mathbb{R}^{3\times3(m+1)}$$

where for $i \in \{0, 1, \ldots, m\}$

$$\Psi_i(s) = \begin{cases} ms - i & \text{for } s \in [\dfrac{i-1}{m}, \dfrac{i}{m}) \\ i + 1 - ms & \text{for } s \in [\dfrac{i}{m}, \dfrac{i+1}{m}] \\ 0 & \text{for } s \notin [\dfrac{i-1}{m}, \dfrac{i+1}{m}] \end{cases}$$

As for the contact force produced by fixed constraints and articulated constraints, supposing

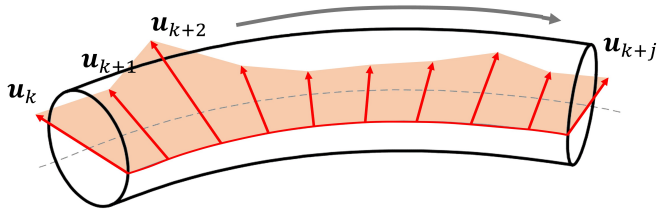

Figure 3.14: Linear interpolation of contact load along arc length.

that they are discretely located on the soft slender rod (EA) with quantities of m_f and m_a respectively, we use two vectors to cover all of them:

$$\boldsymbol{\lambda}_f = [\mathbf{\Lambda}_{f,1}^\top\ \mathbf{\Lambda}_{f,2}^\top\ \ldots\ \mathbf{\Lambda}_{f,m_f}^\top]^\top \in \mathbb{R}^{6m_f}$$

$$\boldsymbol{\lambda}_a = [\mathbf{\Lambda}_{a,1}^\top\ \mathbf{\Lambda}_{a,2}^\top\ \ldots\ \mathbf{\Lambda}_{a,m_a}^\top]^\top \in \mathbb{R}^{6m_a}$$

It should be noted that when the contact area is notably narrow, the rate of change in the contact load is significant, or the force is concentrated, the linearized contact force often requires a finer level of discretization. We have now introduced spatial interpolation of contact field, based on which we can then deduce the weak form of cochlear implant dynamics by taking into account its interaction with cochlea.

3.5.3 Weak form of dynamics

In order to deduce weak form, let us first introduce $\mathbf{\Phi}_\xi$, as presented in Section 2.2.7. For $s \in [0,1]$, by introducing the test function $\mathbf{\Phi}_{\boldsymbol{\xi}}(s)$ as virtual displacement $\boldsymbol{\delta}(s) = \boldsymbol{J}\delta\boldsymbol{q}$, the weak form (3.44) is given by:

$$\begin{aligned}\delta\boldsymbol{q}^\top \int_0^1 \boldsymbol{J}^\top (\boldsymbol{\mathcal{M}}\dot{\boldsymbol{\eta}} - ad_{\boldsymbol{\eta}}^\top \boldsymbol{\mathcal{M}}\boldsymbol{\eta} - \boldsymbol{\Lambda}_i' + \mathrm{ad}_{\boldsymbol{\xi}}^\top \boldsymbol{\Lambda}_i - \boldsymbol{\Lambda}_e \\ - \mathrm{Ad}^*_{\boldsymbol{g}_{bc}} \boldsymbol{\Lambda}_c - \boldsymbol{\Lambda}_f - \mathrm{Ad}^*_{\boldsymbol{g}_{bc}} \mathbf{B}^\top \boldsymbol{\Lambda}_a)\mathrm{ds} = 0\end{aligned} \tag{3.47}$$

Similarly, following the linear interpolation technique presented in Section 2.2.7, by introducing the test function $\mathbf{\Phi}_{\boldsymbol{u}}(s)$ as $\delta\boldsymbol{u} = \boldsymbol{\Psi}\delta\boldsymbol{\lambda}$ for contact constrain (3.42) and (3.43) respectively, their weak form (3.45) is deduced as follows:

$$\delta\boldsymbol{\lambda}_c^\top \int_0^1 \boldsymbol{\Psi}^\top \begin{bmatrix} \mathbf{P}\boldsymbol{g}_{cd}\mathbf{A} + D^*\mathbf{C}_n\boldsymbol{\Psi}\boldsymbol{\lambda}_c \\ \mathrm{Ad}_{\boldsymbol{g}_{cb}}\boldsymbol{\eta} - \mathrm{Ad}_{\boldsymbol{g}_{cd}}\boldsymbol{\eta}_d - W^*\mathbf{C}_t\boldsymbol{\Psi}\boldsymbol{\lambda}_c \end{bmatrix} \mathrm{ds} = 0 \tag{3.48}$$

Up to this point, we have obtained the weak form of the dynamics that takes into account contact. After eliminating terms $\delta\boldsymbol{q}^\top$ and $\delta\boldsymbol{\lambda}_c^\top$ (since they are assumed to be any value), we will arrive at the corresponding Ordinary Differential Equations (ODE) for the dynamics model. This will be elaborated in the upcoming subsection.

3.5.4 Dynamics equation

By reformulating the contact force using $\boldsymbol{\lambda}_n$, $\boldsymbol{\lambda}_f$ and $\boldsymbol{\lambda}_a$, along with the aforementioned definitions, we have successfully transformed the dynamics from the NCP form into a system of DAEs (Differential-Algebraic Equations) solely composed of equality constraints:

$$\boldsymbol{M}\ddot{\boldsymbol{q}} + \boldsymbol{C}\dot{\boldsymbol{q}} - \boldsymbol{K}\boldsymbol{q} = \boldsymbol{P} + \boldsymbol{H}_c\boldsymbol{\lambda}_c + \boldsymbol{H}_f\boldsymbol{\lambda}_f + \boldsymbol{H}_a\boldsymbol{\lambda}_a \tag{3.49}$$

$$\boldsymbol{G}_c - \boldsymbol{E}_c\boldsymbol{\lambda}_c = \boldsymbol{0} \tag{3.50}$$

$$\boldsymbol{G}_f = \boldsymbol{0} \tag{3.51}$$

$$\boldsymbol{G}_a = \boldsymbol{0} \tag{3.52}$$

For ease of description, we define the following operators Vec to assemble discrete matrices together:

$$\underset{i=1}{\overset{N}{\mathrm{Vec}}}(\boldsymbol{X}_i) = [\boldsymbol{X}_1^\top \ \boldsymbol{X}_2^\top \ \dots \ \boldsymbol{X}_N^\top]^\top$$

All the matrices of (3.49)-(3.52) are given by the following definitions:

- $\boldsymbol{M}(\boldsymbol{q}) = \int_0^L \boldsymbol{J}^\top \boldsymbol{\mathcal{M}}\boldsymbol{J}\mathrm{ds} \in \mathbb{R}^{6(n+1)\times 6(n+1)}$, the mass matrix;
- $\boldsymbol{C}(\boldsymbol{q},\dot{\boldsymbol{q}}) = \int_0^L [\boldsymbol{J}^\top(\boldsymbol{\mathcal{M}}\dot{\boldsymbol{J}} - ad^\top_{\boldsymbol{J}\dot{\boldsymbol{q}}}\boldsymbol{\mathcal{M}}\boldsymbol{J}) - \boldsymbol{\Phi}^\top\mathcal{D}\boldsymbol{\Phi}]\mathrm{ds} \in \mathbb{R}^{6(n+1)\times 6(n+1)}$, the Coriolis and damping matrix;
- $\boldsymbol{K} = \int_0^L \bar{\boldsymbol{\Phi}}^\top \mathcal{K}\bar{\boldsymbol{\Phi}}\mathrm{ds} + \boldsymbol{J}^\top(L)\bar{\boldsymbol{\Phi}}(L) \in \mathbb{R}^{6(n+1)\times 6(n+1)}$, the stiffness matrix;
- $\boldsymbol{H}_c(\boldsymbol{q}) = \int_0^L \boldsymbol{J}^\top \mathrm{Ad}^*_{\boldsymbol{g}_{bc}}(\mathbf{B}_n^\top D\mathbf{C}_n + \mathbf{B}_t^\top W\mathbf{C}_t)\boldsymbol{\Psi}\mathrm{ds} \in \mathbb{R}^{6(n+1)\times 3(m+1)}$, the collision contact force matrix;
- $\boldsymbol{H}_f(\boldsymbol{q}) = \underset{i=1}{\overset{m_f}{\mathrm{Vec}}}(\boldsymbol{J}_i) \in \mathbb{R}^{6(n+1)\times 6m_f}$, the force matrix of fixed constraints;

- $\boldsymbol{H}_a(\boldsymbol{q}) = \underset{i=1}{\overset{m_a}{\mathrm{Vec}}}(\boldsymbol{J}_i^\top \mathrm{Ad}^*_{\boldsymbol{g}_{bc,i}} \mathbf{B}_i^\top) \in \mathbb{R}^{6(n+1)\times 3m_a}$, the force matrix of articulated constraints;
- $\boldsymbol{P}(\boldsymbol{q}) = \int_0^L \boldsymbol{J}^\top \boldsymbol{\Lambda}_e \mathrm{ds} + \int_0^1 \boldsymbol{J}^\top \boldsymbol{\mathcal{M}} \mathrm{Ad}_{\boldsymbol{g}}^{-1} \mathrm{ds} \boldsymbol{\mathcal{G}} \in \mathbb{R}^{6(n+1)}$, the contribution of concentrated external load and gravity.
- $\boldsymbol{G}_c(\boldsymbol{q}, \dot{\boldsymbol{q}}) = \int_0^L \boldsymbol{\Psi}^\top \begin{bmatrix} \mathbf{P}\boldsymbol{g}_{cd}\mathbf{A} \\ \mathrm{Ad}_{\boldsymbol{g}_{cb}}\boldsymbol{\eta} - \mathrm{Ad}_{\boldsymbol{g}_{cd}}\boldsymbol{\eta}_d \end{bmatrix} \mathrm{ds} \in \mathbb{R}^{3(m+1)}$, the tangent contact velocity matrix;
- $\boldsymbol{G}_f(\boldsymbol{q}) = \underset{i=1}{\overset{N}{\mathrm{Vec}}} \left(\log(\boldsymbol{g}_{fc,i}^{-1}\boldsymbol{g}_i)\right)^\vee \in \mathbb{R}^{6m_f}$, the fixed constraint vector;
- $\boldsymbol{G}_a(\boldsymbol{q}) = \underset{i=1}{\overset{N}{\mathrm{Vec}}}(\boldsymbol{p}_{a,i} - \mathbf{U}\boldsymbol{g}_{c,i}\mathbf{A}) \in \mathbb{R}^{6m_a}$, the articulated constraint vector;
- $\boldsymbol{E}_c(\boldsymbol{\lambda}_c) = \int_0^L \boldsymbol{\Psi}^\top \begin{bmatrix} D^*\mathbf{C}_n \\ -W^*\mathbf{C}_t \end{bmatrix} \boldsymbol{\Psi} \mathrm{ds} \in \mathbb{R}^{3(m+1)\times 3(m+1)}$, the collision contact constraint matrix;

We have derived the dynamics of the EA considering contact, as delineated in equations (3.49) to (3.52). This set of equations constitutes a DAE system. For simulation purposes, to solve the aforementioned DAE system, it is necessary to discretize it in time domain. In the following chapters, we will introduce the method of time stepping to solve this DAE system.

3.5.5 Time discretization

Time-stepping is a prevalent technique employed for the time discretization of dynamic systems. It has gained significant popularity in the field of robotics for simulation and control purposes. Following the same framework of time discretization mentioned in in Section 2.5, considering a time interval $\left[t_{k-1}, t_k\right]$ and denoting $h = t_k - t_{k-1}$ as the time step, for the explicit representation, the discritization of this time interval is given by:

$$\boldsymbol{q}_k = \boldsymbol{q}_{k-1} + h\dot{\boldsymbol{q}}_{k-1} \ , \ \dot{\boldsymbol{q}}_k = \dot{\boldsymbol{q}}_{k-1} + h\ddot{\boldsymbol{q}}_{k-1}$$

For the implicit representation, the discritization of this time interval is given by:

$$\boldsymbol{q}_k = \boldsymbol{q}_{k-1} + h\dot{\boldsymbol{q}}_k \ , \ \dot{\boldsymbol{q}}_k = \dot{\boldsymbol{q}}_{k-1} + h\ddot{\boldsymbol{q}}_k$$

In our work, we use the implicit representation to ensure convergence of the solution. By taking the implicit equations to (3.49) and using the abbreviation $\widehat{\boldsymbol{M}} = \boldsymbol{M} + h\boldsymbol{C}$, one can get:

$$\mathscr{L}(\dot{\boldsymbol{q}}_k, \boldsymbol{q}_k) = \widehat{\boldsymbol{M}}\dot{\boldsymbol{q}}_k - \boldsymbol{M}\dot{\boldsymbol{q}}_{k-1} - h\boldsymbol{K}\boldsymbol{q}_k - h\boldsymbol{P}$$

Denoting

$$\mathscr{F}(\boldsymbol{q}_k, \boldsymbol{\lambda}_c, \boldsymbol{\lambda}_f, \boldsymbol{\lambda}_a) = \boldsymbol{P} + \boldsymbol{H}_c\boldsymbol{\lambda}_c + \boldsymbol{H}_f\boldsymbol{\lambda}_f + \boldsymbol{H}_a\boldsymbol{\lambda}_a$$

the implicit time discretization of (3.49)-(3.52) is replaced by the following nonlinear algebraic equations:

$$\begin{cases} \mathscr{L}(\dot{\boldsymbol{q}}_k, \boldsymbol{q}_k) - h\mathscr{F}(\boldsymbol{q}_k, \boldsymbol{\lambda}_c, \boldsymbol{\lambda}_f, \boldsymbol{\lambda}_a) = \mathbf{0} & \text{(3.53a)} \\ \boldsymbol{q}_k - h\dot{\boldsymbol{q}}_k - \boldsymbol{q}_{k-1} = \mathbf{0} & \text{(3.53b)} \\ \boldsymbol{G}_c(\boldsymbol{q}_k, \dot{\boldsymbol{q}}_k) - \boldsymbol{E}_c\boldsymbol{\lambda}_c = \mathbf{0} & \text{(3.53c)} \\ \boldsymbol{G}_f(\boldsymbol{q}_k) = \mathbf{0} & \text{(3.53d)} \\ \boldsymbol{G}_a(\boldsymbol{q}_k) = \mathbf{0} & \text{(3.53e)} \end{cases}$$

The unknown variables in the algebraic equations (3.53) consist of $\boldsymbol{q}_k$, $\dot{\boldsymbol{q}}_k$, $\boldsymbol{\lambda}_c$, $\boldsymbol{\lambda}_f$, and $\boldsymbol{\lambda}_a$. Notably, we directly define the normal contact force and friction force on the manifold of $\boldsymbol{\lambda}_n$ and $\boldsymbol{\lambda}_t$. An essential advantage of our method lies in the provision of a smooth system of nonlinear algebraic equations. Consequently, these equations can be solved using widely used techniques such as the gradient method or the Newton-Raphson method.

Integrating the collision detection algorithm from Section 3.3, once the potential contact points are identified, we can establish the contact dynamics equations. Then, using the time stepping method, we can compute the current state of the soft slender rod (EA), facilitating the simulation. In the upcoming chapters, we will introduce the simulation aspect, including a summary of the simulation algorithm, simulation results, parameter discussions, and model validation.

3.6 Simulation

In this section, we have configured various simulation scenarios with the objective of comparing our method to others and analyzing the influence of different model parameters on simulation outcomes. All simulations were conducted within the Matlab environment with CPU Intel(R) Core(TM) i7-7820HQ @2.90GHz.

3.6.1 Simulation Algorithm

The following steps outline the intricate process of simulating contact dynamics, from initializing the system's state to the iterative resolution of dynamics.

1. **Initialization of system state:** Define the initial conditions of the system, including the initial general coordinates $\boldsymbol{q}$ and $\dot{\boldsymbol{q}}$, and external force $\boldsymbol{\Lambda}_e$.

2. **Time stepping:** Decide on a time step for the simulation h.

3. **Geometry and kinematics update:** Update the Geometry and kinematics of soft slender rod via the generalized coordinates $(\boldsymbol{\phi}, \boldsymbol{\theta})$ and $(\dot{\boldsymbol{\phi}}, \dot{\boldsymbol{\theta}})$, including its configuration, velocity and Jacobian matrix of kinematics (Refer to Section 2.2.5.4 and Section 2.2.6.2).

   - Update strain field:
   $$\boldsymbol{\xi}(s) = \boldsymbol{\xi}_0 + (s)\boldsymbol{\theta}, \ \forall s \in [0, L] \tag{3.54}$$
   - Update configuration field:
   $$\boldsymbol{g}_0 = \begin{bmatrix} \exp \tilde{\boldsymbol{\phi}} & \boldsymbol{p}_0 \\ \mathbf{0} & 1 \end{bmatrix} \tag{3.55}$$
   $$\boldsymbol{g}'(s) = \boldsymbol{g}(s)\widehat{\boldsymbol{\xi}}(s), \ \forall s \in [0, L] \tag{3.56}$$
   - Update Jacobian matrix:
   $$\boldsymbol{J}_{\boldsymbol{\alpha}} = \begin{bmatrix} \boldsymbol{R}_0^{\top}(\boldsymbol{\phi})\boldsymbol{J}_l(\boldsymbol{\phi}) & \mathbf{0} \\ \mathbf{0} & \boldsymbol{R}_0^{\top}(\boldsymbol{\phi}) \end{bmatrix}, \ \boldsymbol{J}_0 = \begin{bmatrix} \boldsymbol{J}_{\boldsymbol{\alpha}} & \mathbf{0}_{6\times 6(n+1)} \end{bmatrix} \tag{3.57}$$
   $$\boldsymbol{J}(s) = \boldsymbol{J}_0 + \mathrm{Ad}_{\boldsymbol{g}(s)}^{-1} \int_0^s \mathrm{Ad}_{\boldsymbol{g}(x)} \boldsymbol{\Phi}(x) \mathrm{dx}, \ \forall s \in [0, L] \tag{3.58}$$

4. **Collision detection:** Detect potential collisions or contacts between objects in the simulation. Refer to Section 3.3.1.

5. **Contact constrains:** Formulate all contact constraints. Refer to Section 3.5.1.2.

6. **Contact dynamics:** Formulate the dynamics equations with contact constraints. Refer to Section 3.5.4.

$$\boldsymbol{G}_f = \mathbf{0} \tag{3.59}$$

$$\boldsymbol{G}_a = \mathbf{0} \tag{3.60}$$

$$\boldsymbol{\Lambda}_c - (\mathbf{B}_n^\top D\mathbf{C}_n + \mathbf{B}_t^\top W\mathbf{C}_t)\boldsymbol{u} = \mathbf{0} \tag{3.61}$$

$$\mathbf{P}\boldsymbol{g}_{cd}\mathbf{A} + D^*\mathbf{C}_n\boldsymbol{u} = 0 \tag{3.62}$$

$$\mathrm{Ad}_{\boldsymbol{g}_{cb}}\boldsymbol{\eta} - \mathrm{Ad}_{\boldsymbol{g}_{cd}}\boldsymbol{\eta}_d - W^*\mathbf{C}_t\boldsymbol{u} = \mathbf{0} \tag{3.63}$$

7. **Integration of contact dynamics:** Formulate the contact dynamics as nonlinear equations in each time step using the implicit Euler method. Refer to Section 3.5.5.

$$\mathscr{L}(\dot{\boldsymbol{q}}_k, \boldsymbol{q}_k) - h\mathscr{F}(\boldsymbol{q}_k, \boldsymbol{\lambda}_c, \boldsymbol{\lambda}_f, \boldsymbol{\lambda}_a) = \mathbf{0} \tag{3.64}$$

$$\boldsymbol{q}_k - h\dot{\boldsymbol{q}}_k - \boldsymbol{q}_{k-1} = \mathbf{0} \tag{3.65}$$

$$\boldsymbol{G}_c(\boldsymbol{q}_k, \dot{\boldsymbol{q}_k}) - \boldsymbol{E}_c\boldsymbol{\lambda}_c = \mathbf{0} \tag{3.66}$$

$$\boldsymbol{G}_f(\boldsymbol{q}_k) = \mathbf{0} \tag{3.67}$$

$$\boldsymbol{G}_a(\boldsymbol{q}_k) = \mathbf{0} \tag{3.68}$$

8. **Resolution:** Using the nonlinear solver such as Newton method to solve the nonlinear equations in step 7. After each iteration of nonlinear solver, repeat step 3 to 5 for updating.

9. **Loop back:** Get the states of system and return to step 3. Repeat the process for the next time step until the end of the time interval is reached.

3.6.2 Influence of friction

3.6.2.1 Internal contact

In this test, we insert a soft rod (blue) of length L = 26mm inside a rigid tube (red) along axis x. The diameter of soft rod is 0.3mm at tip and 0.2mm at end. The radius of curvature of the tube is 3mm. The Young modulus of soft rod is 55MPa and Poisson ratio is 0.45. Fig. 3.15 shows the final state of insertion with different friction coefficients. The figure on the right side shows that the soft rod fails to be inserted and sticks inside the tube due to the large friction $\mu = 0.5$, while the figure on left side shows the successful insertion with $\mu = 0.2$. Fig. 3.16 shows the evolution of the norm of the constrained force $\boldsymbol{\Lambda}_b$ at tip with respect of the insertion displacement. The total insertion time is 70 seconds, while the simulation time is 156 seconds. We repeated this experiment in the Finite Element Method (FEM) software SOFA, with a consistent time step, resulting in a computational time of 722 seconds. Compared to the FEM algorithm, our method significantly accelerates computation speed due to its lower system dimensionality.

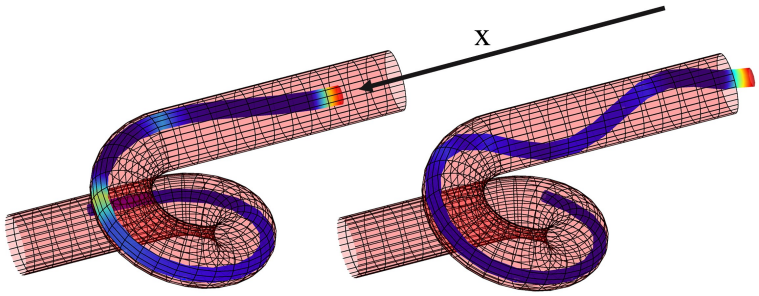

Figure 3.15: Fictional contact in a curved tube. Successful case(left) and buckling case(right). Implicit time step of simulation dt $= 0.05s$. Number of sections: $n = m = 26$. The color shows the contact of rods, which gradually increases from blue to red.

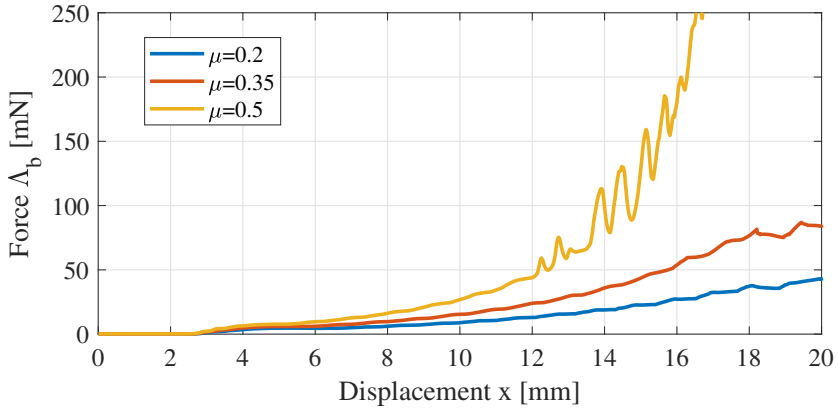

Figure 3.16: The evolution of insertion force with different coefficient of friction.

3.6.2.2 External contact

In this test, we throw a soft rod (blue) towards a rigid obstacle (red). The soft rod is initially positioned horizontally above the obstacle. The length of the soft rod is 30cm and its diameter of two side of are 0.3cm and 0.2cm respectively. The Young modulus of soft rod is 55MPa and Poisson ratio is 0.45. As shown in Fig. 3.17, we test the impact with different coefficient of friction. When the coefficient of friction is small, the soft rod cannot stay on the rigid rod after the collision occurs because there is not enough friction to resist the asymmetrical gravity. Meanwhile, if we increase the coefficient of friction, the soft rod will not slide down.

3.6.3 Comparison with different modeling methods

In this experiment, a soft slender rod comes into contact with external obstacles and naturally sags under the influence of gravity. The soft slender rod is 60cm long with Young's modulus of 3×10^5Pa. We investigate the impact of different existing approaches in the literature on contact behavior, comparing with our proposed method. We compare three discretization strategies: Piecewise Constant Strain (PCS), Global Variable Strain (GVS), and the Piecewise Linear Strain (PLS) that we are using in this work. Subsequently, we utilize Comsol, a general finite element method (FEM) software, to determine the equilibrium position of the soft slender rod,

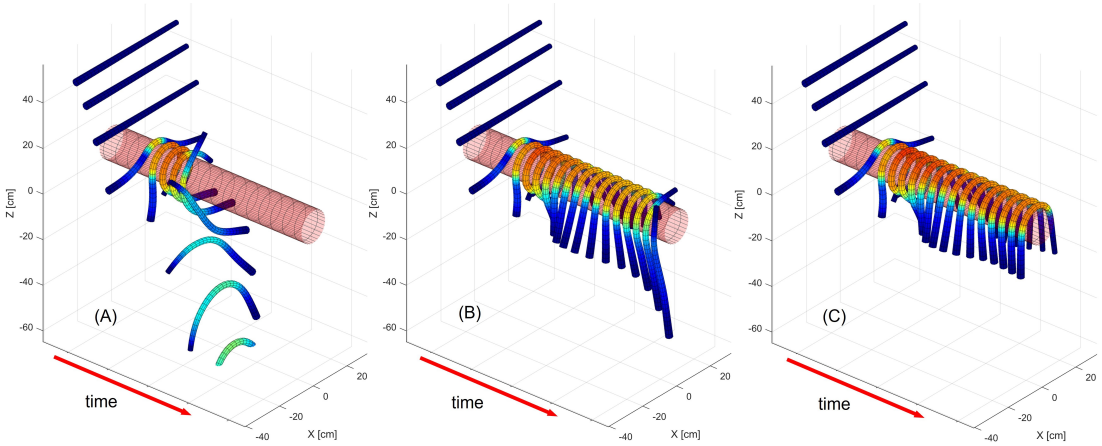

Figure 3.17: Fictional contact under gravity. The configuration of soft rod is plotted every $0.15s$. Number of sections: $n = m = 30$. (A). friction coefficient $\mu = 0$; (B). friction coefficient $\mu = 0.1$; (C). friction coefficient $\mu = 0.2$. Implicit time step of simulation dt $= 0.005s$. The color shows the internal force of rods, which gradually increases from blue to red.

which is used as the reference. The spatial discretization in the Finite Element Method (FEM) employs quadrilateral mesh elements, dividing the rod into 820 elements along the arc axis. The contact algorithm in FEM is implemented using the augmented Lagrangian method. The FEM simulation result is used as the position reference and PLS (divided into 30 sections) is used as the strain reference, comparing with the outcomes of PLS (divided into 5 sections), PCS (divided into 6 sections), and GVS (5th-order polynomial). Except of FEM, all simulations were conducted using the same set of physical parameters and solver.

Table 3.1 presents the errors of different discretization strategies compared to the reference (PLS with 30 sections). These errors encompass both strain (curvature along Y-axis) and position discrepancies along the arc length, defined as follows:

$$e_{\kappa_Y} = \frac{1}{L}\int_0^L |\kappa_Y(s) - \kappa_{Yref}(s)|\mathrm{ds}, \quad e_{\boldsymbol{p}} = \frac{1}{L}\int_0^L \|\boldsymbol{p}(s) - \boldsymbol{p}_{ref}(s)\|\mathrm{ds}$$

Table 3.1: Error of different discretization strategies

Modeling method	DOF	Strain error	Position error
FEM (800 elements)	2460	-	-
PCS (6 sections)	36	0.027 cm^{-2}	0.721 cm
GVS (5 orders)	36	0.026 cm^{-2}	0.941 cm
PLS (5 sections)	36	0.014 cm^{-2}	0.262 cm
PLS (30 sections)	186	-	0.047 cm

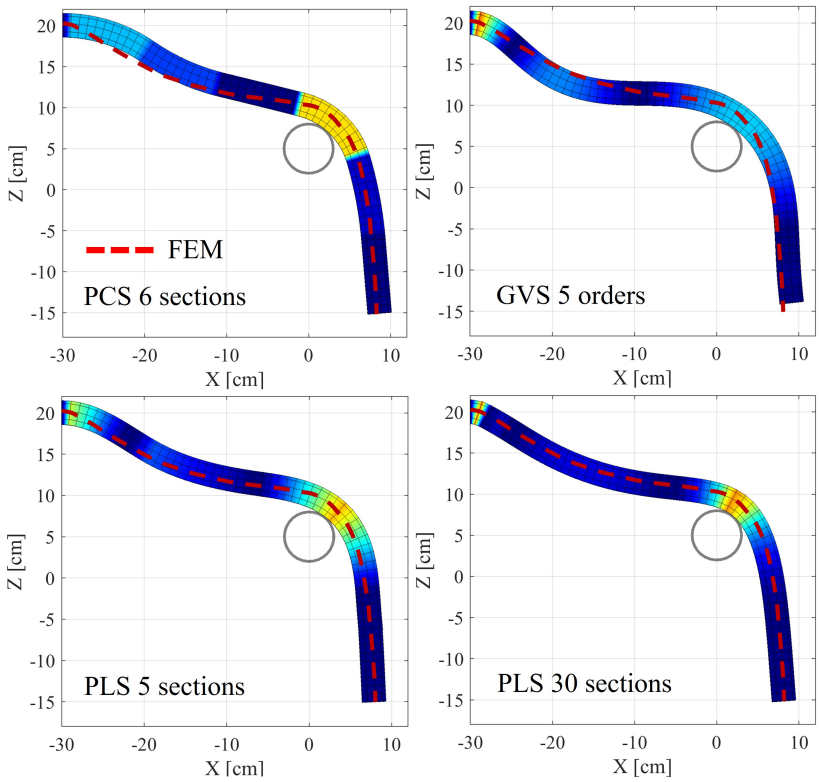

Figure 3.18: A soft rod naturally droops under the action of gravity and contacts with external obstacles.The figure shows the static results obtained using different modeling methods: FEM, PCS, GVS and PLS. The color shows the norm of strain of rods, which gradually increases from blue to red.

The result distinctly reveals that, with an equal degree of freedom, PLS achieves the highest accuracy. This is attributed to the superior local interpolation capabilities of linear interpolation.

Fig. 3.18 showcases the deformation of the soft rod. Due to its constant curvature limitation, PCS necessitates fine discretization for accurately capturing local deformation during contact. Although polynomial interpolation offers continuous differentiability in strain, achieving precise fitting of the contact area's deformation demands an increase in polynomial order. However, high-order polynomials are susceptible to the Runge phenomenon, leading to localized strain distortion and oscillation, thereby challenging the robustness of simulations. In regions with significant local deformation and substantial strain variations, such as the left end of the soft rod and areas in contact with external objects, PLS exhibits superior fitting capabilities. Moreover, The computational results of PLS with 30 sections are closer to the FEM reference compared to the PLS with 5 sections. This observation highlights that, with increasingly precise discretization, computational results converge toward the true values. Fig. 3.19 illustrates the evolution of strain along the arc length of the soft rod for each test.

In summary, in contact scenarios, PLS demonstrates superior accuracy when compared to PCS and GVS with an equivalent degree of freedom. Significantly, as the segmentation of PLS becomes finer, computational results tend to converge, closely aligning with FEM outcomes.

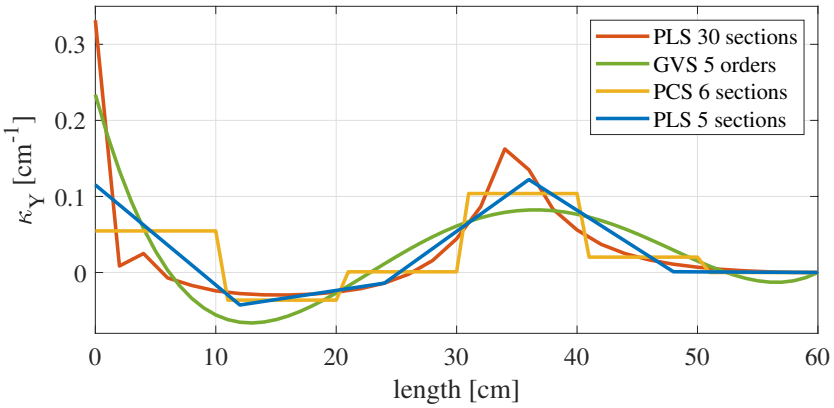

Figure 3.19: The evolution of strain along arc length of soft rod.

3.6.4 Influence of discritization

In this subsection, we compare and analyze the impact of different discretization strategies on the computational results of our model. Specifically, we investigate the case of two intertwined rods initially positioned in a crossed configuration. The rods are then simultaneously twisted, resulting in mutual entanglement until a total twist angle of 540 degrees is reached, as shown in Fig. 3.20. We conduct several tests to examine the effects of different discretization strategies.

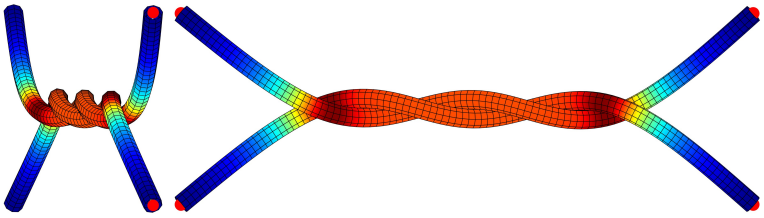

Figure 3.20: Two rods entangled with each other. The color shows the internal force of rods, which gradually increases from blue to red.

Specifically, we fix the number of discrete sections (m) for the contact field and vary the number of discrete sections (n) for the strain field. As shown in Fig. 3.21, we compare the results obtained from different discretization strategies on the contact load. This analysis allows us to understand the trade-offs between accuracy and computational efficiency in our model. Through this comparative analysis, we aim to identify the optimal discretization strategy that balances computational efficiency with accurate representation of the physical phenomena involved in the entanglement process. The insights gained from this analysis will contribute to refining our model and enhancing its predictive capabilities.

From Fig. 3.21, it can be observed that when the number of contact points remains constant, the discretization of the strain field affects the distribution of contact forces. With fewer sections in the strain field, the distribution of contact forces exhibits larger fluctuations. As the strain field is more finely discretized, the distribution of contact forces becomes smoother and the results tend to converge. Therefore, further discretization is meaningless at this point.

Fig. 3.22 shows that when the number of sections in the strain field remains constant,

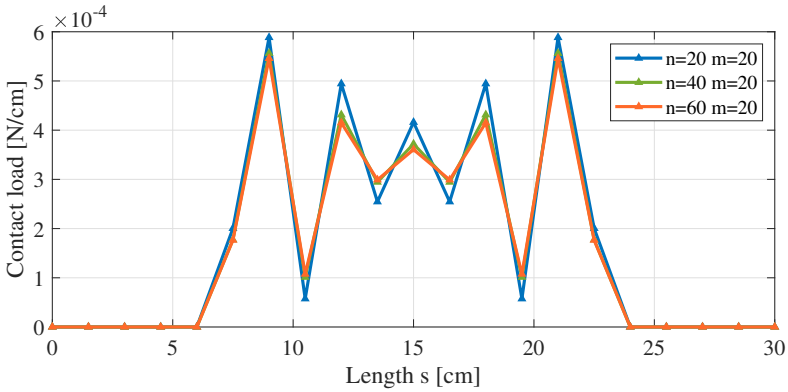

Figure 3.21: The influence of different number of section for strain interpolation on the distribution of contact load.

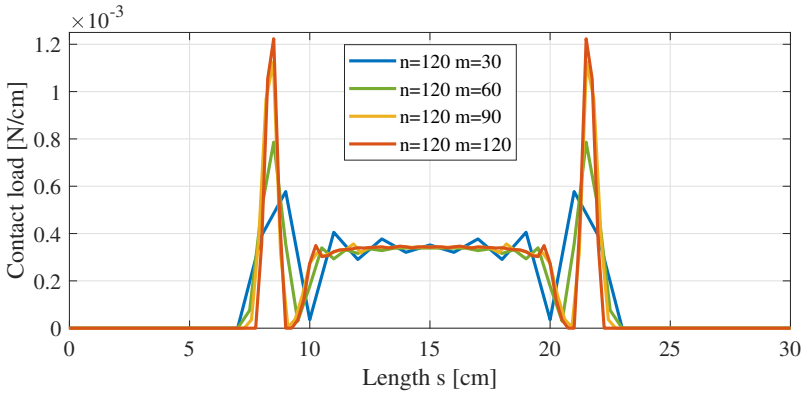

Figure 3.22: The influence of different number of section for contact interpolation on the distribution of contact load.

increasing the number of section of contact field leads to smoother distribution of contact forces and the results tend to converge.

Based on the above results, we can conclude that the ratio between the discretization of the strain field and the contact field is a key factor influencing computational efficiency. When the number of contact points remains constant, excessively fine discretization of the strain field does not significantly affect the computed contact forces. Additionally, the strain field should be discretized more finely than the contact field to ensure that the soft slender rod has enough degrees of freedom to satisfy the contact constraints.

By considering these findings, we can optimize the discretization strategy for our model, achieving a balance between computational efficiency and accuracy in predicting the contact forces and capturing the overall behavior of the soft rod system.

3.6.5 Choice of smooth function

In Section 3.4.5, we mentioned that the Heaviside function used to construct the complementarity conditions can be approximated or equivalently represented by other continuous or smooth

functions. Through simulations, we will explore the influence of different approximation functions on the solution results. Fig. 3.23 illustrates the case of a homogeneous tapered slender rod placed on a plane. In the initial state, the left end of the slender rod is suspended and fixed by a constraint force, while the right end contacts the ground under the influence of gravity. The slender rod has a length of 30cm, density of $3 \times 10^3 \mathrm{kg/m}^3$, Young's modulus of 1Mpa and friction coefficient of 0.5. After the initial state, the left end of the slender rod is released and starts to fall until it collides with the ground, reaching a final equilibrium state. Fig.3.23 shows the steady states obtained using the impact function and different smoothing functions. In all three test groups, the strain field of the slender rod is divided into 30 sections, as well as the contact field. From the distribution of contact loads shown in Fig. 3.23, it can be observed

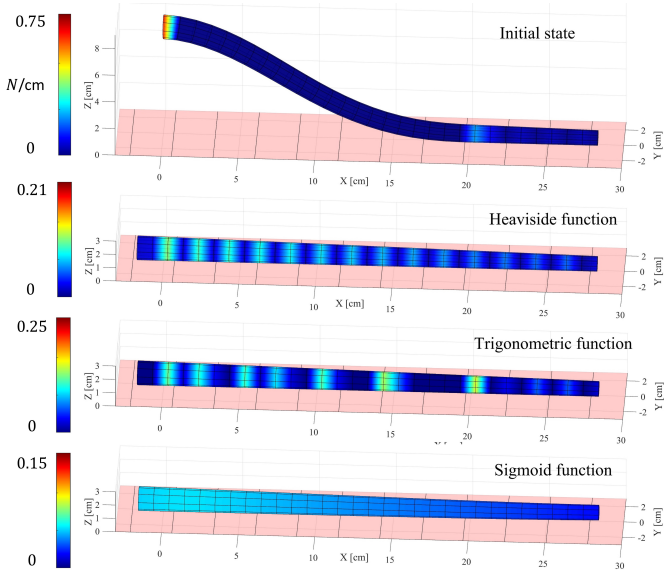

Figure 3.23: Final steady state calculated using different functions. The colors in the plot represent the contact load distribution.

that for the Heaviside function and trigonometric function, which satisfy the complementarity constraints exactly, although the slender rod is in a force-balanced state and remains stationary, not all contact points are activated but some contact points are in a critical state (virtual contact). In this case, due to the discretization of the system, the solution of the mechanical equation system is not unique. For the Heaviside function, as shown in Fig.3.24, the contact force undergoes small jumps during the iteration process, which is also due to the presence of virtual contacts. Since the slack variables associated with virtual contacts are zero, the Heaviside function is discontinuous, resulting in numerical jumps during the iteration. However, this does not occur for the trigonometric function, which remains smooth and continuous. Among the three simulations, the sigmoid function yields results closest to the real solution. As shown in Fig. 3.23, the contact load is smoothly distributed and remains stable during the iteration process. This is because the sigmoid function is an approximation of the complementarity constraint. In this case, there are no virtual contacts where both the contact gap and contact force are zero, and therefore, all contact points are activated, yielding a unique solution.

Based on these findings, we conclude that approximating the impact function with trigonometric functions can address the issue of numerical jumps in critical states. However, in some cases, non-uniqueness of solutions may arise. On the other hand, using the sigmoid function,

although it cannot precisely satisfy the complementarity constraint in the vicinity of critical states, offers better robustness.

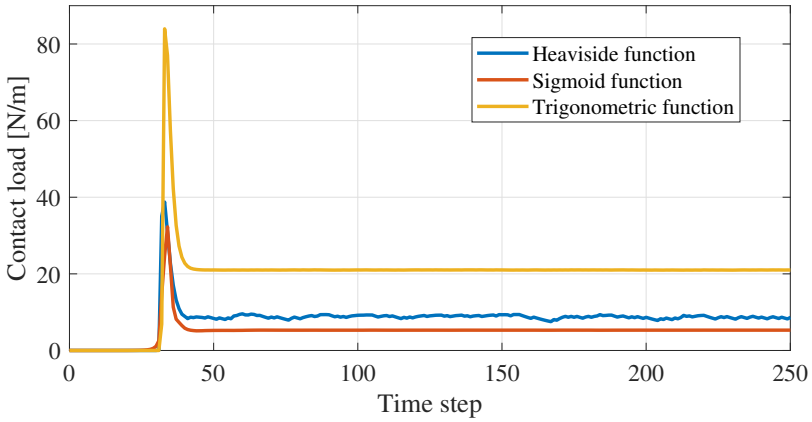

Figure 3.24: Evolution of contact loads over time step iterations. The point of contact is 6 cm from the left end. The time step is set as $0.01s$.

3.7 Experiment towards Cochlear Implantation

The primary aim of our model simulation is to forecast the deformation and contact forces of the implant during the implantation procedure, with the goal of examining the impact of various parameters on this process. To this end, our approach in this section is twofold:

1. Firstly, we validate the model's accuracy via comparative experiments. We establish experimental groups that involve inserting the cochlear implant at varying angles. The deformation and contact forces of the implant are then monitored and compared across both the experimental and simulation processes. This comparative analysis is crucial for verifying the congruence between our simulation results and the actual experimental outcomes.

2. Secondly, our analysis delves into the dynamics of the forces acting on the implant throughout the simulation. We investigate the key factors influencing these forces to gain a deeper understanding of the implantation process's evolution laws. This comprehensive analysis not only reinforces the accuracy of our model but also provides valuable insights into the mechanics of cochlear implantation.

3.7.1 Experiment setup

In the experimental phase of this study, we employed a scaled resin 3D model, provided by OTICON Medical, as a substitute for the actual cochlea. The experimental setup, as depicted in Fig. 3.25, comprised several key components: a model of the cochlea, a base for securing the cochlea, a six-degree-of-freedom force sensor, a Collin implant robot, and the implant available at Pasteur Institute.The parameters of implant are shown in Tab. 3.2.

During the implantation process, the implant is fixed on the probe of the robot end effector, and the doctor manually controls the six degrees of freedom motion of the probe, including

Table 3.2: Experimental parameters of cochlea implant

Length L	25mm	End diameter	0.3mm
Young's modulus	25.2Mpa	Front diameter	0.4mm

rotation and translation, through a remote sensing device. The cochlea is fixed on the base, and a six-degree-of-freedom force sensor (NANO17 - ATI Industrial Automatization) which can resolve down to 0.318 gram-force is installed at the bottom of the cochlea placement. This sensor is used to measure the force acting on the cochlea during the implantation process.

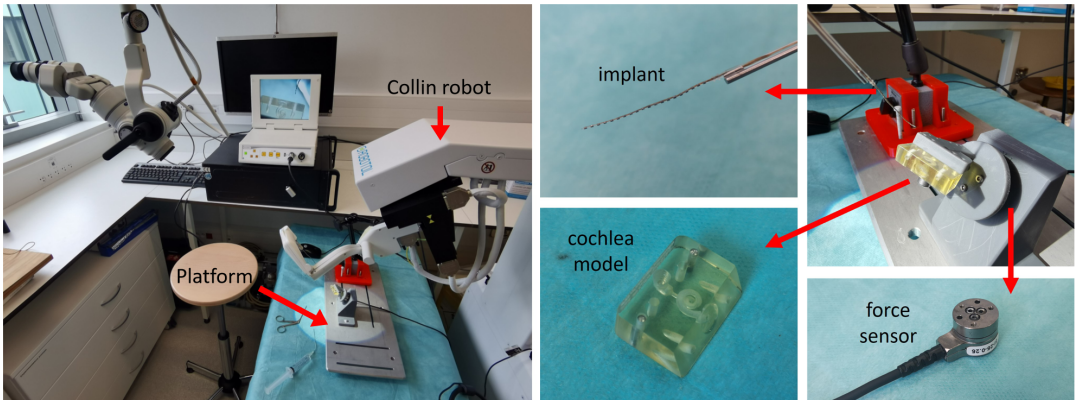

Figure 3.25: Experiment setup.

3.7.2 Insertion with different angles

Drawing upon a substantial corpus of clinical and experimental research, it has been established that the efficacy of cochlear implants is significantly influenced by the implantation angle [129][130]. This angle pertains to the orientation between the direction of implantation and the cochlear entrance. To ascertain the precision of our model, we meticulously crafted a series of simulations and experiments across various implantation angle scenarios. These scenarios were systematically designed to comprehensively evaluate the model's performance under different conditions. The results of these simulations and experiments are illustrated in Fig. 3.26.

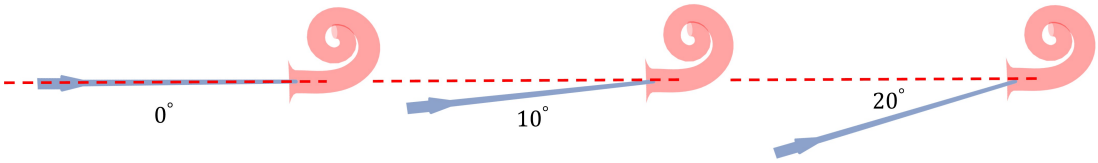

Figure 3.26: Insertion with different angles.

In our experimental setup, the movement of the implant's substrate is constrained within the transverse profile of the cochlea. The direction of its advancement is aligned with the insertion angle, defined in relation to the cochlear entrance. The force applied by the actuator substrate

to the implant, directed along this insertion angle, is referred to as the insertion force. For our experiments, we established three groups, each characterized by distinct insertion angles set at 0°, 10°, and 20° respectively.

This study primarily focuses on exploring how the insertion angle influences the cochlear implantation process. To isolate the variable of insertion angle, we standardized the implant's advancing speed at 1mm/s across all experimental runs. The implant was pushed forward consistently at this speed until it could no longer progress further inside the cochlea, at which point the insertion process was concluded. Throughout this procedure, both the deformation of the implant and the insertion force were meticulously monitored using a camera and a force sensor. These empirical observations were then systematically compared with corresponding model simulations to assess the model's fidelity and reliability.

3.7.3 Experimental result

In this section, we will present the results of our experiments and provide an analysis of these findings.The comparative diagrams of the implantation experiments and simulations at 0 degrees, 10 degrees, and 20 degrees are respectively shown in Fig. 3.27, Fig. 3.28, and Fig. 3.29.

3.7.3.1 Implantation process analysis

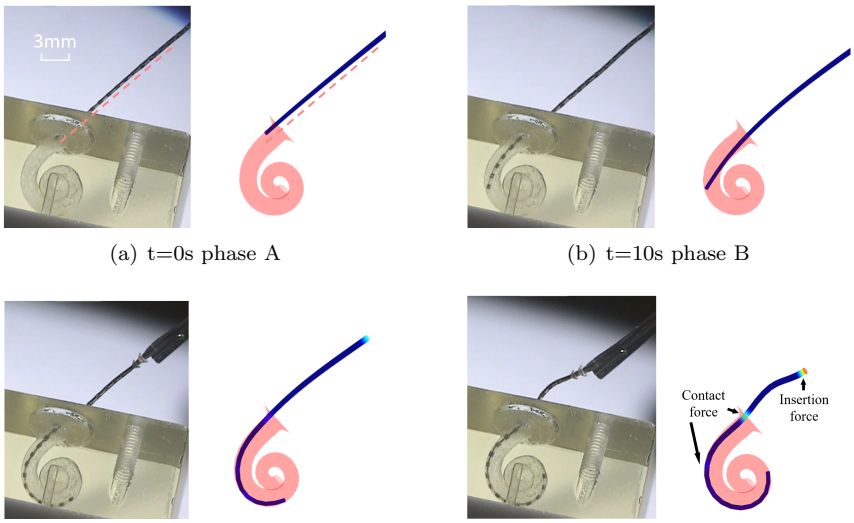

(a) t=0s phase A (b) t=10s phase B

(c) t=20s phase C (d) t=30s phase D

Figure 3.27: Insertion process of experiments and simulations of 0°.

The implantation process can be roughly divided into four stages based on the contact between the implant and the inner wall of the cochlea, as observed from both experiments and simulations. In the first stage, there is no contact or virtual contact between the implant and the inner wall of the cochlea, as shown in Fig. 3.27(a). During this stage, the contact force between the implant and the cochlea is negligible.

In the second stage, there is point contact between the implant and the inner wall, as shown in Fig. 3.27(b). As the implant is pushed forward, its tip touches the inner wall of the cochlea

and slides along it. The implant undergoes deformation due to the contact, but it does not conform to the wall. The contact between the implant and the inner wall is in the form of discrete points.

When the implant deformation is sufficient to conform to the inner wall, the third stage is entered, characterized by continuous line contact, as shown in Fig. 3.27(c). During this stage, a portion of the implant comes into close contact with the inner wall, and the previous point pressure is distributed as line pressure. The friction force also increases with the contact area. As the implant continues to be pushed forward, the radius of the cochlea decreases, leading to an increase in the elastic force, which requires a greater pushing force to maintain the deformation of the implant. Additionally, as the contact area increases, the friction force also gradually increases, leading to an increase in the resistance to pushing. These two factors cause the pushing force to increase exponentially with the pushing distance.

When the cross-sectional stiffness of the implant is insufficient to support the pushing force, buckling occurs, and the implant undergoes significant deformation and bending in the suspended section. At the same time, the contact plane between the implant and the cochlea and the angle between the contact plane and the pushing force change, causing some of the frictional contact to enter a self-locking state. The contact portion of the implant is stuck and cannot continue to move forward, and this is the fourth stage, as shown in Fig. 3.27(d).

The same process mentioned above can also be observed in experiments and simulations with 10-degree and 20-degree implantations, as shown in Fig. 3.28 and Fig. 3.29.

3.7.3.2 Performance of the model

We assess the precision of our model from four key perspectives: the deformation of the implant, the interaction between the implant and the cochlea's inner wall, the magnitude of the pushing force (which equates to the contact force), and the potential for buckling occurrences. The experimental findings indicate a high degree of correlation between the model and actual implantation procedures. Throughout the implantation process, the implant's deformation in the simulation closely mirrors that observed in physical experiments. Moreover, our model adeptly captures the contact dynamics between the implant and the cochlea's inner wall, accurately replicating both the discrete point contact in phase B and the continuous line contact in phase C.

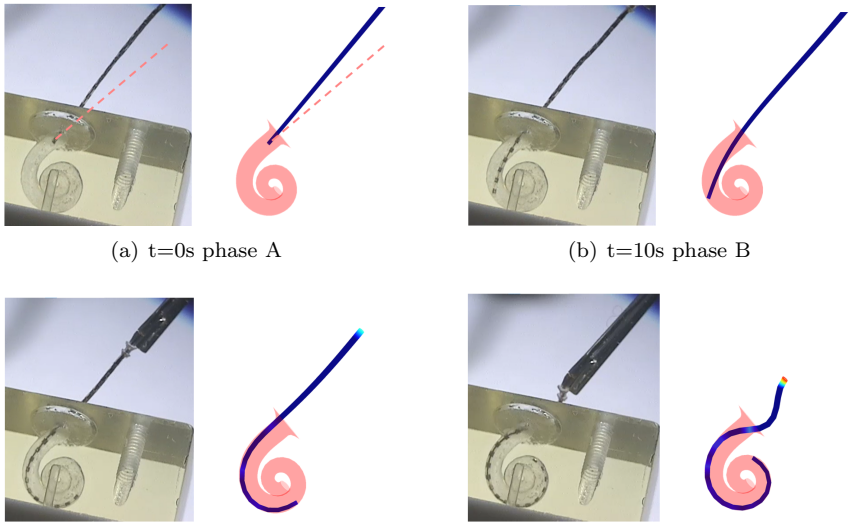

(a) t=0s phase A (b) t=10s phase B

(c) t=20s phase C (d) t=35s phase D

Figure 3.28: Insertion process of experiments and simulations of 10°.

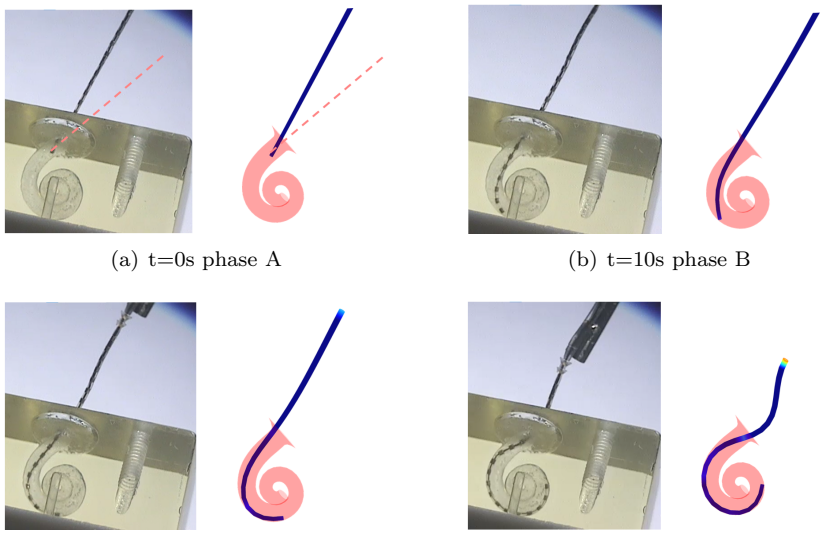

(a) t=0s phase A (b) t=10s phase B

(c) t=20s phase C (d) t=30s phase D

Figure 3.29: Insertion process of experiments and simulations of 20°.

Significantly, the model demonstrates a precise ability to predict the onset of buckling and accurately tracks the progression of this deformation (phase D). To quantify the model's accuracy regarding insertion force, we introduce the Integrated Mean Error (IME) as a metric,

which measure is defined as follows:

$$\text{IME} = \int_0^T |\frac{F_{epm} - F_{sml}}{F_{epm}}|\text{dt}$$

Fig. 3.30 shows that the simulated pushing force can fit well with the evolution of the real pushing force in the experimental process, with IME $< 20\%$.

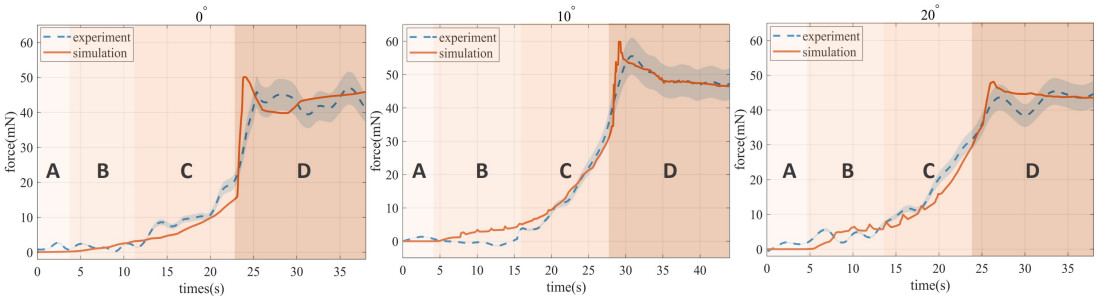

Figure 3.30: The insertion force of experiments and simulations.

3.7.3.3 Influence of the insertion angle

Insights gleaned from both the experimental and simulation phases of our study reveal that the insertion angle notably influences the timing at which the implant enters the locking phase D. In the course of conducting our three experimental trials, we determined that an optimal insertion angle of 10 degrees facilitates the deepest insertion depth. It is crucial to recognize that the ideal insertion angle for cochlear implants varies. This variation is influenced by the specific geometric structure of each cochlea and the physical properties of the implant, such as its stiffness and size. Therefore, accurately identifying the most suitable insertion angle through sophisticated simulation techniques before the actual implantation process is essential. These simulations are key to optimizing the implantation procedure for individual cases and also for optimizing the inertion control which will be discussed in Chapter 4.

3.8 Conclusion

In this chapter, we have developed an innovative contact dynamics model for EA and soft slender rod as well, firmly grounded in the Cosserat theory. This model meticulously addresses the complex geometric relationships, forces, and moments at the contact points, enabling a comprehensive analysis of contact and frictional forces and their influence on the dynamics of EA. This approach is particularly significant when considering the applications to cochlear implants, where such detailed analysis is crucial for the success of implantation procedures.

The formulation of contact constraints has been a cornerstone of our model, accounting not only for non-penetration and force equilibrium but also for the intricate frictional interactions at contact interfaces. By reconstructing these constraints into equality constraints and smoothing the non-smooth aspects, we have enabled the direct solution of the contact dynamics system using general-purpose numerical methods like Newton's method. This enhances the robustness and applicability of our approach, especially in the context of cochlear implants, where precision and reliability are paramount.

The integration of Cosserat theory into our model marks a significant advancement in understanding the contact interactions of soft robots, including cochlear implants. The proposed

model for cochlear implant contact during implantation has been validated against experimental results, demonstrating its accuracy and reliability. This is particularly beneficial for simulating and analyzing the behavior of cochlear implants during the implantation process, leading to improved design and control strategies for these delicate medical devices.

In summary, our contact dynamics model, based on Cosserat theory, offers an essential framework for studying and simulating the contact interactions of EA during cochlear implantation. This model is especially crucial for enhancing cochlear implant simulations and control systems. It significantly aids in designing and operating these complex medical devices. Our research paves new paths for cochlear implant technology and its various applications. Building on the simulated framework of the cochlear implantation, the next chapter will focus on introducing a model-based control algorithm for the implantation process.

Chapter 4

Control of Cochlear Implantation

4.1 Introduction

In Chapters 2 and 3, we provided detailed descriptions of all physical models related to the implantation process of active cochlear implants. This includes the mechanical model of the Electrode Array (EA), the electrical model of the Conducting Polymer Actuator (CPA), and the contact model between the EA and the cochlea. With these models, we are now equipped to simulate the entire implantation process and predict changes in physical quantities, including the deformation of the EA, the implantation force at the base, and the contact force between the EA and the cochlea. In the first chapter, we discussed some challenges that arise during implantation, such as internal friction within the cochlea and incorrect implantation directions, which can lead to failure or incomplete implantation. In this chapter, based on our constructed models, we design control algorithms to overcome these issues. By controlling the implantation trajectory of the base and utilizing the CPA to generate active deformations, we aim to achieve a complete and successful implantation.

The cochlear implantation process, however, presents several technical challenges:

1. Placement Accuracy: Achieving the correct placement of the cochlear implant is essential. Misplacement may lead to inadequate stimulation of the auditory nerves, culminating in suboptimal hearing restoration.

2. Cochlear Integrity: The risk of mechanical damage to the cochlea during implantation is a concern, with potential harm to delicate structures like the basilar membrane, which could impair hearing outcomes.

3. Contact Force Management: The force exerted during implant insertion must be carefully controlled. Excessive force can cause trauma and damage to the cochlea's sensitive internal structures.

4. Implant Deformation: The risk of implant bending or deformation during insertion, potentially causing additional cochlear damage and complicating electrode positioning.

5. Implantation Angle: The angle of implantation is a critical factor, influencing the forces exerted on the cochlear walls. Improper angles can exacerbate mechanical trauma and lead to postoperative complications.

This chapter transforms these clinical challenges into optimization problems, crafting optimal control solutions for various implant types. Through simulations and empirical studies,

we demonstrate that these tailored control strategies effectively meet the outlined objectives, mitigating the common challenges encountered during cochlear implantation.

4.2 Control Objective

In traditional cochlear implant surgeries, manual implantation methods often place high demands on the surgical skills of the otologist. This not only requires the surgeon to have extensive clinical experience but also introduces significant uncertainty in the success rate due to variations in cochlear dimensions among different patients. Using a robotic arm for assistance can mitigate the impact of human factors; however, traditional robotic implantation typically involves inserting the implant along a constant angle. Therefore, determining the implantation angle becomes a crucial issue. In Section 3.6.2 and Section 3.7.3 of Chapter 3, we observed that the success rate and depth of implantation are influenced by various factors, including the insertion angle, cochlear dimensions, friction, and more. To address these challenges, introducing control during the implantation process is necessary. In this section, we will firstly define the control objectives for cochlear implantation:

The objective of the control is to improve the success rate of implantation, specifically by increasing the depth of implantation. The main factor affecting implantation depth during the procedure is the contact force between the implant and the cochlea. When this contact force exceeds a threshold that causes the implant to buckle, further insertion becomes impossible. Therefore, the essence of the control objectives is to ensure the advancement of the implant during the procedure while avoiding a sudden increase in contact force. For this analysis, we propose two control objectives:

1. The first objective is to minimize the contact force during the implantation process.
2. The second objective is to encourage the implant to advance along the spiral centerline of the cochlea, thereby minimizing the distance between the implant and the cochlear centerline.

It's important to note that the emphasis of the control objectives depends on the variables we can control. For passive implants, where there are no actuators within the implant, we can only control the orientation of the implant base. Therefore, tracking the cochlear spiral trajectory is not achievable, and the control objective is solely to reduce insertion force. Conversely, for active implants, we can use actuators to control the shape of the implant and bring it closer to the cochlear central spiral line. In this case, we can aim for both reducing insertion force and tracking the cochlear spiral trajectory. In an extreme scenario where actuators can provide enough torque to track the spiral trajectory perfectly, there would be minimal contact between the implant and the cochlea. In the following chapters, we will discuss each of these scenarios in detail.

4.3 Insertion Force Control (Passive Implant)

In cochlear implantation surgery, the precision of implant placement is paramount. Surgeons typically maneuver the implant into the patient's cochlea, a process requiring meticulous control over the implant's insertion direction. This careful insertion is crucial to minimize the contact force between the implant and the cochlea's inner wall, thereby reducing potential cochlear tissue damage. However, this process is fraught with challenges. One significant obstacle is the "self-locking" phenomenon, where the implant may cease to advance properly due to frictional

forces, becoming stuck inside the cochlea. This occurs when the contact point fails to slide even with increasing pushing force.

Complicating matters further, the implant's low stiffness often leads to buckling, adding complexity to the surgical procedure. In such instances, altering the current insertion direction becomes necessary to resolve buckling and facilitate the implant's progression within the cochlea. Typically, this delicate task is manually executed by the surgeon, often relying on their experience and intuition, assisted by machinery. However, to mitigate human error and increase the success rate of cochlear implantations, the adoption of automated, robot-assisted devices has become increasingly prevalent. The principal benefit of such robotization lies in its ability to follow a preprogrammed or real-time controlled implantation path. By strategically designing this path, it becomes possible to effectively circumvent stick and buckling phenomena, reducing the contact force exerted on the cochlear wall and thereby decreasing the risk of tissue damage.

To achieve these objectives, we have established an optimal path for the robotic device, focusing on two primary goals during the total insertion process:

1. Minimizing the contact force to protect the delicate cochlear structures.
2. Preventing self-locking phenomena, often caused by buckling and frictional forces.

The successful realization of these goals requires a nuanced understanding of the cochlear implant's mechanics. We have simplified the implant model into two primary components: the external and internal structures of the cochlea. The external structure is akin to a fixed beam, with one end anchored at the pushing base and the other hypothetically fixed at the cochlea's entrance. The internal structure, treated as a black box, responds to forces acting on the cross-section at the cochlear entrance. However, our path planning primarily targets the external structure, as the internal changes are inherently linked to it. Given the limited space within the cochlea and the implant's proximity to the inner wall, direct manipulation of the contact force inside the cochlea via base control is challenging. Therefore, our research predominantly focuses on the external structure, conceptualized as a beam with fixed ends, to optimize the implantation path.

4.3.1 Control variable

As shown in Fig. 4.1, the path of insertion is defined as the configuration of the end-effector of robot connecting the head of EA, which is defined by the configuration matrix $\boldsymbol{g}_0$, representing the orientation and position. Our strategy is to change this configuration matrix during the insertion in order to keep the insertion force in the forward direction as much as possible. To facilitate the calculation of the optimal path of the configuration of base in subsequent steps, we first need to parametrize the configuration matrix $\boldsymbol{g}_0$ using vector as the control variable. As we introduced in Section 2.2.5.1, $\boldsymbol{g}_0$ is composed of a rotation matrix $\boldsymbol{R}_0$ and a position vector $\boldsymbol{p}_0$:

$$\boldsymbol{g}_0 = \begin{bmatrix} \boldsymbol{R}_0 & \boldsymbol{p}_0 \\ \boldsymbol{0}^\top & 1 \end{bmatrix} \in SE(3)$$

In order to parameterize the configuration matrix $\boldsymbol{g}_0$ for controlling purpose, in our work, we use the exponential map to define the rotation matrix $\boldsymbol{R}_0$ by a vector $\boldsymbol{\phi}_0 \in \mathbb{R}^3$:

$$SO(3) \ni \boldsymbol{R}_0 = \exp \tilde{\boldsymbol{\phi}}_0 \ , \ \boldsymbol{\phi}_0 \in \mathbb{R}^3 \tag{4.1}$$

Thus the configuration matrix $\boldsymbol{g}_0$ is parameterized by the vector $\boldsymbol{\phi}_0(t)$ and $\boldsymbol{p}_0$. We use vector $\boldsymbol{\alpha} \in \mathbb{R}^6$ to denote their combination, i.e., $\boldsymbol{\alpha} = [\boldsymbol{\phi}_0^\top \ , \ \boldsymbol{p}_0^\top]^\top$. After defining the control variable $\boldsymbol{\alpha}$, let us focus on the control objective of passive implantation.

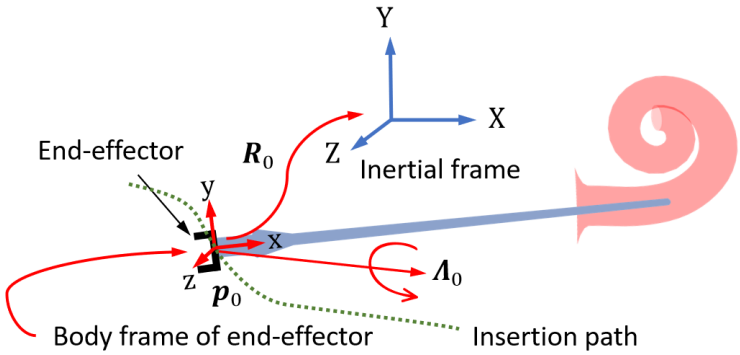

Figure 4.1: The configuration of base can be represented as a rotation matrix and a position vector.

4.3.2 Control objective

In actual cochlear implant procedures, the propulsion force exerted on the Electrode Array (EA) by the end-effector of the robotic arm can be measured. Due to the interactions involved, this propulsion force intuitively reflects the force applied by the EA on the cochlea during implantation. Therefore, in this section, our control objective is to reduce the magnitude of the propulsion force by altering the moving direction of the end-effector. During the implantation, the optimal configuration vector $\boldsymbol{\alpha}(t)$ of the path should minimize the norm of insertion force $\boldsymbol{\Lambda}_0$:

$$\underset{\boldsymbol{\alpha}(t)}{\arg\min} \quad \mathscr{H} = \frac{1}{2}\boldsymbol{\Lambda}_0^\top(\boldsymbol{\alpha})\boldsymbol{\Lambda}_0(\boldsymbol{\alpha}) \tag{4.2}$$

subject to mechanical model and constraints, which will be introduce in the following subsections.

4.3.3 Control constraint

It's noteworthy that the minimization problem defined above only sets the optimization goal, which is to minimize the implantation force. Obviously, the strategy that minimizes the implantation force is to stop advancing the implant; at this point, minimizing the implantation force is in contradiction with advancement. Therefore, when formulating control strategies, we need not only to minimize the implantation force but also to ensure that the implant is continuously advancing. This requires us to add some constraints to the above minimization problem. In order to find the $\boldsymbol{\alpha}(t)$ satisfying the minimization (4.2) without losing forward insertion speed, our method is as follows:

Firstly, we define point $\boldsymbol{p}_a$ as the center of the cochlear entrance expressed in the global frame (see Fig. 4.2). The velocity of the end-effector can be decomposed into a radial velocity $\boldsymbol{v}_\parallel$ directed towards point $\boldsymbol{p}_a$ and a tangential velocity $\boldsymbol{v}_\perp$ perpendicular to the line connecting end-effector and $\boldsymbol{p}_a$, as shown in Fig. 4.2. Throughout the implantation, the radial velocity $\boldsymbol{v}_\parallel$ of the end-effector's movement remains positive, i.e., $v_\parallel \geq 0$. In this case, the distance between $\boldsymbol{p}_a$ and $\boldsymbol{p}_0$, denoting as d_a, can be computed by the radial velocity $v_\parallel$:

$$d_a(t) = L - v_\parallel t$$

where L is the initial distance between these two points, t represents the time.

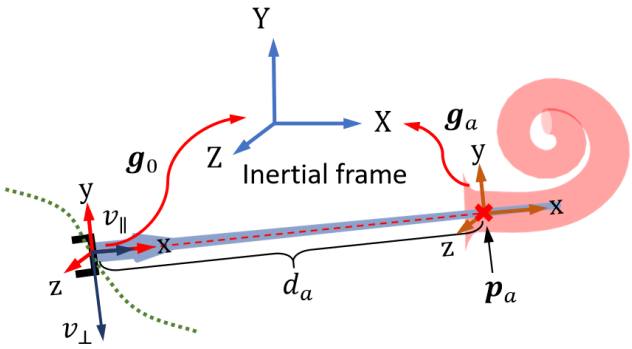

Figure 4.2: Throughout the implantation process, the orientation of the end-effector is meticulously maintained so that it continuously points towards the center of the cochlear entrance. The velocity of end-effector can be decomposed into a radial velocity v_r directed towards point $\boldsymbol{p}_a$ and a tangential velocity $v_\perp$ revolving around $\boldsymbol{p}_a$.

Throughout the implantation, the direction of the end-effector (the x-axis of body frame of end-effector) always points towards the center of the cochlear entrance, the point $\boldsymbol{p}_a$, as shown in Fig. 4.2 . We define a frame $\mathcal{A}$ at $\boldsymbol{p}_a$, which has the same rotation of the end-effector. As a result, the configuration of this frame can be represented as follows:

$$\boldsymbol{g}_a = \begin{bmatrix} \boldsymbol{R}_0 & \boldsymbol{p}_a \\ \boldsymbol{0} & 1 \end{bmatrix}$$

In this case, the configuration $\boldsymbol{g}_0$ should satisfy the following equation:

$$\boldsymbol{g}_0 = \boldsymbol{g}_a \underbrace{\begin{bmatrix} 1 & 0 & 0 & -d_a(t) \\ 0 & 1 & 0 & 0 \\ 0 & 0 & 1 & 0 \\ 0 & 0 & 0 & 1 \end{bmatrix}}_{\boldsymbol{g}_r} \tag{4.3}$$

where $\boldsymbol{g}_r$ represents the transformation matrix from $\boldsymbol{g}_0$ to $\boldsymbol{g}_a$. (4.3) signifies the constraint imposed on the end-effector. Throughout the implantation process, the configuration of the end-effector must consistently adhere to (4.3), ensuring that the implantation can continuously advance towards the entrance of the cochlea without any backward movement.

In the subsequent Section 4.3.4, we will be exploring the differential relationship between configuration $\boldsymbol{g}_0$ and parameter variable $\boldsymbol{\phi}_0$. This exploration is closely tied to the kinematic model. To facilitate a clearer and more straightforward exposition, we will preemptively present the kinematic model of the end-effector, specifically tailored to operate within the constraints we have outlined. Once we fix the point $\boldsymbol{p}_a$, from (4.3) we can see that $\boldsymbol{g}_a$ only depends on the rotation matrix $\boldsymbol{R}_0$. As $\boldsymbol{R}_0$ is parameterized by the vector $\boldsymbol{\phi}_0$, consequently, $\boldsymbol{g}_a$ is now parameterized by the vector $\boldsymbol{\phi}_0$. Let us now deduce the kinematics of the end-effector with respect to $\boldsymbol{\phi}_0$ under constraint (4.3). Reviewing kinematics equation (2.30) in Section 2.2.6, the angular velocity of frame $\mathcal{A}$ with respect to body frame can be deduced as follows:

$$\boldsymbol{w}_a = \boldsymbol{R}_0^\top \boldsymbol{J}_l \dot{\boldsymbol{\phi}}_0 \tag{4.4}$$

where $\boldsymbol{J}_l$ is the left Jacobian of $\boldsymbol{R}_0$ with respect to $\boldsymbol{\phi}_0$, given by the following formula:

$$\boldsymbol{J}_l(\boldsymbol{\phi}_0) = \mathbf{I}_3 + \frac{1-\cos\phi_0}{\phi_0^2}\tilde{\boldsymbol{\phi}}_0 + \frac{\phi_0 - \sin\phi_0}{\phi_0^3}\tilde{\boldsymbol{\phi}}_0^2$$

Finally, we can deduce the velocity twist with respect to body frame of end-effector as the following equation:

$$\boldsymbol{\eta}_0 = \boldsymbol{J}_{\phi_0}\dot{\boldsymbol{\phi}}_0 \tag{4.5}$$

where

$$\boldsymbol{J}_{\phi_0} = \mathrm{Ad}_{\boldsymbol{g}_r}\begin{bmatrix}\boldsymbol{R}_0^\top \boldsymbol{J}_l \\ \mathbf{0}\end{bmatrix}$$

with $\mathrm{Ad}_{\boldsymbol{g}_r}$ is the transformation matrix which transfer velocity twist from the frame $\mathcal{A}$ to the body frame of end-effector. This formulation will be used in the following subsection to solve the proposed optimization problem (4.6)-(4.9).

4.3.4 The mathematical problem of control

We've established the control objective and constraints. Next, we need to delve into the mechanical equations of the EA under these control constraints, subsequently formulating the control strategy based on the mechanical model. However, factoring in all the contact constraints and forces of EA inside cochlea significantly complicates the computation. Their abundance not only increases the number of variables but also adds complexity to the dimensions of the mechanical equations. Therefore, in our approach to constructing the control strategy, we simplify the contact model by assuming that the Electrode Array (EA) is fixedly constrained at the first contact point $\boldsymbol{p}_c(s_c)$, which can be determined via our collision detection algorithm in Section 3.3.1. Specifically, we suppose the case of minimization is that $\boldsymbol{p}_a$ is fixed and $v_\perp = 0$, thus that the movement of end-effector is constrained is a sphere whose center is $\boldsymbol{p}_a$ and radial is d_a, as illustrated in Fig. 4.3.

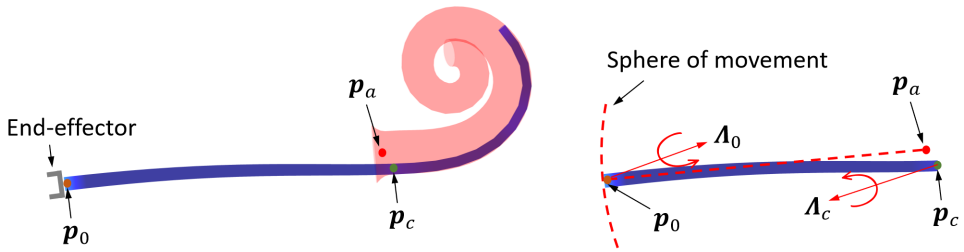

Figure 4.3: The left image shows the EA (Electrode Array) being implanted, while the right image displays the corresponding simplified model at that moment. The simplified model is a beam with fixed constraints at both ends, where the left end is fixed by the end-effector, and the right end is fixed by the contact point in the cochlea.

Given the slow pace of the implantation process, we can assume that the EA remains in a quasi-static state throughout. Now, we first establish the minimization problem by incorporating our objective function and all the control constraints:

$$\arg\min_{\boldsymbol{\phi}_0} \quad \mathscr{H} = \frac{1}{2}\boldsymbol{\Lambda}_0^\top \boldsymbol{\Lambda}_0 \tag{4.6}$$

subject to

$$\boldsymbol{K}\boldsymbol{q} - \boldsymbol{J}_0^\top \boldsymbol{\Lambda}_0 - \boldsymbol{J}_c^\top \boldsymbol{\Lambda}_c = \boldsymbol{0} \tag{4.7}$$

$$\boldsymbol{g}(0) - \boldsymbol{g}_0 = \boldsymbol{0} \tag{4.8}$$

$$\boldsymbol{g}(s_c) - \boldsymbol{g}_c = \boldsymbol{0} \tag{4.9}$$

where $\boldsymbol{J}_0$ and $\boldsymbol{J}_c$ are the Jacobian of kinematics at arc length $s = 0$ and $s = s_c$. The Jacobian of kinematics has been defined in (2.22), Section 2.2.6.2. The aforementioned equations (4.7)-(4.9) delineate the relationship between the configurations of the two tips of the EA and the respective constraint forces at these points. In essence, if we determine the configurations $\boldsymbol{g}_0$ and $\boldsymbol{g}_c$, we can deduce the constraint forces $\boldsymbol{\Lambda}_0$ and $\boldsymbol{\Lambda}_c$ by solving (4.7)-(4.9). If we know $\boldsymbol{g}_c$, our control strategy is to find the best configuration $\boldsymbol{g}_0$, i.e., the best parameter $\boldsymbol{\phi}$ of $\boldsymbol{g}_0$, which can minimize the constrain force (i.e., insertion force) $\boldsymbol{\Lambda}_0$ satisfying (4.7)-(4.9).

To achieve this, wo need to know the gradient of $\boldsymbol{\Lambda}_0$ with respect to $\boldsymbol{\phi}$ in order to introduce the Newton method for minimizing the insertion force. In our work, we will find this gradient dy making the variation of (4.7)-(4.9). The variation of (4.7) is as follows:

$$\boldsymbol{K}\delta\boldsymbol{q} - \boldsymbol{J}_0^\top \delta\boldsymbol{\Lambda}_0 - \boldsymbol{J}_c^\top \delta\boldsymbol{\Lambda}_c = \boldsymbol{0} \tag{4.10}$$

Note that the variation of (4.8) and (4.9) are defined within $SE(3)$ space, which is not conducive to gradient determination. Therefore, we first need to find their the equivalent algebraic formulation. Defining the following variation:

$$\mathbb{R}^6 \ni \delta\boldsymbol{\zeta} = (\boldsymbol{g}^{-1}\delta\boldsymbol{g})^\vee = \boldsymbol{J}\delta\boldsymbol{q},\ \forall s \in [0, L]$$

where $\boldsymbol{J}$ is the Jacobian of kinematics. The variations of (4.8) and (4.9) are equivalent to the following equations:

$$\delta\boldsymbol{g}(0) - \delta\boldsymbol{g}_0 = \boldsymbol{0} \Longleftrightarrow \delta\boldsymbol{\zeta}(0) - \delta\boldsymbol{\zeta}_0 = \boldsymbol{J}_0\delta\boldsymbol{q} - \boldsymbol{J}_{\phi_0}\delta\boldsymbol{\phi}_0 = \boldsymbol{0} \tag{4.11}$$

$$\delta\boldsymbol{g}(s_c) = \boldsymbol{0} \Longleftrightarrow \delta\boldsymbol{\zeta}(s_c) = \boldsymbol{J}_c\delta\boldsymbol{q} = \boldsymbol{0} \tag{4.12}$$

Consequently, we are able to consolidate these two equations along with equation (4.10) into a more compact formulation:

$$\underbrace{\begin{bmatrix} \boldsymbol{K} & -\boldsymbol{J}_0^\top & \boldsymbol{J}_c^\top \\ \boldsymbol{J}_0 & \boldsymbol{0} & \boldsymbol{0} \\ \boldsymbol{J}_c & \boldsymbol{0} & \boldsymbol{0} \end{bmatrix}}_{\boldsymbol{W}_h} \begin{bmatrix} \delta\boldsymbol{q} \\ \delta\boldsymbol{\Lambda}_0 \\ \delta\boldsymbol{\Lambda}_c \end{bmatrix} = \underbrace{\begin{bmatrix} \boldsymbol{0} \\ \boldsymbol{J}_{\phi_0} \\ \boldsymbol{0} \end{bmatrix}}_{\boldsymbol{J}_h} \delta\boldsymbol{\phi}_0 \tag{4.13}$$

We can now find the relationship between $\delta\boldsymbol{\Lambda}_0$ and $\delta\boldsymbol{\phi}_0$:

$$\delta\boldsymbol{\Lambda}_0 = \boldsymbol{C}_h\boldsymbol{W}_h^\dagger\boldsymbol{J}_h\delta\boldsymbol{\phi}_0 \tag{4.14}$$

where $\boldsymbol{C}_h = [\boldsymbol{0}_{6\times N}\ \boldsymbol{\mathrm{I}}_{6\times 6}\ \boldsymbol{0}_{6\times 6}]$, with N being the dimension of $\boldsymbol{q}$. The gradient of $\boldsymbol{\Lambda}_0$ with respect to $\boldsymbol{\phi}_0$ can be then deduced as $\frac{\partial\boldsymbol{\Lambda}_0}{\partial\boldsymbol{\phi}_0} = \boldsymbol{C}_h\boldsymbol{W}_h^\dagger\boldsymbol{J}_h$. Consequently, the gradient of the objective function in (4.6) is:

$$\frac{\partial\mathscr{H}}{\partial\boldsymbol{\phi}_0} = \boldsymbol{\Lambda}_0^\top\frac{\partial\boldsymbol{\Lambda}_0}{\partial\boldsymbol{\phi}_0} = \boldsymbol{\Lambda}_0^\top\boldsymbol{C}_h\boldsymbol{W}_h^\dagger\boldsymbol{J}_h$$

After obtaining the gradient of the objective function with respect to the optimization variables $\boldsymbol{\phi}_0$, we can then employ common numerical minimization algorithms to solve for $\boldsymbol{\phi}_0$, such as the Newton's method.

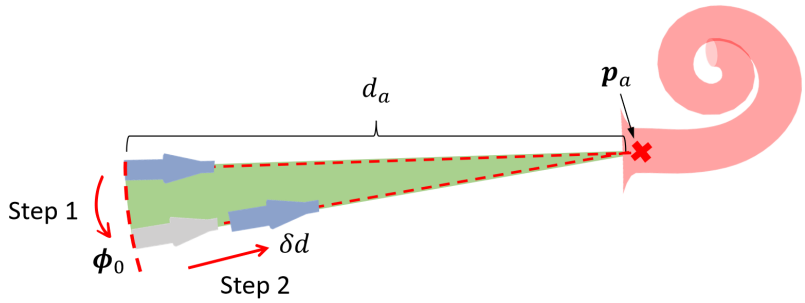

Figure 4.4: In each control loop, the parameters $\boldsymbol{\phi}_0$ of the optimal path at the current moment is first calculated by the optimization algorithm, and then the implant is pushed forward at a constant rate δd along this angle. This process is repeated for each subsequent loop.

In this subsection, we have established the minimization problem for optimizing the implantation force when the point $\boldsymbol{p}_a$ and the sphere of movement available to the end-effector is specified. We also provided the analytical gradient for solving this minimization problem. This allows us to iteratively use the analytical gradient to find the orientation of the end-effector that corresponds to minimizing the implantation force. In the following subsection, we will introduce the overall steps of the implantation process.

4.3.5 Insertion process

We divide the insertion process into two steps at each moment, as shown in Fig. 4.4:

1. The first step is to change the orientation of end-effector. The end-effector is constrained on the spherical surface (the red dotted line in the figure) about the reference point $\boldsymbol{p}_a$ with radius d_a. The end-effector is then moved on this surface until finding the optimal orientation which minimize the insertion force Λ_0 by solving (4.6).

2. At the next step, holding the this orientation, the end-effector move forward by distance δd, which equals to $v_{\parallel}\delta t$ (we set $v_{\parallel}$ as constant). Then, the first step is repeated on the new spherical surface followed by the second translation step.

These two steps alternate during the implantation until finishing the total insertion.

To conclude the control of passive implant, we first simplify the cochlear implant model to a fixed-end beam model to focus on the external part of the cochlea. Next, we generate a force model based on the mechanics of the cochlea and simulate the force distribution during the implantation process. Based on this, we calculate the optimal path for the cochlear implant by solving the minimization problem (4.6). The following sections will present the simulations and experimental results.

4.3.6 Simulation and experiment

4.3.6.1 Initial state and parameter settings

For the numerical simulation of path planning, the material and geometric parameters of the implant, as well as the geometric parameters of the cochlea, are kept consistent with the parameters mentioned in the model validation Section 3.7. As shown in the Fig. 4.5, the initial position of the implant is set along the central axis at the entrance of the cochlea. Subsequently,

the optimization algorithm starts iterating and calculating the optimal trajectory. The iterative step size for the orientation angles of the end base of the implant is set to 0.01 rad, and the step size for each forward advancement is set to 0.02 m. The initial angle of the optimal path are set as 0°, 10° and 20° respectively. With these settings, we obtained the optimal path by our proposed method, as shown in Fig. 4.5.

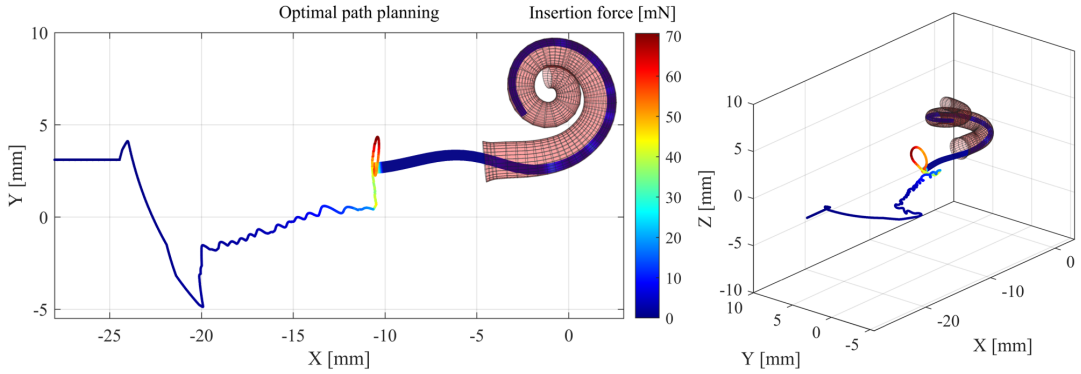

Figure 4.5: Optimal path of simulation.

4.3.6.2 Analysis of the optimal path

The optimal path shown in Fig. 4.5 is characterized by three distinct stages:

1. Initially, the implant does not contact the cochlea, resulting in a zero-valued iterative Jacobian matrix for orientation angles. During this phase, the implant's base remains static in terms of angle and moves forward linearly.

2. In the second stage, as the implant makes contact with the cochlea's inner wall, constraint forces emerge at its base, leading to changes in the Jacobian matrix and subsequent variations in the orientation angles, following the gradient descent direction.

3. The final stage is marked by a point where adjusting the base angle no longer aligns the constraint forces with the forward direction, indicating an onset of buckling and the limit of advancement.

As our model is close to the real implantation, which has been confirmed in the model validation Section 3.7, we believe that the optimal path computed form simulation can be used directly for the real implantation and the accuracy of open-loop control is sufficient to meet our requirements. The implementation of the deduced open-loop control will be presented in the next subsection.

4.3.6.3 Experiment setup

In the experimental phase of this study, we employed a scaled resin 3D model, provided by OTICON Medical, as a substitute for the actual cochlea. The experimental setup, as depicted in Fig. 4.6, comprised several key components: a model of the cochlea, a base for securing the cochlea, a six-degree-of-freedom force sensor, a Meca500 robot whose end-effector has 6 degrees of freedom, and the implant.

During the implantation process, the implant is fixed on the probe of the robot end effector. The cochlea is fixed on the base, and a six-degree-of-freedom force sensor (NANO17 - ATI Industrial Automatization) which can resolve down to 0.318 gram-force is installed at the bottom of the cochlea placement. This sensor is used to measure the force acting on the cochlea during the implantation process.

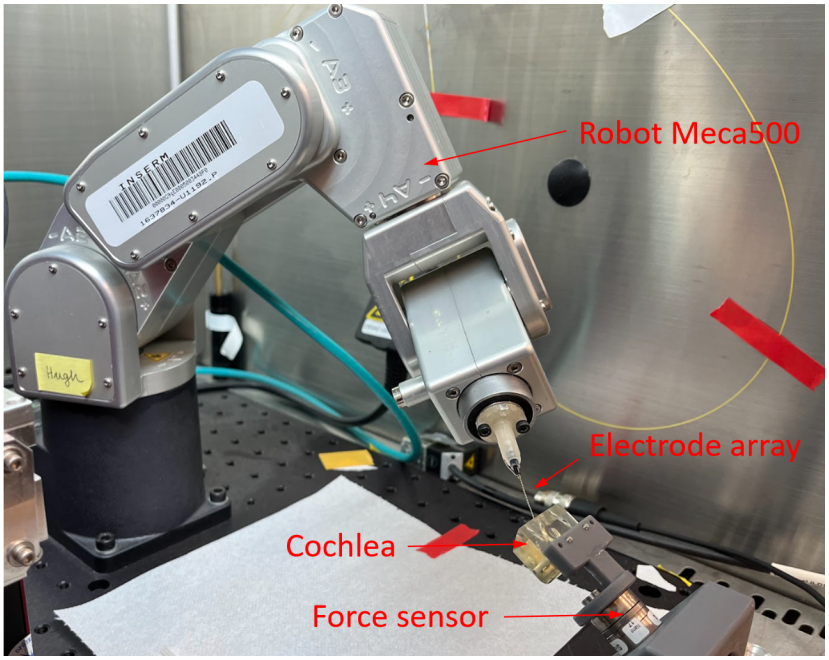

Figure 4.6: Experiment setup.

4.3.6.4 Experimental results

After implementing the optimal open-loop control sequences obtained from simulation, Fig. 4.7 presents the maximum insertion depths recorded for the implant, comparing the constant angle approach with the optimal path. Each experimental group, repeated five times under identical conditions, showed varying maximum insertion depths for different angles in the constant angle approach. The deepest insertion, reaching up to 310 degrees, occurred at a zero-degree angle, and the depth decreased as the angle increased.

Conversely, using the optimized path, the final maximum insertion depth consistently converged to 310 degrees across all experimental groups, regardless of their initial angles. Moreover, the insertion force followed a similar trend for different initial angles, which confirms the robustness of our method, as shown in Fig. 4.8.

In this section, we introduced the control objectives and methods for passive cochlear implants. Both simulations and experiments suggest that the proposed methods can enhance the implantation depth to some extent and adapt to the needs of various initial implantation angles. In the following section, we will discuss the control methods for active cochlear implants.

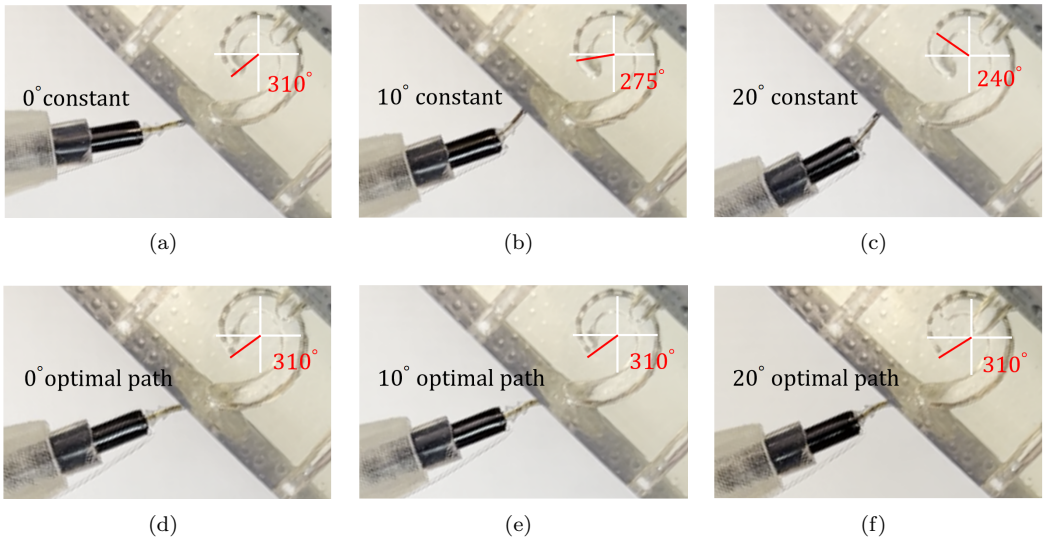

Figure 4.7: Insertion result of constant direction and optimal path from different initial orientation.

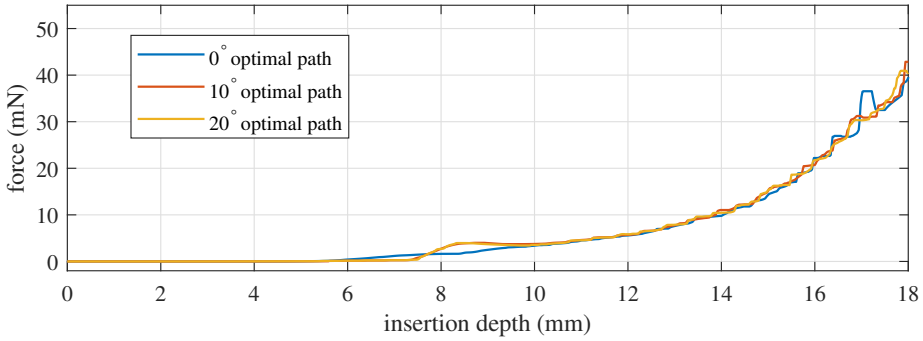

Figure 4.8: The measured insertion force of different cases: the implantation start form different initial angle.

4.4 Trajectory Tracking Control (Active Implant)

The previous section focused on the optimal control of passive cochlear implant. Now, we turn our attention to active cochlear implants. As active implant has more degree of freedom for control comparing with passive implant, the goal of this section is to explore optimal control strategies for considering the active deformation of EA during implantation.

4.4.1 Control objective

First, we clarify the control objective here, which is to enable the implant to closely follow the spiral centerline of the cochlea during the insertion process through active deformation. To

define this objective, we evenly select several control points on the implant, and corresponding follower reference points are chosen along the spiral trajectory. The controller should minimize the distance between the control points on the implant and the follower reference points.

As shown in the Fig. 4.9, we select m control points $\{\boldsymbol{p}_1, \ldots, \boldsymbol{p}_m\}$ on the implant, with the distance $\{\boldsymbol{l}_1, \ldots, \boldsymbol{l}_m\}$ between them. Similarly, m follower reference points $\{\boldsymbol{p}_{r1}, \ldots, \boldsymbol{p}_{rm}\}$ are placed on the spiral trajectory. During the implantation, we assume that the EA is inserted by the end-effector of robot horizontally, with the constant insertion velocity $v_{\parallel}$. The follower points also move during the implantation. Specifically, they move forward along the center line of cochlea at the movement rate same as $v_{\parallel}$.

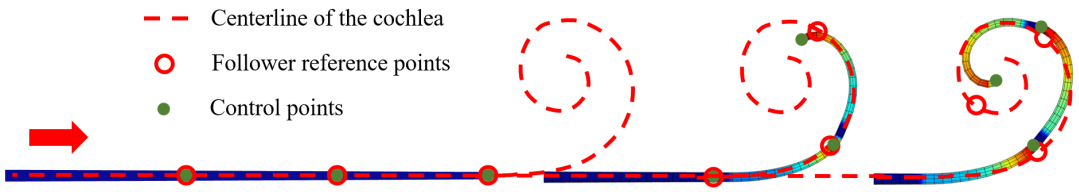

Figure 4.9: cochlear implant.

For the i-th control point located at s_i, its coordinates $\boldsymbol{p}_i$ can be calculated using the following formula:

$$\boldsymbol{p}_i = \boldsymbol{D}\boldsymbol{g}_i\boldsymbol{E} \tag{4.15}$$

Here, $\boldsymbol{g}_i$ is the configuration tensor of the disc of implant at length s_i. Matrices $\boldsymbol{D}$ and $\boldsymbol{E}$ are used to extract position vectors from the configuration tensor, with

$$\boldsymbol{D} = \begin{bmatrix}\mathbf{I}_{3\times 3} & \mathbf{0}\end{bmatrix}, \ \boldsymbol{E} = \begin{bmatrix}0 & 0 & 0 & 1\end{bmatrix}^{\top}$$

For the i-th reference point $\boldsymbol{p}_{ri}$, it moves on the center line of cochlea with the movement rate as the end-effecter. In this case, The arc length corresponding to $\boldsymbol{p}_{ri}$ is $s_{ei} = s_{ei}(0) + v_{\parallel}t$, where $s_{ei}(0)$ is its initial arc length, $v_{\parallel}$ is the radial velocity of insertion, t is the insertion time. Consequently, the position of $\boldsymbol{p}_{ri}$ at time t can be calculated as follows:

$$\boldsymbol{p}_{ri} = \boldsymbol{D}\boldsymbol{g}_e(s_{ei})\boldsymbol{E} \tag{4.16}$$

where$\boldsymbol{g}_e$ is the configuration tensor of cochlea, deduced in Section 3.2.2. Up to this point, we can define the control objective for trajectory tracking:

$$\underset{\boldsymbol{V}_{in}(t)}{\arg\min} \quad \mathscr{H} = \Sigma_{i=1}^{i=m} w_i \int_{t_0}^{t_f} \|\boldsymbol{p}_{ri}(t) - \boldsymbol{p}_i(t)\|^2 \mathrm{dt} \tag{4.17}$$

This control objective illustrates that the EA should be close to the center line of the cochlea as much as possible during the implantation. After defining the control objective, now we need to consider the contact constraint in order to establish the complete minimization problem.

4.4.2 Control constraint

As we defined the control problem as a minimization issue in the above subsection, the system's model is considered a constraint for the minimization problem. Here, we recall the coupling

model of the active cochlear implant, as deduced in Chapter 2, Section 2.4. First is the electrical model, which involves the relationship between the input voltage to the Conducting Polymer Actuator (CPA) and the driving torque generated by the CPA. The electrical model is as follows:

$$\boldsymbol{A}\dot{\boldsymbol{z}} + \boldsymbol{B}\boldsymbol{z} = \boldsymbol{U}\boldsymbol{V}_{in} \tag{4.18}$$

Here, $\boldsymbol{z}$ represents the moment generated by CPA, $\boldsymbol{V}_{in}$ represents the input voltage. $\boldsymbol{A}$, $\boldsymbol{B}$ and $\boldsymbol{U}$ are the matrices of system, defined in Section 2.4.1.

As for mechanical model, we consider that the EA is at quasi-static state as the implantation moves very slowly. We also ignore the contribution of gravity since it is very small compared to the internal elastic force due to the small size of EA. Under this assumption, the mechanical model is as follows:

$$\boldsymbol{K}\boldsymbol{q} + \boldsymbol{H}\boldsymbol{z} = \boldsymbol{0} \tag{4.19}$$

where $\boldsymbol{K}$ represents the stiffness matrix of EA, defined in Section 2.2.8, and $\boldsymbol{H}$ represents the input matrix of EA, defined in Section 2.4.2.

4.4.3 Minimization problem

Having established the control objective and constraints, we are now in a position to define the complete minimization problem as our control strategy:

$$\underset{\boldsymbol{V}_{in}(t)}{\arg\min} \quad \mathscr{H} = \Sigma_{i=1}^{i=m} w_i \int_{t_0}^{t_f} \|\boldsymbol{p}_{ri}(t) - \boldsymbol{p}_i(t)\|^2 \mathrm{dt} \tag{4.20}$$

$$\boldsymbol{A}\dot{\boldsymbol{z}} + \boldsymbol{B}\boldsymbol{z} = \boldsymbol{U}\boldsymbol{V}_{in} \tag{4.21}$$

$$\boldsymbol{K}\boldsymbol{q} + \boldsymbol{H}\boldsymbol{z} = \boldsymbol{0} \tag{4.22}$$

$$\boldsymbol{p}_i = \boldsymbol{D}\boldsymbol{g}_i\boldsymbol{E} \ , \ i = 1, \ldots, m \tag{4.23}$$

In this context, $\boldsymbol{V}_{in}$ refers to the system's input, whereas the charge variable $\boldsymbol{z}$ and the strain variable $\boldsymbol{q}$ represent the system's states. Furthermore, $\boldsymbol{p}_i$ signifies the system's output. w_i denotes the weight of each control point. The interval $[t_0, t_f]$ denotes the rolling time window for optimization.

It is clear that the above optimization objective is defined as the trajectory error, while the system model is established as the optimization constraints. To solve this optimization problem, we first need to discretize the time window. Let's define the time step as $h = (t_f - t_0)/M$, with M being the discretization number of time interval $[t_0, t_f]$. In this way, the time window can be discretized into a sequence of time steps: $[t_0, t_1, \ldots, t_M]$, where $t_k = t_0 + kh$, $k = 0, \ldots, M$, with $t_M = t_f$. Within this time window, the system's states, outputs, and inputs are also discretized into sequences, with the variables in the sequence corresponding to each time point in the time sequence.

After discretization, we can approximate the time integral in the optimization objective as follows:

$$\mathscr{H}_d = \Sigma_{i=1}^{i=m} w_i \Sigma_{k=1}^{k=M} \|\boldsymbol{p}_{ri}(t_k) - \boldsymbol{p}_i(t_k)\|^2 h$$

The system's model can also be rewritten in a discrete form over time. To ensure convergence, we employ the implicit Euler method to discretize the differential equation (4.21) of system as follows:

$$\boldsymbol{A}(\boldsymbol{z}(t_{k+1}) - \boldsymbol{z}(t_k)) + h\boldsymbol{B}\boldsymbol{z}(t_{k+1}) = h\boldsymbol{U}\boldsymbol{V}_{in}(t_{k+1}) \tag{4.24}$$

Therefore, the discretized optimal control problem can be written as follows:

$$\underset{\bar{\boldsymbol{V}}_{in}}{\arg\min} \quad \mathscr{H}_d = \Sigma_{i=1}^{i=m} w_i \Sigma_{k=1}^{k=M} \|\boldsymbol{p}_{ri}(t_k) - \boldsymbol{D}\boldsymbol{g}_i(t_k)\boldsymbol{E}\|^2 h \tag{4.25}$$

subject to

$$(\boldsymbol{A} + h\boldsymbol{B})\boldsymbol{z}(t_{k+1}) - \boldsymbol{A}\boldsymbol{z}(t_k) - h\boldsymbol{U}\boldsymbol{V}_{\boldsymbol{in}}(t_{k+1}) = \boldsymbol{0} \ , \ k = 0, \ldots, M-1 \tag{4.26}$$

$$\boldsymbol{K}\boldsymbol{q}(t_{k+1}) + \boldsymbol{H}\boldsymbol{z}(t_{k+1}) = \boldsymbol{0} \ , \ k = 1, \ldots, M-1 \tag{4.27}$$

$$\boldsymbol{p}_i(t_k) - \boldsymbol{D}\boldsymbol{g}_i(t_k)\boldsymbol{E} = \boldsymbol{0} \ , \ i = 1, \ldots, m \ , \ k = 1, \ldots, M \tag{4.28}$$

$$\boldsymbol{V}_{ina} \leq \boldsymbol{V}_{in}(t_k) \leq \boldsymbol{V}_{inb} \ , \ k = 1, \ldots, M \tag{4.29}$$

where $\bar{\boldsymbol{V}}_{in}$ is the input sequence as $\bar{\boldsymbol{V}}_{in} = [\boldsymbol{V}_{in}(t_1)^\top, \ldots, \boldsymbol{V}_{in}(t_M)^\top]^\top$. $\boldsymbol{V}_{ina}$ and $\boldsymbol{V}_{inb}$ are the lower and upper bounds of the input voltage.

To solve this problem, various strategies are available: for situations involving a fixed time frame, optimal control is ideal, concentrating on identifying the best actions within this specified duration. On the other hand, Model Predictive Control (MPC) excels in dynamic contexts, employing a moving window approach to consistently revise control decisions in response to evolving conditions. In our work, since the implantation is continuously moving on, we will select a moving time window in order to implement MPC.

4.4.4 Shooting and multi-shooting method

In control theory, the above optimization problem falls under the category of optimal control or Model Predictive Control (MPC). The core idea behind MPC is to find a sequence of input commands that minimizes a cost function associated with the control problem [131]. The basic approach to solving it is the shooting method. With knowledge of the initial state of the rolling time window, we can start with an initial guess for the input sequence. We can then use the system model (4.24) to propagate the system's state at each moment within the rolling time window. This allows us to compute the corresponding cost function value for the entire time window. By finding the relationship between the cost function and the input sequence, i.e., by calculating the Jacobian matrix between them, we can use gradient descent or Newton's method to determine the direction of iterations for the input sequence. Multiplying this direction by an iteration step size provides a new input sequence. This process is repeated iteratively until the extremum of the cost function is reached.

This method has the advantage of being straightforward because the optimization variable is solely the input sequence [131]. The system state sequence can be derived from the input sequence through the model. However, in many cases, this method's robustness is limited, and it can lead to issues with convergence, especially for highly nonlinear systems.

For nonlinear systems, a more stable alternative is the multi-shooting method. The multi-shooting method is an enhanced approach to optimization, especially beneficial when dealing with highly nonlinear systems. It divides the time window into smaller subintervals, optimizing inputs within each one [132]. This method offers greater robustness, as it reduces convergence issues, parallel processing capabilities for faster computations, and the ability to react to changes in the system more rapidly. It's well-suited for handling constraints and adapts to a wide range of systems, making it a versatile choice for controlling complex systems. The difference between this method and the shooting method lies in treating the state sequence within the time window as unknown variables, to be solved together with the input sequence. To achieve

this, we introduce an augmented variable that incorporates all the variables within the time sequence. We define $\bar{\boldsymbol{z}}$ and $\bar{\boldsymbol{q}}$ as:

$$\bar{\boldsymbol{p}} = [\boldsymbol{p}(t_1)^\top, \ldots, \boldsymbol{p}(t_M)^\top]^\top \ , \ \bar{\boldsymbol{z}} = [\boldsymbol{z}(t_1)^\top, \ldots, \boldsymbol{z}(t_M)^\top]^\top \ , \ \bar{\boldsymbol{q}} = [\boldsymbol{q}(t_1)^\top, \ldots, \boldsymbol{q}(t_M)^\top]^\top$$

Based on (4.24), the dynamic equation of electric model within the entire time window is as follows:

$$\begin{aligned} \underbrace{\begin{bmatrix} (\boldsymbol{A}+h\boldsymbol{B})_1 & & & \\ -\boldsymbol{A}_2 & (\boldsymbol{A}+h\boldsymbol{B})_2 & & \\ & \ddots & \ddots & \\ & & -\boldsymbol{A}_M & (\boldsymbol{A}+h\boldsymbol{B})_M \end{bmatrix}}_{\bar{\boldsymbol{A}}} \begin{bmatrix} \boldsymbol{z}(t_1) \\ \boldsymbol{z}(t_2) \\ \vdots \\ \boldsymbol{z}(t_M) \end{bmatrix} - \underbrace{\begin{bmatrix} \boldsymbol{A}_1 \boldsymbol{z}(t_0) \\ \\ \end{bmatrix}}_{\bar{\boldsymbol{z}}_0} \\ = \underbrace{\begin{bmatrix} \boldsymbol{U} & & & \\ & \boldsymbol{U} & & \\ & & \ddots & \\ & & & \boldsymbol{U} \end{bmatrix}}_{\bar{\boldsymbol{U}}} \begin{bmatrix} \boldsymbol{V}_{in}(t_1) \\ \boldsymbol{V}_{in}(t_2) \\ \vdots \\ \boldsymbol{V}_{in}(t_M) \end{bmatrix} \end{aligned} \tag{4.30}$$

Based on (4.22), the static equation of mechanic model within the entire time window is:

$$\underbrace{\begin{bmatrix} \boldsymbol{K} & & & \\ & \boldsymbol{K} & & \\ & & \ddots & \\ & & & \boldsymbol{K} \end{bmatrix}}_{\bar{\boldsymbol{K}}} \begin{bmatrix} \boldsymbol{q}(t_1) \\ \boldsymbol{q}(t_2) \\ \cdots \\ \boldsymbol{q}(t_M) \end{bmatrix} + \underbrace{\begin{bmatrix} \boldsymbol{H} & & & \\ & \boldsymbol{H} & & \\ & & \ddots & \\ & & & \boldsymbol{H} \end{bmatrix}}_{\bar{\boldsymbol{H}}} \begin{bmatrix} \boldsymbol{z}(t_1) \\ \boldsymbol{z}(t_2) \\ \vdots \\ \boldsymbol{z}(t_M) \end{bmatrix} = \boldsymbol{0} \tag{4.31}$$

The optimization problem associated with the multi-shooting method is as follows:

$$\underset{\bar{\boldsymbol{V}}_{in}, \bar{\boldsymbol{z}}, \bar{\boldsymbol{q}}}{\arg\min} \quad \mathscr{H}_d = \Sigma_{i=1}^{i=m} w_i \Sigma_{k=1}^{k=M} \|\boldsymbol{p}_{ri}(t_k) - \boldsymbol{D}\boldsymbol{g}_i(t_k)\boldsymbol{E}\|^2 h \tag{4.32}$$

subject to

$$\bar{\boldsymbol{A}}\bar{\boldsymbol{z}} - \bar{\boldsymbol{z}}_0 - \bar{\boldsymbol{U}}\bar{\boldsymbol{V}}_{in} = \boldsymbol{0} \tag{4.33}$$

$$\bar{\boldsymbol{K}}\bar{\boldsymbol{q}} + \bar{\boldsymbol{H}}\bar{\boldsymbol{z}} = \boldsymbol{0} \tag{4.34}$$

$$\bar{\boldsymbol{V}}_{ina} \leq \bar{\boldsymbol{V}}_{in} \leq \bar{\boldsymbol{V}}_{inb} \tag{4.35}$$

From a numerical computation perspective, the problem described above is a Nonlinear Programming (NLP) problem. Due to the high degree of nonlinearity in both its objective function and optimization constraints, solving it poses a challenge. In the following subsection, we will introduce how to solve such problems by linearizing them via Sequence Quadratic Programming method.

4.4.5 Sequence quadratic programming

Sequence Quadratic Programming (SQP) method is flexible and can handle both equality and inequality constraints. It ensures that the updated solution satisfies the constraints within specified tolerances. The core idea of SQP method is to decompose complex nonlinear optimization problems into a sequence of quadratic programming subproblems. Each subproblem

is obtained by linearizing the original problem near the current estimated solution using Taylor series expansion, resulting in a quadratic objective function. SQP iteratively solves these sub-problems to gradually approach the optimal solution of the original problem. It is a local search method that provides a local approximation of the original problem and seeks better solutions in the vicinity of the current solution. SQP has global convergence properties and can find the global optimal solution when the problem has one. This method performs exceptionally well in addressing nonlinear, constrained optimization problems, particularly in applications that demand highly accurate numerical optimization [133].

We first transform the objective function (4.32) into a quadratic form:

$$\mathscr{H}_d = \frac{1}{2}\Sigma_{k=1}^{k=M} \boldsymbol{f}_k^\top \boldsymbol{Q} \boldsymbol{f}_k$$

where

$$\boldsymbol{f}_k = \begin{bmatrix} \boldsymbol{p}_{r1}(t_k) - \boldsymbol{D}\boldsymbol{g}_1(t_k)\boldsymbol{E} \\ \vdots \\ \boldsymbol{p}_{rm}(t_k) - \boldsymbol{D}\boldsymbol{g}_m(t_k)\boldsymbol{E} \end{bmatrix}, \ \boldsymbol{Q} = \begin{bmatrix} w_1 h & & \\ & \ddots & \\ & & w_m h \end{bmatrix}$$

After the Taylor expansion, the quadratic programming (QP) subproblem for (4.32)-(4.35) becomes [134]:

$$\underset{\Delta\bar{\boldsymbol{V}}_{in}, \Delta\bar{\boldsymbol{z}}, \Delta\bar{\boldsymbol{q}}}{\arg\min} \quad \mathscr{H}_d = \Sigma_{k=1}^{k=M} (\boldsymbol{f}_k^\top \boldsymbol{Q} \mathcal{J}_k \Delta\bar{\boldsymbol{q}} + \frac{1}{2}\Delta\bar{\boldsymbol{q}}^\top \mathcal{H}_k \Delta\bar{\boldsymbol{q}}) \tag{4.36}$$

subject to

$$\bar{\boldsymbol{A}}(\bar{\boldsymbol{z}} + \Delta\bar{\boldsymbol{z}}) - \bar{\boldsymbol{z}}_0 - \bar{\boldsymbol{U}}(\bar{\boldsymbol{V}}_{in} + \Delta\bar{\boldsymbol{V}}_{in}) = \boldsymbol{0} \tag{4.37}$$

$$\bar{\boldsymbol{K}}(\bar{\boldsymbol{q}} + \Delta\bar{\boldsymbol{q}}) + \bar{\boldsymbol{H}}(\bar{\boldsymbol{z}} + \Delta\bar{\boldsymbol{z}}) = \boldsymbol{0} \tag{4.38}$$

$$\bar{\boldsymbol{V}}_{ina} \leq \bar{\boldsymbol{V}}_{in} + \Delta\bar{\boldsymbol{V}}_{in} \leq \bar{\boldsymbol{V}}_{inb} \tag{4.39}$$

where $\mathcal{J}_k$ denotes the Jacobian of $\boldsymbol{f}_k$ with respect to $\boldsymbol{q}(t_k)$ and $\mathcal{H}_k$ denotes the Hessian matrix of $\frac{1}{2}\boldsymbol{f}_k^\top \boldsymbol{Q} \boldsymbol{f}_k$ with respect to $\boldsymbol{q}(t_k)$. For the details of the derivation process of (4.36) from Taylor expansion, we refer to [134]. To solve the aforementioned sub-QP, it is essential for us to understand how to compute the Jacobian $\mathcal{J}_k$ and Hessian matrices $\mathcal{H}_k$. We will delve into the details of this in the upcoming subsections..

4.4.6 Computation of Jacobian matrix $\mathcal{J}$ and Hessian matrix $\mathcal{H}$

First, we will describe how to compute the analytical solution for the Jacobian matrix $\mathcal{J}$. For any point $\boldsymbol{p}$ on the center line of implant, its velocity in global frame can be represented by the equation below via the Jacobian matrix of kinematics:

$$\dot{\boldsymbol{p}} = \boldsymbol{R}\boldsymbol{v} = \begin{bmatrix} \boldsymbol{0}_{3\times3} & \boldsymbol{R} \end{bmatrix} \boldsymbol{\eta} = \begin{bmatrix} \boldsymbol{0}_{3\times3} & \boldsymbol{R}_i \end{bmatrix} \boldsymbol{J}\dot{\boldsymbol{q}}$$

where $\boldsymbol{R}$ is the rotation matrix of disc at $\boldsymbol{p}$. $\boldsymbol{J}$ is the Jacobian of kinematics at $\boldsymbol{p}$.

Using the chain rule for differentiation, we can obtain an alternative expression for velocity:

$$\dot{\boldsymbol{p}} = \frac{\partial \boldsymbol{p}}{\partial \boldsymbol{q}}\dot{\boldsymbol{q}}$$

Comparing the two expressions of $\dot{\boldsymbol{p}}$, the following equation can be deduced:

$$\frac{\partial \boldsymbol{p}}{\partial \boldsymbol{q}}\dot{\boldsymbol{q}} = \begin{bmatrix} \boldsymbol{0}_{3\times3} & \boldsymbol{R}_i \end{bmatrix} \boldsymbol{J}\dot{\boldsymbol{q}}$$

Accordingly, the partial derivative of $\boldsymbol{p}$ with respect to $\boldsymbol{q}$ is given by

$$\frac{\partial \boldsymbol{p}}{\partial \boldsymbol{q}} = \begin{bmatrix} \mathbf{0}_{3\times 3} & \boldsymbol{R} \end{bmatrix} \boldsymbol{J}$$

Substituting this partial derivative into the definition of the Jacobian, we get:

$$\mathcal{J}_k = -\begin{bmatrix} \frac{\partial (\boldsymbol{D}\boldsymbol{g}_1(t_k)\boldsymbol{E})}{\partial \boldsymbol{q}_k} \\ \vdots \\ \frac{\partial (\boldsymbol{D}\boldsymbol{g}_m(t_k)\boldsymbol{E})}{\partial \boldsymbol{q}_k} \end{bmatrix} = \begin{bmatrix} \frac{\partial \boldsymbol{p}_1(t_k)}{\partial \boldsymbol{q}_k} \\ \vdots \\ \frac{\partial \boldsymbol{p}_m(t_k)}{\partial \boldsymbol{q}_k} \end{bmatrix} = -\begin{bmatrix} \begin{bmatrix} \mathbf{0}_{3\times 3} & \boldsymbol{R}_1(t_k) \end{bmatrix} \boldsymbol{J}_1(t_k) \\ \vdots \\ \begin{bmatrix} \mathbf{0}_{3\times 3} & \boldsymbol{R}_m(t_k) \end{bmatrix} \boldsymbol{J}_m(t_k) \end{bmatrix}$$

Next, to simplify the computation, we can approximate the Hessian matrix using the deduced Jacobian [134]:

$$\mathcal{H}_k = \mathcal{J}_k^\top \mathcal{J}_k$$

Once we have the Jacobian and Hessian matrices in hand, we can outline the SQP loop algorithm for minimizing the problem described by equations (4.32) through (4.35). The specific steps for solving this problem are as follows:

1. Initialization: Start with an initial estimate for the solution to the optimization problem (4.32)-(4.35).

2. Quadratic Programming Subproblem Construction: Linearize the nonlinear objective and constraint functions around the current estimate of the solution using Taylor series expansion. This results in a quadratic approximation to the problem in the form of a QP subproblem (4.36)-(4.39).

3. Solve the QP Subproblem: Use a QP solver to find the solution to the quadratic programming subproblem. This solution provides an updated estimate for the decision variables.

4. Update Variables: Update the decision variables with the solution obtained from the QP subproblem.

$$\bar{\boldsymbol{V}}_{in} = \bar{\boldsymbol{V}}_{in} + c\Delta\bar{\boldsymbol{V}}_{in} \ , \ \bar{\boldsymbol{z}} = \bar{\boldsymbol{z}} + c\Delta\bar{\boldsymbol{z}} \ , \ \bar{\boldsymbol{q}} = \bar{\boldsymbol{q}} + c\Delta\bar{\boldsymbol{q}}$$

   where the parameter c is the step length, which can be determined by merit function.

5. Convergence Check: Check for convergence by examining criteria such as the change in the objective function value or the satisfaction of constraint violations. If the convergence criteria are met, the optimization process terminates. If not, return to step 2 and repeat the process.

6. Termination Criteria: The optimization process continues until the termination criteria are met, such as a predefined number of iterations or when the convergence criteria are satisfied.

7. Output: The final solution $\bar{\boldsymbol{V}}_{in}, \bar{\boldsymbol{z}}, \bar{\boldsymbol{q}}$, which is the optimal to the original nonlinear optimization problem (4.32)-(4.35), is obtained after the SQP iterations are completed.

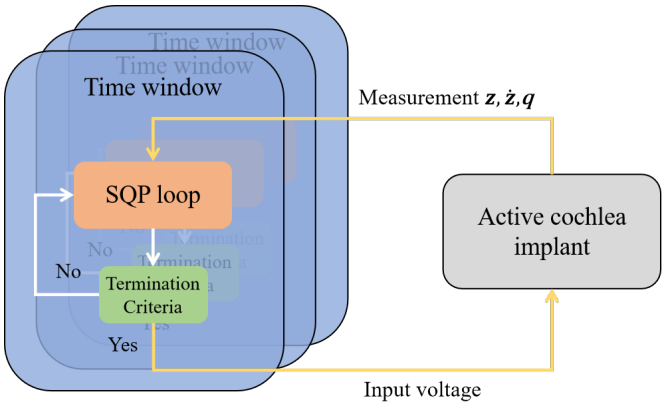

Figure 4.10: Optimal control framework of cochlea implant.

4.4.7 Control Algorithm Summary

Based on the proposed SQP loop, the overall optimal control process is outlined as follows:

1. System Modeling: Establish the dynamic model of the active implant, covering both its electrical and mechanical behaviors. (4.21)-(4.23)

2. Time Discretization: Split time into discrete intervals using a fixed time step h. (4.24)

3. Formulate the Optimization Problem: Define the optimization problem, consisting of the rolling time window, an objective function and constraints that guide the system's behavior. (4.32)-(4.35)

4. Closed-Loop Control:

   -Measurement: Measure the current system state, including electric charge $\boldsymbol{z}(t_0)$ and strain $\boldsymbol{q}(t_0)$.

   -Optimization: Use Sequential Quadratic Programming to optimize control inputs.

   -Control Input Application: Apply the first value $\boldsymbol{V}_{in}(t_0)$ of the optimized input sequence $\bar{\boldsymbol{V}}_{in}$.

   -Iterate and Update: Repeat this process for each time window to ensure the implant tracking the trajectory, as shown in Fig. 4.10.

In summary, to conclude the control of active implant, we initially defined an optimization objective based on trajectory tracking. Subsequently, we revisited the coupled model of the active cochlear implant discussed in Chapter 2, incorporating this model as an optimization constraint. This led to the formulation of an optimization problem based on a rolling time window, namely Model Predictive Control (MPC). We addressed the established optimization problem using the multi-shooting method and ultimately solved it using Sequential Quadratic Programming (SQP). In the following section, we will present the related simulation design and the results of these simulations.

4.4.8 Simulation

In this section, we will focus on the simulation aspect of control for active cochlear implants, including an enumeration of different structural designs of active cochlear implants and an analysis of the simulation results for each design. In order to investigate the impact of various design structures on control tracking effectiveness, specifically the number, placement, and length of the CPA, we have configured three sets of simulations, each involving the implant with a different number of actuators and varying the number of control points. The details are as follows:

Case 1. Two actuators and two control points

In the first simulation, we configure the implant to have a length of 26mm, consisting of two conducting polymer actuators, with each actuator measuring 7mm in length. The geometric structure of the active implant is depicted in Fig. 4.11.

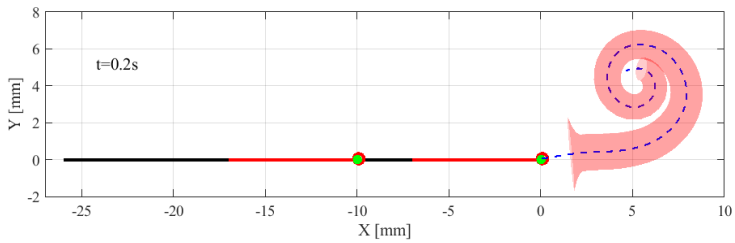

Figure 4.11: Active implant with two actuators and two control points. The black section symbolizes the EA, while the red section denotes the CPA. The red hollow circles indicate the follower reference points, and the green dots represent the control points.

Case 2. Three actuators and three control points

In the second simulation, we configure the implant to have a length of 26mm, consisting of three conducting polymer actuators, with each actuator measuring 7mm in length. The geometric structure of the active implant is depicted in Fig. 4.12. The red regions in the illustration indicate sections containing conducting polymer actuators. Charging initiates for each actuator, starting from the extreme left.

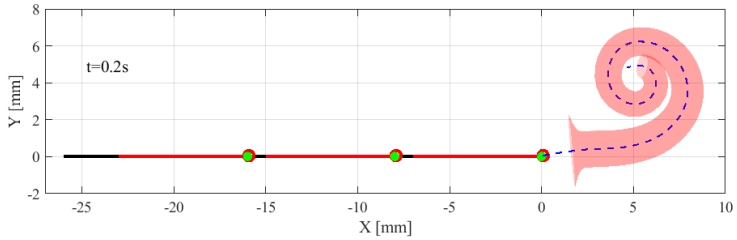

Figure 4.12: Active implant with three actuators and three control points.

Case 3. Four actuators and five control points

In the last simulation, we configure the implant to have a length of 26mm, consisting of four conducting polymer actuators, with each actuator measuring 5mm in length. The spacing between control points gradually decreases from the left end to the right end of the implant. The geometric structure of the active implant is depicted in Fig. 4.13.

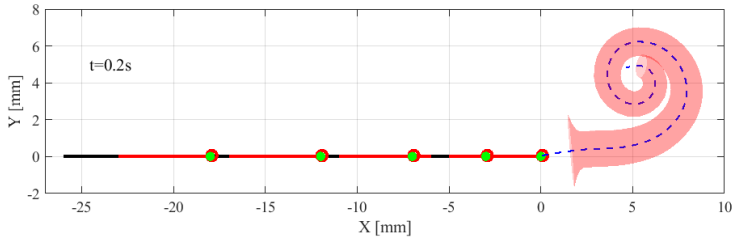

Figure 4.13: Active implant with four actuators and five control points.

For all simulations, the input voltage is limited to a range of ±3 volts, i.e., $V_{in} \in [-3\text{V}, 3\text{V}]$. The sampling time of discrete system is $h = 0.1s$. The implant advances at a speed of $0.1\text{mm}/s$. At each sampling instant,we retrieve the current optimal input voltage using the controller algorithm developed in Section 4.4.7 and subsequently feed it into the simulation.

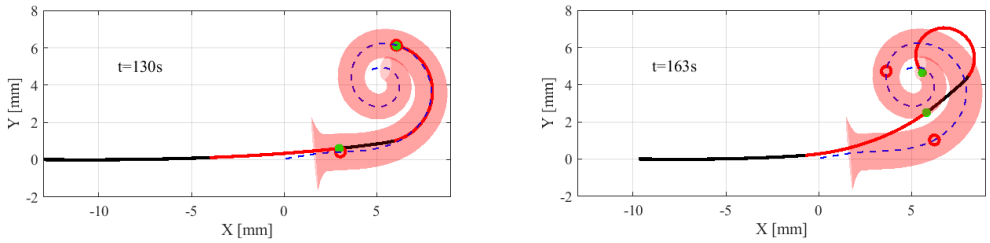

(a) t=130s (b) t=163s

Figure 4.14: Active implant optimal control tracking simulation of case 1.

Fig. 4.14, Fig. 4.15 and Fig. 4.16 respectively illustrate the optimal control simulation process for cases 1, 2 and 3, including the geometric poses of the implant at various time points and the evolution of input voltage over time. The reference trajectory followed by the implant is the center line of cochlea, as indicated by the blue line in the diagram. Since our objective is to test the trajectory tracking performance of the active cochlear implant relative to the cochlear centerline, without involving the calculation of contact forces, we do not consider the contact between the Electrode Array (EA) and the cochlea in any of our simulations.

The simulation results for Case 1 are presented in Fig. 4.14. It is clear that, due to the limited degrees of freedom provided by the two actuators, notable discrepancies emerge in the latter stages of the active implantation process. Specifically, there are significant errors in the distance between the control points and the target points. Furthermore, a substantial misalignment occurs between the shape of the implant and the cochlear centerline, resulting in the implant breaching the inner walls of the cochlea, as vividly depicted in Fig. 4.14.(b). Hence, the success of the active implant in effectively following the cochlear's spiral centerline largely hinges on the quantity of both actuators and control points. This means that having an adequate number of these components plays a pivotal role in the implant's performance. As we observed, the greater the number of actuators and control points, the better the implant's ability to avoid contact with the cochlear walls and remain close to the spiral centerline, thereby enhancing the overall implantation process.

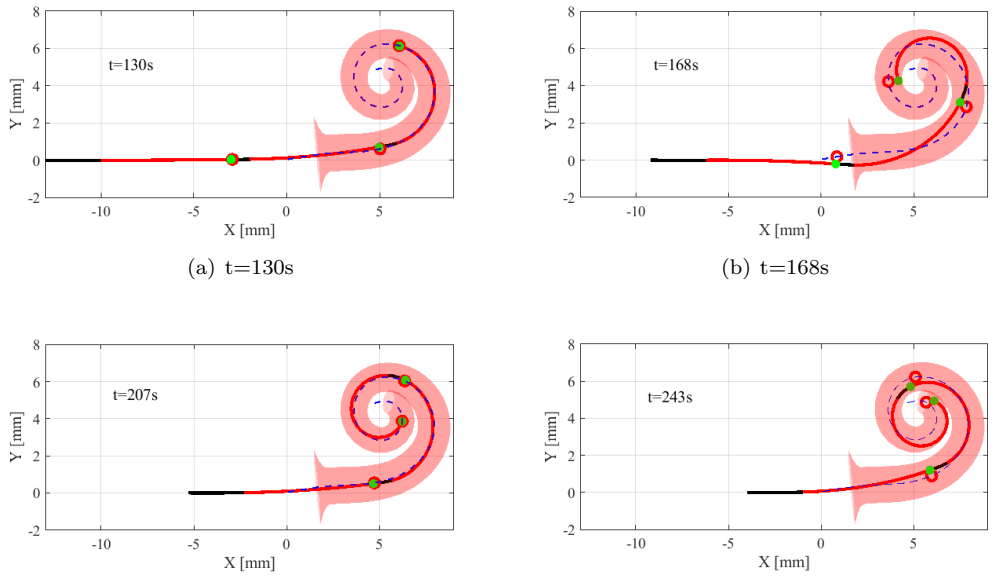

(a) t=130s (b) t=168s

(c) t=207s (d) t=243s

Figure 4.15: Active implant optimal control tracking simulation of case 2.

This challenging scenario is mitigated in Case 2 and Case 3, where the augmentation of both the number of actuators and control points brings about a substantial improvement. The simulation results demonstrate the successful insertion of both configurations of the active implant into the cochlea without contacting its inner wall. In the case of three drivers and three control points, occasional challenges arise in effectively tracking the target points. Moreover, certain sections of the implant struggle to conform seamlessly to the cochlear centerline, as portrayed in Fig. 4.15.(b) and Fig. 4.15.(d). However, this scenario sees improvement when adopting four drivers and expanding the control points to five, as depicted in Fig. 4.16.(b) and 4.16.(d). Despite having fewer degrees of freedom than the control points, the optimal control algorithm minimizes the positional error of control points, ensuring a more precise fit of the implant to the cochlear centerline. In essence, adopting the trajectory-tracking approach during cochlear implantation proves advantageous as it effectively prevents any undesirable contact between the active implant and the inner walls of the cochlea. This methodology not only minimizes the force exerted during the procedure but also reduces the risk of cochlear damage and the occurrence of buckling phenomena, contributing to an overall improvement in the depth of implantation.

In scenarios with fewer actuators or control points, as seen in Fig. 4.14, the implant's shape deviates from the ideal path due to the limitations of controlling actuators, which may not provide sufficient torque to conform to the cochlear's intricate shape. This limitation is particularly pronounced in the latter stages of the implantation process, as the implant reaches regions with higher curvature. However, it's essential to note that, under typical safe voltage conditions, the electrically controlled polymer actuators can sometimes reach their voltage constraints, as indicated in Fig. 4.17. The implant reaches a location along the cochlear centerline where the curvature is particularly high, the voltage applied to the rearmost actuator

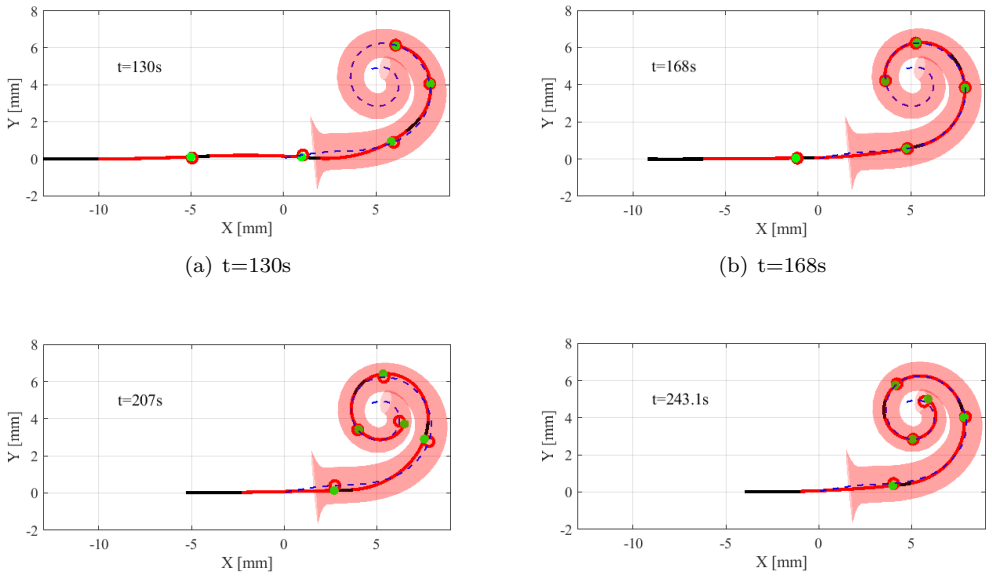

(a) t=130s (b) t=168s

(c) t=207s (d) t=243s

Figure 4.16: Active implant optimal control tracking simulation of case 3.

escalates, reaching a critical threshold of 3 volts. By implementing voltage limit constraints in the controller, we can effectively mitigate this issue, ensuring that the implant remains within safe electrical boundaries. This observation underscores the importance of electrical safety during the implantation procedure.

Furthermore, the spacing between the control points decreases progressively from the left end to the right end of the implant. This arrangement is tailored to adapt to the cochlear's natural shape, where the cochlear's curvature is more pronounced toward its center. Consequently, having more control points towards the end of the implant accommodates the cochlear's increasing curvature, enabling more precise tracking of the spiral centerline. This adaptation ensures that the implant's shape closely adheres to the cochlear's contour, particularly as it approaches the highly curved regions, thereby minimizing the risk of contact with the cochlear walls and improving the implant's insertion depth.

However, it is crucial to acknowledge that this approach comes with its own set of challenges. The requirement for multiple actuators to provide the necessary degrees of freedom can lead to increased structural complexity, thereby elevating the difficulty in manufacturing. Moreover, when operating within the constraints of safe electrical voltages for in vivo applications, electrolytic polymer actuators often face inherent limitations. These limitations primarily manifest as an inability to generate the required torque for the implant to bend into its desired state. This restriction in torque delivery has a significant impact on the active implant's performance. In essence, it restricts the implant's capacity to closely follow the cochlear centerline. Regardless of the effort and adjustments made in structure design, the limitations of the actuators become a decisive factor.

To address these challenges, an alternative strategy involves utilizing fewer actuators and incorporating a hybrid control method. This hybrid approach synergistically combines force

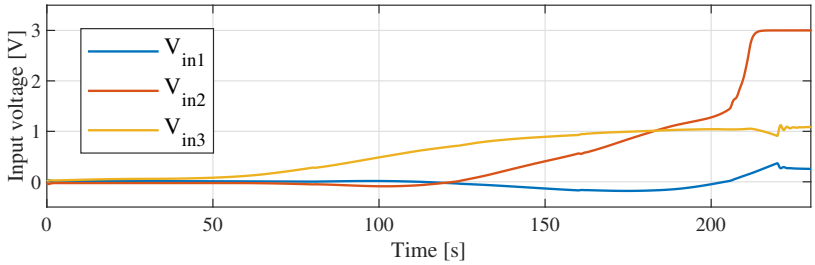

Figure 4.17: Optimal input voltage of case 2.

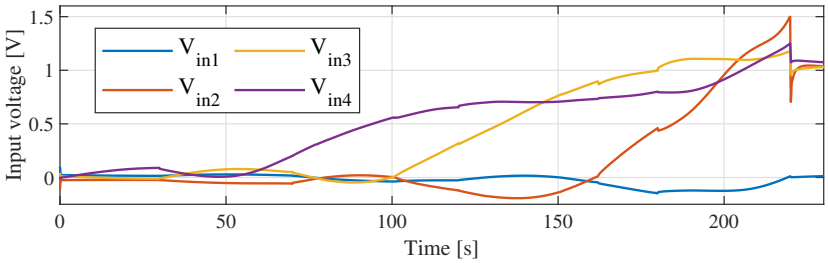

Figure 4.18: Optimal input voltage of case 3.

control, as discussed in Section 4.3, with trajectory control presented in Section 4.4. The primary goal is to mitigate contact between the implant and the cochlea while concurrently minimizing the thrust force applied during the implantation process.

This hybrid methodology introduces a novel dimension to cochlear implantation, aiming to strike a balance between the intricacies of control precision and the practicality of implementation. The subsequent chapters will delve into the intricacies of this method.

4.5 Hybrid Control Considering Contact

Before delving into the contents of this subsection, it's worth revisiting the control objectives set out at the beginning of this chapter regarding cochlear implantation. As we move forward, these objectives will lay the foundation for introducing the concept of hybrid control. For hybrid control, our control objectives are as follows:

$$\underset{\boldsymbol{\phi}_0, \boldsymbol{V}_{in}}{\arg\min} \quad \mathscr{H} = \int_0^T w_a \mathcal{F}(t) + w_b \mathcal{D} dt \tag{4.40}$$

where $\mathcal{F}(t)$ is the insertion force during the insertion and $\mathcal{D}$ is the mean distance between implant and the spiral centerline of the cochlea. w_a and w_b are two weighting coefficients. In the hybrid control approach we've discussed in this chapter, the control variables consist of the orientation of the end-effector ($\boldsymbol{\phi}_0$), as well as the input voltage to the conducting polymer actuators ($\boldsymbol{V}_{in}$).

To solve the aforementioned optimization problem (4.40), we have divided it into two sequential optimization steps. This technique has been widely employed in numerical computing for multi-objective optimization [135]. We've devised a two-step approach to tackle this hybird

optimization problem: optimizing the insertion force and tracking the trajectory. In the first step, we focus on controlling the insertion force. This entails adjusting the position and orientation of the implant base, leveraging the control method we discussed in the initial chapter. Throughout this phase, we keep the input voltage to the actuators constant.

Once we've successfully completed the first step, we transition to the second phase. Here, we maintain the position and orientation of the base in a fixed state while actively controlling the input voltages. The objective in this phase is to ensure that the control points on the implant closely adhere to the predetermined target trajectory.

It's worth noting that the performance of the actuators may impose certain limitations. As a result, during the actual implantation process, the implant might still come into contact with the walls of the cochlea. Therefore, in the second step, we take this into account by incorporating a the contact model presented in Chapter 3. We'll delve into the specifics of the control strategy for this scenario and highlight how it differs from what we discussed in the previous Section 4.4.

The comprehensive framework for our hybrid control approach is depicted in Fig. 4.19. This approach not only enhances the precision of the implantation process but also addresses potential challenges posed by contact with the cochlear walls.

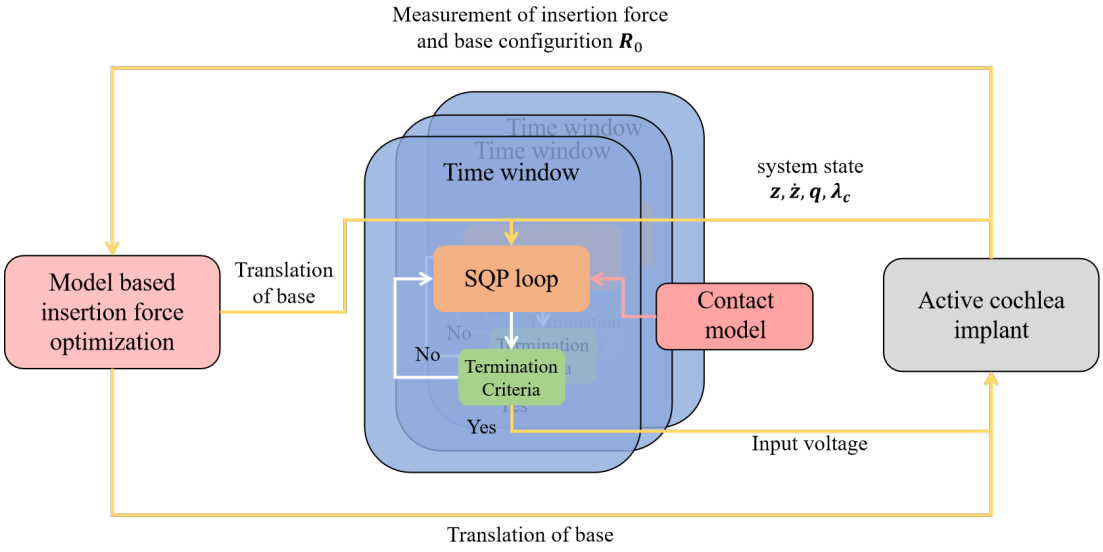

Figure 4.19: Framework of hybrid control considering contact. The hybrid control strategy is executed in two phases. The first step involves controlling the end-effector to minimize the implantation force. Once the position of the end-effector is stabilized, we proceed to the second phase of model predictive control. Considering the contact between the EA and the cochlea, we incorporate the contact forces obtained from simulations into our control model. We then calculate the optimal input voltage to drive the CPA, inducing deformation in the EA so that it conforms to the cochlear centerline.

4.5.1 Optimization Problem for the Second Control Step

In the above mentioned second control step, the introduced contact model will modify the optimization problem (4.25) of the previous subsection in order to minimize the tracking error

and control effort with respect to the target trajectory while considering the contact forces between the active implant and the cochlear wall. The optimization problem can be formulated as follows:

$$\underset{\boldsymbol{V}_{in}(t)}{\arg\min} \quad \mathscr{H} = \Sigma_{i=1}^{i=m} w_i \int_{t_f}^{t_d} \|^2 \boldsymbol{p}_{ri}(t) - \boldsymbol{p}_i(t)\| \mathrm{dt} \tag{4.41}$$

subject to

$$\boldsymbol{A}\dot{\boldsymbol{z}} + \boldsymbol{B}\boldsymbol{z} = \boldsymbol{U}\boldsymbol{V}_{\boldsymbol{in}} \tag{4.42}$$

$$\boldsymbol{K}\boldsymbol{q} + \boldsymbol{H}\boldsymbol{z} + \boldsymbol{H}_c\boldsymbol{\lambda}_c = \boldsymbol{0} \tag{4.43}$$

$$\boldsymbol{G}_c - \boldsymbol{E}_c\boldsymbol{\lambda}_c = \boldsymbol{0} \tag{4.44}$$

$$\boldsymbol{p}_i = \boldsymbol{D}\boldsymbol{g}_i\boldsymbol{E} \ , \ i = 1, \ldots, m \tag{4.45}$$

where the item $\boldsymbol{H}_c\boldsymbol{\lambda}_c$ in (4.43) denotes the contribution of contact force to the mechanic model. (4.44) represents the contact constraint, as we introduced in Section 3.5.4. In this optimization problem, we apply the same SQP-based solving approach as presented in Section 4.4. Consequently, we won't delve into the details of the solution method here.

4.5.2 Simulation

In order to emphasize the necessity of the proposed control algorithm, we first conducted simulation of the structure without any control mechanisms implemented. The average Young's modulus of the implant material was set at 30 MPa, and a friction coefficient of 0.25 was considered in the simulation. The structural configuration used in these experiments is depicted in the Fig. 4.20. The results showed that during the initial stages of the implantation process, buckling occurred.

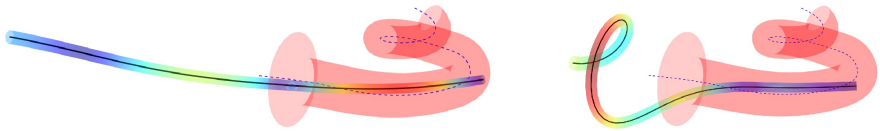

Figure 4.20: Bulking occurs during the insertion without control.

Fig. 4.21 illustrates the variation of insertion force over time during the implantation process. As depicted in the Fig. 4.21, there is a sharp increase in insertion force at around 110 seconds, indicating the occurrence of buckling in the implant. This preliminary simulation serve as the baseline, providing the motivation for the development of control strategies to overcome the buckling and ensure successful implantation.

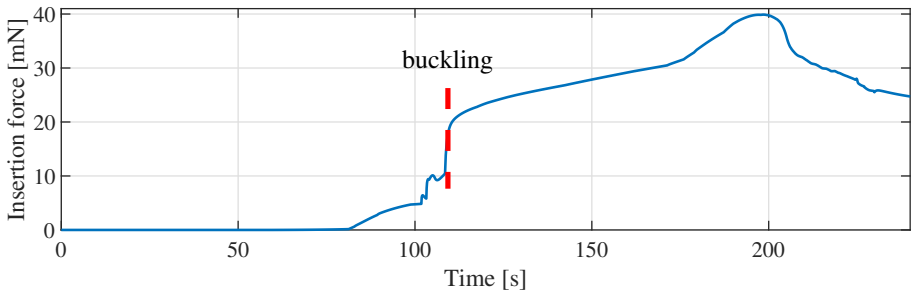

Figure 4.21: Insertion force of buckling scenario.

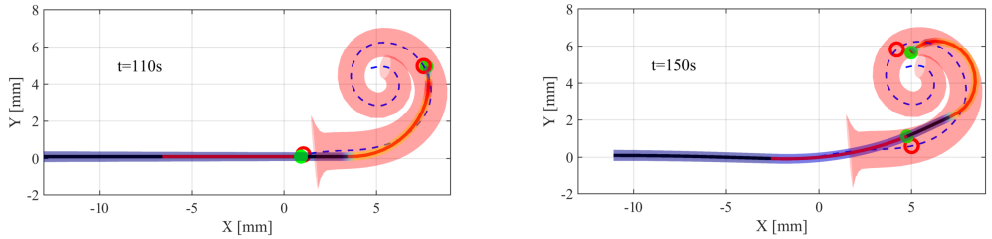

(a) t=110s (b) t=150s

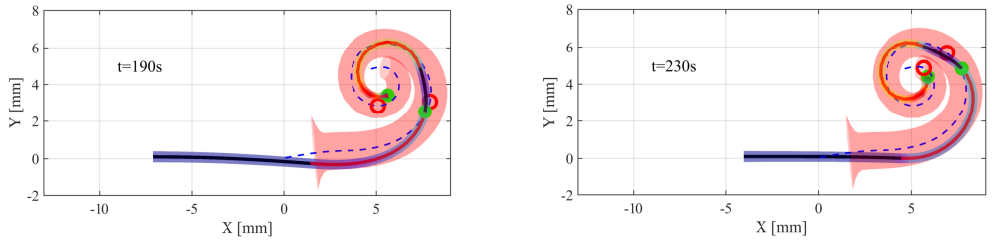

(c) t=190s (d) t=230

Figure 4.22: Trajectory tracking control simulation in case of two actuator and two control points.

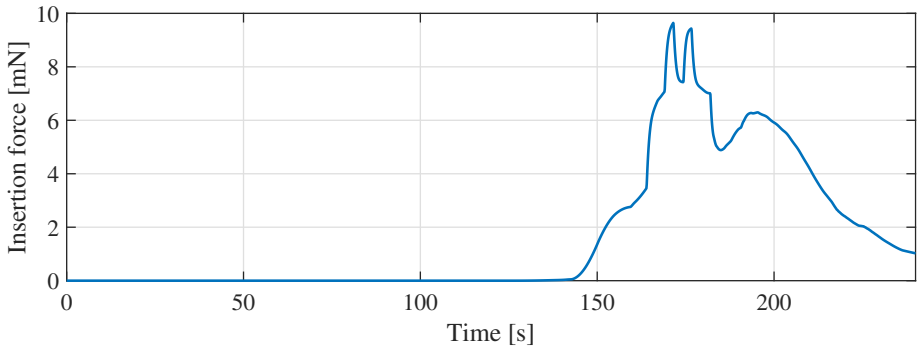

Figure 4.23: Insertion force of trajectory tracking control considering the contact.

As discussed in the simulation of Section 4.4, it became evident that when the implant's actuators lack the necessary performance, the implant struggles to accurately follow the cochlear trajectory and might breach the cochlear wall, as observed in Case 1 of the simulation subsection in Fig. 4.14. The control strategy proposed here has been developed to address precisely this scenario.

In the following set of simulations, we maintain the same implant configuration as in Case 1 (Fig. 4.11), which includes two actuators and two control points. This choice allows us to investigate how this control approach can mitigate the challenges posed by insufficient actuator performance, such as avoiding the influence of undesirable penetrations while navigating the

cochlear structure. The input voltage applied to the actuators is regulated within the range of ±3 volts to prioritize safety when interacting with the human body. Additionally, there are constraints on the orientation of the implant base. It must maintain an angle of less than thirty degrees concerning the horizontal axis at the entrance to the cochlea. This specific constraint is vital to ensure the implant's ability to navigate effectively within the confined and sensitive space at the cochlear entrance. These limitations and regulations collectively contribute to the safety and feasibility of the implantation process.

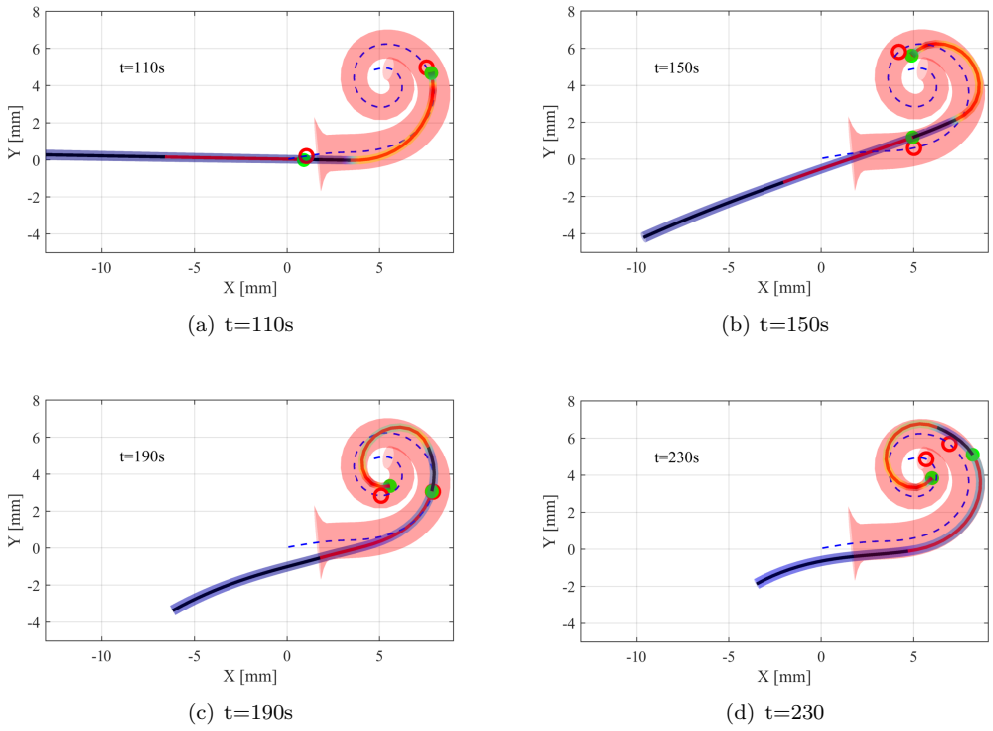

(a) t=110s (b) t=150s

(c) t=190s (d) t=230

Figure 4.24: Hybrid control simulation in case of two actuator and two control points.

The initial simulation focuses exclusively on trajectory tracking control, while simultaneously maintaining a consistent angle of advancement for the implant base. A notable distinction from the previous chapter is the inclusion of a contact model accounting for interactions between the implant and the cochlea. Fig. 4.22 provides a comprehensive visual representation of the control simulation procedure, while Fig. 4.23 effectively portrays the dynamic fluctuations in insertion force experienced throughout the implantation process.

Following the initial simulation, the second simulation incorporates hybrid control strategies. In this scenario, trajectory tracking is seamlessly combined with optimization of the implant base's angular progression. Once again, we maintain the inclusion of the contact model, accounting for the interactions between the implant and the cochlea. Fig. 4.24 provides a visual representation of this integrated control simulation process, while Fig. 4.25 illustrates the dynamic variations in insertion force during the implantation process.

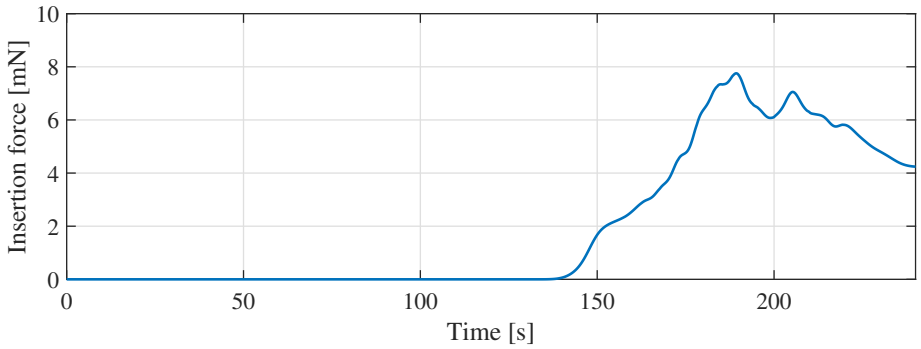

Figure 4.25: Insertion force.

4.6 Conclusion

In this chapter, we have meticulously designed and evaluated various optimal controllers tailored to distinct control objectives for cochlear implantation. Our approach has been bifurcated based on the type of cochlear implant: passive and active.

For passive cochlear implants, which lack internal actuators, we developed an optimal implantation path controller. Empirical evidence from our experiments suggests that this path planning significantly enhances implantation depth. By meticulously calculating the optimal path, we have been able to guide the implant more deeply into the cochlea, potentially improving the auditory outcomes for recipients.

In contrast, for active cochlear implants equipped with actuators, we designed a controller based on model predictive control. This advanced controller aims to achieve precise trajectory tracking along the cochlear spiral's central axis. Our simulations demonstrate that, with a sufficient number of actuators, the controller can effectively guide the implant's electrode array along the desired path within the cochlea. This capability is crucial for avoiding contact between the electrode sequence and the cochlear walls during implantation, thereby minimizing potential damage and enhancing the safety and effectiveness of the procedure.

Furthermore, we combined the principles underlying these two approaches to create a hybrid optimal controller that considers the contact model. This controller is particularly relevant when the number of actuators is insufficient to ensure that the electrode sequence precisely follows the cochlear spiral's central axis. In such scenarios, inevitable contact with the cochlear walls occurs. The hybrid controller, equipped with the contact model, adeptly manages both the implantation path and actuator input voltages. This dual control mechanism significantly reduces the contact force, thereby mitigating the risk of cochlear damage and optimizing the implantation process.

Chapter 5

Conclusion and Perspectives

5.1 Conclusion

In recent years, significant advancements have been made in cochlear implant technology, especially in mechanical modeling, simulation, and control. However, challenges such as computational complexity and simulation precision persist. This thesis, details substantial progress in Active Cochlear Implants (ACI) technology.

In Chapter 2 of this thesis, we significantly advanced Active Cochlear Implants (ACI) by enhancing their system modeling. Our primary achievement was developing a sophisticated mechanical model for the Electrode Array, blending Cosserat rod theory with Lie group integration. This resulted in a model that accurately mirrors the actual system with reduced complexity and excels in managing nonlinear dynamics. We also created an electronic-mechanical model for the Electronic Conducting Polymer, simplifying complexities and precisely controlling deformations. An innovative parameter identification method and a custom visual identification system were introduced to address uncertainties in physical parameters. The chapter culminates with a comprehensive coupling model integrating both EA and ECP components, marking a significant leap in model-based control for ACIs. These developments pave the way for more refined, efficient, and effective cochlear implant models, setting the stage for future research in this field.

Chapter 3 introduces a pioneering contact dynamics model for soft robots, based on Cosserat theory. This model provides a detailed analysis of the complex geometrical relationships, forces, and moments at contact points, crucial for understanding the dynamics of soft robots and particularly vital in cochlear implant technology. We have successfully established and refined contact constraints, incorporating non-penetration, force balance, and frictional interactions. These advancements enable direct resolution of the contact dynamics system, significantly enhancing the model's accuracy and reliability, as validated against empirical results. This model is not only critical for improving cochlear implant design and control strategies but also marks a significant leap in the field of soft slender robotics. Looking forward, we aim to extend this framework to include robots with integrated actuation mechanisms, such as cable, tendon, or magnet-driven systems, thereby broadening the scope of our research in cochlear implant control and simulation. This work not only advances cochlear implant technology but also opens new avenues in the application of soft robotics.

In Chapter 4 of our research, we have developed and evaluated various optimal controllers for cochlear implantation, tailored to address specific requirements of both passive and active cochlear implants. For passive implants, which lack internal actuators, we introduced an

optimal path controller that significantly deepens the implantation, potentially enhancing auditory outcomes. For active implants, equipped with actuators, we crafted a model predictive control-based controller aimed at ensuring precise trajectory following within the cochlea. This is crucial for preventing damage during implantation by avoiding contact with cochlear walls. Additionally, recognizing scenarios where the number of actuators might be insufficient, we innovated a hybrid optimal controller that combines both approaches and includes the contact model. This hybrid system adeptly manages implantation path and actuator inputs, significantly reducing contact force and thereby minimizing cochlear damage, optimizing the overall implantation process. This chapter signifies a pivotal advancement in cochlear implant technology, offering sophisticated control strategies to improve safety and efficacy in cochlear implant procedures.

Overall, this thesis advances ACI technology, laying a foundation for future work and enhancing auditory experiences for CI recipients. The methodologies and insights from this study pave the way for more refined, efficient, and effective CI models, contributing significantly to the field.

5.2 Perspectives

5.2.1 Patient's cochlea specific

In our current research endeavors, we focus on simulations and control strategies grounded in the established 3D dimensions of the cochlea. It is essential to recognize, however, that individual variations in cochlear size are significant, necessitating the acquisition of specific 3D measurements for each patient prior to cochlear implant surgery. Typically, this process involves utilizing CT (Computed Tomography) scans to acquire detailed images of a patient's cochlear structure.

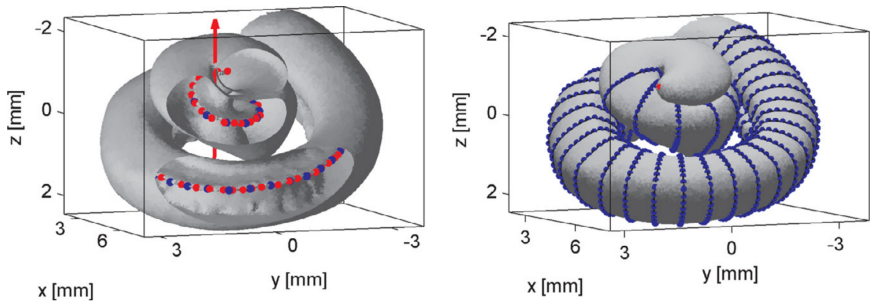

Figure 5.1: A curved structure representing the cochlear skeleton is derived (left). This skeleton is then used to parameterize cross-sections of the surface, resulting in a cochlear shape description based on corresponding pseudo-landmarks (right). [30]

Our methodology commences with a high-resolution CT scan of the patient's temporal bone, encompassing the cochlea. These scans are adept at capturing the intricate details of the inner ear's anatomy, thus providing invaluable data for our research. Post-scan, we employ sophisticated software to process these images. Through a combination of algorithms and image processing techniques, we convert these two-dimensional slices into a comprehensive three-dimensional model of the patient's cochlea. It's worth noting that recent advancements in CT technology have facilitated the creation of algorithms robust against artifacts, specifically

for automatic segmentation of the inner ear's anatomy in post-cochlear-implantation scans [136, 137]. Once we have acquired the 3D spatial data of the cochlea, we can establish a three-dimensional analytical model of the cochlea through data fitting. This can involve using spline curves to fit the central axis of the cochlea as well as the cross-sectional profiles of the cochlea, as shown in Fig. 5.1. After that, we can then use the proposed methods in Chapters 3 and 4 to model and control the implant implantation.

This 3D model is not merely instrumental for our simulation and control strategy development, but it also serves as an essential preoperative tool for surgeons. It enables more precise planning of cochlear implant procedures, tailored to each patient's unique anatomical structure. For example, understanding the exact dimensions and shape of the cochlea allows surgeons to select the most suitable implant type and size, and strategize the insertion angle and depth to minimize trauma while maximizing auditory outcomes. Moreover, employing CT scans in cochlear implant surgery is crucial for examining the electro-neural interface in cochlear implant users. This involves correlating CT scan results with electrode-modiolar distances and patient outcomes, particularly in terms of auditory response thresholds and speech understanding [138]. Such comprehensive assessments are vital in improving the effectiveness of cochlear implant surgeries and ensuring optimal auditory rehabilitation for patients.

5.2.2 Modeling of anatomical structure of inner ear

In the field of cochlear implant surgery, our current research primarily focuses on the simulation and control of the implantation process. However, our approach is based solely on the structure of the cochlea itself, without taking into account the influence of surrounding ear structures. This narrow focus overlooks a critical aspect of the surgical environment.

The inner ear, beyond the cochlea, comprises various anatomical structures, including blood vessels, facial nerve and bones, as shown in Fig. 5.2. These elements pose significant constraints during surgery, particularly affecting the movement and operational scope of the robotic tools used in the procedure. The presence of these structures around the cochlea can significantly limit the path of implantation. Therefore, avoiding any damage or interference with these delicate tissues is crucial during the surgery.

Acknowledging the complexity of the inner ear environment is thus vital for the advancement of cochlear implant surgeries. Future research and development in this field need to address two key areas:

1. Development of a Comprehensive 3D Model: The creation of an intricate 3D geometric model of the entire inner ear structure is essential. This model should not only detail the cochlea but also include the surrounding tissues, vessels, and bones. The aim is to establish a clear understanding of the available space for implantation, facilitating the planning and execution of the surgery with greater precision.

2. Enhanced Path Planning for Implantation: Considering the potential contact between the robotic end effector and the external structures of the cochlea, it becomes imperative to integrate obstacle avoidance strategies in the surgical procedure. This involves formulating a new implantation pathway that minimizes the risk of tissue damage while ensuring the effective placement of the cochlear implant.

By incorporating these elements into cochlear implant surgery, we can significantly improve the safety, accuracy, and outcomes of the procedure. In future work, we can geometrically model other external tissue structures of the cochlea and incorporate them as obstacle constraints in the optimization problem to solve for the optimal implantation trajectory.

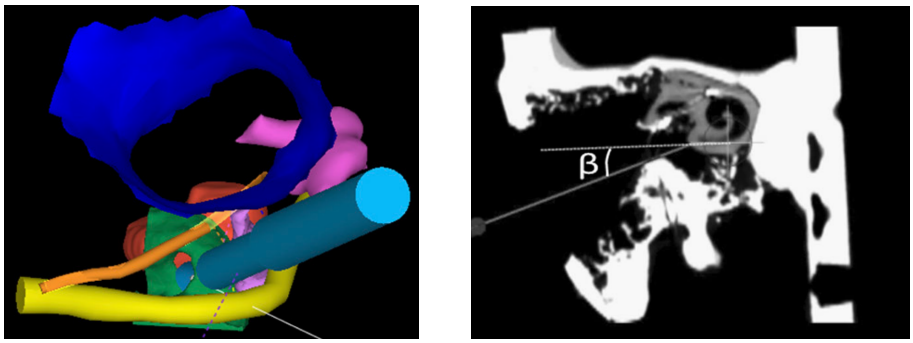

(a) (b)

Figure 5.2: (a) Red coloration represents the cochlear segmentation, which is automatically computed by the software. Green coloration indicates the bony overhang, also automatically calculated by the software. The facial nerve is depicted with yellow coloration, while the external ear canal is shown in dark blue. The ossicles are highlighted in pink, and the chorda tympani is marked in orange. Lastly, the drill's position along the automated trajectory is shown in light blue shading. [139] (b) Cross-sectional view of the temporal bone, where the angle β in the diagram indicates the range of motion of the implantation tool (end-effector) outside the cochlear window. [140]

5.2.3 From simulation to clinic test

In future endeavors, it's essential to move beyond the confines of modeling and controlling cochlear implants in simulated environments to conducting clinical trials with real cochleae. This transition is a critical step in validating and refining the theoretical models and control systems we've developed for cochlear implants. To ensure the safety and effectiveness of these implants, real-world testing is indispensable.

An ideal starting point for this transition would be animal studies. Testing on animal cochleae allows us to closely examine the practical application and impact of the implants in a living system, which can differ significantly from simulated environments. These animal trials would provide invaluable insights into how the implants interact with biological tissues, the nuances of implant positioning and control, and the overall biocompatibility of the devices.

In summary, integrating real cochleae testing, starting with animal studies, is a crucial step in the advancement of cochlear implant technology. It bridges the gap between theoretical models and practical application, paving the way for more effective, safe, and reliable cochlear implants in the future.

5.2.4 From cochlear implantation to other applications

In our research, we have conducted extensive physical modeling of the electrode array in cochlear implants, accurately simulated the 3D structure of the cochlea, and analyzed the mechanical interactions between the electrode array and the cochlea. Based on these models, we further designed an optimized control algorithm to enhance the precision and safety of the implantation surgery. The innovation of these technologies lies not only in their significant implications for cochlear implant surgery but also in their potential applications in other medical surgeries that require precise modeling and control.

Specifically, our technology can be applied to the following types of surgeries:

- Ventriculoscopic Surgery: This surgery utilizes a tube-like tool similar to an endoscope for precise navigation within the brain's ventricles. The operational precision required here is similar to that in the placement of the electrode array in cochlear implant surgeries.
- Cardiac Catheterization Surgery: In this type of surgery, a slender catheter must be accurately placed inside the heart, paralleling the complexity of implanting electrodes in cochlear surgery and similarly relying on detailed vascular models.
- Minimally Invasive Neurosurgery: In this type of surgery, tiny tools are used to operate within the brain or spinal cord, which may involve micro actuators, requiring the same level of fine manipulation and accuracy as in the implantation of cochlear electrodes.
- Gastrointestinal Endoscopic Surgery: In these surgeries, a flexible tube-like endoscope operates in the narrow spaces of the gastrointestinal tract, presenting technical challenges similar to those encountered in navigating the narrow cochlear passages.

By applying our innovations in cochlear implant technology to these surgeries, we can not only enhance their safety and efficacy but also bring new technological advancements and therapeutic possibilities to these specific surgical fields.

Appendix A

Theoretical Background for Modeling

A.1 Rigid body Motions

To describe the configuration of the rigid body in 3D space, only the position and orientation of the body frame with respect to the fixed frame need to be specified. The configuration of the frame attached to the body with respect to a fixed reference frame can be expressed as a 4×4 matrix, which not only stands for the configuration of a frame, but can also be used to translate and rotate a vector or a frame, and change the representation of a vector or a frame from coordinates in one frame to ones in another frame.

The angular and linear velocities are combined together into a six-dimensional (6D) vector called a twist, while torques and forces are packaged together into a 6D vector called a wrench. The twist, wrench, and Newton-Euler formulation lay the foundation for the kinematic and dynamic analysis of manipulators, and they allow a global description of rigid-body motion without being affected by singularities due to the use of local coordinates. In the following, we will briefly illustrate these concepts.

A.1.1 Rotation Matrices

There are nine entries in the rotation matrix $\boldsymbol{R}$, however, only three can be chosen independently due to the unit norm and orthogonality conditions. The set of 3×3 rotation matrices forms the special orthogonal group $SO(3)$, which can be defined as follows.

Definition 1. *The special orthogonal group $SO(3)$, known as the group of rotation matrices, is the set of all 3×3 real matrices $\boldsymbol{R}$ that satisfy*

$$\boldsymbol{R}^\top \boldsymbol{R} = \mathbf{I}_3$$

and

$$\det \boldsymbol{R} = +1$$

where the additional constraint $\det \boldsymbol{R} = +1$ means that only right-handed frames are allowed.

A rotation matrix $\boldsymbol{R}$ aims at representing an orientation, changing the reference frame, and rotating a vector or a frame.

A.1.2 Angular Velocities

The rotation matrix $\boldsymbol{R}(t)$ describes the orientation of the body frame with respect to the fixed frame at time t. $\boldsymbol{\omega}_A$ and $\boldsymbol{\omega}_B$ are defined as the vector representations of the same angular velocity $\boldsymbol{\omega}$ in inertial frame and body frame at time t, respectively. Thus, the time evolution of rotation matrix can be obtained

$$\dot{\boldsymbol{R}} = \boldsymbol{\omega}_A \times \boldsymbol{R} = \widetilde{\boldsymbol{\omega}}_A \boldsymbol{R} \tag{A.1}$$

where $\widetilde{\boldsymbol{\omega}}_A$ is a 3×3 skew-symmetric matrix representation of $\boldsymbol{\omega}_A \in \mathbb{R}^3$.

Definition 2. *Given a vector* $\boldsymbol{a} = \begin{bmatrix} a_1 & a_2 & a_3 \end{bmatrix}^\top$, *define*

$$\widetilde{\boldsymbol{a}} = \begin{bmatrix} 0 & -a_3 & a_2 \\ a_3 & 0 & -a_1 \\ -a_2 & a_1 & 0 \end{bmatrix}$$

as a 3×3 *skew-symmetric matrix representation of* $\boldsymbol{a}$*; that is,*

$$\widetilde{\boldsymbol{a}} = -\widetilde{\boldsymbol{a}}^\top$$

The set of all 3×3 real skew symmetric matrices is called $so(3)$ which is the Lie algebra of the special orthogonal group $SO(3)$. A useful property involving rotation and skew symmetric matrices is introduced as follows.

Proposition 1. *Given any* $\boldsymbol{\omega} \in \mathbb{R}^3$ *and* $\boldsymbol{R} \in SO(3)$*, the following equality always holds:*

$$\boldsymbol{R}\widetilde{\boldsymbol{\omega}}\boldsymbol{R}^\top = \widetilde{\boldsymbol{R}\boldsymbol{\omega}}$$

Post-multiplying both sides of (A.1) by $\boldsymbol{R}^\top$ to obtain

$$\widetilde{\boldsymbol{\omega}}_A = \dot{\boldsymbol{R}}\boldsymbol{R}^\top$$

To obtain the angular velocity $\boldsymbol{\omega}_B$ expressed in the body frame from $\boldsymbol{\omega}_A$, we have

$$\boldsymbol{\omega}_B = \boldsymbol{R}^\top \boldsymbol{\omega}_A,$$

which can also be expressed in skew-symmetric matrix representation using the Proposition 1 as follows

$$\widetilde{\boldsymbol{\omega}}_B = \boldsymbol{R}^\top \dot{\boldsymbol{R}}$$

Finally, we discovered that pre-or post-multiplying $\dot{\boldsymbol{R}}$ by $\boldsymbol{R}^\top$ leads to a skew-symmetric representation of the angular velocity vector, either in fixed- or body-frame.

A.1.3 Homogeneous Transformation Matrices

A natural choice of representations for the orientation and position of a rigid body is to use a rotation matrix $\boldsymbol{R} \in SO(3)$ to describe the orientation of the body frame $\{B\}$ in the fixed frame $\{A\}$ and a vector $\boldsymbol{p} \in \mathbb{R}^3$ to stand for the origin of the body frame in the fixed frame. They are packaged into a single matrix as follows.

Definition 3. *The special Euclidean group SE(3), regarded as the group of homogeneous transformation matrices, is the set of all* 4×4 *real matrices* $\boldsymbol{T}$ *of the form:*

$$\boldsymbol{T} = \begin{bmatrix} \boldsymbol{R} & \boldsymbol{p} \\ \boldsymbol{0} & 1 \end{bmatrix}$$

where $\boldsymbol{R} \in SO(3)$ *and* $\boldsymbol{p} \in \mathbb{R}^3$ *is a column vector.*

The same representation can also be used for a rigid body transformation between two coordinate frames.

A.1.4 Twists

The infinitesimal version of the screw motion is called a twist, which describes the instantaneous velocity of a rigid body in terms of linear and angular components, and plays an important role in formulation of the kinematics and dynamics of robotic mechanisms. The homogeneous transformation matrix $\boldsymbol{T}$ represents the configuration of body frame as seen from the inertial coordinate frame. To obtain the velocity twists in the moving frame and fixed frame, we will calculate $\boldsymbol{T}^{-1}\dot{\boldsymbol{T}}$ and $\dot{\boldsymbol{T}}\boldsymbol{T}^{-1}$, respectively. The calculation of $\boldsymbol{T}^{-1}\dot{\boldsymbol{T}}$ yields

$$\boldsymbol{T}^{-1}\dot{\boldsymbol{T}} = \begin{bmatrix} \boldsymbol{R}^\top & -\boldsymbol{R}^\top\boldsymbol{p} \\ \boldsymbol{0} & 1 \end{bmatrix} \begin{bmatrix} \dot{\boldsymbol{R}} & \dot{\boldsymbol{p}} \\ \boldsymbol{0} & 0 \end{bmatrix} = \begin{bmatrix} \boldsymbol{R}^\top\dot{\boldsymbol{R}} & \boldsymbol{R}^\top\dot{\boldsymbol{p}} \\ \boldsymbol{0} & 0 \end{bmatrix} = \begin{bmatrix} \widetilde{\boldsymbol{\omega}}_B & \boldsymbol{v}_B \\ \boldsymbol{0} & 0 \end{bmatrix}$$

where $\boldsymbol{R}^\top\dot{\boldsymbol{R}} = \widetilde{\boldsymbol{\omega}}_B$ is just the skew-symmetric matrix representation of the angular velocity expressed in the body frame, $\dot{\boldsymbol{p}}$ represents the linear velocity of the origin of body frame expressed in the fixed frame, while $\boldsymbol{v}_B$ is the linear velocity expressed in the body frame. The angular and linear velocities are merged into a single 6D vector called body velocity twist, and it is given by

$$\boldsymbol{\eta}_B = \begin{bmatrix} \boldsymbol{w}_B \\ \boldsymbol{v}_B \end{bmatrix} \in \mathbb{R}^6$$

Just as a skew-symmetric matrix representation of an angular velocity vector, a matrix representation of a twist can be formulated as

$$\widehat{\boldsymbol{\eta}}_B = \boldsymbol{T}^{-1}\dot{\boldsymbol{T}} = \begin{bmatrix} \widetilde{\boldsymbol{\omega}}_B & \boldsymbol{v}_B \\ \boldsymbol{0} & 0 \end{bmatrix} \in se(3)$$

where the symbol$\widehat{\ }$represents the isomorphism between the vector space $\mathbb{R}^6$ and $se(3)$.

Next, the calculation of $\dot{\boldsymbol{T}}\boldsymbol{T}^{-1}$ is given by

$$\dot{\boldsymbol{T}}\boldsymbol{T}^{-1} = \begin{bmatrix} \dot{\boldsymbol{R}} & \dot{\boldsymbol{p}} \\ \boldsymbol{0} & 0 \end{bmatrix} \begin{bmatrix} \boldsymbol{R}^\top & -\boldsymbol{R}^\top\boldsymbol{p} \\ \boldsymbol{0} & 1 \end{bmatrix} = \begin{bmatrix} \dot{\boldsymbol{R}}\boldsymbol{R}^\top & \dot{\boldsymbol{p}} - \dot{\boldsymbol{R}}\boldsymbol{R}^\top\boldsymbol{p} \\ \boldsymbol{0} & 0 \end{bmatrix} = \begin{bmatrix} \widetilde{\boldsymbol{w}}_A & \boldsymbol{v}_A \\ \boldsymbol{0} & 0 \end{bmatrix}$$

where $\dot{\boldsymbol{R}}\boldsymbol{R}^\top = \widetilde{\boldsymbol{w}}_A$ represents the angular velocity expressed in the fixed frame, and $\boldsymbol{v}_A$ is the instantaneous velocity of the point on this body expressed in the fixed frame. As we did above, $\boldsymbol{w}_A$ and $\boldsymbol{v}_A$ are assembled into a 6D spatial velocity twist, and its matrix representation can be expressed as

$$\widehat{\boldsymbol{\eta}}_A = \dot{\boldsymbol{T}}\boldsymbol{T}^{-1} = \begin{bmatrix} \widetilde{\boldsymbol{w}}_A & \boldsymbol{v}_A \\ \boldsymbol{0} & 0 \end{bmatrix} \in se(3)$$

Finally, we will find out the relationship of the velocity twists in the frames $\{A\}$ and $\{B\}$, $\boldsymbol{\eta}_A$ from $\boldsymbol{\eta}_B$ is then given by

$$\boldsymbol{\eta}_A = [\boldsymbol{T}\widehat{\boldsymbol{\eta}}_B\boldsymbol{T}^{-1}]^\vee = \begin{bmatrix} \boldsymbol{R}\widetilde{\boldsymbol{w}}_B\boldsymbol{R}^\top & -\boldsymbol{R}\widetilde{\boldsymbol{w}}_B\boldsymbol{R}^\top\boldsymbol{p} + \boldsymbol{R}\boldsymbol{v}_B \\ \boldsymbol{0} & 0 \end{bmatrix}^\vee = \underbrace{\begin{bmatrix} \boldsymbol{R} & \boldsymbol{0}_{3\times3} \\ \widetilde{\boldsymbol{p}}\boldsymbol{R} & \boldsymbol{R} \end{bmatrix}}_{\mathrm{Ad}_{\boldsymbol{T}}} \boldsymbol{\eta}_B \tag{A.2}$$

where the symbol $\vee$ is an operator about mapping a matrix into a vector, and Ad represents the Adjoint representation defined in Appendix B.

A.1.5 Exponential Coordinate Representation

Every rigid body motion can be realized by unifying a rotation about a fixed axis and a translation parallel to this axis [141]. Considering the above definition of the matrix representation of the body velocity twist $\boldsymbol{\eta}_B$, we have

$$\dot{\boldsymbol{T}} = \boldsymbol{T}\widehat{\boldsymbol{\eta}}_B$$

which is a differential equation on a Lie group. If $\widehat{\boldsymbol{\eta}}_B$ is independent of time t, the analytical solution of this equation can be formulated as

$$\boldsymbol{T}(t) = \boldsymbol{T}(0)e^{\widehat{\boldsymbol{\eta}}_B t} \tag{A.3}$$

where $\boldsymbol{T}(0)$ is the initial configuration of a rigid body, and $e^{\widehat{\boldsymbol{\eta}}_B t}$ maps an element of the Lie algebra $\widehat{\boldsymbol{\eta}}_B \in se(3)$ into an element of the Lie group $\boldsymbol{T} \in SE(3)$.

According to the Proposition 2.9 in [142], every rigid transformation $\boldsymbol{T}$ can be written as the exponential of some twist. In (A.3), the exponential map can be viewed as a local parameterization that provides solutions to a linear differential equation on a Lie group. The exponential of a twist as a mapping from initial to final configurations is especially important when we investigate the kinematics of robotic mechanisms in the following chapters.

A.1.6 Wrenches

A generalized force acting on a rigid body consists of a linear component (pure force) and an angular component (pure torque). Just as the linear and angular components of velocities merged as twists, we can also merge torques and forces into a single 6D vector called wrench as

$$\boldsymbol{\mathcal{F}} = \begin{bmatrix} \boldsymbol{m} \\ \boldsymbol{f} \end{bmatrix}$$

Recalling that the dot product of a force and a velocity is a power which is a coordinate-independent quantity, therefore, we have

$$\boldsymbol{\eta}_B^\top \boldsymbol{\mathcal{F}}_B = \boldsymbol{\eta}_A^\top \boldsymbol{\mathcal{F}}_A \tag{A.4}$$

where $\boldsymbol{\mathcal{F}}_A$ and $\boldsymbol{\mathcal{F}}_B$ represent the wrenches expressed in the frames $\{A\}$ and $\{B\}$, respectively. Substituting (A.2) into (A.4) yields

$$\boldsymbol{\eta}_B^\top \boldsymbol{\mathcal{F}}_B = (\mathrm{Ad}_{\boldsymbol{T}} \boldsymbol{\eta}_B)^\top \boldsymbol{\mathcal{F}}_A$$

which always holds for all $\boldsymbol{\eta}_B$, and simplifies to

$$\boldsymbol{\mathcal{F}}_B = \mathrm{Ad}_{\boldsymbol{T}}^\top \boldsymbol{\mathcal{F}}_{\mathrm{A}} \tag{A.5}$$

It can be seen from (A.5) that the relation of $\boldsymbol{\mathcal{F}}_A$ and $\boldsymbol{\mathcal{F}}_B$ is given by the Adjoint representation.

A.2 Newton–Euler Formulation

Typically, the dynamic equations for the robots are deduced by using one of two methods: by means of Newton's and Euler's dynamic equations, known as the Newton–Euler formulation for the rigid body, or by the Lagrangian dynamic formulation obtained from the kinetic and potential energy of the robot.

The Lagrangian dynamics is extremely effective for robots with fewer DoFs, however, the calculations will become cumbersome for the robots with more DoFs [143]. On the contrary, the Newton–Euler formulation yields efficient recursive algorithms for the forward or inverse dynamics which can also be assembled into closed-form analytical formulations.

It should be emphasized that the Newton–Euler formulation allows computationally efficient implementation, especially for the robots with more DoFs, without the need for differentiation. The resulting motion equations are the same as those derived by using the energy-based Lagrangian approach.

A.2.1 Dynamics of A Rigid Body

A rigid body can be regarded as composing of a number of rigidly connected particles, where the particle i has mass m_i. The vector $\boldsymbol{r}_i = [x_i, y_i, z_i]$ is the fixed location of i in the body frame, where the origin of this frame, called center of mass, is the point such that $\sum_i m_i \boldsymbol{r}_i = 0$. Assuming that the body is moving with a body twist $\boldsymbol{\eta}_B = (\boldsymbol{w}_B, \boldsymbol{v}_B)$, and the vector $\boldsymbol{p}_i$ is the time-varying position of m_i in the inertial frame, which is initially located at $\boldsymbol{r}_i$, we then have

$$\dot{\boldsymbol{p}}_i = \boldsymbol{v}_B + \boldsymbol{\omega}_B \times \boldsymbol{p}_i$$

$$\ddot{\boldsymbol{p}}_i = \dot{\boldsymbol{v}}_B + \dot{\boldsymbol{\omega}}_B \times \boldsymbol{p}_i + \boldsymbol{\omega}_B \times (\boldsymbol{v}_B + \boldsymbol{\omega}_B \times \boldsymbol{p}_i)$$

Replacing $\boldsymbol{p}_i$ on the right-hand side with $\boldsymbol{r}_i$ and adopting the skew-symmetric notation yield

$$\ddot{\boldsymbol{p}}_i = \dot{\boldsymbol{v}}_B + \widetilde{\dot{\boldsymbol{\omega}}}_B \boldsymbol{r}_i + \widetilde{\boldsymbol{\omega}}_B \boldsymbol{v}_B + \widetilde{\boldsymbol{\omega}}_B^2 \boldsymbol{r}_i$$

According to the statement of the Newton's second law, the force acting on the particle i is given by

$$\boldsymbol{f}_i = m_i(\dot{\boldsymbol{v}}_B + \widetilde{\dot{\boldsymbol{\omega}}}_B \boldsymbol{r}_i + \widetilde{\boldsymbol{\omega}}_B \boldsymbol{v}_B + \widetilde{\boldsymbol{\omega}}_B^2 \boldsymbol{r}_i)$$

and the torque is formulated as

$$\boldsymbol{m}_i = \widetilde{\boldsymbol{r}}_i \boldsymbol{f}_i$$

The total force and torque acting on the rigid body can be expressed as the wrench $\boldsymbol{\mathcal{F}}_B$:

$$\boldsymbol{\mathcal{F}}_B = \begin{bmatrix} \boldsymbol{m}_B \\ \boldsymbol{f}_B \end{bmatrix} = \begin{bmatrix} \sum_i \boldsymbol{m}_i \\ \sum_i \boldsymbol{f}_i \end{bmatrix}$$

For any vector $\boldsymbol{a}, \boldsymbol{b} \in \mathbb{R}^3, \widetilde{\boldsymbol{a}} = -\widetilde{\boldsymbol{a}}^\top$, $\widetilde{\boldsymbol{a}}\boldsymbol{b} = -\widetilde{\boldsymbol{b}}\boldsymbol{a}$, and $\widetilde{\boldsymbol{a}}\widetilde{\boldsymbol{b}} = (\widetilde{\boldsymbol{b}}\widetilde{\boldsymbol{a}})^\top$, the expressions for $\boldsymbol{f}_B$ and $\boldsymbol{m}_B$ can be simplified. Recalling that $\sum_i m_i \boldsymbol{r}_i = 0$, thus $\sum_i m_i \widetilde{\boldsymbol{r}}_i = 0$. In terms of the linear dynamics (Newton's equation), we have

$$\begin{aligned} \boldsymbol{f}_B &= \sum_i m_i(\dot{\boldsymbol{v}}_B + \widetilde{\dot{\boldsymbol{\omega}}}_B \boldsymbol{r}_i + \widetilde{\boldsymbol{\omega}}_B \boldsymbol{v}_B + \widetilde{\boldsymbol{\omega}}_B^2 \boldsymbol{r}_i) \\ &= \sum_i m_i(\dot{\boldsymbol{v}}_B + \widetilde{\boldsymbol{\omega}}_B \boldsymbol{v}_B) \underbrace{- \sum_i m_i \widetilde{\boldsymbol{r}}_i \dot{\boldsymbol{\omega}}_B - \sum_i m_i \widetilde{\boldsymbol{r}}_i \widetilde{\boldsymbol{\omega}}_B \boldsymbol{\omega}_B}_{0} = m(\dot{\boldsymbol{v}}_B + \widetilde{\boldsymbol{\omega}}_B \boldsymbol{v}_B) \end{aligned}$$

After that, focusing on the rotational dynamics (Euler's equation), we can obtain

$$\begin{aligned} \boldsymbol{m}_B &= \sum_i m_i \widetilde{\boldsymbol{r}}_i(\dot{\boldsymbol{v}}_B + \widetilde{\dot{\boldsymbol{\omega}}}_B \boldsymbol{r}_i + \widetilde{\boldsymbol{\omega}}_B \boldsymbol{v}_B + \widetilde{\boldsymbol{\omega}}_B^2 \boldsymbol{r}_i) \\ &= \underbrace{\sum_i m_i \widetilde{\boldsymbol{r}}_i \dot{\boldsymbol{v}}_B + \sum_i m_i \widetilde{\boldsymbol{r}}_i \widetilde{\boldsymbol{\omega}}_B \boldsymbol{v}_B}_{0} + \sum_i m_i \widetilde{\boldsymbol{r}}_i(\widetilde{\dot{\boldsymbol{\omega}}}_B \boldsymbol{r}_i + \widetilde{\boldsymbol{\omega}}_B^2 \boldsymbol{r}_i) \\ &= \sum_i m_i \widetilde{\boldsymbol{r}}_i(\widetilde{\dot{\boldsymbol{\omega}}}_B \boldsymbol{r}_i + \widetilde{\boldsymbol{\omega}}_B^2 \boldsymbol{r}_i) = \sum_i m_i(-\widetilde{\boldsymbol{r}}_i^2 \dot{\boldsymbol{\omega}}_B - \widetilde{\boldsymbol{r}}_i^{\mathrm{T}} \widetilde{\boldsymbol{\omega}}_B^{\mathrm{T}} \widetilde{\boldsymbol{r}}_i \boldsymbol{\omega}_B) \\ &= \sum_i m_i(-\widetilde{\boldsymbol{r}}_i^2 \dot{\boldsymbol{\omega}}_B - \widetilde{\boldsymbol{\omega}}_B \widetilde{\boldsymbol{r}}_i^2 \boldsymbol{\omega}_B) = \left(-\sum_i m_i \widetilde{\boldsymbol{r}}_i^2\right) \dot{\boldsymbol{\omega}}_B + \widetilde{\boldsymbol{\omega}}_B \left(-\sum_i m_i \widetilde{\boldsymbol{r}}_i^2\right) \boldsymbol{\omega}_B \\ &= \boldsymbol{\mathcal{I}}_B \dot{\boldsymbol{\omega}}_B + \widetilde{\boldsymbol{\omega}}_B \boldsymbol{\mathcal{I}}_B \boldsymbol{\omega}_B \end{aligned}$$

where $\boldsymbol{\mathcal{I}}_B = -\sum_i m_i \widetilde{\boldsymbol{r}}_i^2 \in \mathbb{R}^{3\times 3}$ is the rotational inertia matrix of the rigid body, and it is symmetric and positive definite matrix.

A.2.2 Twist-Wrench Formulation of Rigid-body Dynamics

The above linear and the rotational dynamics can be written as the following combined form:

$$\begin{bmatrix} \boldsymbol{m}_B \\ \boldsymbol{f}_B \end{bmatrix} = \begin{bmatrix} \boldsymbol{\mathcal{I}}_B & \mathbf{0} \\ \mathbf{0} & m\mathbf{I} \end{bmatrix} \begin{bmatrix} \dot{\boldsymbol{\omega}}_B \\ \dot{\boldsymbol{v}}_B \end{bmatrix} - \begin{bmatrix} \widetilde{\boldsymbol{\omega}}_B & \mathbf{0} \\ \widetilde{\boldsymbol{v}}_B & \widetilde{\boldsymbol{\omega}}_B \end{bmatrix}^\top \begin{bmatrix} \boldsymbol{\mathcal{I}}_B & \mathbf{0} \\ \mathbf{0} & m\mathbf{I} \end{bmatrix} \begin{bmatrix} \boldsymbol{\omega}_B \\ \boldsymbol{v}_B \end{bmatrix}$$

And then, each term of the above formulation can be specified by using the following definition and notation:

$$\boldsymbol{\mathcal{M}}_B = \begin{bmatrix} \boldsymbol{\mathcal{I}}_B & \mathbf{0} \\ \mathbf{0} & m\mathbf{I} \end{bmatrix}, \quad \mathrm{ad}_{\boldsymbol{\eta}_B} \triangleq \begin{bmatrix} \widetilde{\boldsymbol{\omega}}_B & \mathbf{0} \\ \widetilde{\boldsymbol{v}}_B & \widetilde{\boldsymbol{\omega}}_B \end{bmatrix} \in \mathbb{R}^{6\times 6}$$

Therefore, the rigid-body dynamics in the body frame can be written as

$$\boldsymbol{\mathcal{F}}_B = \boldsymbol{\mathcal{M}}_B \dot{\boldsymbol{\eta}}_B - \mathrm{ad}_{\boldsymbol{\eta}_B}^\top \boldsymbol{\mathcal{M}}_B \boldsymbol{\eta}_B \tag{A.6}$$

This equation gives a global description of the motion equations for a rigid body subject to the external wrench.

Appendix B

Lie Group Framework

Definition 4. *A group G is a set of elements g with a composition operation which satisfies the group axioms involving associativity, the neutral element, the inverse element, and closure. A Lie group G is a set that has compatible structures of a group and a smooth manifold. Compatible means that the natural maps defined on the group are smooth i.e. the maps $(f,h) \mapsto fh$ and $f \mapsto f^{-1}$ are smooth. The two requirements can be combined to the single requirement that the mapping $(f,h) \mapsto f^{-1}h$ be a smooth mapping of the product manifold into G.*

Therefore, mathematically speaking, a Lie group is a smooth and differentiable manifold equipped with a group structure such that the operations of group multiplication and inversion are smooth. Not every Lie group is isomorphic to a matrix Lie group. In this context, however, we have restricted our attention to matrix Lie groups for the purpose of minimizing prerequisites and keeping the discussion as concrete as possible.

Definition 5. *The Lie algebra $\mathfrak{g}$ is the tangent space at the identity of a Lie group. A finite-dimensional real or complex Lie algebra is a finite dimensional real or complex vector space $\mathfrak{g}$, together with a map $[\cdot,\cdot]$ from $\mathfrak{g} \times \mathfrak{g}$ into $\mathfrak{g}$ with the following properties:*

1. *Bilinearity: $[aX + bY, Z] = a[X,Z] + b[Y,Z]$, $[Z, aX + bY] = a[Z,X] + b[Z,Y]$, for all $X, Y, Z \in \mathfrak{g}$.*
2. *The Alternating property: $[X,X] = 0$ for all $X \in \mathfrak{g}$.*
3. *Anticommutativity: $[X,Y] = -[Y,X]$ for all $X, Y \in \mathfrak{g}$.*

where $\mathfrak{g}$ is a Lie algebra with bracket operation given by

$$[X,Y] = XY - YX$$

Definition 6. *If $\mathfrak{g}$ is a Lie algebra and X is an element of $\mathfrak{g}$, define a linear map $\mathrm{ad}_X : \mathfrak{g} \to \mathfrak{g}$ by*

$$\mathrm{ad}_X Y = [X,Y]$$

The map $X \mapsto \mathrm{ad}_X$ is the adjoint map or adjoint representation.

The adjoint representation (or adjoint action) of a Lie group G is a way of representing the elements of the group as linear transformations of the group's Lie algebra, considered as a vector space. Let $\psi : G \to \mathrm{Aut}(G)$ be the mapping $g \mapsto \psi_g$, with $\mathrm{Aut}(G)$ the automorphism group of G and $\psi_g : G \to G$ given by the inner automorphism (conjugation) $\psi_g(h) = ghg^{-1}$. This ψ is a Lie group homomorphism.

Since $g \mapsto \psi_g$ is a Lie group homomorphism, $g \mapsto \mathrm{Ad}_g$ is also a group homomorphism. Hence, the map $\mathrm{Ad} : G \to \mathrm{Aut}(\mathfrak{g}), g \mapsto \mathrm{Ad}_g$ is a group representation called the adjoint representation of G. Some properties of the adjoint representation is given by

$$(\mathrm{Ad}_g)^{-1} = \mathrm{Ad}_{g^{-1}}$$

$$\mathrm{Ad}_{g_1 g_2} = \mathrm{Ad}_{g_1} \mathrm{Ad}_{g_2}$$

It is a typical feature of Lie theory of continuous groups to associate Lie algebra and Lie groups by employing the matrix exponential map.

Bibliography

[1] R Cecchini and Giuseppe Pelosi. Alessandro volta and his battery. *IEEE Antennas and Propagation Magazine*, 34(2):30–37, 1992.

[2] Guillaume-Benjamin Duchenne. *Selections from the Clinical Works of Dr. Duchenne (de Boulogne).*, volume 105. New Sydenham Society, 1883.

[3] CS Hallpike and AF Rawdon-Smith. The "wever and bray phenomenon." a study of the electrical response in the cochlea with especial reference to its origin. *The Journal of Physiology*, 81(3):395, 1934.

[4] Marc D Eisen. Djourno, eyries, and the first implanted electrical neural stimulator to restore hearing. *Otology & neurotology*, 24(3):500–506, 2003.

[5] William F House. Cochlear implants. *Annals of Otology, Rhinology & Laryngology*, 85(3_suppl):3–3, 1976.

[6] William F House and Jack Urban. Long term results of electrode implantation and electronic stimulation of the cochlea in man. *Annals of Otology, Rhinology & Laryngology*, 82(4):504–517, 1973.

[7] Albert Mudry and Mara Mills. The early history of the cochlear implant: a retrospective. *JAMA otolaryngology–head & neck surgery*, 139(5):446–453, 2013.

[8] Robert J Fretz and Ralph P Fravel. Design and function: a physical and electrical description of the 3m house cochlear implant system. *Ear and Hearing*, 6(3):14S–19S, 1985.

[9] Richard M Warren. *Auditory perception: A new synthesis*, volume 109. Elsevier, 2013.

[10] Katherine Riojas et al. *Making cochlear-implant electrode array insertion less invasive, safer, and more effective through design, magnetic steering, and impedance sensing.* PhD thesis, 2021.

[11] Yehoash Raphael and Richard A Altschuler. Structure and innervation of the cochlea. *Brain research bulletin*, 60(5-6):397–422, 2003.

[12] Joseph B Nadol Jr. Hearing loss. *New England Journal of Medicine*, 329(15):1092–1102, 1993.

[13] AR Cody and IJ Russell. Outer hair cells in the mammalian cochlea and noise-induced hearing loss. *Nature*, 315(6021):662–665, 1985.

[14] Guang-Di Chen and Laurence D Fechter. The relationship between noise-induced hearing loss and hair cell loss in rats. *Hearing research*, 177(1-2):81–90, 2003.

[15] Kate Slade, Christopher J Plack, and Helen E Nuttall. The effects of age-related hearing loss on the brain and cognitive function. *Trends in Neurosciences*, 43(10):810–821, 2020.

[16] Olivier Macherey and Robert P Carlyon. Cochlear implants. *Current Biology*, 24(18):R878–R884, 2014.

[17] Charles C Finley, Timothy A Holden, Laura K Holden, Bruce R Whiting, Richard A Chole, Gail J Neely, Timothy E Hullar, and Margaret W Skinner. Role of electrode placement as a contributor to variability in cochlear implant outcomes. *Otology & neurotology*, 29(7):920–928, 2008.

[18] Anandhan Dhanasingh and Claude Jolly. An overview of cochlear implant electrode array designs. *Hearing research*, 356:93–103, 2017.

[19] Michelle Moran, Richard C Dowell, Claire Iseli, and Robert JS Briggs. Hearing preservation outcomes for 139 cochlear implant recipients using a thin straight electrode array. *Otology & Neurotology*, 38(5):678–684, 2017.

[20] Chiara Perazzini, Mathilde Puechmaille, Nicolas Saroul, Olivier Plainfossé, Laura Montrieul, Justine Bécaud, Laurent Gilain, Pascal Chabrot, Louis Boyer, and Thierry Mom. Fluoroscopy guided electrode-array insertion for cochlear implantation with straight electrode-arrays: a valuable tool in most cases. *European Archives of Oto-Rhino-Laryngology*, 278:965–975, 2021.

[21] Katherine E Riojas, Trevor L Bruns, Josephine Granna, Robert J Webster III, and Robert F Labadie. Robotic pullback technique of a precurved cochlear-implant electrode array using real-time impedance sensing feedback. *International Journal of Computer Assisted Radiology and Surgery*, 18(3):413–421, 2023.

[22] Arie Gordin, Blake Papsin, and Karen Gordon. Packing of the cochleostomy site affects auditory nerve response thresholds in precurved off-stylet cochlear implants. *Otology & Neurotology*, 31(2):204–209, 2010.

[23] Maura Cosetti and J Thomas Roland Jr. Cochlear implant electrode insertion. *Operative Techniques in Otolaryngology-Head and Neck Surgery*, 21(4):223–232, 2010.

[24] Jan Christoffer Luers and Karl-Bernd Hüttenbrink. Surgical anatomy and pathology of the middle ear. *Journal of anatomy*, 228(2):338–353, 2016.

[25] Robert F Labadie, Pallavi Chodhury, Ebru Cetinkaya, Ramya Balachandran, David S Haynes, Micahel R Fenlon, Andrzej S Jusczyzck, and J Michael Fitzpatrick. Minimally invasive, image-guided, facial-recess approach to the middle ear: demonstration of the concept of percutaneous cochlear access in vitro. *Otology & Neurotology*, 26(4):557–562, 2005.

[26] Adrien A Eshraghi, Ronen Nazarian, Fred F Telischi, Suhrud M Rajguru, Eric Truy, and Chhavi Gupta. The cochlear implant: historical aspects and future prospects. *The Anatomical Record: Advances in Integrative Anatomy and Evolutionary Biology*, 295(11):1967–1980, 2012.

[27] Laura K Holden, Jill B Firszt, Ruth M Reeder, Rosalie M Uchanski, Noël Y Dwyer, and Timothy A Holden. Factors affecting outcomes in cochlear implant recipients implanted with a perimodiolar electrode array located in scala tympani. *Otology & neurotology: official publication of the American Otological Society, American Neurotology Society [and] European Academy of Otology and Neurotology*, 37(10):1662, 2016.

[28] Teresa A Zwolan and Gregory Basura. Determining cochlear implant candidacy in adults: limitations, expansions, and opportunities for improvement. In *Seminars in Hearing*, volume 42, pages 331–341. Thieme Medical Publishers, Inc. 333 Seventh Avenue, 18th Floor, New York, NY ..., 2021.

[29] Ihab K Sefein. Surgical complications and morbidity in cochlear implantation. *The Egyptian Journal of Otolaryngology*, 34:33–41, 2018.

[30] Hans Martin Kjer. Modelling of the human inner ear anatomy and variability for cochlear implant applications. 2016.

[31] Saad Jwair, Adrianus Prins, Inge Wegner, Robert J Stokroos, Huib Versnel, and Hans GXM Thomeer. Scalar translocation comparison between lateral wall and perimodiolar cochlear implant arrays-a meta-analysis. *The Laryngoscope*, 131(6):1358–1368, 2021.

[32] Anandhan Dhanasingh and Claude Jolly. Review on cochlear implant electrode array tip fold-over and scalar deviation. *Journal of Otology*, 14(3):94–100, 2019.

[33] D Bradley Welling, Raul Hinojosa, Bruce J Gantz, and Jen-Tin Lee. Insertional trauma of multichannel cochlear implants. *The Laryngoscope*, 103(9):995–1001, 1993.

[34] Frank Risi. Considerations and rationale for cochlear implant electrode design-past, present and future. *The journal of international advanced otology*, 14(3):382, 2018.

[35] Daniele De Seta, Hannah Daoudi, Renato Torres, Evelyne Ferrary, Olivier Sterkers, and Yann Nguyen. Robotics, automation, active electrode arrays, and new devices for cochlear implantation: A contemporary review. *Hearing Research*, 414:108425, 2022.

[36] Marco Caversaccio, Kate Gavaghan, Wilhelm Wimmer, Tom Williamson, Juan Ansò, Georgios Mantokoudis, Nicolas Gerber, Christoph Rathgeb, Arne Feldmann, Franca Wagner, et al. Robotic cochlear implantation: surgical procedure and first clinical experience. *Acta oto-laryngologica*, 137(4):447–454, 2017.

[37] Renato Torres, Huan Jia, Mylène Drouillard, Jean-Loup Bensimon, Olivier Sterkers, Evelyne Ferrary, and Yann Nguyen. An optimized robot-based technique for cochlear implantation to reduce array insertion trauma. *Otolaryngology–Head and Neck Surgery*, 159(5):900–907, 2018.

[38] Jason Pile and Nabil Simaan. Modeling, design, and evaluation of a parallel robot for cochlear implant surgery. *IEEE/ASME Transactions on Mechatronics*, 19(6):1746–1755, 2014.

[39] Luca Ferrarini, Berit M Verbist, Hans Olofsen, Filiep Vanpoucke, Johan HM Frijns, Johan HC Reiber, and Faiza Admiraal-Behloul. Autonomous virtual mobile robot for three-dimensional medical image exploration: Application to micro-ct cochlear images. *Artificial Intelligence in Medicine*, 43(1):1–15, 2008.

[40] Jian Zhang, Wei Wei, Jienan Ding, J Thomas Roland Jr, Spiros Manolidis, and Nabil Simaan. Inroads toward robot-assisted cochlear implant surgery using steerable electrode arrays. *Otology & neurotology*, 31(8):1199–1206, 2010.

[41] Omid Majdani, Thomas S Rau, Stephan Baron, Hubertus Eilers, Claas Baier, Bodo Heimann, Tobias Ortmaier, Sönke Bartling, Thomas Lenarz, and Martin Leinung. A robot-guided minimally invasive approach for cochlear implant surgery: preliminary results of a temporal bone study. *International journal of computer assisted radiology and surgery*, 4:475–486, 2009.

[42] Jan-Philipp Kobler, Daniel Beckmann, Thomas S Rau, Omid Majdani, and Tobias Ortmaier. An automated insertion tool for cochlear implants with integrated force sensing capability. *International journal of computer assisted radiology and surgery*, 9:481–494, 2014.

[43] Daniel Schurzig, Robert F Labadie, Andreas Hussong, Thomas S Rau, and Robert J Webster III. Design of a tool integrating force sensing with automated insertion in cochlear implantation. *IEEE/ASME Transactions on mechatronics*, 17(2):381–389, 2011.

[44] Sykopetrites Vittoria, Ghizlene Lahlou, Renato Torres, Hannah Daoudi, Isabelle Mosnier, Stéphane Mazalaigue, Evelyne Ferrary, Yann Nguyen, and Olivier Sterkers. Robot-based assistance in middle ear surgery and cochlear implantation: first clinical report. *European Archives of Oto-Rhino-Laryngology*, 278:77–85, 2021.

[45] Ahmad Itawi, Sofiane Ghenna, Guillaume Tourrel, Sébastien Grondel, Cedric Plesse, Tran Minh Giao Nguyen, Frederic Vidal, Yinoussa Adagolodjo, Lingxiao Xun, Gang Zheng, et al. Smart electrode array for cochlear implants. In *2023 IEEE 36th International Conference on Micro Electro Mechanical Systems (MEMS)*, pages 452–455. IEEE, 2023.

[46] Lingxiao Xun, Gang Zheng, Sofiane Ghenna, Alexandre Kruszewski, Eric Cattan, Christian Duriez, and Sebastien Grondel. Modeling and control of conducting polymer actuator. *IEEE/ASME Transactions on Mechatronics*, 28(1):495–506, 2022.

[47] Daniel Bautista-Salinas, Mohamed EMK Abdelaziz, Burak Temelkuran, Eric M Yeatman, Charlie T Huins, and Ferdinando Rodriguez y Baena. Towards a functional atraumatic self-shaping cochlear implant. *Macromolecular Materials and Engineering*, 307(1):2100620, 2022.

[48] Josephine Granna, Thomas S Rau, Thien-Dang Nguyen, Thomas Lenarz, Omid Majdani, and Jessica Burgner-Kahrs. Toward automated cochlear implant insertion using tubular manipulators. In *Medical Imaging 2016: Image-Guided Procedures, Robotic Interventions, and Modeling*, volume 9786, pages 430–437. SPIE, 2016.

[49] Faqi Hu, Yu Xue, Jingkun Xu, and Baoyang Lu. Pedot-based conducting polymer actuators. *Frontiers in Robotics and AI*, 6:114, 2019.

[50] Thor Morales Bieze, Frederick Largilliere, Alexandre Kruszewski, Zhongkai Zhang, Rochdi Merzouki, and Christian Duriez. Finite element method-based kinematics and closed-loop control of soft, continuum manipulators. *Soft robotics*, 5(3):348–364, 2018.

[51] Gina Olson, Ross L Hatton, Julie A Adams, and Yiğit Mengüç. An euler–bernoulli beam model for soft robot arms bent through self-stress and external loads. *International Journal of Solids and Structures*, 207:113–131, 2020.

[52] Lukas Lindenroth, Junghwan Back, Adrian Schoisengeier, Yohan Noh, Helge Würdemann, Kaspar Althoefer, and Hongbin Liu. Stiffness-based modelling of a hydraulically-actuated soft robotics manipulator. In *2016 IEEE/RSJ International Conference on Intelligent Robots and Systems (IROS)*, pages 2458–2463. IEEE, 2016.

[53] Hareesh Godaba, Fabrizio Putzu, Taqi Abrar, Jelizaveta Konstantinova, and Kaspar Althoefer. Payload capabilities and operational limits of eversion robots. In *Towards Autonomous Robotic Systems: 20th Annual Conference, TAROS 2019, London, UK, July 3–5, 2019, Proceedings, Part II 20*, pages 383–394. Springer, 2019.

[54] Alyssa Novelia. *Discrete Elastic Rods for Simulating Soft Robot Limbs*. University of California, Berkeley, 2018.

[55] Hai-Jun Su. A pseudorigid-body 3r model for determining large deflection of cantilever beams subject to tip loads. 2009.

[56] Blake Jones, Seyed Alireza Rohani, Nelson Ong, Tarek Tayeh, Ahmad Chalabi, Sumit K Agrawal, and Hanif M Ladak. A virtual-reality training simulator for cochlear implant surgery. *Simulation & Gaming*, 50(2):243–258, 2019.

[57] Shaoping Huang, Deshan Meng, Xueqian Wang, Bin Liang, and Weining Lu. A 3d static modeling method and experimental verification of continuum robots based on pseudo-rigid body theory. In *2019 IEEE/RSJ International Conference on Intelligent Robots and Systems (IROS)*, pages 4672–4677. IEEE, 2019.

[58] Frederic Boyer and Federico Renda. Poincare's equations for cosserat media: Application to shells. *Journal of Nonlinear Science*, 27:1–44, 2017.

[59] Deng-Qing Cao and Robin W Tucker. Nonlinear dynamics of elastic rods using the cosserat theory: Modelling and simulation. *International Journal of Solids and Structures*, 45(2):460–477, 2008.

[60] Yin Haibin, Kong Cheng, Li Junfeng, and Yang Guilin. Modeling of grasping force for a soft robotic gripper with variable stiffness. *Mechanism and Machine Theory*, 128:254–274, 2018.

[61] John Daniel Till. On the statics, dynamics, and stability of continuum robots: Model formulations and efficient computational schemes. 2019.

[62] John Till, Vincent Aloi, and Caleb Rucker. Real-time dynamics of soft and continuum robots based on cosserat rod models. *The International Journal of Robotics Research*, 38(6):723–746, 2019.

[63] Federico Renda, Frédéric Boyer, Jorge Dias, and Lakmal Seneviratne. Discrete cosserat approach for multisection soft manipulator dynamics. *IEEE Transactions on Robotics*, 34(6):1518–1533, 2018.

[64] Frédéric Boyer, Vincent Lebastard, Fabien Candelier, and Federico Renda. Dynamics of continuum and soft robots: A strain parameterization based approach. *IEEE Transactions on Robotics*, 37(3):847–863, 2020.

[65] Federico Renda, Michele Giorelli, Marcello Calisti, Matteo Cianchetti, and Cecilia Laschi. Dynamic model of a multibending soft robot arm driven by cables. *IEEE Transactions on Robotics*, 30(5):1109–1122, 2014.

[66] Xiaotian Zhang, Fan Kiat Chan, Tejaswin Parthasarathy, and Mattia Gazzola. Modeling and simulation of complex dynamic musculoskeletal architectures. *Nature communications*, 10(1):4825, 2019.

[67] Daniela Rus and Michael T Tolley. Design, fabrication and control of soft robots. *Nature*, 521(7553):467–475, 2015.

[68] Olivier Goury, Yann Nguyen, Renato Torres, Jeremie Dequidt, and Christian Duriez. Numerical simulation of cochlear-implant surgery: towards patient-specific planning. In *Medical Image Computing and Computer-Assisted Intervention–MICCAI 2016: 19th International Conference, Athens, Greece, October 17-21, 2016, Proceedings, Part I 19*, pages 500–507. Springer, 2016.

[69] Pierre Schegg and Christian Duriez. Review on generic methods for mechanical modeling, simulation and control of soft robots. *Plos one*, 17(1):e0251059, 2022.

[70] David E Stewart. Rigid-body dynamics with friction and impact. *SIAM review*, 42(1):3–39, 2000.

[71] Tamer M Wasfy and Ahmed K Noor. Computational strategies for flexible multibody systems. *Appl. Mech. Rev.*, 56(6):553–613, 2003.

[72] A Munjiza and KRF Andrews. Penalty function method for combined finite–discrete element systems comprising large number of separate bodies. *International Journal for numerical methods in engineering*, 49(11):1377–1396, 2000.

[73] Jonas Spillmann, Markus Becker, and Matthias Teschner. Non-iterative computation of contact forces for deformable objects. 2007.

[74] Victor J Milenkovic and Harald Schmidl. Optimization-based animation. In *Proceedings of the 28th annual conference on Computer graphics and interactive techniques*, pages 37–46, 2001.

[75] Danny M Kaufman, Timothy Edmunds, and Dinesh K Pai. Fast frictional dynamics for rigid bodies. In *ACM SIGGRAPH 2005 Papers*, pages 946–956. 2005.

[76] David E Stewart and Jeffrey C Trinkle. An implicit time-stepping scheme for rigid body dynamics with inelastic collisions and coulomb friction. *International Journal for Numerical Methods in Engineering*, 39(15):2673–2691, 1996.

[77] Kenny Erleben. Velocity-based shock propagation for multibody dynamics animation. *ACM Transactions on Graphics (TOG)*, 26(2):12–es, 2007.

[78] Christian Duriez, Frederic Dubois, Abderrahmane Kheddar, and Claude Andriot. Realistic haptic rendering of interacting deformable objects in virtual environments. *IEEE transactions on visualization and computer graphics*, 12(1):36–47, 2005.

[79] Miguel A Otaduy, Rasmus Tamstorf, Denis Steinemann, and Markus Gross. Implicit contact handling for deformable objects. In *Computer Graphics Forum*, volume 28, pages 559–568. Wiley Online Library, 2009.

[80] David Harmon, Etienne Vouga, Breannan Smith, Rasmus Tamstorf, and Eitan Grinspun. Asynchronous contact mechanics. In *ACM SIGGRAPH 2009 papers*, pages 1–12. 2009.

[81] Sarah Niebe and Kenny Erleben. Numerical methods for linear complementarity problems in physics-based animation. *Synthesis Lectures on Computer Graphics and Animation*, 7(1):1–159, 2015.

[82] Pierre Alart and Alain Curnier. A mixed formulation for frictional contact problems prone to newton like solution methods. *Computer methods in applied mechanics and engineering*, 92(3):353–375, 1991.

[83] Alain Curnier and Pierre Alart. A generalized newton method for contact problems with friction. *Journal de mécanique théorique et appliquée*, 1988.

[84] Steven P Dirkse and Michael C Ferris. The path solver: a nommonotone stabilization scheme for mixed complementarity problems. *Optimization methods and software*, 5(2):123–156, 1995.

[85] Florence Bertails-Descoubes, Florent Cadoux, Gilles Daviet, and Vincent Acary. A non-smooth newton solver for capturing exact coulomb friction in fiber assemblies. *ACM Transactions on Graphics (TOG)*, 30(1):1–14, 2011.

[86] Gilles Daviet, Florence Bertails-Descoubes, and Laurence Boissieux. A hybrid iterative solver for robustly capturing coulomb friction in hair dynamics. In *Proceedings of the 2011 SIGGRAPH Asia Conference*, pages 1–12, 2011.

[87] Danny M Kaufman, Rasmus Tamstorf, Breannan Smith, Jean-Marie Aubry, and Eitan Grinspun. Adaptive nonlinearity for collisions in complex rod assemblies. *ACM Transactions on Graphics (TOG)*, 33(4):1–12, 2014.

[88] Vincent Acary and Bernard Brogliato. *Numerical methods for nonsmooth dynamical systems: applications in mechanics and electronics*. Springer Science & Business Media, 2008.

[89] Gagan Kaur, Raju Adhikari, Peter Cass, Mark Bown, and Pathiraja Gunatillake. Electrically conductive polymers and composites for biomedical applications. *Rsc Advances*, 5(47):37553–37567, 2015.

[90] Hao He, Lei Zhang, Xin Guan, Hanlin Cheng, Xixia Liu, Suzhu Yu, Jun Wei, and Jianyong Ouyang. Biocompatible conductive polymers with high conductivity and high stretchability. *ACS applied materials & interfaces*, 11(29):26185–26193, 2019.

[91] Elisabeth Smela. Conjugated polymer actuators for biomedical applications. *Advanced materials*, 15(6):481–494, 2003.

[92] Toribio Fernández Otero. Towards artificial proprioception from artificial muscles constituted by self-sensing multi-step electrochemical macromolecular motors. *Electrochimica Acta*, 368:137576, 2021.

[93] Frédéric Vidal, Cédric Plesse, Dominique Teyssié, and Claude Chevrot. Long-life air working conducting semi-ipn/ionic liquid based actuator. *Synthetic Metals*, 142(1-3):287–291, 2004.

[94] M Ghaffari, W Kinsman, Y Zhou, S Murali, Q Burlingame, M Lin, RS Ruoff, and QM Zhang. Retracted: Aligned nano-porous microwave exfoliated graphite oxide ionic actuators with high strain and elastic energy density. *Advanced Materials*, 25(43):6277–6283, 2013.

[95] Lauréline Seurre, Kätlin Rohtlaid, Giao TM Nguyen, Caroline Soyer, Sofiane Ghenna, Sébastien Grondel, Frédéric Vidal, Barthélemy Cagneau, Cédric Plesse, and Eric Cattan. Demonstrating full integration process for electroactive polymer microtransducers to realize soft microchips. In *2020 IEEE 33rd International Conference on Micro Electro Mechanical Systems (MEMS)*, pages 917–920. IEEE, 2020.

[96] Indrek Must, Veiko Vunder, Friedrich Kaasik, Inga Põldsalu, Urmas Johanson, Andres Punning, and Alvo Aabloo. Ionic liquid-based actuators working in air: The effect of ambient humidity. *Sensors and Actuators B: Chemical*, 202:114–122, 2014.

[97] Kwang J Kim and Satoshi Tadokoro. Electroactive polymers for robotic applications. *Artificial Muscles and Sensors*, 23:291, 2007.

[98] Cédric Plesse, Frédéric Vidal, Hyacinthe Randriamahazaka, Dominique Teyssié, and Claude Chevrot. Synthesis and characterization of conducting interpenetrating polymer networks for new actuators. *Polymer*, 46(18):7771–7778, 2005.

[99] Kätlin Rohtlaid, Lauréline Seurre, Giao TM Nguyen, Garrett Curley, Caroline Soyer, Sébastien Grondel, Frédéric Vidal, Cédric Plesse, and Eric Cattan. Pedot: Pss-based micromuscles and microsensors fully integrated in flexible chips. *Smart Materials and Structures*, 29(9):09LT01, 2020.

[100] Chuc Huu Nguyen, Gursel Alici, and Gordon Wallace. An advanced mathematical model and its experimental verification for trilayer conjugated polymer actuators. *IEEE/ASME Transactions on Mechatronics*, 19(4):1279–1288, 2013.

[101] A Mazzoldi, A Della Santa, and D De Rossi. Conducting polymer actuators: Properties and modeling. In *Polymer sensors and actuators*, pages 207–244. Springer, 2000.

[102] Meisam Farajollahi, Farrokh Sassani, Naser Naserifar, Adelyne Fannir, Cédric Plesse, Giao TM Nguyen, Frédéric Vidal, and John DW Madden. Characterization and dynamic charge dependent modeling of conducting polymer trilayer bending. *Smart Materials and Structures*, 25(11):115044, 2016.

[103] Meisam Farajollahi, Ashwin Usgaocar, Yuta Dobashi, Vincent Woehling, Cédric Plesse, Frédéric Vidal, Farrokh Sassani, and John DW Madden. Nonlinear two-dimensional transmission line models for electrochemically driven conducting polymer actuators. *IEEE/ASME Transactions on Mechatronics*, 22(2):705–716, 2016.

[104] Gou Nishida, Kentaro Takagi, Bernhard Maschke, and Takaaki Osada. Multi-scale distributed parameter modeling of ionic polymer-metal composite soft actuator. *Control Engineering Practice*, 19(4):321–334, 2011.

[105] Amir Ali Amiri Moghadam, Abbas Kouzani, Keivan Torabi, Akif Kaynak, and Mohsen Shahinpoor. Development of a novel soft parallel robot equipped with polymeric artificial muscles. *Smart Materials and Structures*, 24(3):035017, 2015.

[106] Ning Liu, Yongxin Wu, and Yann Le Gorrec. Energy-based modeling of ionic polymer–metal composite actuators dedicated to the control of flexible structures. *IEEE/ASME Transactions on Mechatronics*, 26(6):3139–3150, 2021.

[107] Jasim Khawwaf, Jinchuan Zheng, Rifai Chai, Renquan Lu, and Zhihong Man. Adaptive microtracking control for an underwater ipmc actuator using new hyperplane-based sliding mode. *IEEE/ASME Transactions on Mechatronics*, 24(5):2108–2117, 2019.

[108] Gunesh P Rajan, Georgios Kontorinis, and Jafri Kuthubutheen. The effects of insertion speed on inner ear function during cochlear implantation: a comparison study. *Audiology and Neurotology*, 18(1):17–22, 2012.

[109] Kush Panara, David Shahal, Rahul Mittal, and Adrien A Eshraghi. Robotics for cochlear implantation surgery: challenges and opportunities. *Otology & neurotology*, 42(7):e825–e835, 2021.

[110] Frederic Venail, Brett Bell, Mohamed Akkari, Wilhelm Wimmer, Tom Williamson, Nicolas Gerber, Kate Gavaghan, Francois Canovas, Stefan Weber, Marco Caversaccio, et al. Manual electrode array insertion through a robot-assisted minimal invasive cochleostomy: feasibility and comparison of two different electrode array subtypes. *Otology & neurotology*, 36(6):1015–1022, 2015.

[111] Robert Frederick Labadie, Jack H Noble, Benoit M Dawant, Ramya Balachandran, Omid Majdani, and J Michael Fitzpatrick. Clinical validation of percutaneous cochlear implant surgery: initial report. *The Laryngoscope*, 118(6):1031–1039, 2008.

[112] Wilhelm Wimmer, Frederic Venail, Tom Williamson, Mohamed Akkari, Nicolas Gerber, Stefan Weber, Marco Caversaccio, Alain Uziel, Brett Bell, et al. Semiautomatic cochleostomy target and insertion trajectory planning for minimally invasive cochlear implantation. *BioMed research international*, 2014, 2014.

[113] Mathieu Miroir, Yann Nguyen, Guillaume Kazmitcheff, Evelyne Ferrary, Olivier Sterkers, and Alexis Bozorg Grayeli. Friction force measurement during cochlear implant insertion: application to a force-controlled insertion tool design. *Otology & neurotology*, 33(6):1092–1100, 2012.

[114] Haihong Li, Lingxiao Xun, and Gang Zheng. Piecewise linear strain cosserat model for soft slender manipulator. *IEEE Transactions on Robotics*, pages 1–18, 2023.

[115] Frederic Boyer, Vincent Lebastard, Fabien Candelier, and Federico Renda. Dynamics of continuum and soft robots: A strain parameterization based approach. *IEEE Transactions on Robotics*, 37(3):847–863, 2021.

[116] Ngoc Tan Nguyen, Yuta Dobashi, Caroline Soyer, Cédric Plesse, Giao TM Nguyen, Frédéric Vidal, Eric Cattan, Sébastien Grondel, and John DW Madden. Nonlinear dynamic modeling of ultrathin conducting polymer actuators including inertial effects. *Smart Materials and Structures*, 27(11):115032, 2018.

[117] Yuan Hang Cheng and Jing Wang. A motion image detection method based on the inter-frame difference method. In *Applied Mechanics and Materials*, volume 490, pages 1283–1286. Trans Tech Publ, 2014.

[118] Feng Zhao and Xiaoou Tang. Preprocessing and postprocessing for skeleton-based fingerprint minutiae extraction. *Pattern Recognition*, 40(4):1270–1281, 2007.

[119] Lingxiao Xun, Gang Zheng, Sofiane Ghenna, Alexandre Kruszewski, Éric Cattan, Christian Duriez, and Sébastien Grondel. Modeling and control of conducting polymer actuator. *IEEE/ASME Transactions on Mechatronics*, 28(1):495–506, 2023.

[120] Federico Renda, Frédéric Boyer, Jorge Dias, and Lakmal Seneviratne. Discrete cosserat approach for multisection soft manipulator dynamics. *IEEE Transactions on Robotics*, 34(6):1518–1533, 2018.

[121] Hartmut Prautzsch, Wolfgang Boehm, and Marco Paluszny. *Bézier and B-spline techniques*, volume 6. Springer, 2002.

[122] Kenneth Langstreth Johnson and Kenneth Langstreth Johnson. *Contact mechanics*. Cambridge university press, 1987.

[123] Costanza Armanini, Irfan Hussain, Muhammad Zubair Iqbal, Dongming Gan, Domenico Prattichizzo, and Federico Renda. Discrete cosserat approach for closed-chain soft robots: Application to the fin-ray finger. *IEEE Transactions on Robotics*, 37(6):2083–2098, 2021.

[124] Peter Wriggers and Tod A Laursen. *Computational contact mechanics*, volume 2. Springer, 2006.

[125] Evan Drumwright and Dylan A Shell. Modeling contact friction and joint friction in dynamic robotic simulation using the principle of maximum dissipation. In *Algorithmic Foundations of Robotics IX: Selected Contributions of the Ninth International Workshop on the Algorithmic Foundations of Robotics*, pages 249–266. Springer, 2011.

[126] Olvi L Mangasarian. Equivalence of the complementarity problem to a system of nonlinear equations. *SIAM Journal on Applied Mathematics*, 31(1):89–92, 1976.

[127] Aurél Galántai. Properties and construction of ncp functions. *Computational Optimization and Applications*, 52:805–824, 2012.

[128] Olvi Mangasarian and Chunhui Chen. A class of smoothing functions for nonlinear and mixed complementarity problems. Technical report, 1994.

[129] David M Landsberger, Maja Svrakic, J Thomas Roland Jr, and Mario Svirsky. The relationship between insertion angles, default frequency allocations, and spiral ganglion place pitch in cochlear implants. *Ear and hearing*, 36(5):e207–e213, 2015.

[130] Philipp Aebischer, Georgios Mantokoudis, Stefan Weder, Lukas Anschuetz, Marco Caversaccio, and Wilhelm Wimmer. In-vitro study of speed and alignment angle in cochlear implant electrode array insertions. *IEEE transactions on biomedical engineering*, 69(1):129–137, 2021.

[131] Abdul Afram and Farrokh Janabi-Sharifi. Theory and applications of hvac control systems–a review of model predictive control (mpc). *Building and Environment*, 72:343–355, 2014.

[132] Christian Kirches, Leonard Wirsching, Hans Georg Bock, and Johannes P Schlöder. Efficient direct multiple shooting for nonlinear model predictive control on long horizons. *Journal of Process Control*, 22(3):540–550, 2012.

[133] Lorenz T Biegler. Efficient solution of dynamic optimization and nmpc problems. In *Nonlinear model predictive control*, pages 219–243. Springer, 2000.

[134] Immanuel M Bomze, Vladimir F Demyanov, Roger Fletcher, Tamás Terlaky, and Roger Fletcher. The sequential quadratic programming method. *Nonlinear Optimization: Lectures given at the CIME Summer School held in Cetraro, Italy, July 1-7, 2007*, pages 165–214, 2010.

[135] Gade Pandu Rangaiah. *Multi-objective optimization: techniques and applications in chemical engineering*, volume 5. world scientific, 2016.

[136] Robert F Labadie, Ramya Balachandran, Jack H Noble, Grégoire S Blachon, Jason E Mitchell, Fitsum A Reda, Benoit M Dawant, and J Michael Fitzpatrick. Minimally invasive image-guided cochlear implantation surgery: first report of clinical implementation. *The Laryngoscope*, 124(8):1915–1922, 2014.

[137] Fitsum A Reda, Theodore R McRackan, Robert F Labadie, Benoit M Dawant, and Jack H Noble. Automatic segmentation of intra-cochlear anatomy in post-implantation ct of unilateral cochlear implant recipients. *Medical image analysis*, 18(3):605–615, 2014.

[138] Christopher J Long, Timothy A Holden, Gary H McClelland, Wendy S Parkinson, Clough Shelton, David C Kelsall, and Zachary M Smith. Examining the electro-neural interface of cochlear implant users using psychophysics, ct scans, and speech understanding. *Journal of the Association for Research in Otolaryngology*, 15:293–304, 2014.

[139] Alice Barbara Auinger, Valerie Dahm, Rudolfs Liepins, Dominik Riss, Wolf-Dieter Baumgartner, and Christoph Arnoldner. Robotic cochlear implant surgery: imaging-based evaluation of feasibility in clinical routine. *Frontiers in Surgery*, 8:742219, 2021.

[140] Renato Torres, Guillaume Kazmitcheff, Daniele Bernardeschi, Daniele De Seta, Jean Loup Bensimon, Evelyne Ferrary, Olivier Sterkers, and Yann Nguyen. Variability of the mental representation of the cochlear anatomy during cochlear implantation. *European Archives of Oto-Rhino-Laryngology*, 273:2009–2018, 2016.

[141] Stanislao Grazioso, Giuseppe Di Gironimo, and Bruno Siciliano. A geometrically exact model for soft continuum robots: The finite element deformation space formulation. *Soft robotics*, 6(6):790–811, 2019.

[142] Richard M Murray, Zexiang Li, and S Shankar Sastry. *A mathematical introduction to robotic manipulation*. CRC press, 2017.

[143] Kevin M Lynch and Frank C Park. *Modern robotics*. Cambridge University Press, 2017.

Résumé

Selon les statistiques de l'Organisation Mondiale de la Santé, plus de 5% de la population mondiale, soit 360 millions de personnes, souffrent d'une perte auditive invalidante (328 millions d'adultes et 32 millions d'enfants). Les aides auditives sont utilisées avec succès pour les personnes partiellement malentendantes. Les aides auditives traditionnelles, bien qu'efficaces pour la perte auditive partielle, sont souvent insuffisantes pour les individus souffrant de surdité sévère. Dans de tels cas, la chirurgie d'implant cochléaire s'impose comme une solution préférable. Cependant, l'implantation manuelle traditionnelle se heurte aux complexités de l'anatomie humaine et aux subtilités des procédures. Parmi les principaux défis figurent les risques de lésions des structures sensibles telles que le nerf facial et la propension de l'électrode à se plier à l'intérieur de la cochlée, empêchant ainsi une implantation complète. Malgré la précision des techniques manuelles, la visibilité limitée et la forte dépendance à la stabilité et à l'expertise du chirurgien comportent intrinsèquement des risques.

Ces dernières années, des avancées significatives ont été réalisées dans la technologie des implants cochléaires, notamment dans la modélisation mécanique, la simulation et le contrôle. Cependant, des défis tels que la complexité computationnelle et la précision des simulations persistent. Cette thèse détaille des progrès substantiels dans la technologie des Implants Cochléaires Actifs (ICA).

Le Chapitre 1 de cette thèse offre une introduction approfondie au contexte du sujet étudié. Il se concentre sur les implants cochléaires actifs, en détaillant l'origine et l'évolution des implants cochléaires, leur principe de fonctionnement, ainsi que l'état actuel des techniques chirurgicales utilisées pour leur implantation. Ce chapitre examine également les défis majeurs auxquels cette technologie est confrontée, tels que les limitations techniques, les complications chirurgicales et les variations des résultats chez les patients. En réponse à ces défis, nous proposons des solutions innovantes et des stratégies de recherche visant à améliorer l'efficacité et la fiabilité des implants cochléaires. Ainsi, ce chapitre pose les bases pour une compréhension complète des enjeux et des avancées dans le domaine des implants cochléaires actifs, tout en mettant en lumière les perspectives futures de cette technologie révolutionnaire.

Dans le chapitre 2 de cette thèse, nous avons considérablement avancé les Implants Cochléaires Actifs en améliorant leur modélisation systémique. Notre principale réalisation a été le développement d'un modèle mécanique sophistiqué pour l'Array d'Électrodes (EA), combinant la théorie des tiges de Cosserat avec l'intégration de groupe de Lie. Cela a résulté en un modèle qui reflète avec précision le système réel avec une complexité réduite et excelle dans la gestion des dynamiques non linéaires. Nous avons également créé un modèle électro-mécanique pour le Polymère Conducteur Électronique (ECP), simplifiant les complexités et contrôlant précisément les déformations. Une méthode innovante d'identification de paramètres et un système d'identification visuelle personnalisé ont été introduits pour adresser les incertitudes des paramètres physiques. Le chapitre se termine par un modèle de couplage complet intégrant les composants EA et ECP, marquant un bond significatif dans le contrôle basé sur modèle pour les ICA. Ces

développements ouvrent la voie à des modèles d'implants cochléaires plus raffinés, efficaces et efficaces, préparant le terrain pour la recherche future dans ce domaine.

Le chapitre 3 présente un modèle pionnier de dynamique de contact pour les robots mous, basé sur la théorie de Cosserat. Dans ce chapitre, nous nous appuyons sur le modèle mécanique de l'array d'électrodes introduit dans le chapitre deux. Nous étendons le modèle de Cosserat pour englober les phénomènes de contact, établissant un modèle de contact détaillé entre l'array d'électrodes et la paroi cochléaire. Ce développement comprend l'identification des instances de contact, l'analyse des forces de contact et de friction, le tout intégré de manière complexe avec le modèle de poutre de Cosserat. Le modèle de contact fournit une analyse détaillée des relations géométriques complexes, des forces et des moments aux points de contact, cruciaux pour comprendre la dynamique des robots mous et particulièrement vitaux dans la technologie des implants cochléaires. Nous avons réussi à établir et à affiner les contraintes de contact, incorporant la non-pénétration, l'équilibre des forces et les interactions frictionnelles. Ces avancées permettent une résolution directe du système de dynamique de contact, améliorant considérablement la précision et la fiabilité du modèle, comme validé contre des résultats empiriques. Ce modèle est non seulement crucial pour améliorer la conception et les stratégies de contrôle des implants cochléaires, mais marque également un progrès significatif dans le domaine des robots minces et souples. À l'avenir, nous visons à étendre ce cadre pour inclure des robots avec des mécanismes d'actuation intégrés, tels que les systèmes entraînés par câble, tendon ou aimant, élargissant ainsi le champ de notre recherche en contrôle et simulation d'implants cochléaires. Ce travail fait non seulement progresser la technologie des implants cochléaires mais ouvre également de nouvelles voies dans l'application de la robotique souple.

Dans le chapitre 4 de notre recherche, nous avons développé et évalué divers contrôleurs optimaux pour l'implantation cochléaire, adaptés aux besoins spécifiques des implants cochléaires passifs et actifs. Pour les implants passifs, qui manquent d'actuateurs internes, nous avons introduit un contrôleur de trajectoire optimal qui approfondit considérablement l'implantation, améliorant potentiellement les résultats auditifs. Pour les implants actifs, équipés d'actuateurs, nous avons élaboré un contrôleur basé sur la commande prédictive de modèle visant à garantir un suivi de trajectoire précis dans la cochlée. Cela est crucial pour prévenir les dommages pendant l'implantation en évitant le contact avec les parois cochléaires. De plus, reconnaissant les scénarios où le nombre d'actuateurs pourrait être insuffisant, nous avons innové un contrôleur optimal hybride qui combine les deux approches et inclut le modèle de contact. Ce système hybride gère habilement le chemin d'implantation et les entrées des actuateurs, réduisant considérablement la force de contact et minimisant ainsi les dommages cochléaires, optimisant le processus d'implantation dans son ensemble. Ce chapitre signifie un progrès pivot dans la technologie des implants cochléaires, offrant des stratégies de contrôle sophistiquées pour améliorer la sécurité et l'efficacité des procédures d'implant cochléaire.

Le chapitre 5 constitue une conclusion et des perspectives, résumant les principales avancées dans la technologie des implants cochléaires actifs et explorant les orientations futures de la recherche. Dans les chapitres précédents, nous avons détaillé le modèle mécanique des implants cochléaires, le modèle de dynamique de contact, ainsi que le développement de contrôleurs optimisés, des avancées qui visent à améliorer la performance et la sécurité des implants cochléaires.

La partie conclusion de ce chapitre revoit les progrès significatifs réalisés dans la technologie des implants cochléaires, notamment en modélisation mécanique, simulation et contrôle, tout en mentionnant les défis tels que la complexité computationnelle et la précision des simulations. Ensuite, plusieurs directions de recherche futures sont proposées, incluant la création de modèles tridimensionnels spécifiques à la cochlée des patients, qui aideraient à personnaliser les stratégies chirurgicales, ainsi que la modélisation d'autres structures anatomiques de l'oreille interne, cruciale pour la planification et la réalisation des interventions chirurgicales.

De plus, nous prévoyons de transposer les résultats obtenus en environnement simulé à des essais cliniques réels, notamment à travers des études sur des animaux afin de tester les nouvelles technologies en conditions pratiques. Ces essais permettront de valider les améliorations technologiques et d'évaluer leur impact sur le fonctionnement des implants cochléaires dans des situations réelles. Enfin, ce chapitre explore également les applications potentielles de ces technologies dans d'autres interventions médicales nécessitant une modélisation et un contrôle précis. Parmi ces interventions figurent les chirurgies ventriculoscopiques, les interventions de cathétérisation cardiaque, les chirurgies neurochirurgicales mini-invasives et les interventions endoscopiques gastro-intestinales. L'extension de ces technologies à d'autres domaines médicaux pourrait révolutionner les techniques chirurgicales et améliorer les résultats pour les patients. En somme, ce chapitre ne se contente pas de récapituler les résultats de la recherche sur la technologie des implants cochléaires, mais offre également des orientations claires et une vision étendue pour les recherches et applications futures. Il met en lumière les perspectives d'amélioration continue et les possibilités d'innovation dans le domaine des implants cochléaires et au-delà.

Dans l'ensemble, cette thèse fait progresser la technologie ICA, jetant les bases pour des travaux futurs et améliorant les expériences auditives pour les bénéficiaires de l'implant cochléaire. Les méthodologies et les perspectives de cette étude ouvrent la voie à des modèles de l'implant cochléaire plus raffinés, efficaces et efficaces, contribuant de manière significative au domaine.

Modélisation et Commande de L'implant Cochléaire Active

Résumé en français

Selon les statistiques de l'Organisation Mondiale de la Santé, plus de 5% de la population mondiale, soit 360 millions de personnes, souffre de pertes auditives invalidantes. Les aides auditives traditionnelles ne sont généralement pas suffisantes pour ceux atteints de surdité sévère, rendant la chirurgie d'implant cochléaire une meilleure solution. Cependant, l'implantation manuelle traditionnelle est confrontée à des défis dus à la complexité de l'anatomie humaine et aux détails procéduraux, tels que le risque de dommages au nerf facial et la tendance de l'array d'électrodes à se courber dans la cochlée. Pour résoudre ces problèmes, cette thèse propose un nouveau modèle électronique et mécanique utilisant la théorie des tiges de Cosserat, qui réduit la complexité et améliore la simulation et le contrôle en temps réel par rapport aux modèles traditionnels à éléments finis. La recherche innove également dans l'identification des paramètres en intégrant un système visuel pour mesurer la courbure de l'actuateur, dérivant ainsi les paramètres physiques à travers un nouveau modèle de couplage électro-mécanique non linéaire. De plus, nous développons un système de contrôle optimisé basé sur le nouveau modèle électro-mécanique. Des tests rigoureux par des expériences et des simulations ont prouvé son efficacité pour améliorer la précision et la sécurité des chirurgies d'implant cochléaire.

Mots-clefs: Chirurgie de l'implant cochléaire, l'array d'électrodes , théorie des tiges de Cosserat, commande.

Summary in English

According to the World Health Organization's statistics, over 5% of the global population, or 360 million people, suffer from disabling hearing loss. Traditional hearing aids typically do not suffice for those with severe deafness, making cochlear implant surgery a better solution. However, traditional manual implantation faces challenges due to the complexities of human anatomy and procedural details, such as the risk of damaging the facial nerve and the tendency of the electrode array to bend within the cochlea. To address these issues, this thesis proposes a new electronic and mechanical model using Cosserat rod theory, which reduces complexity and improves real-time simulation and control compared to traditional finite element models. The research also innovates in parameter identification by integrating a visual system to measure actuator curvature, thus deriving physical parameters through a novel nonlinear electro-mechanical coupling model. Additionally, we develops an optimized control system based on the new electro-mechanical model. Rigorous testing through experiments and simulations has proven its effectiveness in enhancing the precision and safety of cochlear implant surgeries.

Keywords: Cochlear implant surgery, electrode array, Cosserat rod theory, control.